

Magazine of Civil Engineering

108(8), 2021

ISSN
2712-8172





ПОЛИТЕХ
Санкт-Петербургский
политехнический университет
Петра Великого

Инженерно-строительный институт
Центр дополнительных профессиональных программ
195251, г. Санкт-Петербург, Политехническая ул., 29,
тел/факс: 552-94-60, www.stroikursi.spbstu.ru,
stroikursi@mail.ru

**Приглашает специалистов организаций, вступающих в СРО,
на курсы повышения квалификации (72 часа)**

Код	Наименование программы	Виды работ*
Курсы по строительству		
БС-01-04	«Безопасность и качество выполнения общестроительных работ»	п.1,2, 3, 5, 6, 7, 9, 10, 11, 12, 13, 14
БС-01	«Безопасность и качество выполнения геодезических, подготовительных и земляных работ, устройства оснований и фундаментов»	1,2,3,5
БС-02	«Безопасность и качество возведения бетонных и железобетонных конструкций»	6,7
БС-03	«Безопасность и качество возведения металлических, каменных и деревянных конструкций»	9,10,11
БС-04	«Безопасность и качество выполнения фасадных работ, устройства кровель, защиты строительных конструкций, трубопроводов и оборудования»	12,13,14
БС-05	«Безопасность и качество устройства инженерных сетей и систем»	15,16,17,18,19
БС-06	«Безопасность и качество устройства электрических сетей и линий связи»	20,21
БС-08	«Безопасность и качество выполнения монтажных и пусконаладочных работ»	23,24
БС-12	«Безопасность и качество устройства мостов, эстакад и путепроводов»	29
БС-13	«Безопасность и качество выполнения гидротехнических, водолазных работ»	30
БС-14	«Безопасность и качество устройства промышленных печей и дымовых труб»	31
БС-15	«Осуществление строительного контроля»	32
БС-16	«Организация строительства, реконструкции и капитального ремонта. Выполнение функций технического заказчика и генерального подрядчика»	33
Курсы по проектированию		
БП-01	«Разработка схемы планировочной организации земельного участка, архитектурных решений, мероприятий по обеспечению доступа маломобильных групп населения»	1,2,11
БП-02	«Разработка конструктивных и объемно-планировочных решений зданий и сооружений»	3
БП-03	«Проектирование внутренних сетей инженерно-технического обеспечения»	4
БП-04	«Проектирование наружных сетей инженерно-технического обеспечения»	5
БП-05	«Разработка технологических решений при проектировании зданий и сооружений»	6
БП-06	«Разработка специальных разделов проектной документации»	7
БП-07	«Разработка проектов организации строительства»	8
БП-08	«Проектные решения по охране окружающей среды»	9
БП-09	«Проектные решения по обеспечению пожарной безопасности»	10
БП-10	«Обследование строительных конструкций и грунтов основания зданий и сооружений»	12
БП-11	«Организация проектных работ. Выполнение функций генерального проектировщика»	13
Э-01	«Проведение энергетических обследований с целью повышения энергетической эффективности и энергосбережения»	
Курсы по инженерным изысканиям		
И-01	«Инженерно-геодезические изыскания в строительстве»	1
И-02	«Инженерно-геологические изыскания в строительстве»	2,5
И-03	«Инженерно-гидрометеорологические изыскания в строительстве»	3
И-04	«Инженерно-экологические изыскания в строительстве»	4
И-05	«Организация работ по инженерным изысканиям»	7

*(согласно приказам Минрегионразвития РФ N 624 от 30 декабря 2009 г.)

**По окончании курса слушателю выдается удостоверение о краткосрочном повышении
квалификации установленного образца (72 ак. часа)**

Для регистрации на курс необходимо выслать заявку на участие, и копию диплома об образовании по телефону/факсу: 8(812) 552-94-60, 535-79-92, , e-mail: stroikursi@mail.ru.

Magazine of Civil Engineering

SCHOLAR JOURNAL

ISSN 2712-8172

Свидетельство о государственной регистрации:
Эл № ФС77-77906 от 19.02.2020,
выдано Роскомнадзором

Специализированный научный журнал.

Выходит с 09.2008.

Включен в Перечень ВАК РФ

Индексируется в БД Scopus

Периодичность: 8 раз в год

Учредитель и издатель:

Санкт-Петербургский политехнический университет
Петра Великого

Адрес редакции:

195251, СПб, ул. Политехническая, д. 29

Главный редактор:

Екатерина Александровна Линник

Научный редактор:

Виталий Владимирович Сергеев

Заместитель главного научного редактора:

Галина Леонидовна Козинец

Редакционная коллегия:

PhD, проф. Т. Аввад;
д.т.н., проф. М.И. Бальзанников
д.т.н., проф. А.И. Белостоцкий;
к.т.н., проф. А.И. Боровков;
д.т.н., проф. А. Бородинец;
PhD, проф. М. Велькович;
PhD, проф. Р.Д. Гарг;
PhD, М.Р. Гарифуллин;
Dr.-Ing, проф. Т. Грис;
д.т.н., проф. Т.А. Дацюк;
д.т.н., проф. В.В. Елистратов;
Dr.-Ing., проф. Т. Кэрки;
д.т.н., проф. Д.В. Козлов;
д.т.н., доцент С.В. Корниенко;
д.т.н., проф. Ю.Г. Лазарев;
д.т.н., проф. М.М. Мухаммадиев;
Dr.-Ing. Habil., проф. Х. Пастернак;
Dr.-Ing., проф. Ф. Рёгинер;
д.т.н., проф. Т.З. Султанов;
д.т.н., проф. М.Г. Тягунов;
акад. РАН, д.т.н., проф. М.П. Федоров;
Dr.-Ing., проф. Д. Хецк;
д.г.-м.н. А.Г. Шашкин;
д.т.н. В.Б. Штильман

Дата выхода: 30.12.2021

© ФГАОУ ВО СПбПУ, 2021

© Иллюстрация на обложке: Илья Смагин

Magazine of Civil Engineering

SCHOLAR JOURNAL

ISSN 2712-8172

Peer-reviewed scientific journal

Start date: 2008/09

8 issues per year

Publisher:

Peter the Great St. Petersburg Polytechnic University

Indexing:

Scopus, Web of Science (ESCI, RSCI), Compendex,
EBSCO, Google Academia, Index Copernicus, ProQuest,
Ulrich's Serials Analysis System, CNKI

Corresponding address:

29 Polytechnicheskaya st., Saint-Petersburg, 195251,
Russia

Editor-in-chief:

Ekaterina A. Linnik

Science editor:

Vitaly V. Sergeev

Deputy chief science editor:

Galina L. Kozinetc

Editorial board:

T. Awwad, PhD, professor
M.I. Balzannikov, D.Sc., professor
A.I. Belostotsky, D.Sc., professor
A.I. Borovkov, PhD, professor
A. Borodinecs, Dr.Sc.Ing., professor
M. Veljkovic, PhD, professor
R.D. Garg, PhD, professor
M. Garifullin, PhD, postdoctorant
T. Gries, Dr.-Ing., professor
T.A. Datsyuk, D.Sc., professor
V.V. Elistratov, D.Sc., professor
T. Kärki, Dr.-Ing., professor
D.V. Kozlov, D.Sc., professor
S.V. Korniyenko, D.Sc., professor
Yu.G. Lazarev, D.Sc., professor
M.M. Muhammadiev, D.Sc., professor
H. Pasternak, Dr.-Ing.habil., professor
F. Rögener, Dr.-Ing., professor
T.Z. Sultanov, D.Sc., professor
M.G. Tyagunov, D.Sc., professor
M.P. Fedorov, D.Sc., professor
D. Heck, Dr.-Ing., professor
A.G. Shashkin, D.Sc.
V.B. Shtilman, D.Sc.

Date of issue: 30.12.2021

© Peter the Great St. Petersburg Polytechnic University.
All rights reserved.

© Coverpicture – Ilya Smagin

Contacts:

E-mail: mce@spbstu.ru

Web: <http://www.engstroy.spbstu.ru>

Contents

Liu, S.H., Shi, Y., Zhao, Y.D., Sun, R. Interaction and control measures of shallow-buried shield twin tunnels with small clear-distance	10801
Jamalpour Najmabad, S., Seyed Razzaghi, M., Nateghi Alahi, F. Application of SMA anchors to the seismic performance of tanks	10802
Ngo, V.T. Effectiveness of base-isolated low-rise masonry building under excitation from earthquakes	10803
Manchikanti, S., Pavan Kumar, R. Physical and mechanical properties of construction and demolition waste	10804
Abdo, Sh., Galishnikova, V.V., Fawzy, A.M. Properties of recycled aggregate pervious concrete modified with Styrene Butadiene Rubber Latex	10805
Cherfa, H., Nechnech, A., Saoudi, N., Ait Mokhtar, K. Mechanical properties of slag sand mixture used in road pavements	10806
Shendkar, M., Beiraghi, H., Mandal, S. Effect of irregularity on seismic design parameters of RC-infilled structures	10807
Al-Rousan, R. Behavior of CFT steel columns damaged by thermal shock	10808
Dushimimana, A., Singirankabo, E., Kathumbi, L.K. Effective seismic response control of buildings with sliding bearings	10809
Miah, M.J., Miah, M.S., Paul, S.C., Kong, S.Y., Babafemi, A.J., Ali, M.K., Patoary, M.M.H. Waste iron powder as aggregate and binder in mortar production	10810
Kencanawati, N.N., Rofaida, A., Sugiarta, I.W., Beriman, A., Putri, A.I.T. Properties of tropically sourced timber subjected to elevated temperature	10811
Mailyan, L.R., Stel'makh, S.A., Shcherban', E.M. Differential characteristics of concrete in centrifugally spun and vibrospun building structures	10812
Mirsaidov, M.M., Sultanov, T.Z., Yarashov, J.Y. Strength of earth dams considering elastic-plastic properties of soil	10813
Ivanov, K.S. Thermal conductivity of granular insulation in conditions of soil freezing	10814
Alkhimenko, A.A., Shaposhnikov, N.O., Kharkov, A.A., Strekalovskaya, D.A., Alekseeva, E.L., Kovalev, M.A., Shishkova, M.L. Corrosion resistance of steel structures in marine conditions	10815



DOI: 10.34910/MCE.108.1

Interaction and control measures of shallow-buried shield twin tunnels with small clear-distance

S.H. Liu^a , Y. Shi^b , Y.D. Zhao^{*a, c} , R. Sun^a 

^a Central South University, Changsha City, Hunan Province, China

^b Cccc Second Harbour Engineering Company Design & Research Institute Co., Wuhan, China

^c School of Civil Engineering, Yancheng Institute of Technology, Yancheng City, Jiangsu Province, China

*E-mail: y.d.zhao@ycit.edu.cn

Keywords: earth pressure balance (EPB) shield, twin tunnels, tunnelling interaction, finite element method, ABAQUS, testing

Abstract. When constructing small clear-distance tunnels in complex geotechnical conditions, there are many challenges including intolerable ground movement, face failure, and potential damage to adjacent tunnel. This paper focused on the study of small clear-distance shield tunnel construction in the typical upper-soft and lower-hard stratum. Numerical analyses are conducted to estimate the influence of the new tunneling on the existing tunnel. In addition, partition wall accompanied by cement-soil mixing pile is adopted as the control measure. The results demonstrate that the construction of the new tunnel has a big impact on the stability of the existing tunnel. The seal roof block should not be placed on the top region. The obviously influenced region of the existing tunnel agrees with the excavation diameter of the new tunnel, so monitoring in this region should be strengthened. Moreover, the safety control effect has been verified by numerical analysis and field test. This study provides a basis for the design and construction of tunnels with shallow buried depths and small clear-distances.

1. Introduction

With the development of urban metro network, many shield twin tunnels with small clear-distances have been excavated in shallow strata [1–4]. However, previous studies have shown that tunneling construction often significantly affects the existing tunnel structure [5–10] and the excavation of a tunnel in a shallow stratum can lead to the collapse of the tunnel face and overlarge surface subsidence [11–14]. Construction of such tunnels may incur severe accidents because of high construction difficulty and risk.

The interaction mechanism of shallow-buried or small clear-distance shield twin tunnels is a significant issue that has aroused the interest of many investigators. Many researchers have carried out analytical studies [15–19], model tests [20–22], field tests [23–27] and numerical simulations [28–33] to study the interaction mechanisms of shallow-buried or small clear-distance shield twin tunnels. Among them, numerical simulation is usually used in the analysis of shield tunnelling as an efficient and low-cost method. Three-dimensional finite element calculation [5] was presented to investigate the effect of tunneling on an adjacent tunnel. The interaction between two parallel tunnels was investigated through a series of numerical simulations [30]. Another numerical model [6] was presented to evaluate ground displacement surrounding the two tunnels. The finite element method was used to explore the influence of the relative position of two circular tunnels on the soil movement and to examine the internal forces in the lining [5]. A numerical model [31] was presented to evaluate the face stability of a shallow-shield tunnel. The collapse mechanism [19, 32] was presented to investigate the face stability of a shallow tunnel. The discrete element method [33] was used to investigate the face stability analysis of shallow shield tunnels. However, few

Liu, S.H., Shi, Y., Zhao, Y.D., Sun, R. Interaction and control measures of shallow-buried shield twin tunnels with small clear-distance. Magazine of Civil Engineering. 2021. 108(8). Article No. 10801. DOI: 10.34910/MCE.108.1

© Liu, S.H., Shi, Y., Zhao, Y.D., Sun, R., 2021. Published by Peter the Great St. Petersburg Polytechnic University.



This work is licensed under a CC BY-NC 4.0

publications have concentrated on the interaction mechanism of shallow-buried shield twin tunnels with small clear-distance. Consequently, the interaction mechanism of shallow-buried shield twin tunnels with small clear-distance needs to be further studied so as to provide an accurate basis for effective control measures of the tunnel. The objects of research are listed as following, 1. deformation of the ground surface; 2. mechanical responses of the first tunnel; 3. reasonable control measures under the condition of shallow-buried twin tunnels with small clear-distance. For this reason, and the goals of the research is listed as following are listed as following, 1. acquiring the settlement troughs; 2. calculating the displacement and internal force of tunnel; 3. comparing the opening status; 4. verifying the effectiveness of control measures.

In this paper, considering the effect of the segment joint, a three-dimensional numerical model of the shield tunnel segment is established based on practical engineering, and the interaction of shallow-buried twin tunnels with small clear-distance is studied. In addition, an effective control measure is applied to the field, which can be verified as an effective method not only by numerical results but also by field tests.

2. Methods

2.1. Formulation of the problem

The main route of the intercity railway tunnel 2, which at Chencun, Guangzhou, between the 'Chencun' station in the south and the 'Guangzhou South' station in the Southern part of the city, consists of two tubes 8.5 m in external diameter and 3969 m in length. Two EPBs are working to excavate the twin tunnels. The tunnel segment is made of C50 concrete, with an external diameter of 8.5 m, a thickness of 0.4 m and a width of 1.6 m. Moreover, M30 high-strength bolts are used for circumferential and longitudinal connections of the tunnel segments. The principal strata, where the twin tunnels are situated, is comprised of silt, fine sand, strongly weathered mudstone and weathered mudstone, as shown in Fig. 1. Note that the clear-distance between these tunnels is 3.1 m and burial depth is 5.5 m within the region of shield launching. The construction procedure of the twin tunnels is that the first tunnel (existing tunnel) has been completed before the construction of the second tunnel (new tunnel).

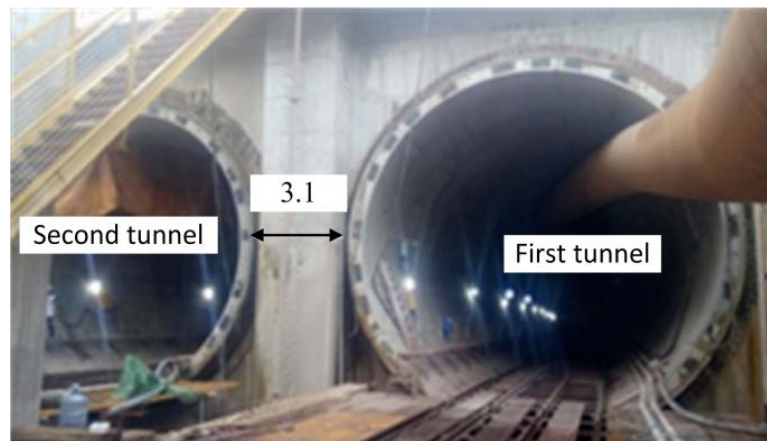


Figure 1(a). Profile of the tunnel: Condition of the launching shaft (Unit: m).

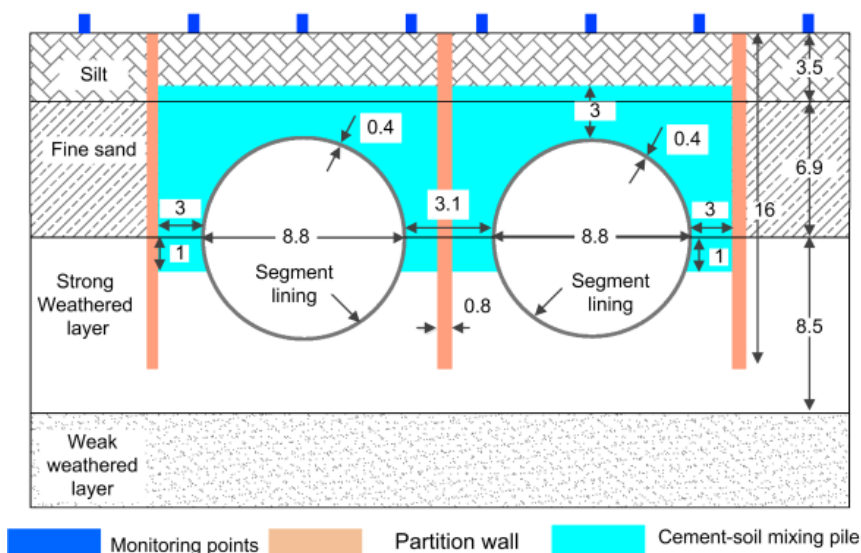


Figure 1(b). Profile of the tunnel: Geological condition (Unit: m).

In view of the aforementioned conditions around the tunnels, the tunneling work in this area is faced with such challenges as upper-soft and lower-hard stratum, shallow burial depth, and small clear-distance. Therefore, the stability of the first tunnel, which might be influenced by the tunneling of the second one, must be ensured to keep the safety of the whole transport line and the surrounding environment.

2.2. Method for solving the problem

Numerical simulation [5, 7, 8, 28–33, 35] is a commonly-used reliable method for the evaluation and investigation of civil engineering projects because it has the advantages of data visualization, high speed of solution and low cost. Finite Element Method (FEM) is applied in this paper to accurately analyze the influence mechanism between these shield tunnels. Partition wall accompanied by cement-soil mixing pile (Fig. 1 and Fig. 2) is adopted as the control measure for ensuring the safety of the tunneling. The pre-reinforcement range of cement-soil mixing piles is 26.7 m (X) × 8.4 m (Y) × 70 m (Z), with the partition wall consisting of three diaphragm walls (0.8 m (X) × 16 m (Y) × 18 m (Z)) as shown in Fig. 1 and Fig. 2. Meanwhile, field test method is applied to verify the effect of the control measure.

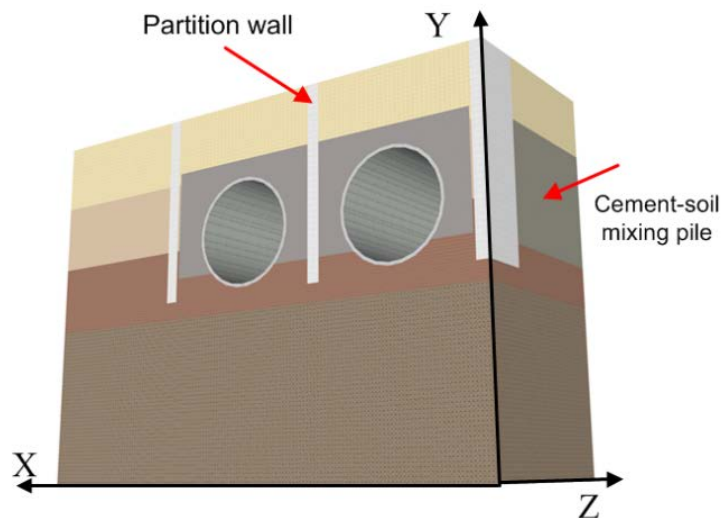


Figure 2. Diagrammatic sketch of the control measure in field.

2.3. Three-dimensional Finite Element Model

A typical three-dimensional numerical model is established by using ABAQUS [34] software. To reduce the boundary effect, the model is 80 m (X) × 40 m (Y) × 40 m (Z) (Fig. 3), consisting of 155,596 elements. Therefore, a complete three-dimensional finite element model considering soil, segment lining, shield, connection bolts and grouting is established.

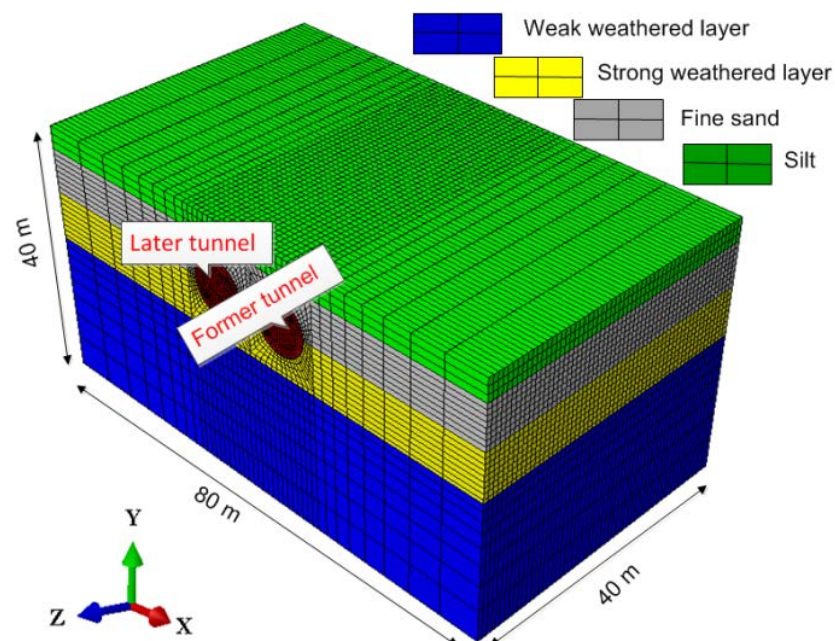


Figure 3. Three-dimensional numerical model.

In view of the discontinuous deformation of the segmental lining, the discontinuous contact model is established for segments of the first excavated tunnel (see Fig. 4), and the remaining lining is assumed to be an equivalent homogeneous structure. Among them, the discontinuous contact model of the segment joint applies the coulomb-contact friction model with a friction coefficient of 0.83 (same as the rubber gasket) [28, 40]. Moreover, the connection bolt between different segments is simulated by beam element (B31) with embedded method, and stagger-jointed assembling method is applied between adjacent segments, same as the actual construction process. For the equivalent homogeneous segments part, the stiffness reduction factor η is 0.746, which is obtained from the equivalent test of discontinuous contact numerical simulation [41].

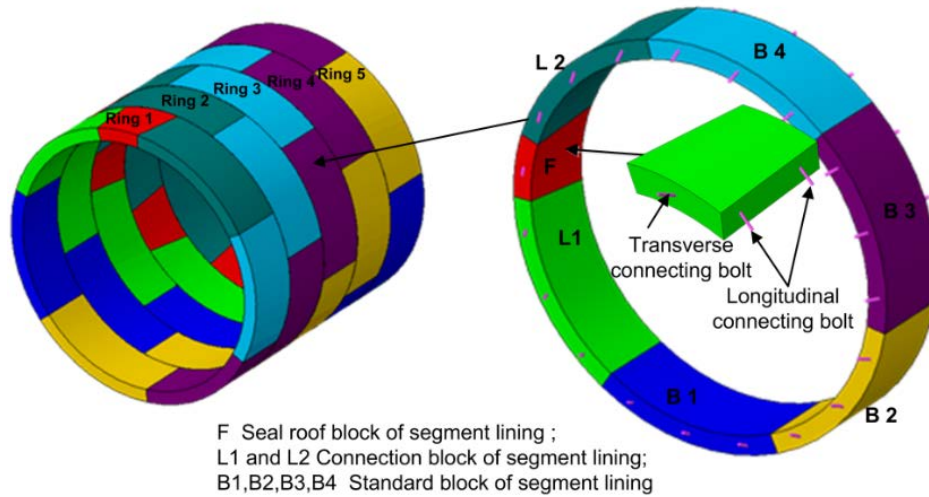


Figure 4. Numerical model of the segment lining.

The shield is simulated by a homogeneous circle with an 8.8 m outer diameter, a 9.6 m length and a 0.15 m thickness. The effect of cutter head and chamber on the excavation surface is equivalent to the soil warehouses pressure and the cutter head torque, as shown in Fig. 5 [35, 37]. Especially, the thickness of the backwall grouting is 0.15 m, and the grouting pressure is simulated by a uniform load of 0.27 MPa [35, 39, 42].

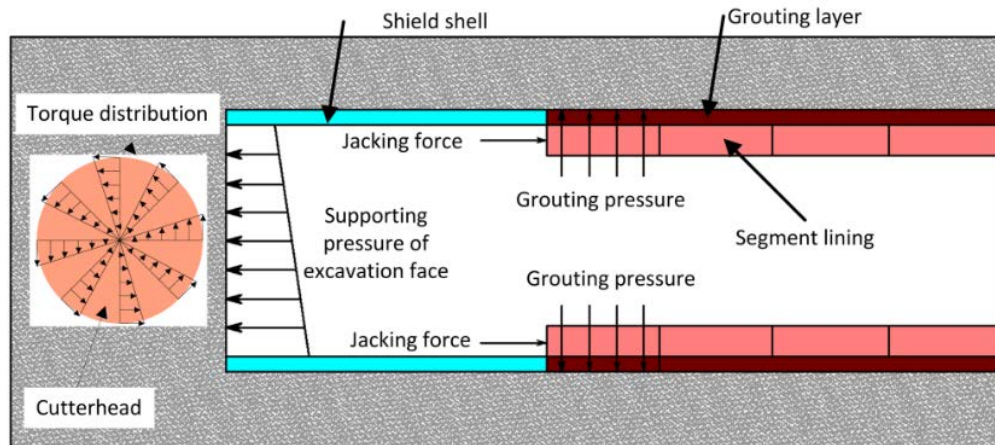


Figure 5. Simulation of the shield tunneling.

For the mechanical boundary, the lateral and bottom surfaces of the numerical model are subjected to normal constraints, and the top surface is a free boundary [5, 7, 8, 28–33, 35]. Soil, segments and shield are simulated by solid elements in the numerical model with C3D8 element. The linear elastic model for isotropic material is used to simulate the segments, shield and connection bolt. And the Mohr-Coulomb model for isotropic material is used to simulate the soil. According to the actual construction sequence, the model change command is used to simulate the tunnel excavation and the assembly process of the segments. The physical properties of materials in the numerical simulation are listed in Table 1.

Table 1. Parameters of the material in the numerical model.

Material	H [m]	ρ [g/cm ³]	E [MPa]	μ	c [kPa]	φ [°]	K_0
Silt	4.5	1.6	10	0.42	10	12	0.45
Fine sand	6.9	1.9	24	0.25	0	26	0.33
Strong weathered layer	8.5	2.0	90	0.39	30	30	0.39
Weak weathered layer	—	2.5	800	0.29	300	38	0.3
Segmental lining(second tunnel)	0.4	2.5	25750	0.2	/	/	/
Segmental lining(first tunnel)	0.4	2.5	34500	0.2	/	/	/
Connecting bolt	—	7.9	206000	0.3	/	/	/
Grouting layer (before hardening)	0.15	1.8	100	0.35	/	/	/
Grouting layer (after hardening)	0.15	2.0	800	0.3	/	/	/

Note: H is thickness; ρ is density; E is modulus; μ is Poisson's ratio; c is cohesion; φ is friction angel; K_0 is lateral pressure coefficient.

3. Results and Discussion

3.1. The Settlement Troughs

First, the settlement troughs determined by the ABAQUS [34] numerical model are analyzed. In general, the settlement trough shape following the Gaussian function may be expected for tunneling in the field condition, for which the symmetrical trough profile about the tunnel center line should exist. Fig. 6 shows transverse settlement trough profiles at ground surface, and after complete passage of the EPB from the control section. It can be seen that the troughs of the ground surface follow Gaussian function. And the ground surface presents a settlement distribution with a single peak after completion of the first tunnel and the maximum settlement is 14.2 mm. In addition, the ground surface presents a settlement distribution with double peaks after completion of the second tunnel; and the maximum settlement is 15.5 mm, which is less than the requirements of standard [43, 44]. As expected [6, 10, 23, 25], the final settlement profiles are asymmetric. This means that the maximum settlement is not on the mid-line between the two tunnels. The shape of the settlement trough is in consistent with that proposed by other researchers [5, 6, 10, 23–25, 30, 36] based on experience in metro engineering worldwide.

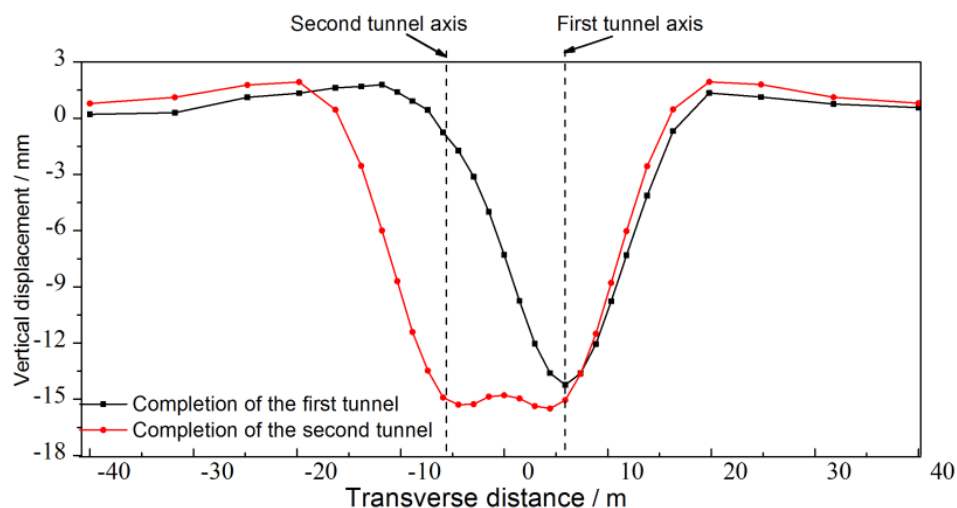


Figure 6. Settlement trough of the ground surface.

Through the comparison of two curves, it can be seen that tunneling of the second tunnel mainly causes the extension of the disturbed area and increases the width of the settlement trough [6, 10, 23, 25]. Moreover, the tunneling of the second tunnel has little influence on the peak value of ground surface trough. This is because the soil sensitivity to the secondary disturbance has been reduced due to the stress release of the soil caused by the construction of the first tunnel.

3.2. Displacement and internal force of the first tunnel

Fig. 7 and Fig. 8 respectively show the total displacement and additional displacement of Ring 3 of the first tunnel. It can be known from the results that the tunnel deformation is symmetrical, and its maximum value is 1.78‰ of the external diameter of segmental lining (D), which satisfies the requirements of standard [43, 44]. The construction of the second tunnel makes the deformation of the first tunnel move away from the second tunnel, resulting in the asymmetric deformation of the segmental lining. A similar rule was found by Kavvadas et al. [28] for tunneling in soft clay.

The seal roof block is in the top region of Ring 3, so that the stiffness of top structure is less than that of the bottom structure [40]. Moreover, as the tunnel passes through the upper-soft and lower-hard stratum, the lower mudstone is stronger than the upper layer, so the upper soil is weaker than lower one in anti-disturbing performance. For this reason, top part of the segment suffers severe displacement than the bottom part.

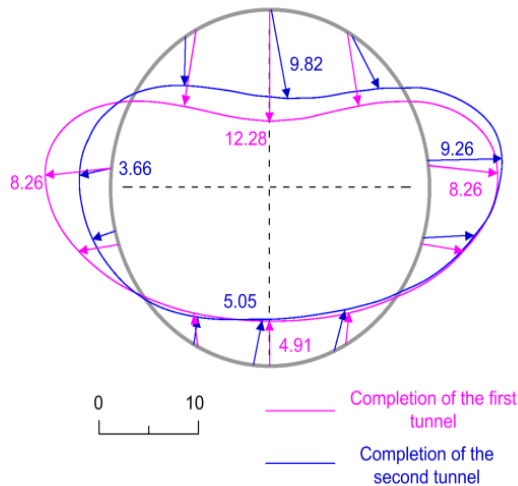


Figure 7. Total displacement of Ring 3 (Unit: mm).

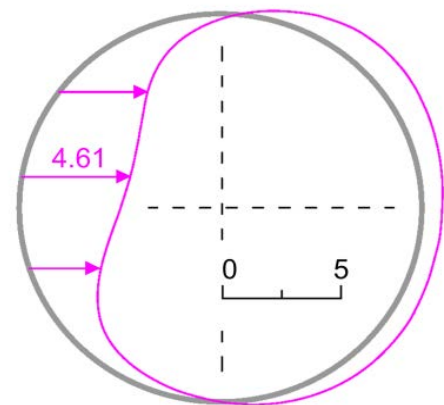


Figure 8(a). Additional horizontal displacement of Ring 3 (Unit: mm).

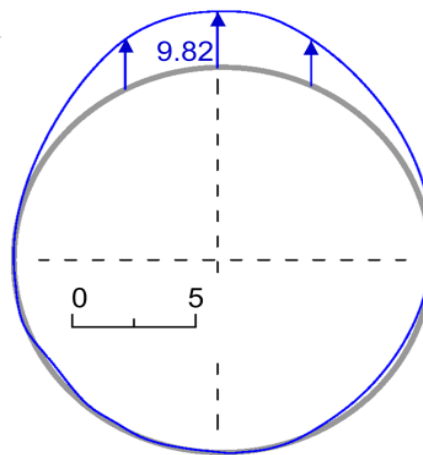


Figure 8(b). Additional vertical displacement of Ring 3 (Unit: mm).

In order to analyze the impact of the second tunnel on the first tunnel, the points (horizontal and vertical) of the maximum additional displacement of Ring 3 are taken as the characteristic points for analysis. The distance between the cutter head and the monitoring section is defined as L . When the cutter head fails to reach the monitoring section of the first tunnel, L is negative. Fig. 9 is the displacement curve at Points A and B of Ring 3. It can be seen that:

I. When $L < -D$ (D is the outer diameter of the shield machine), shear stress and soil warehouses pressure have litter influence on the segments.

II. When $-D < L < 0$, the influence of shear stress and soil pressure is obvious. The deformation rate of the segment increases with the decrease of distance, and the deformation rate reaches peak value once $L = 0$.

III. When $0 < L < D$, the deformation of the segment increases with the progress of tunneling and the deformation rate gradually decreases; and the deformation value reaches the peak value when $L = D$.

IV. When $L > D$, due to the grouting pressure, the deformation of the segment decreases and will level off finally.

The response of the segment lining significantly increases with the decreasing distance when $-D < L < D$. Therefore, this area is the major influenced area and the monitoring of this area should be strengthened during construction.

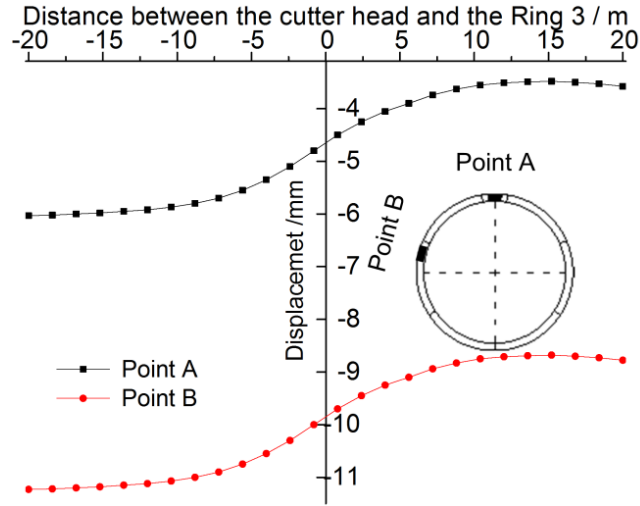


Figure 9. Displacement Curve at Points A and B.

Fig. 10 is a schematic view showing the joint opening of the first lining structure, and Fig. 11 is a curve showing the opening variation of the longitudinal joint in Ring 3.

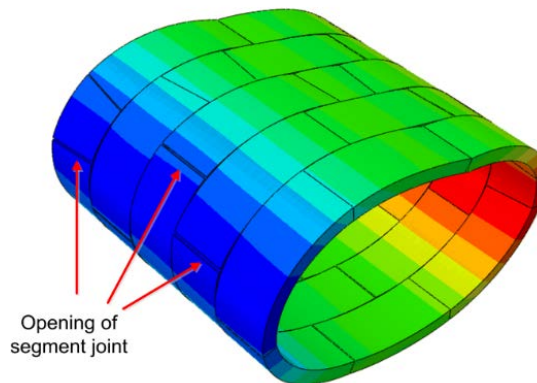


Figure 10. Opening status of the segmental lining.

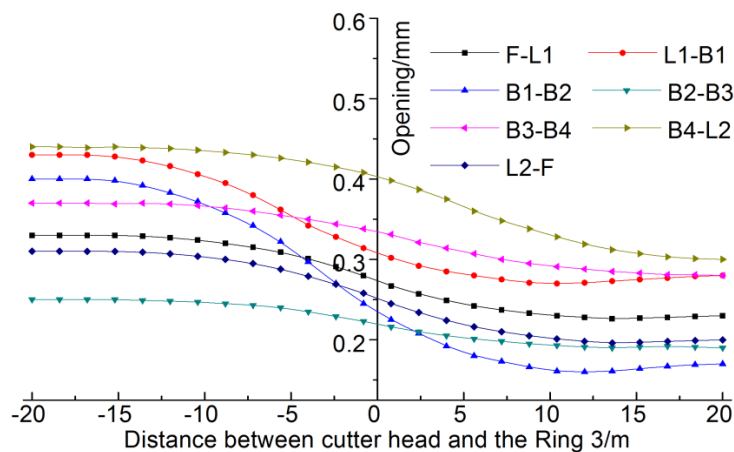


Figure 11. Opening curves of segments in Ring 3.

As shown in Fig. 10, the longitudinal joint opening is obvious, the horizontal joint of the segmental tends to open outwards, and the vertical joint has a tendency to open inside. The hinged action of the bolts provides certain continuity between the segments.

The opening variation of the longitudinal joint in Ring 3 of the first tunnel (Fig. 11) shows that:

I. When $L = -20$, that is, after completing the construction of the first tunnel, the largest opening of the longitudinal joint is 0.44 mm, which satisfies the requirements [43].

II. When $-20 < L < D$, the joint opening gradually reduces, which is affected by the lateral loading caused by the construction of the second tunnel.

III. When $L > D$, the joint opening remains basically unchanged.

The variation law of the joint opening during the construction of the second tunnel is the same as the variation law of the additional deformation of the segment.

Fig. 12 and 13 respectively are the additional stress and maximum principal stress of the segments. Due to the hinge effect of the bolts between the segments, the internal force of the segment is discontinuous at the joint. The maximum tensile stress is 2.44 MPa at the vault region, which exceeds the design value of the tensile strength of C50 concrete (1.89 MPa). Furthermore, the maximum additional tensile stress around the joint area (0.58 MPa) is significantly larger than that in other areas along with longitudinal direction, which exceeds the stress control standard [45, 46].

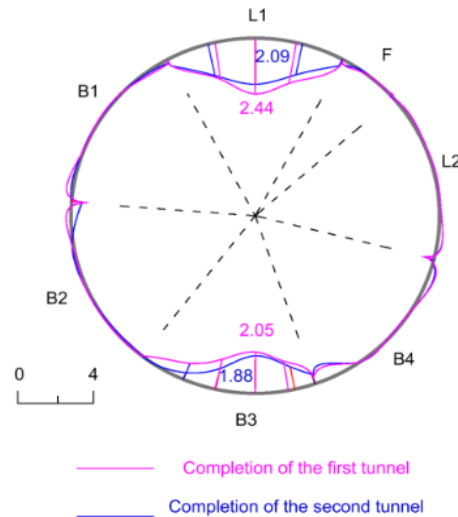


Figure 12. Maximum principal stress distribution of Ring 3 (Unit: MPa).

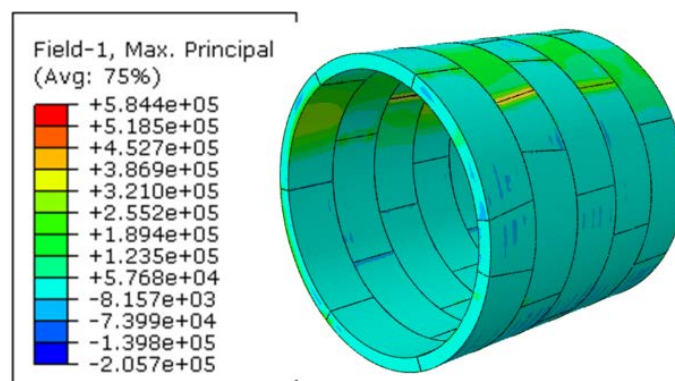


Figure 13. Additional tensile stress distribution of the first tunnel.

3.3. Safety control effect

Fig. 14 and 15 are the maximum principal stress and additional tensile stress contours of the first segments, respectively. It can be seen that after taking safety control measure, the maximum tensile stress of the first segmental lining is 1.7 MPa, smaller than the tensile strength design value of the segmented concrete; the maximum additional tensile stress of the segmental lining is 0.29 MPa, which satisfies the stress control standard [45, 46].

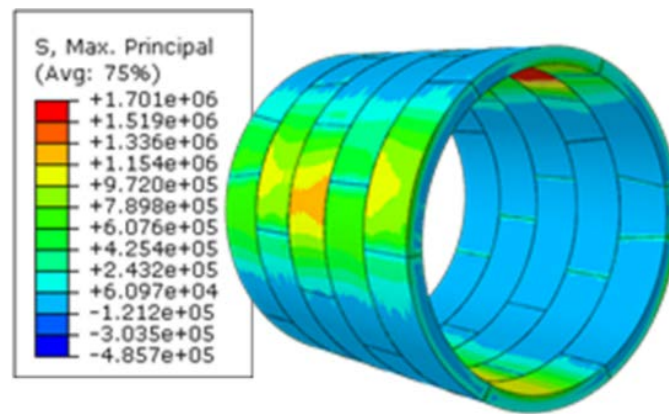


Figure 14(a). The effect of control measure to the first tunnel: Maximum principal stress.

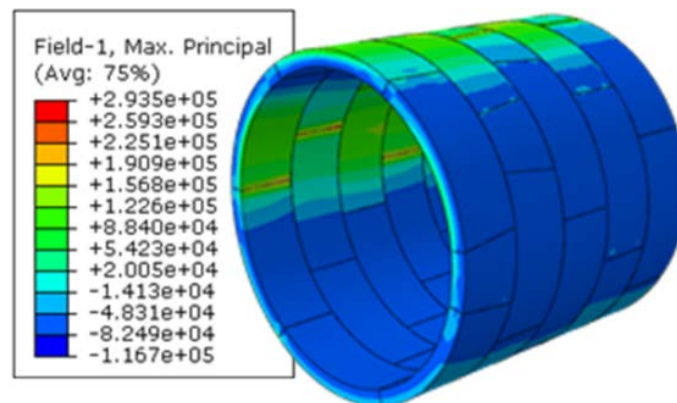


Figure 14(b). The effect of control measure to the first tunnel: Additional tensile stress.

Fig. 15 shows the additional horizontal displacement of the first segmental lining. The maximum additional displacement is 2.43 mm, which meets the requirements of the specification [43, 44].

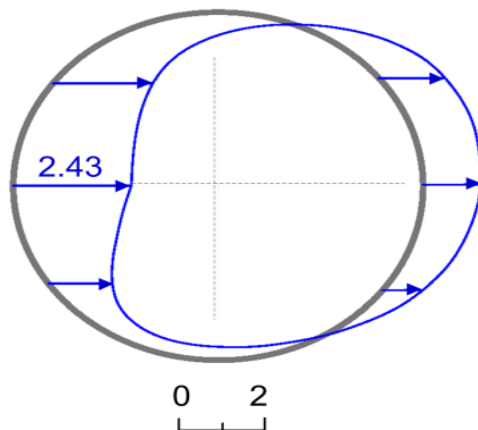


Figure 15(a). Additional horizontal displacement: Filed test results (Unit: mm).

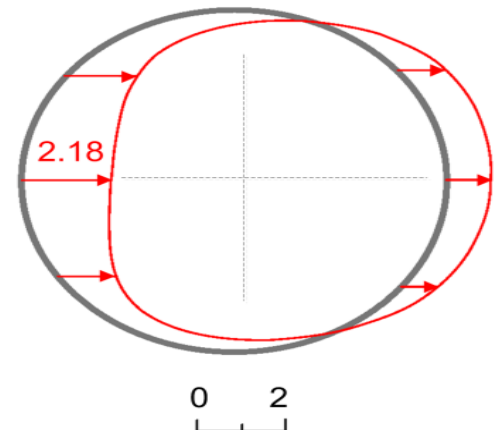


Figure 15(b). Additional horizontal displacement: Numerical results (Unit: mm).

Fig. 16 shows the surface settling trough after taking safety control measure. It can be seen from Fig. 16 that the maximum settlement is 14.16 mm, which can meet the control standard [43, 44]. In addition, the field test is conducted to monitor the settlement of the ground surface. Both the field results and the numerical simulation results are smaller than the control standard, and the law of tested settlement trough and additional horizontal displacement distribution agree with the numerical simulation results. Therefore, conclusions can be drawn that the numerical simulation results are reasonable and reliable, and the pre-reinforcement control measure of partition wall accompanied by cement soil mixing pile is effective.

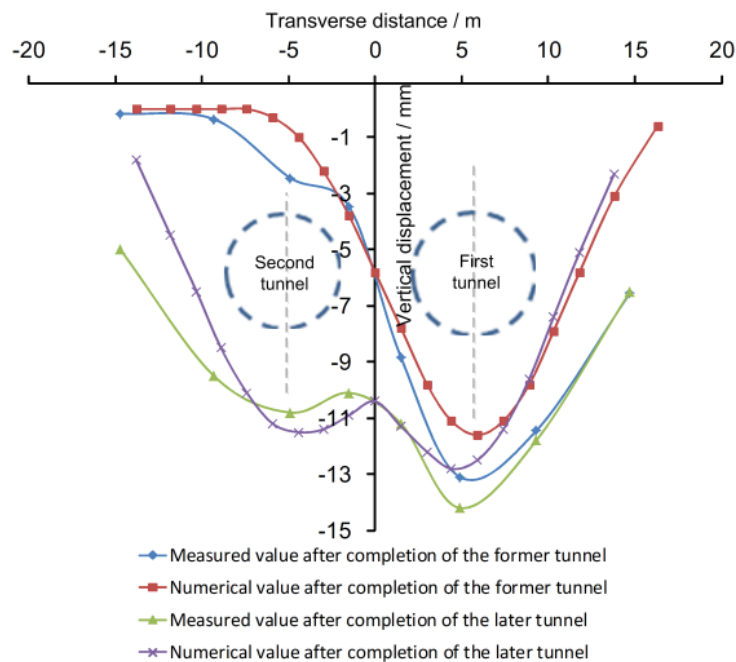


Figure 16. Settlement trough of the ground surface after conducting control measure.

4. Conclusions

This study discusses the interaction and control of shallow-buried twin tunnels with small clear-distance. The following points are outlined as the outcomes of this study.

1. The tunneling process of the new tunnel has a big impact on the stability of the existing tunnel under the condition of shallow burial depth and small clear-distance. The unsafe additional tensile stress 2.44 MPa might be obtained at the vault region, which exceeds the design value of the tensile strength of C50 concrete (1.89 MPa).
2. The seal roof block should not be placed on the top region in cases where the shield tunnel needs to go through the upper-soft and lower-hard composite stratum, the total displacement of the whole ring could be obtained in the seal roof block 12.28 mm.
3. The obviously influenced region of the existing tunnel agrees with the excavation diameter ($-D < L < D$) of the new tunnel, so monitoring in this region should be strengthened.
4. This study demonstrates that the stability of designed structure cannot be ensured and reinforcement is thus required during tunneling. Pre-reinforcement control measure of partition wall accompanied by cement-soil mixing piles has been verified as an effective control method by field tests and numerical results, the maximum settlement could be controlled within 14.16 mm.

5. Acknowledgments

Natural Science Foundation of Jiangsu Higher Education Institutions (No.21KJB560012).

Open Fund of Key Laboratory for Advanced Technology in Environmental Protection of Jiangsu Province (No.JBGS031).

References

1. Jiang, Q., Song, S.G., Li, T., Wang, K., Gu, R.H. Study on surrounding rock stability of small clear-distance twin highway tunnel with eight lanes. *Geotechnical and Geological Engineering*. 2019. 37(2). Pp. 593–598. DOI: 10.1007/s10706-018-0629-1
2. Hamdy, H.H.A., Enieb, M., Abdelmoamen Khalil, A., Ahmed, A.S.H. Twin tunnel configuration for Greater Cairo metro line. No. 4. *Computers and Geotechnics*. 2015. 68. Pp. 66–77. DOI: 10.1016/j.compgeo.2015.03.015
3. Lei, M.F., Lin, D.Y., Yang, W.C., Shi, C.H., Peng, L.M., Huang, J. Model test to investigate failure mechanism and loading characteristics of shallow-bias tunnels with small clear distance. *Journal of Central South University*. 2016. 23(12). Pp. 3312–3321. DOI: 10.1007/s11771-016-3397-1
4. Shi, C., Cao, C., Lei, M. Construction technology for a shallow-buried underwater interchange tunnel with a large span. *Tunnelling and Underground Space Technology*. 2017. 70. Pp. 317–329. DOI: 10.1016/j.tust.2017.09.009
5. Hage Chehade, F., Shahrour, I. Numerical analysis of the interaction between twin-tunnels: Influence of the relative position and construction procedure. *Tunnelling and Underground Space Technology*. 2008. 23(2). Pp. 210–214. DOI: 10.1016/j.tust.2007.03.004

6. Fang, Q., Tai, Q., Zhang, D., Wong, L.N.Y. Ground surface settlements due to construction of closely-spaced twin tunnels with different geometric arrangements. *Tunnelling and Underground Space Technology*. 2016. 51. Pp. 144–151. DOI: 10.1016/j.tust.2015.10.031
7. Do, N.A., Dias, D., Oreste, P., Djeran-Maigre, I. Three-dimensional numerical simulation of a mechanized twin tunnels in soft ground. *Tunnelling and Underground Space Technology*. 2014. 42. Pp. 40–51. DOI: 10.1016/j.tust.2014.02.001
8. Yang, X.L., Sui, Z.R. Numerical simulation of construction sequence for shallow embedded bias tunnels with small clear distance. *Journal of Central South University (Science and Technology)*. 2007. 38(4). Pp. 764–770.
9. Chen, J.F., Kang, C.Y., Shi, Z.M. Displacement monitoring of parallel closely spaced highway shield tunnels in marine clay. *Marine Georesources and Geotechnology*. 2015. 33(1). Pp. 45–50. DOI: 10.1080/1064119X.2013.784833
10. Chen, R.P., Zhu, J., Liu, W., Tang, X.W. Ground movement induced by parallel EPB tunnels in silty soils. *Tunnelling and Underground Space Technology*. 2011. 26(1). Pp. 163–171. DOI: 10.1016/j.tust.2010.09.004
11. Zhang, P., Chen, R.P., Wu, H.N., Liu, Y. Ground settlement induced by tunneling crossing interface of water-bearing mixed ground: A lesson from Changsha, China. *Tunnelling and Underground Space Technology*. 2020. 96. 103224. DOI: 10.1016/j.tust.2019.103224
12. Huang, F., Ou, R., Li, Z., Yang, X., Ling, T. Limit analysis for the face stability of a shallow-shield tunnel based on a variational approach to the blow-out failure mode. *International Journal of Geomechanics*. 2018. 18(6). Pp. 04018038. DOI: 10.1061/(asce)gm.1943-5622.0001150
13. Kirsch, A. Experimental investigation of the face stability of shallow tunnels in sand. *Acta Geotechnica*. 2010. 5(1). Pp. 43–62. DOI: 10.1007/s11440-010-0110-7
14. Boonyarak, T., Phisitkul, K., Ng, C.W., Teeparaksa, W., Aye, Z.Z. Observed ground and pile group responses due to tunneling in Bangkok stiff clay. *Canadian Geotechnical Journal*. 2014. 51(5). Pp. 479–495. DOI: 10.1139/cgj-2013-0082
15. Fu, J., Yang, J., Yan, L., Abbas, S.M. An analytical solution for deforming twin-parallel tunnels in an elastic half plane. *International Journal for Numerical and Analytical Methods in Geomechanics*. 2015. 39(5). Pp. 524–538. DOI: 10.1002/nag.2322
16. Yang, X.L., Zhang, J.H., Jin, Q.Y., Ma, J.Q. Analytical solution to rock pressure acting on three shallow tunnels subjected to unsymmetrical loads. *Journal of Central South University*. 2013. 20(2). Pp. 528–535. DOI: 10.1007/s11771-013-1515-x
17. Gong, J., Lei, X., Xia, C. Analysis of field measurement and theoretical calculation on rock pressure in shallow-buried twin tunnels with small spacing. *Chinese Journal of Rock Mechanics and Engineering*. 2010. 29 (SUPPL. 2). Pp. 4139–4145.
18. Huang, F., Ou, R., Li, Z., Yang, X., Ling, T. Limit Analysis for the Face Stability of a Shallow-Shield Tunnel Based on a Variational Approach to the Blow-Out Failure Mode. *International Journal of Geomechanics*. 2018. 18(6). Pp. 04018038. DOI: 10.1061/(asce)gm.1943-5622.0001150
19. Ding, W., Liu, K., Shi, P., Li, M., Hou, M. Face stability analysis of shallow circular tunnels driven by a pressurized shield in purely cohesive soils under undrained conditions. *Computers and Geotechnics*. 2019. 107 (April 2018). Pp. 110–127. DOI: 10.1016/j.compgeo.2018.11.025
20. Chapman, D.N., Ahn, S.K., Hunt, D.V.L., Chan, A.H.C. The use of model tests to investigate the ground displacements associated with multiple tunnel construction in soil. *Tunnelling and Underground Space Technology*. 2006. 21(3–4). Pp. 413. DOI: 10.1016/j.tust.2005.12.059
21. Lei, M.F., Lin, D.Y., Yang, W.C., Shi, C.H., Peng, L.M., Huang, J. Model test to investigate failure mechanism and loading characteristics of shallow-bias tunnels with small clear distance. *Journal of Central South University*. 2016. 23(12). Pp. 3312–3321. DOI: 10.1007/s11771-016-3397-1
22. Lei, M., Peng, L., Shi, C. Model test to investigate the failure mechanisms and lining stress characteristics of shallow buried tunnels under unsymmetrical loading. *Tunnelling and Underground Space Technology*. 2015. 46. Pp. 64–75. DOI: 10.1016/j.tust.2014.11.003
23. Sirivachiraporn, A., Phienweij, N. Ground movements in EPB shield tunneling of Bangkok subway project and impacts on adjacent buildings. *Tunnelling and Underground Space Technology*. 2012. 30. Pp. 10–24. DOI: 10.1016/j.tust.2012.01.003
24. Zhang, Z.X., Zhang, H., Yan, J.Y. A case study on the behavior of shield tunneling in sandy cobble ground. *Environmental earth sciences*. 2013. 69(6). Pp. 1891–1900. DOI: 10.1007/s12665-012-2021-4
25. Koukoutas, S.P., Sofianos, A.I. Settlements due to single and twin tube urban EPB shield tunnelling. *Geotechnical and Geological Engineering*. 2015. 33(3). Pp. 487–510. DOI: 10.1007/s10706-014-9835-7
26. Kirsch, A. Experimental investigation of the face stability of shallow tunnels in sand. *Acta Geotechnica*. 2010. 5(1). Pp. 43–62. DOI: 10.1007/s11440-010-0110-7
27. Cao, L., Fang, Q., Zhang, D., Chen, T. Subway station construction using combined shield and shallow tunnelling method: Case study of Gaojiayuan station in Beijing. *Tunnelling and Underground Space Technology*. 2018. 82 (September). Pp. 627–635. DOI: 10.1016/j.tust.2018.09.010
28. Kavvadas, M., Litsas, D., Vazaios, I., Fortsakis, P. Development of a 3D finite element model for shield EPB tunnelling. *Tunnelling and Underground Space Technology*. 2017. 65. Pp. 22–34. DOI: 10.1016/j.tust.2017.02.001
29. Moeinossadat, S.R., Ahangari, K. Estimating maximum surface settlement due to EPBM tunneling by Numerical-Intelligent approach—A case study: Tehran subway line 7. *Transportation Geotechnics*. 2019. 18. Pp. 92–102. DOI: 10.1016/j.trgeo.2018.11.009
30. Ng, C.W., Lee, K.M., Tang, D.K. Three-dimensional numerical investigations of new Austrian tunnelling method (NATM) twin tunnel interactions. *Canadian Geotechnical Journal*. 2004. 41(3). Pp. 523–539. DOI: 10.1139/t04-008
31. Huang, F., Ou, R., Li, Z., Yang, X., Ling, T. Limit Analysis for the Face Stability of a Shallow-Shield Tunnel Based on a Variational Approach to the Blow-Out Failure Mode. *International Journal of Geomechanics*. 2018. 18(6). Pp. 04018038. DOI: 10.1061/(asce)gm.1943-5622.0001150
32. Li, P., Wang, F., Zhang, C., Li, Z. Face stability analysis of a shallow tunnel in the saturated and multilayered soils in short-term condition. *Computers and Geotechnics*. 2019. 107 (November 2018). Pp. 25–35. DOI: 10.1016/j.compgeo.2018.11.011
33. Chen, R.P., Tang, L.J., Ling, D.S., Chen, Y.M. Face stability analysis of shallow shield tunnels in dry sandy ground using the discrete element method. *Computers and Geotechnics*. 2011. 38(2). Pp. 187–195. DOI: 10.1016/j.compgeo.2010.11.003
34. Dassault Simulia International Inc. ABAQUS v 6.4. 2011.

35. Mirhabibi, A., Soroush, A. Effects of building three-dimensional modeling type on twin tunneling-induced ground settlement. *Tunnelling and Underground Space Technology*. 2013. 38. Pp. 224–234. DOI: 10.1016/j.tust.2013.07.003
36. Fang, Y., He, C., Nazem, A., Yao, Z., Grasmick, J. Surface settlement prediction for EPB shield tunneling in sandy ground. *KSCE Journal of Civil Engineering*. 2017. 21(7). Pp. 2908–2918. DOI: 10.1007/s12205-017-0989-8
37. Eskandari, F., Goharrizi, K.G., Hooti, A. The impact of EPB pressure on surface settlement and face displacement in intersection of triple tunnels at Mashhad metro. *Geomechanics and Engineering*. 2018. 15(2). Pp. 769–774. DOI: 10.12989/gae.2018.15.2.769
38. Hilar, M., Tuan, N.T. Evaluation of the surface settlement above the prague metro line an extension constructed by two shields. *Acta Polytechnica*. 2016. 56(6). Pp. 448–454. DOI: 10.14311/AP.2016.56.0448
39. Shah, R.A., Lavasan, A., Peila, D., Todaro, C., Luciani, A., Schanz, T. Numerical study on backfilling the tail void using a two-component grout. *Journal of Materials in Civil Engineering*. 2018. 30(3). 04018003. DOI: 10.1061/(ASCE)MT.1943-5533.0002175
40. Wang, S.M., Yu, Q.Y., Peng, B., He, X.F., Yao, J.B. Three-dimensional discontinuous contact model for shield tunnels with double-layer lining based on plastic-damage model. *Chin J Rock Mech Eng*. 2016. 35. Pp. 303–311.
41. Li, Y.J. Application of discontinuous contact computational model in mechanical behavior of shield lining. Doctoral dissertation, Beijing Jiaotong University. 2012.
42. Sharghi, M., Chakeri, H., Ozcelik, Y. Investigation into the effects of two component grout properties on surface settlements. *Tunnelling and Underground Space Technology*. 2017. 63. Pp. 205–216. DOI: 10.1016/j.tust.2017.01.004
43. Ministry of Housing and Urban-Rural Development, People's Republic of China. Code for construction and acceptance of shield tunnelling method. 2017. GB 50446-2017.
44. Ministry of Housing and Urban-Rural Development, People's Republic of China. Code for monitoring measurement of urban rail transit engineering. 2013. GB 50911-2013.
45. Koizumi, A. Design of shield tunnel segments: from the limited state method to the allowable stress method. 2010.

Contacts:

Shouhua Liu, 18945087415@163.com

Yao Shi, 734169065@qq.com

Yiding Zhao, zhaoyiding89@126.com

Rui Sun, 3617384841@qq.com



DOI: 10.34910/MCE.108.2

Application of SMA anchors to the seismic performance of tanks

S. Jamalpour Najmabad^a, M. Seyed Razzaghi^{*a}, F. Nateghi Alahi^b

^a Department of Civil Engineering, Qazvin Branch, Islamic Azad University, Qazvin, Iran

^b Structural Engineering Research center, International Institute of Earthquake Engineering and Seismology (IIEES), Tehran, Iran

*E-mail: razzaghi.m@gmail.com

Keywords: liquid storage tank, SMA anchor bolts, uplift, incremental dynamic analysis (IDA), near-field earthquake records, forward directivity

Abstract. This paper is aimed at investigating the feasibility of using shape memory alloy (SMA) materials as anchor bolts in steel liquid storage tanks. The seismic performance of a case study liquid storage tank anchored with steel and SMA bolts is evaluated. For this purpose, a parametric study is performed to determine the optimum length and diameter of the anchor bolts which results in the minimum tank uplift. Furthermore, incremental dynamic analyses (IDAs) are performed to gain insights into the effects of the axial stiffness of the anchor bolts on the uplift of the tank. The uncertainties regarding the seismic input, i.e., the record-to-record variability and seismic intensity, are taken into account by selecting a set of near-field earthquake ground motion records with and without forward directivity. It should be noted that peak ground acceleration (PGA) is chosen as the intensity measure in IDAs. According to the results, using steel anchor bolts significantly reduces the uplift of the tank due to their high axial stiffness, which may result in a severe damage at the connection as a result of high axial forces in the bolts. Conversely, the self-centering feature of SMA anchor bolts allow the tank to undergo a limited uplift, which also leads to significant energy absorption. Furthermore, the Incremental dynamic analysis results show that tanks anchored with SMA bolts are less sensitive to the frequency content of the seismic input compared to the tanks anchored with steel bolts. Based on the findings of this research, it is possible to reduce the required diameter of the anchor bolts and eliminate the residual deformation of the anchorage system after a severe seismic event by using SMA anchor bolts.

1. Introduction

Seismic vulnerability assessment of buildings in urban areas is one of the priorities of crisis management institutions for planning to reduce risks in the future. On the other hand, storage facilities play a key role in modern production industries, as their functionality is essential for the proper operation of a wide range of petrochemical and processing operations. Therefore, health monitoring of the tanks and investigating possible damage under earthquakes is very important. Accordingly, much research has been done on the behavior of the tanks.

Liquid storage tanks are thin-walled structures utilized for storing a wide range of liquids such as water, oil, or even hazardous materials [1–3]. Because of the crucial function of these structures, their seismic performance is significantly important as seen in past earthquakes [4]. The damage due to such strong vibrations can lead to devastating consequences such as extensive fire due to the leakage of flammable substances such as oil as well as damage caused by wave turbulence [5]. Therefore, evaluation of the seismic vulnerability of such structures has attracted the attention of several researchers and

Jamalpour Najmabad, S., Seyed Razzaghi, M., Nateghi Alahi, F. Application of SMA anchors to the seismic performance of tanks. Magazine of Civil Engineering. 2021. 108(8). Article No. 10802. DOI: 10.34910/MCE.108.2

© Jamalpour Najmabad, S., Seyed Razzaghi, M., Nateghi Alahi, F., 2021. Published by Peter the Great St. Petersburg Polytechnic University



This work is licensed under a CC BY-NC 4.0

practicing engineers during the recent decades [6]. The results of some of those researches and practical experiences have been implemented in design codes AWWA [7, 8].

The Seismic performance of cylindrical liquid storage tanks during the occurred seismic events has indicated the notable seismic vulnerability of these structures [9–16]. Most of the existing old steel storage tanks are un-anchored. Unanchored tanks are simply rested on their foundation without any clamps, and hence they are prone to uplift and consequently, a wide variety of failure mechanisms such as shell buckling and failure of their pipes during destructive earthquakes. On the other hand, anchored tanks are clamped to their foundations. Failure of anchor bolts and shell buckling are among the common failure modes of these tanks. In this regard, many studies were aimed at investigating the effect of design parameters on their potential failure modes [17]. The effect of height to diameter (H/D) ratio evaluated on the critical horizontal peak ground acceleration of anchored steel liquid storage tanks. It was shown that the critical acceleration was reduced with increasing H/D. In addition, was studied the effects of base flexibility on the seismic performance of liquid storage tanks. According to the results, base flexibility may increase the seismic vulnerability of tanks. Furthermore, the insufficient effective embedded length or cutting off anchor bolts may lead to partial or total pull-out of the anchor bolts, which imposes a great damage to the anchoring system. In some cases, inadequate material strength results in failure of the anchor bolts due to excessive strain [18]. In another study by Hamdan [19], reported a list of field observations for tanks suffering from anchor bolts damage due to uplift under seismic excitation. To overcome this limitation, some researchers evaluated the seismic vulnerability of liquid storage tanks isolated with different isolation systems [20–22]. However, implementing such systems can be economically inefficient due the costs associated with their installation and maintenance. An alternative method is to provide anchors to clamp the tank to its foundation. It has been shown that this technique can noticeably reduce the seismic vulnerability of tanks [23]. The main shortcoming of this method is that a considerable number of anchors should be provided in order to fully restrain the tank bottom. Another problem with steel anchor bolts is the residual uplift of the tank after a strong ground motion. This phenomenon, in many cases, results in a significant damage to the anchorage system, which necessitates its total replacement.

On the other hand, shape memory alloy (SMA) materials can recover their inelastic deformations after unloading. Such a special behavior leads to flag-shaped hysteresis loops, which can eliminate the residual drifts at a lower energy dissipation rate as compared to steel [24]. However, due to the lower modulus of elasticity of SMA bars, they undergo larger deformations under seismic forces. Previous studies investigated the behavior of SMA materials in different applications such as dampers [25], concrete reinforcements [26], and bolts in self-centering steel columns [27].

In this study, has been investigated the seismic behavior of liquid storage tanks anchored by using SMA anchor bolts for the first time and steel bolts. SMA anchors can reduce the damage to the tank through self-centering effect. Herein, the tank uplift under near-field earthquake ground motions with and without forward directivity is investigated through performing Incremental Dynamic Analysis (IDA) [28]. The tank has been modeled in three conditions: un-anchored, anchored with steel and SMA mechanical anchors. Finally, the results are compared with those of the anchored tanks with un-anchor tank.

2. Materials and Methods

2.1. Specifications of the studied tank

The liquid storage tank considered in the study is a tank which suffered uplift and shell buckling during the Silakhor earthquake in 2006 in west of Iran. The tank is supported by a reinforced concrete foundation and is used for storage of fuel oil with density of 920 kg/m^3 . It should be noted that the tank was 90 % full during the seismic event. The properties of the steel used in the tank are tabulated in Table 1 and Fig. 1 shows the geometry of the tank [29].

Table 1 Properties of the steel used in the tank [29].

Material	Density (kg/m^3)	Modulus of elasticity (GPa)	Tangent modulus (GPa)	Yield stress (MPa)	Poisson ratio
Steel	7850	210	4×10^3	240	0.3

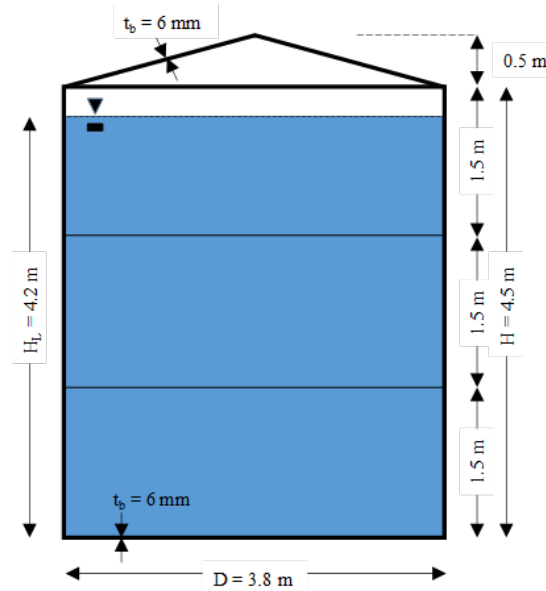


Figure 1. Geometry of the tank used in this study [29].

2.2. Analytical modeling

There is a wide variety of methods to characterize the dynamic behavior of tank-fluid systems. Commercial software usually provides Finite Element (FE) and Finite Volume (FV) techniques to model tank-fluid systems. However, these methods usually require a significant computational effort, which limits their application in practice. In this regard, other simplified models have been proposed to characterize the liquid motion at a lower computational cost without notably compromising the accuracy of the results [30, 31]. In this study, is employed to simulate the liquid motion inside the tank. This model uses an equivalent mass-spring system, which consists of an impulsive component with mass M_0 and a convective component with mass M_1 . The convective component is attached to the tank walls by means of a spring with stiffness K_1 , which enables it to oscillate during an excitation. The dynamic properties of the equivalent system are calculated as follows:

$$M_0 = M \frac{\tanh(1.7 D/h)}{1.7 D/h}, \quad (1)$$

$$M_1 = M \frac{0.83 \tanh(1.6 D/h)}{1.6 D/h}, \quad (2)$$

$$K_1 = 3 \frac{M_1^2 gh}{M D^2}, \quad (3)$$

where M is the total mass of the liquid, D and h represent the radius and height of the tank, respectively, and g is the gravitational acceleration. The natural period of vibration of the liquid inside the tank T is calculated as given below:

$$T = 2\pi \sqrt{\frac{M_1}{K_1}}. \quad (4)$$

The elevations of the impulsive and convective components are respectively denoted by h_0 and h_1 , which are calculated by the expressions given below:

$$h_0 = \frac{3}{8} h \left\{ 1 + \alpha \left[\frac{M}{M_1} \left(\frac{D}{h} \right)^2 - 1 \right] \right\}, \quad (5)$$

$$h_1 = h \left[1 - \frac{1}{3} \frac{M}{M_1} \left(\frac{D}{h} \right)^2 - 0.63\beta \frac{D}{h} \sqrt{0.28 \left(\frac{M}{M_1} \frac{D}{h} \right)^2 - 1} \right], \quad (6)$$

where $\alpha = 1.33$ and $\beta = 2.0$.

Herein the abovementioned model is implemented in OpenSEES platform [32]. To do so, zero Length element is used to model the convective component of the numerical model described above. The impulsive and convective components are located at elevations h_0 and h_1 , respectively, to establish a more accurate numerical model of the tank. In addition, the numerical model built in OpenSEES software is observable in Fig. 2.

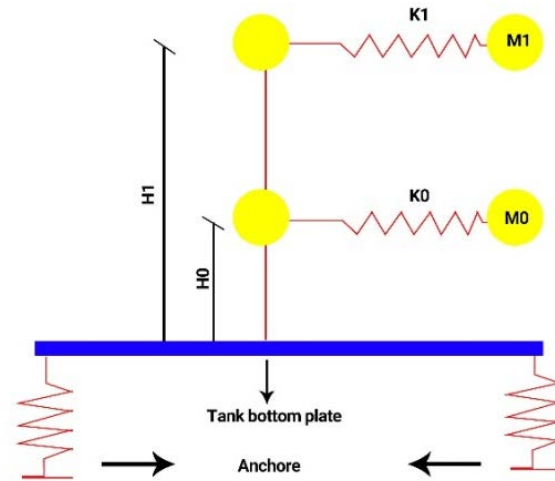
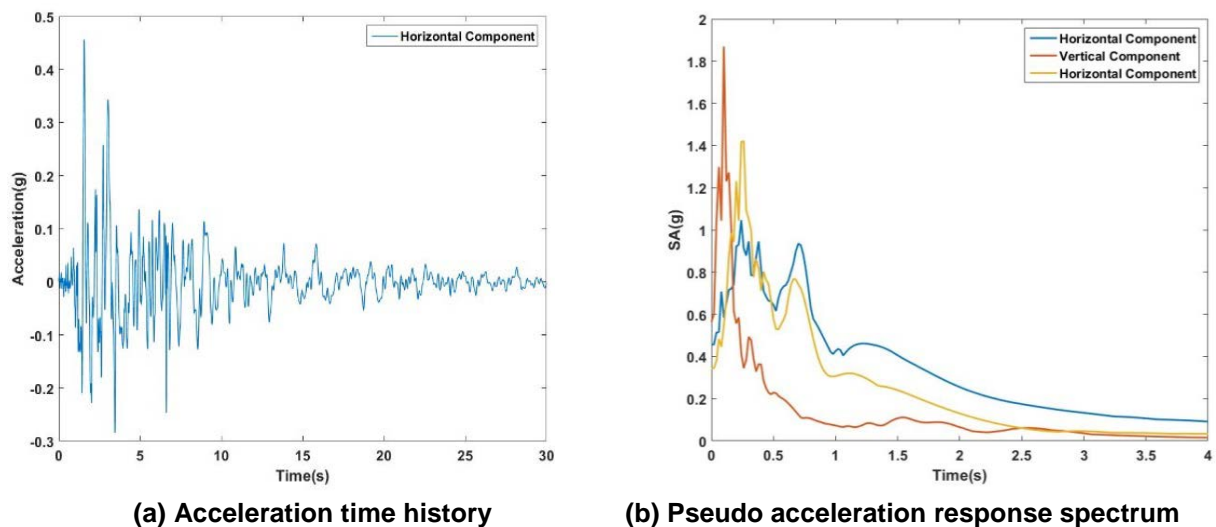


Figure 2. Numerical model of the study tank.

2.3. Model verification

As previously mentioned, in this study, the seismic performance of cylindrical tank which was moderately damaged during the Silakhor earthquake of March 2006 in western Iran was evaluated. The actual seismic performance of the tank was evaluated in different numerical studies [33, 34]. In order to verify the results of numerical analysis, the studied tank was numerically analyzed under the acceleration time history of Silakhor earthquake recorded at Chalancholan station. Fig. 3(a) and Fig. 2(b) show the acceleration time history and pseudo acceleration response spectrum of Silakhor record, respectively. The model adopted for the bottom plate of the tank, which the uplift of the tank was calculated as the vertical displacement of a beam. The maximum estimated tank uplift is compared to that previously estimated by other researchers [32, 33].



(a) Acceleration time history

(b) Pseudo acceleration response spectrum

Figure 3. Silakhor record.

The uplift of the tank subjected to the selected record calculated in different studies are compared in Table 2. As indicated in this table, the model adopted in this study, satisfactorily simulates the dynamic behavior of the case study tank.

Table 2. The tank uplift in different studies.

Model	This study	Eshghi and Razzaghi[33]	Miladi and Razzaghi[29]
Tank uplift (mm)	36	36.8	40

On the other hand, in this study, a Nickel-Titanium (Ni-Ti)-based SMA is employed for anchor bolts, which is among the most widely used SMAs in practice. The properties of the SMA material used in the present work are tabulated in Table 3.

Table 3. Properties of SMA.

Modulus of elasticity (GPa)	Austenite-to-martensite start stress (GPa)	Austenite-to-martensite finish stress (GPa)	Martensite-to-austenite start stress (GPa)	Martensite-to-austenite finish stress (GPa)
42	0.35	0.45	0.1	0.01

To verify the SMA element used, the cyclic behavior of SMA wires studied by DesRoches et al. [35] was investigated. To this end, the cyclic behavior of an SMA bar with diameter of 25.4 mm subjected to the standard cyclic loading protocol was determined using OpenSEES in order to verify the model adopted in this study. Fig. 4 shows the cyclic stress-strain diagram of the numerical model along with that obtained through experiment. As illustrated in this figure, the numerical cyclic behavior is in good agreement with that of the experiment.

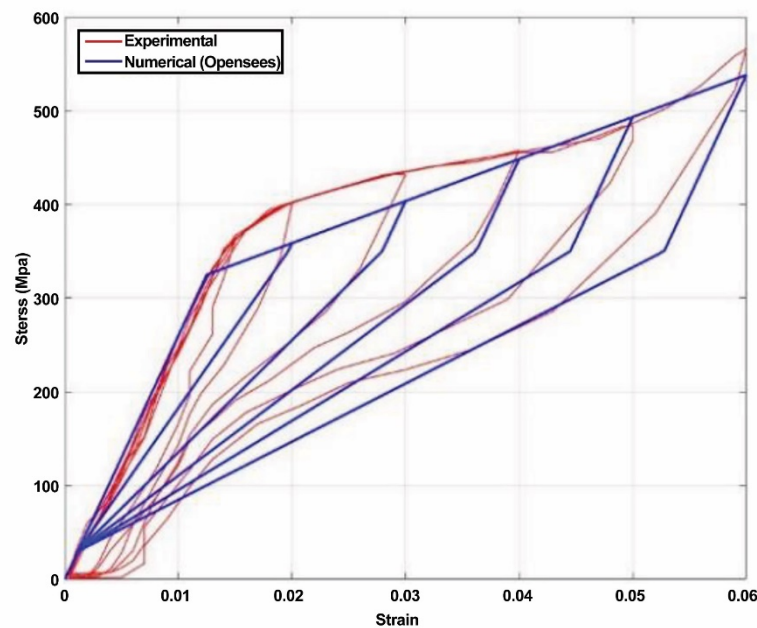


Figure 4. Numerical versus experimental cyclic behavior of SMA bar with diameter of 25.4 mm.

3. Results and Discussion

3.1. Numerical analysis

3.1.1. Preliminary analyses

In order to investigate the effect of mechanical anchors as retrofit tools for the studied tanks, seismic analyses are conducted. To this end, two types of mechanical anchors are considered: regular structural steel and SMA anchor bolt. A parametric study is conducted on the studied tanks in terms of the diameter and the length of anchor bolts. Note that the anchor bolts diameter is varied between 2 and 14 mm and their lengths are varied within the range of 100-250 mm. Nonlinear response history analyses are performed utilizing the acceleration time history of Silakhor earthquake. The results are illustrated in Fig. 5(a) and 5(b) for regular and SMA anchor bolts, respectively.

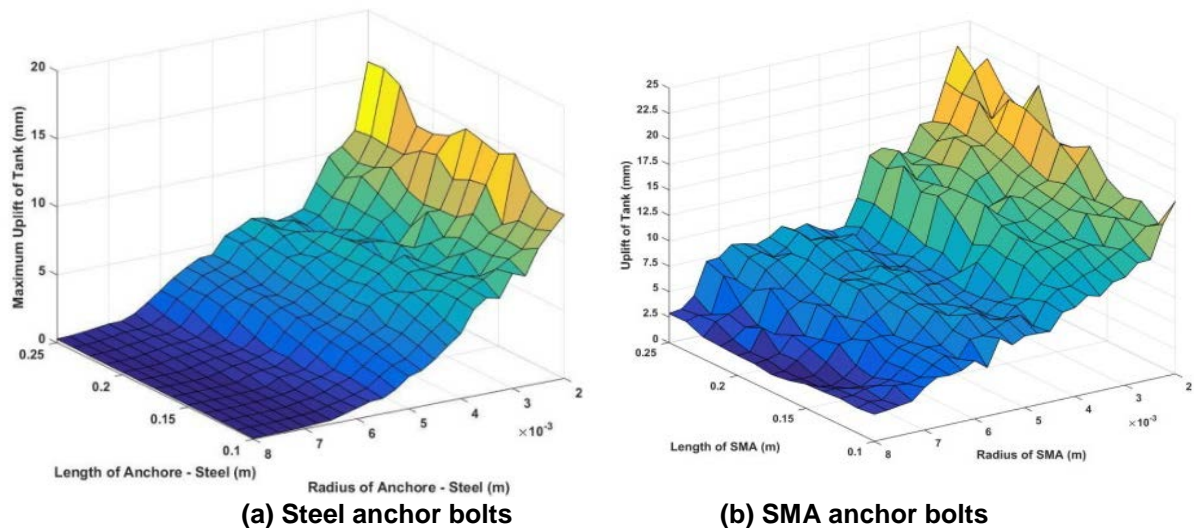


Figure 5. Effect of length and diameter of anchor bolts on the uplift of liquid storage tanks.

As it can be observed and in other research [18, 37, 38], the uplift of the storage tank reduces with increasing stiffness of anchor bolts. According to the properties and capability of SMA in energy dissipation, the large deformations experienced by the tank are reduced acceptably, without causing permanent deformation in SMA. This characteristic of SMA reduces the total force transmitted from the base to the tank, which is beneficial to its protection against potential damage due to strong ground motions. It should be noted that based on the analysis results, for SMA anchor bolts, a diameter of 10 mm and length of 12 cm, results in the minimum uplift. On the other hand, for steel anchor bolts, a diameter of 14 mm and length 12 cm, yielded the best results regarding the uplift of the tank. The maximum axial force developed in the anchor bolts with the aforementioned dimensions is 27 tons, which is remarkably smaller than the critical buckling load 1640 kN.

3.2. Complementary analysis

In order to obtain a comprehensive understanding of the effect of regular steel and SMA anchors on seismic performance of tanks, complementary analyses are conducted. To this end, incremental dynamic analyses are performed using acceleration time histories of 14 natural earthquake ground motion records. Selecting appropriate strong ground motions is an important step in every response history analysis. The specification of suitable strong ground motion depends on the characteristics of the seismic source and site such as fault mechanism, level of seismicity, and probabilistic distribution of the earthquake intensity [36]. In this study, 14 near-field earthquake ground motions including 7 ground motions with forward directivity and 7 ground motions without forward directivity, hereinafter referred to as records set 1 and set 2, respectively, are selected. All of the selected records show a distinct pulse in their time histories and possess a shear wave velocity of 375 m/s and higher, which are consistent with the characteristics of relatively stiff sites. Table 3 presents the properties of records with and without forward directivity.

Table 3. Properties of ground motions with forward directivity.

Name	Earthquake name	Station name	Magnitude	Rrup (km)	PGA (g)	PGV/PGA (s)
E1	Northridge-01	Sylmar – Olive View Med FF	6.69	5.3	0.8634	0.1534
E2	Northridge-01	LA Dam	6.69	5.92	0.426	0.1755
E3	Loma Prieta	Gilroy – Gavilan Coll	6.93	9.96	0.358	0.0867
E4	Loma Prieta	LGPC	6.93	3.88	0.607	0.0848
E5	Chi-Chi_Taiwan	TCU052	7.62	0.66	0.428	0.3850
E6	Morgan Hill	Gilroy Array #6	6.19	9.87	0.292	0.1248
E7	Chi-Chi_Taiwan	TCU076	7.62	2.74	0.446	0.1390

Name	Earthquake name	Station name	Magnitude	Rrup (km)	PGA (g)	PGV/PGA (s)
E8	Loma Prieta	BRAN	6.93	10.72	0.525	0.0717
E9	Northridge-01	Simi Valley – Katherine Rd	6.69	13.42	0.653	0.0419
E10	Chi-Chi_Taiwan	CHY006	7.62	9.76	0.371	0.1602
E11	Chi-Chi_Taiwan	TCU089	7.62	9	0.337	0.0934
E12	Landers	Joshua Tree	7.28	11.03	0.275	0.0254
E13	San Fernando	Lake Hughes #12	6.61	19.3	0.376	0.0210
E14	N. Palm Springs	Cabazon	6.06	7.92	0.213	0.0352

Furthermore, Figs (a) and (b) show the pseudo acceleration response spectra of set 1 and set 2 records, respectively. The selected records exhibit a good variability in terms of frequency content and can excite both of the impulsive and convective modes of the liquid storage tank and in some cases, the natural frequency of the tank is very close to the dominant frequency of the records.

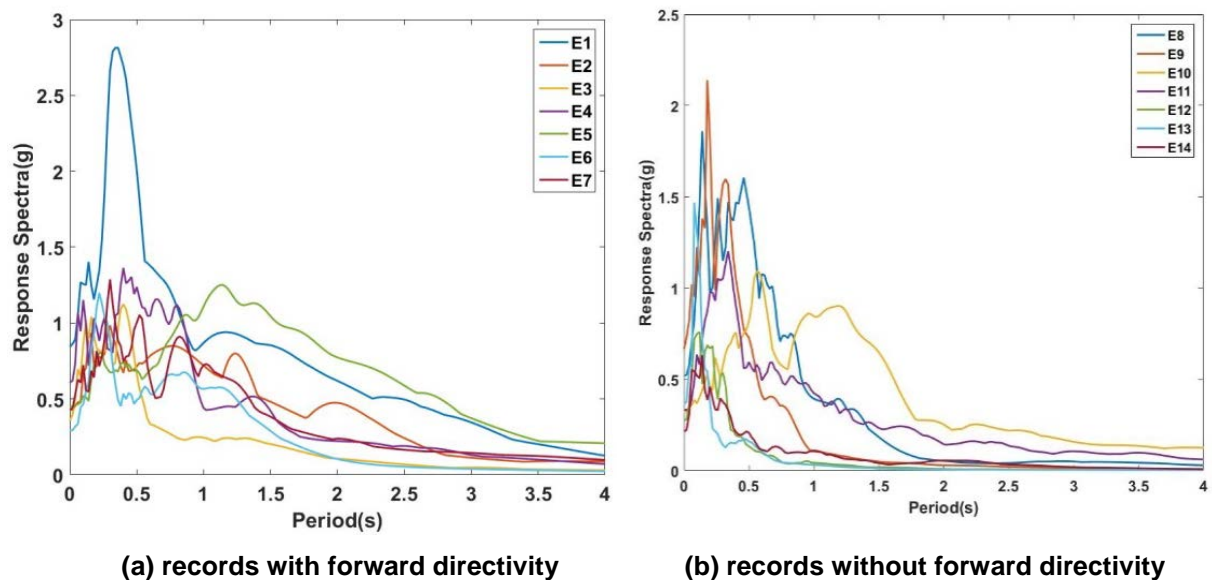


Figure 6. Pseudo acceleration response spectrum.

3.2.1. Comparison of the hysteretic behavior of steel and SMA anchor bolts

In this section, a comparison is made between the behaviors of tanks anchored with the optimal SMA and steel anchor bolts. Fig. 7 (a)-(d) illustrate the tank uplift with respect to the axial force of the bolt for E1, E2, E8, and E9 earthquake ground motions. With reference to these figures, SMA bolts demonstrate a significant energy dissipation through stable hysteresis loops except for the E1 record, which is not strong enough to cause nonlinear behavior. The self-centering characteristic of SMA anchor bolts is evident in these figures, which favors the seismic performance of the tank through facilitating proper energy dissipation with limited uplift. Furthermore, the hysteretic behavior of SMA anchor bolts is more uniform under near-field ground motions without forward directivity, i.e., E8 and E9 records. However, abrupt changes are observed in the hysteresis loops under near-field ground motion with forward directivity E2 due to its pulse-type characteristic.

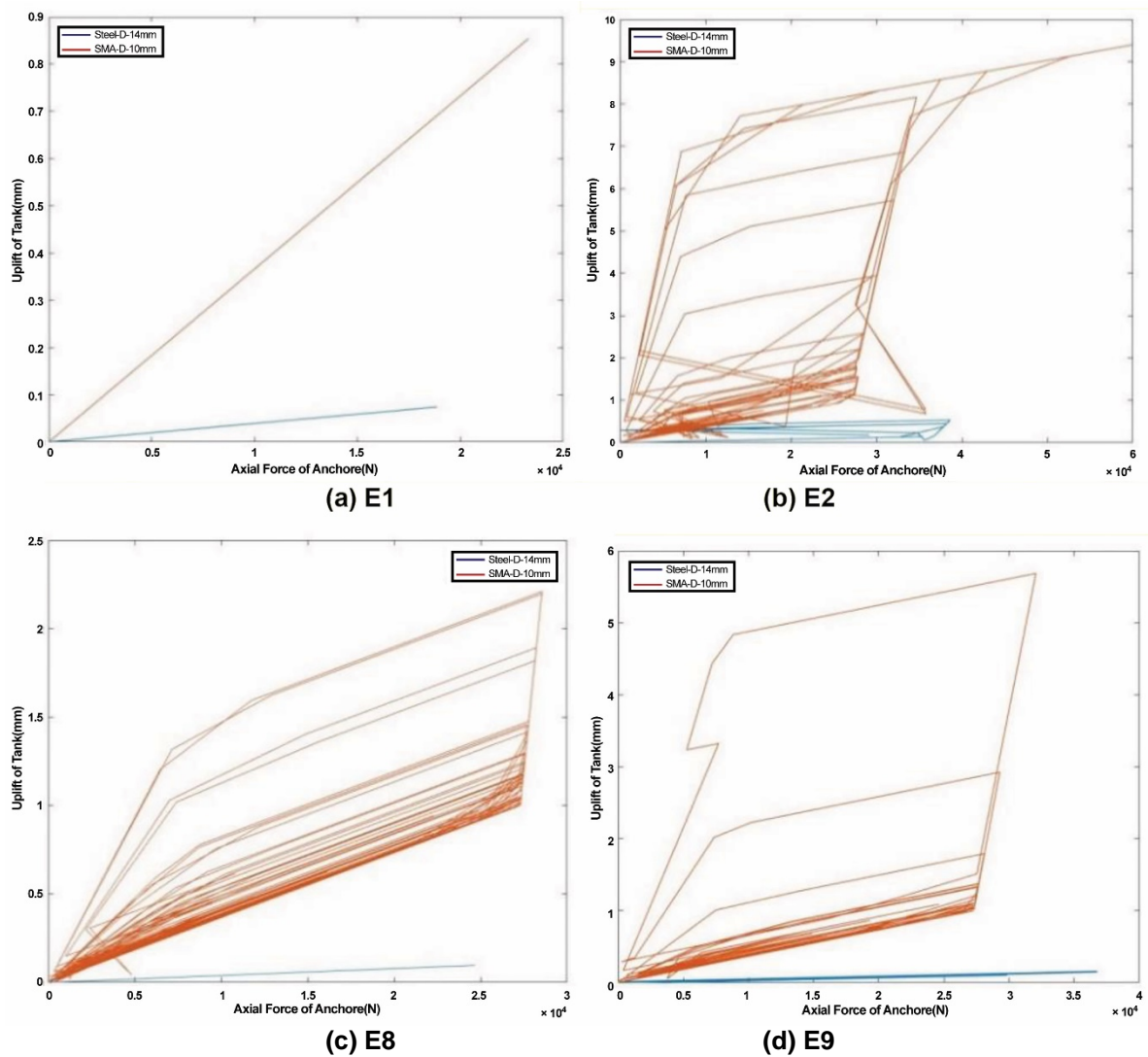


Figure 7. Comparison between hysteretic behavior of steel and SMA anchor bolts under different earthquake records.

3.2.2. Incremental Dynamic Analysis (IDA)

Incremental dynamic analyses (IDAs) are performed on tanks anchored with steel and SMA bolts with different axial stiffness to gain insights into their seismic performance under a wide range of earthquake severities. It should be noted that the tank uplift is selected as the engineering demand parameter (EDP) in IDAs. Furthermore, the uncertainties associated with seismic input including uncertainties in seismic intensity and record-to-record variability are taken into account. The uncertainties associated with the intensity of the seismic event are addressed by defining an Intensity Measure (IM). In the present work, peak ground acceleration (PGA) is selected as IM, which is varied in the range of 0.1–1.0 g. On the other hand, the uncertainties for a fixed intensity are taken into account by employing a set of near-field ground motion records with and without forward directivity as given in Table 4, which are scaled to a common value of IM.

3.2.2.1. IDAs of tanks anchored with steel bolts

Fig. 8(a)-(d) show the IDA results of tanks anchored with steel bolts subjected to E1, E2, E8, and E9 earthquake records.

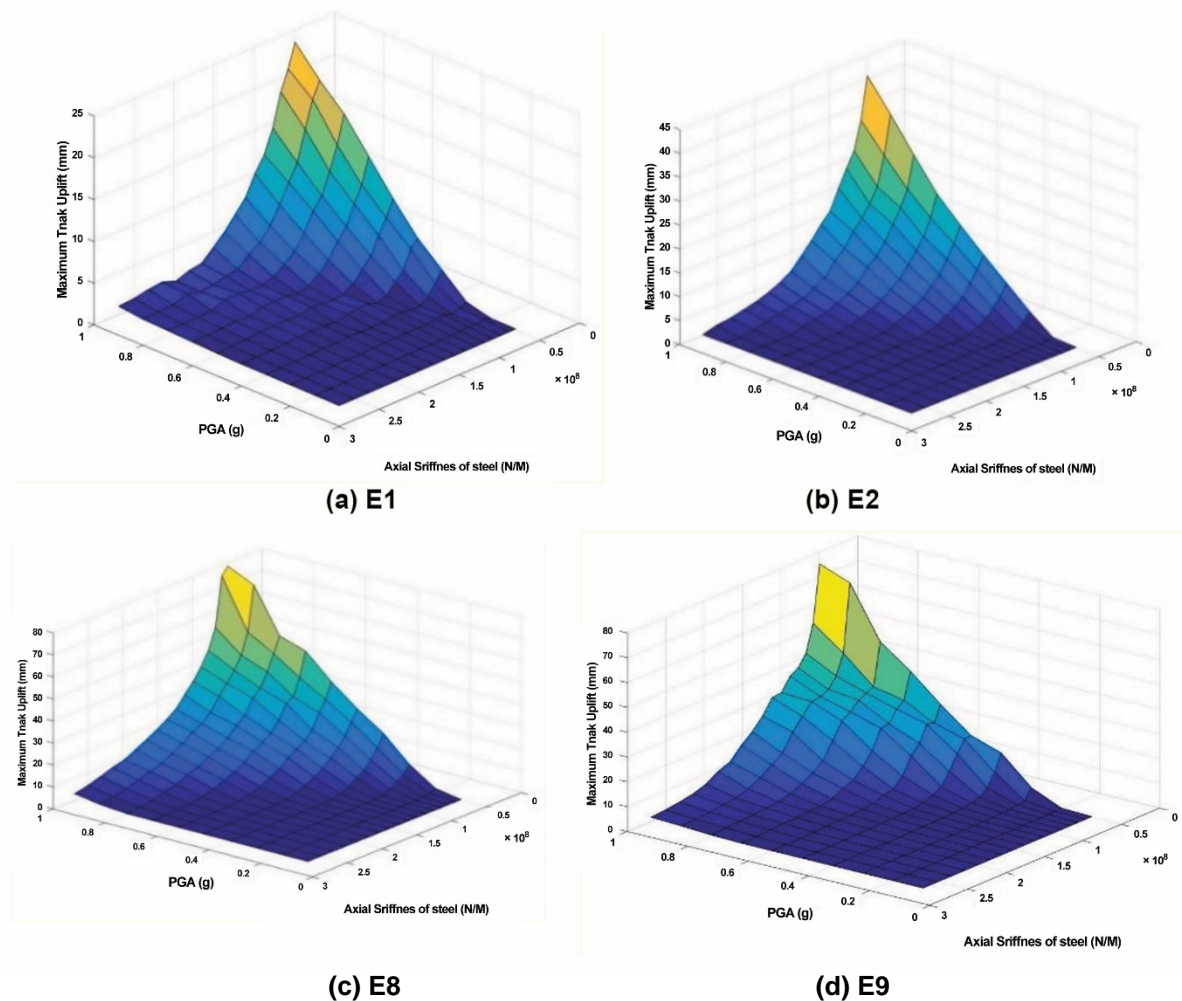


Figure 8. IDA results of tanks anchored with steel bolts.

As it can be observed, the maximum tank uplift under each of these earthquake ground motions decreases with increasing axial stiffness of the steel anchor bolt: at very high axial stiffness of steel anchor bolt, the uplift of the tank approaches zero and the bolt rigidly moves with tank. Conversely, the tank uplift escalates with decreasing stiffness of the bolt, which can result in instability of the system. In order to control the displacement in the tank, the stiffness of the restraints must be defined, because if the stiffness is high, it may cause serious damage to the tank, and if it is low, energy dissipation may not be done by the anchor. Note that the range of stiffness defined in this study was based on engineering judgment and trial and error. Furthermore, it is observed that the frequency content of the seismic input has a profound influence on the uplifting behavior of liquid storage tanks. Given a constant stiffness of the anchor bolt, the tank subjected to a near-field earthquake ground motion record with forward directivity exhibits a notably larger uplift than the same tank subjected to a record without forward directivity. For the sake of illustration, for a fixed axial stiffness of 0.5×10^7 N/m and PGA of 1.0 g, the uplift of the tank subjected to the record E9 is approximately 78 % larger than that of the tank subjected to the record E2. This can be attributable to the pulse-type nature of near-field ground motions with forward directivity, which exerts a very large amount of input energy on the structure in a very short period of time.

3.2.2.2. IDAs of tanks anchored with SMA bolts

Figs. (a)-(d) demonstrate the IDA results of tanks anchored with SMA bolts subjected to E1, E2, E8, and E9 earthquake records. Similar to the tanks anchored with steel bolts, the maximum tank uplift reduces with increasing values of the bolt's stiffness. Unlike steel bolts, SMA bolts exhibit nonlinear behavior when PGA exceeds a certain value. This is beneficiary to the seismic performance of the tank, since the SMA bolt dissipates energy through nonlinear deformation. Furthermore, the uplift of the tank anchored with SMA bolts is considerably larger than that of the tank anchored with steel bolts. As a case in point, for an equal axial stiffness of 0.5×10^7 N/m and PGA of 1.0 g, the maximum uplift of the tank anchored with SMA bolts is approximately 300 % larger compared to that of the tank anchored with steel bolts under E2 earthquake record. In fact, the self-centering feature of SMA materials enables the tank to undergo a limited uplift which in turn enhances the seismic performance of the tank through energy dissipation and reducing the force transmitted to the tank. Moreover, comparing the uplifting behavior of the tanks anchored with SMA bolts

under near-field ground motions with and without forward directivity indicates that they are less sensitive to the frequency content of the seismic input. The tank's uplift under the record E9 is about 17 % larger than that obtained under the record E2 for axial stiffness of 0.5×10^7 N/m and PGA of 1.0 g, whereas the corresponding value for the tank anchored with steel bolts is 78 %. Therefore, it can be concluded that SMA anchor bolts show a satisfactory performance under both near-field earthquake ground motions with and without forward directivity.

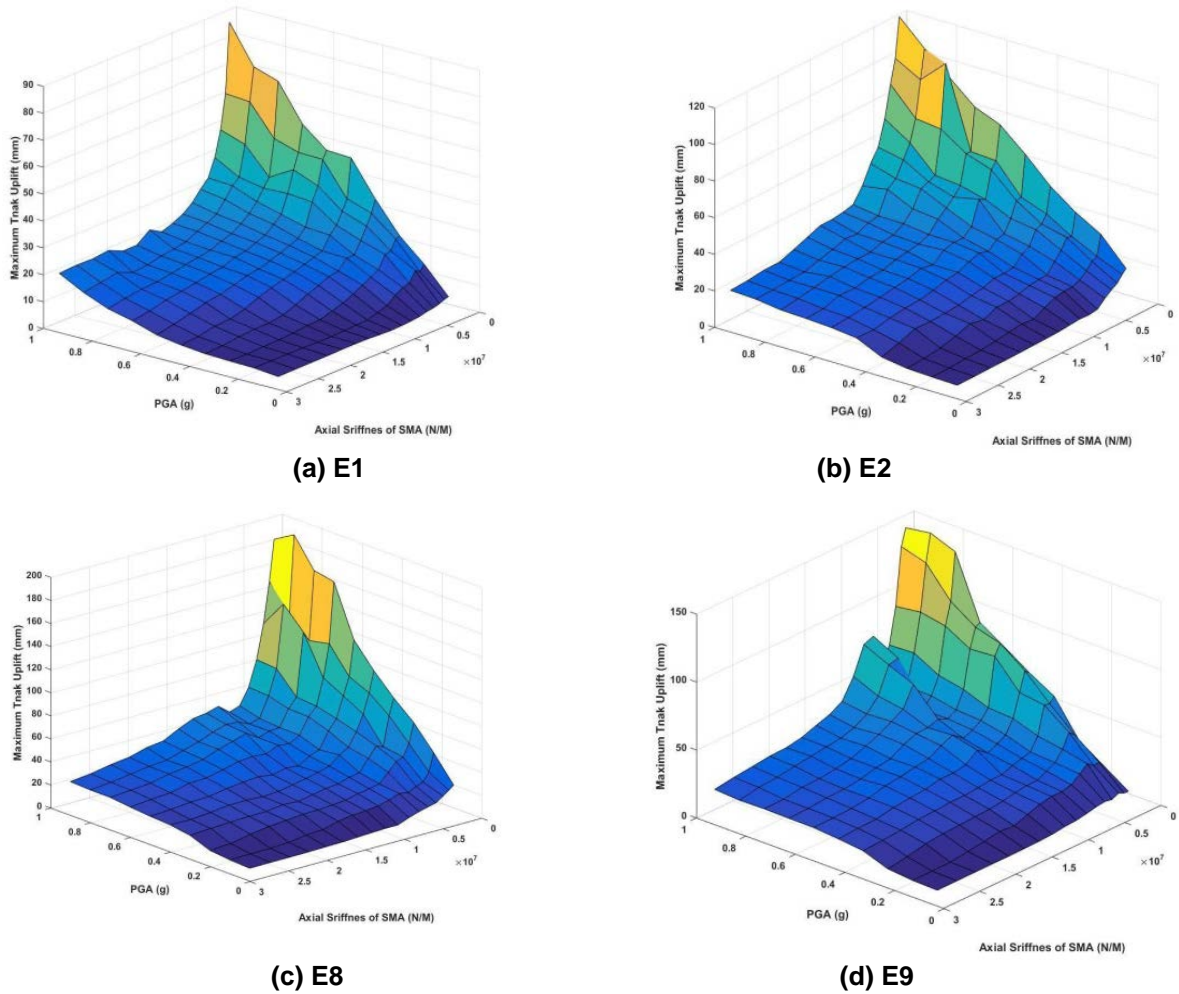


Figure 9. IDA results of tanks anchored with SMA bolts.

In Fig. 10, maximum, minimum and average uplift values of SMA anchor are compared with steel anchor in different PGAs.

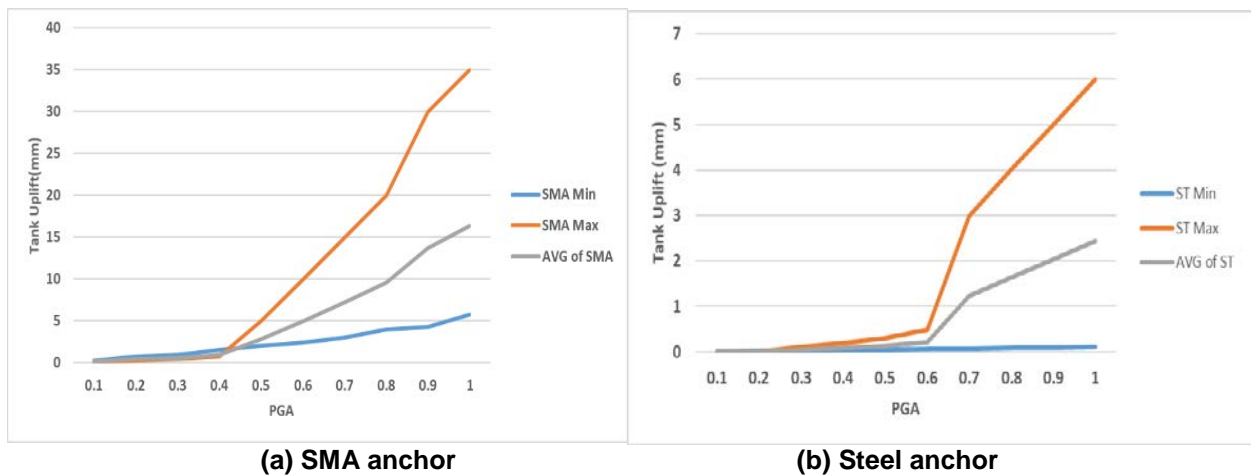


Figure 10. Maximum, minimum and average uplift of tank.

As shown in Fig. 10, the average uplift in tank with SMA is 15 times that of the tank with steel anchor. Therefore, the SMA is allowed limited and controlled lifting.

4. Conclusions

Since most of the anchors used so far in the research and construction of tanks are made of steel, they usually suffer from multiple damages after the earthquake. The use of the SMAs results in the return of deformations and the absence of residual deformation in the anchors, which provides service after the earthquake.

This study investigates the viability of using SMA materials as anchor bolts in liquid storage tanks subjected to seismic excitation, which has not been studied yet. For this purpose, the seismic response of an existing steel liquid storage tank anchored with steel and SMA anchor bolts is evaluated in order to compare the performance of SMA bolts with steel bolts. First, a parametric study is carried out to determine the relatively optimum diameter and length of the anchor bolts based on the tank's uplift. Thereafter, IDAs are performed to gain insights into the seismic response of steel liquid storage tanks anchored with steel and SMA bolts with varying axial stiffness. In the analyses, the record-to-record variability and uncertainties in seismic intensity are taken into account. A set of near-field earthquake ground motion records with and without forward directivity is selected as the seismic input for the nonlinear time history analysis of the tank. Based on the analysis, the following results are obtained:

1. Implementing an anchorage system significantly reduces the residual uplift of the tank, which in turn reduces the damage induced by the strong ground motion. Furthermore, high axial stiffness of steel anchor bolts does not allow the tank to undergo a limited uplift, and thus the risk of experiencing a severe damage at the connection caused by high axial forces escalates.

2. The unique characteristics of SMA anchor bolts facilitates a limited uplift, according to the stability equations proposed by codes [8] to reduce the uplift of tanks, which is accompanied by high energy absorption by these anchor bolts under seismic excitations. In addition, using SMA anchor bolts instead of regular steel bolts, reduces the required diameter of anchor bolts. Although SMA anchor bolts undergo a larger deformation than steel anchor bolts during earthquake excitation, their residual deformation is close to zero, and therefore there is no need to replace them after a severe earthquake.

3. The residual deformation in steel anchor bolts under severe ground excitation can be so large that makes performs and necessitates the replacement of the anchorage system, which imposes a great cost. Based on the uplifting behavior of tanks anchored with steel and SMA bolts, it can be concluded that SMA bolts are less sensitive to the frequency content of the seismic input and perform satisfactorily under both near-field earthquake ground motions with and without forward directivity.

4. Due to the performance of SMAs, the allowable uplift to the tank anchored with SMA is, on average, about 15 times the uplift in the tanks anchored with steel, because the tank with steel anchors has high axial stiffness than the SMA. In case of uplift in the tank with steel anchors, the anchors and the body of the tank are damaged and must be replaced after the earthquake.

References

1. Shoaie, P., Orimi, H.T. A combined control strategy using tuned liquid dampers to reduce displacement demands of base-isolated structures: a probabilistic approach. *Struct. Civil. Eng.* 2019. 13 (4). Pp. 890–903.
2. Sahraeian, S.M.S., Takemura, J., Seki, S. An investigation about seismic behavior of piled raft foundation for oil storage tanks using centrifuge modelling. *Soil Dyn. Earthq. Eng.* 2018. No. 104. Pp. 210–227.
3. Vela, R.J.M., Brunesi, E., Nascimbene, R. Derivation of floor acceleration spectra for an industrial liquid tank supporting structure with braced frame systems. *Eng. Struct.* 2018. No. 171. Pp. 105–122.
4. Zhao, M., Zhou, J. Review of seismic studies of liquid storage tanks. *Structural Engineering and Mechanics.* 2018. 65 (5). Pp. 557–572.
5. Sun, J., Cui, L., Li, X., Wang, Z., Liu, W., Lv, Y. Vibration mode decomposition response analysis of large floating roof tank isolation considering swing effect. *Earthquakes and Structures.* 2018. 15 (4). Pp. 411–417.
6. Zhang, R., Cheng, X., Guan, Y., Tarasenko, A.A. Seismic response analysis of an unanchored vertical vaulted-type tank. *Earthquakes and Structures.* 2017. 13 (1). Pp. 67–77.
7. France, D.L. American Water Works Association (AWWA), AWWA D-100. Denver (CO). American Water Works Association, USA. 2005.
8. Sommers, M. American Petroleum Institute (API), Welded storage tanks for oil storage, API 650. Washington (DC), American Petroleum Institute Standard, USA. 2003.
9. Swan, S.W., Miller, D.D., Yanev, P.I. The Morgan hill earthquake of April 24, 1984 – Effects on industrial facilities, buildings, and other facilities. *Earthq. Spectra.* 1985. 1 (3). Pp. 457–568.
10. Manos, G.C., Clough, R.W. Tank damage during the May 1983 Coalinga earthquake. *Earthq. Eng. Struct. Dyn.* 1985. 13 (4). Pp. 449–466.
11. Manos, G.C. Evaluation of the earthquake performance of anchored wine tanks during the San Juan, Argentina 1977 earthquakes, *Earthq. Eng. Struct. Dyn.* 1991. 20 (12). Pp. 1099–1114.
12. Eshghi, S., Zare, M., Assadi, K., Razzaghi, M., Ahari, M., Motamedi, M. Reconnaissance report on 26 December 2003 Bam earthquake. International Institute of Earthquake Engineering (IIEES). 2004.

13. Eshghi, S., Razzaghi, M.S. Performance of industrial facilities in the 2003 Bam, Iran. *Earthquake, Earthq. Spectra*. 2005. 21 (1). Pp. 395–410.
14. Brunesi, E., Nascimbene, R., Pagani, M., Beilic, D. Seismic performance of storage steel tanks during the May 2012 Emilia, Italy, earthquakes, *J. Perform. Constr. Facil.* 2015. 29 (5). Pp. 4014137.
15. Zareian, F., Sampere, C., Sandoval, V., McCormick, D.L., Moehle, J., Leon, R. Reconnaissance of the Chilean wine industry affected by the 2010 Chile offshore Maule earthquake. *Earthq. Spectra*. 2012. 28 (S1). Pp. 503–512.
16. Fisher, E.C., Liu, J. February. Seismic Behavior of Cylindrical Fluid-Filled Steel Tanks. In *Structures Congress*. Denver, Colorado, 2017. 772 p.
17. Virella, J.C., Godoy, L.A., Suárez, L.E. Dynamic buckling of anchored steel tanks subjected to horizontal earthquake excitation. *J. Constr. Steel Res.* 2006. 62 (6). Pp. 521–531.
18. Kildashti, K., Mirzadeh, N., Samali, B. Seismic vulnerability assessment of a case study anchored liquid storage tank by considering fixed and flexible base restraints. *Thin-Walled Structures*. 2018. No. 123. Pp. 382–394.
19. Hamdan, F.H. Seismic behaviour of cylindrical steel liquid storage tanks. *J. Constr. Steel Res.* 2000. No. 53. Pp. 307–333.
20. Saha, S.K., Sepahvand, K., Matsagar, V.A., Jain, A.K., Marburg, S. Fragility analysis of base-isolated liquid storage tanks under random sinusoidal base excitation using generalized polynomial chaos expansion-based simulation. *J. Struct. Eng.* 2016. 142 (10). Pp. 4016059.
21. Saha, S.K., Matsagar, V.A., Chakraborty, S. Uncertainty quantification and seismic fragility of base-isolated liquid storage tanks using response surface models. *Probabilistic Eng. Mech.* 2016. No. 43. Pp. 20–35.
22. Bagheri, S., Farajian, M. The effects of input earthquake characteristics on the nonlinear dynamic behavior of FPS isolated liquid storage tanks. *Journal of Vibration and Control*. 2018. 24 (7). Pp. 1264–1282.
23. Tavakoli Joorabi, A., Razzaghi, M.S. Seismic fragility analysis of retrofitted steel tanks considering corrosion. *Proceedings of the Institution of Civil Engineers-Structures and Buildings*. 2019. 172 (10). Pp. 712–720.
24. Abraik, E., Youssef, M.A. Seismic fragility assessment of super elastic shape memory alloy reinforced concrete shear walls. *J. Build. Eng.* 2018. No. 19. Pp. 142–153.
25. Luo, X., Ge, H., Usami, T. Parametric study on damage control design of SMA dampers in frame-typed steel piers, *Front. Archit. Civ. Eng. China*. 2009. 3 (4). 384 p.
26. Zafar, A., Andrawes, B. Experimental flexural behavior of SMA-FRP reinforced concrete beam, *Front. Struct. Civ. Eng.* 2013. 7 (4). Pp. 341–355.
27. Wang, B., Zhu, S., Qiu, C.X., Jin, H. High-performance self-centering steel columns with shape memory alloy bolts: Design procedure and experimental evaluation. *Eng. Struct.* 2019. No. 182. Pp. 446–458.
28. Shoaee, P., Orimi, H.T., Zahrai, S.M. Seismic reliability-based design of inelastic base-isolated structures with lead-rubber bearing systems. *Soil Dyn. Earthq. Eng.* 2018. No. 115. Pp. 589–605.
29. Miladi, S., Razzaghi, M.S. Failure analysis of an un-anchored steel oil tank damaged during the Silakhor earthquake of 2006 in Iran. *Eng. Fail. Anal.* 2019. No. 96. Pp. 31–43.
30. Housner, G.W. The dynamic behavior of water tanks. *Bulletin of the seismological society of America*. 1963. 53(2). Pp. 381–387.
31. Ruiz, R.O., Garcia, D.L., Taflanidis, A.A. An efficient computational procedure for the dynamic analysis of liquid storage tanks. *Eng. Struct.* 2015. No. 85. Pp. 206–218.
32. Mazzoni, S., McKenna, F., Scott, M.H., Fenves, G. *OpenSees users manual*. PEER, Univ. California. Berkeley, USA, 2004.
33. Eshghi, S., Razzaghi, M.S. Performance of cylindrical liquid storage tanks in Silakhor, Iran earthquake of March 31, 2006. *Bull. New Zeal. Soc. Earthq. Eng.* 2007. 40 (4). Pp. 173–182
34. Ormeño, M., Larkin, T., Chouh, N. Influence of uplift on liquid storage tanks during earthquakes. *Coupled Syst. Mech.* 2012. 1(4). Pp. 311–324.
35. DesRoches, R., McCormick, J., Delemont, M. Cyclic properties of super-elastic shape memory alloy wires and bars. *J. Struct. Eng.* 2004. 130(1). Pp. 38–46.
36. Alexandra, T., Taflanidis, A.A., Galasso, C. Validation of stochastic ground motion model modification by comparison to seismic demand of recorded ground motions. *Bulletin of Earthquake Engineering*. 2019. 17 (6). Pp. 2871–2898.
37. Rondon, A., Guzey, S. Evaluation of the Anchor-Bolt Chair Design Considering Localized Stresses in the Shell of Anchored Storage Tanks. In *Pressure Vessels and Piping Conference*, American Society of Mechanical Engineers. Vancouver, 2016. V005T09A00p.
38. Phan, H.N., Paolacci, F. Fluid-structure interaction problems: an application to anchored and unanchored steel storage tanks subjected to seismic loadings. *arXiv preprint arXiv.1805.00679*. 2018.

Contacts:

Saeid Jamalpour Najmabad, saeidjamalpournajmabad@gmail.com

Mehran Seyed Razzaghi, razzaghi.m@gmail.com

Fariborz Nateghi Alahi, nateghi@iiees.ac.ir



DOI: 10.34910/MCE.108.3

Effectiveness of base-isolated low-rise masonry building under excitation from earthquakes

V.T. Ngo 

Thuyloi University, 175 Tay Son, Dong Da, Hanoi, Vietnam

E-mail: thuyet.kcct@tlu.edu.vn

Keywords: masonry building, base isolation, seismic isolation technology, seismic vulnerability, fiber reinforced elastomeric isolator, floor acceleration response, inter-storey drift response, earthquake

Abstract. Low-rise masonry building is one of the most commonly adopted structural types even in earthquake prone regions in developing countries. The building is generally susceptible to damage due to earthquake induced motion and may suffer partial or total collapse. Un-bonded fiber reinforced elastomeric isolator (U-FREI) is a relatively new seismic base isolator and is expected to be an attractive option for seismic mitigation of low-rise buildings. In this paper, the effectiveness of a base-isolated masonry building supported on U-FREIs subjected to earthquakes is investigated by finite element (FE) analysis using SAP2000. The prototype building is a two-storey masonry building located at Tawang, Arunachal Pradesh State, India and is the first such U-FREIs supported prototype low-rise building constructed anywhere in the world. Mechanical characteristics of U-FREIs obtained from both experiments and FE analysis are utilized in defining the nonlinear property of the model used for simulating U-FREIs. The force-deformation behaviour of the isolator is modelled as bi-linear hysteretic behaviour, which can be effectively used to model all isolation system in practice. Time history analysis of the building for both fixed-base (FB) and base-isolated (BI) conditions under the action of various recorded real earthquakes are investigated. Comparison of the dynamic response of both FB and BI buildings is computed to evaluate the effectiveness of the base isolation system. The FE analysis results show that floor acceleration and inter-storey drift responses of the BI building under earthquakes are significantly lesser than those of the FB building. U-FREIs are recommended for seismic isolation of low-rise masonry building.

1. Introduction

Low-rise building, especially masonry building, which includes residential quarters, schools, government offices, markets, etc., is one of the most commonly adopted structural types in developing countries like India, Bangladesh, Nepal, Indonesia, etc. Vast majority of these buildings are also located in high seismicity regions. The building can sustain gravity loads very easily due to high compressive strength of masonry, but are highly susceptible to ground shaking due to their low tensile as well as shear strength making them often susceptible to damage. Thus, mitigation of seismic vulnerability of the buildings is an important area of research.

Base isolation system is a class of passive control system which can reduce the seismic vulnerability of a structure located in high seismic regions. The system decouples the building from the horizontal components of earthquake ground motion by interposing structural elements with low horizontal stiffness between the foundation and superstructure. Thus, it results in reduction in the magnitude of fundamental frequency of the base-isolated structure to a much lower value than both its fixed-base frequency and the predominant frequency range of the ground motion. The goal is to simultaneously reduce inter-storey drifts and floor accelerations to limit or avoid damage, not only to structure but also to its contents.

Ngo, V.T. Effectiveness of base-isolated low-rise masonry building under excitation from earthquakes. Magazine of Civil Engineering. 2021. 108(8). Article No. 10803. DOI: 10.34910/MCE.108.3

© Ngo, V.T., 2021. Published by Peter the Great St. Petersburg Polytechnic University



This work is licensed under a CC BY-NC 4.0

Conventionally, a laminated elastomeric isolators consisting of elastomer / rubber layers interleaved and bonded with thin steel reinforcing plates and commonly known as steel reinforced elastomeric isolator (SREI) are used. This class of isolators is very stiff in the vertical direction, but is highly flexible in horizontal direction to deflect the earthquake energy associated with strong ground motion. However, SREI has some disadvantages, limiting its use in low cost low-rise buildings. The limitations are mainly due to their heavy weight as well as cost and thus restricting their applications primarily in important and expensive buildings. The development of light weight, less expensive isolators has made implementation of the seismic isolation technology to low-rise masonry building vulnerable to seismic ground motions, feasible.

Seismic isolators designed using layers of elastomer / rubber vulcanized with thin layers of bi-directional fiber fabric as reinforcement [1] are known as fiber reinforced elastomeric isolators (FREI). Both weight and height of isolators can be reduced by replacing steel with fiber fabric as reinforcement material. Traditionally SREIs are installed in any structure by connecting the top end plate of the isolator with the bottom surface of superstructure and bottom end plate with the top of foundation, and hence SREIs are also called as bonded isolator. Study on un-bonded fiber reinforced elastomeric isolator (U-FREI) is a significant step towards enhancement of ease of installation of isolators in buildings. Heavy steel-end-plates are not provided in U-FREIs and these devices are installed at the interface of foundation and superstructure without any connection. Thus, elastomer layers at top and bottom of U-FREIs will be in frictional contact with superstructure and foundation respectively. Reduced weight and ease of installation would thus facilitate implementation of U-FREIs for control of seismic response of low-rise vulnerable lifeline buildings in developing countries.

Various studies have been conducted with the purpose of evaluating the seismic vulnerability or the effectiveness of base isolation systems. The fragility function was developed to determine optimum design parameters of isolation devices to maximize effectiveness of seismically-isolated bridges in California, United States of America (USA) [2]. The study showed that the mechanical properties of isolation devices had a significant influence on the damage probability of isolated bridges. An analytic review of various modern methods for seismic insulation was conducted [3]. The seismic vulnerability assessment of typical bridge classes supported on elastomeric bearings in eastern Canada was studied by [4]. The methods to determine the optimal damping parameters for seismic isolation systems were developed by [5]. The study was conducted for both linear and nonlinear damping model of seismic isolation system. The seismic vulnerability assessment of a class of bridge retrofitted with seismic-isolation devices in Canada was presented by [6]. The reduction of acceleration response of base-isolated (BI) three-storey building with lead plug bearings constructed at Indian Institute of Technology Guwahati, India as compared to that of fixed-base (FB) building was studied by [7]. The seismic vulnerability of a retrofitted historical masonry structure in Bayburt Yakutiye Mosque, Turkey using base isolation was investigated [8]. Most of these above-mentioned studies were carried out on base-isolated structures with conventional SREIs.

In view of the above, U-FREI is relatively new seismic base isolator and is expected to be effective in reducing the seismic vulnerability of low-rise buildings. Some studies in literature have been conducted with the purpose of evaluating the mechanical properties of the U-FREIs [9–13]. In recent time, a few studies have been investigated the effectiveness of BI low-rise buildings supported on U-FREIs. Shake table tests of BI buildings supported on U-FREIs were carried out to ascertain its effectiveness in controlling seismic response by [14–16]. A little effort to apply the FREIs for low-rise buildings was presented by [17, 18]. Most of these studies were carried out the seismic performance evaluation of scaled model of low-rise building supported on U-FREIs. Thus, the effectiveness of base isolated prototype masonry building supported on prototype U-FREIs under the action of earthquakes should be further studied.

This study presents seismic performance evaluation of prototype low-rise masonry building supported on square U-FREIs by finite element (FE) analysis. A prototype masonry building supported on U-FREIs at Tawang, Arunachal Pradesh State, India is considered for this study. The building is simulated by three-dimensional (3D) nonlinear FE model for FB and BI conditions using SAP2000. Dynamic responses of both FB and BI buildings under the action of various recorded real time history ground motions of earthquakes are investigated. Comparison of floor acceleration and inter-storey drift responses of both FB and BI buildings is carried out to evaluate the effectiveness of the BI building under earthquakes. In addition, the hysteresis loops of the U-FREIs under these earthquakes are also investigated.

2. Research subject and Method

2.1. Research subject

A two-storey base-isolated stone masonry building located at Tawang, Arunachal Pradesh State, India is considered for this study. The building is supported on square U-FREIs for seismic isolation. This is the first U-FREI supported prototype low-rise masonry building constructed anywhere in the world [17].

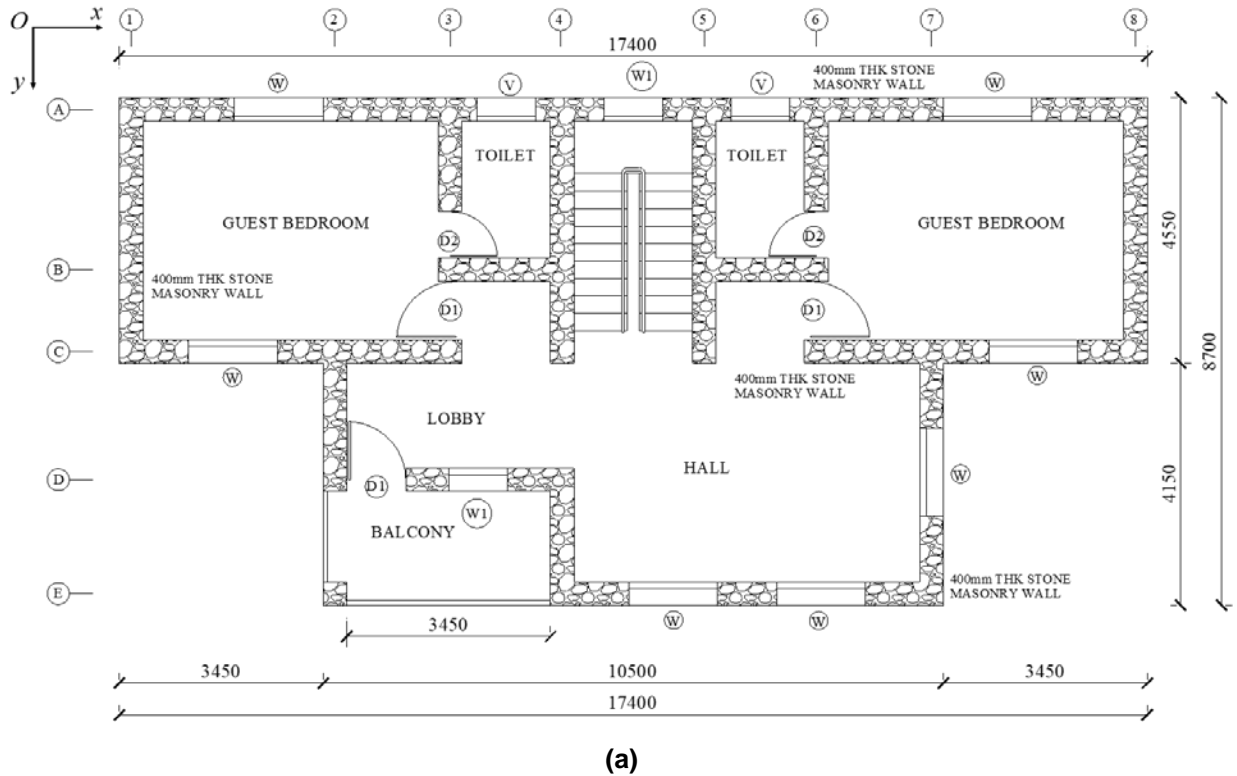
Such the buildings are representative of the common building types in the north-eastern part of India even in the highest seismic zone (zone V) [19].

In the prototype building, the structure is comprising of two main components including of stone masonry walls and reinforced concrete floors. The roof is covered by galvanized iron sheets, which are supported on truss structures. A view of the building is shown in Fig. 1. A typical floor plan of the building is shown in Fig. 2a. U-FREIs are placed between the two beams (level A and B) without any connections at fourteen numbers of locations shown in Fig. 2b.



Figure 1. A view of the prototype base-isolated building [17].

Base isolation using square U-FREIs for the building is designed to resist strong ground motions. Total fourteen square U-FREIs are used, which comprises of nine isolators of 250×250×100 mm size and five isolators of 310×310×100 mm size. Each isolator is made from eighteen elastomer layers interleaved and bonded with seventeen layers of carbon fiber reinforcement sheets. The thickness of each elastomer layer is 5.0 mm, while that of each fiber layer is 0.55 mm and total height of each bearing is 100 mm. The shear modulus of elastomer (G) is 0.90 N/mm² and the elastic modulus of carbon fiber laminate (E) is 40000 N/mm².



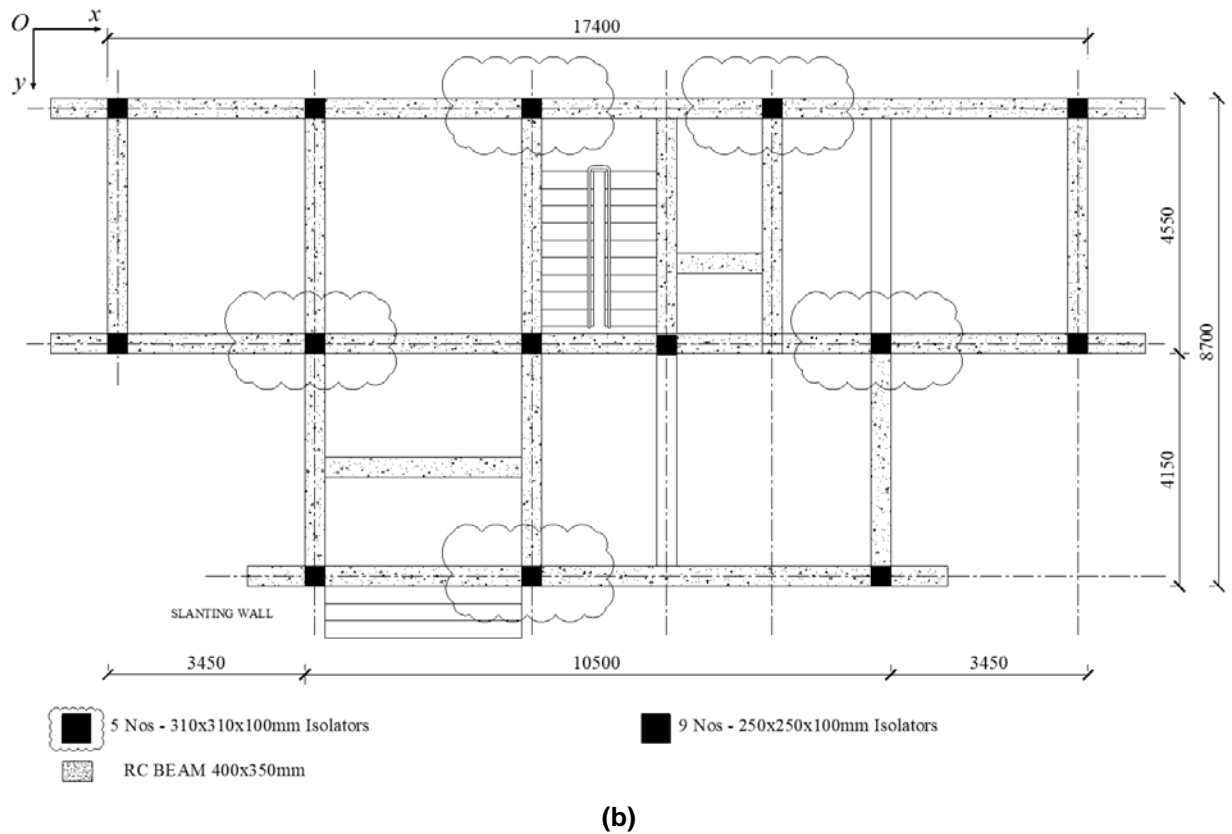


Figure 2. Plan views of the building [17]: a – Typical floor plan; b – Plan showing locations of base isolators.

2.2. Numerical method

Three-dimensional FE model of BI masonry building as shown in Fig. 3 is simulated in SAP2000 nonlinear [20]. Isolators are modelled by rubber isolator element defined under link type of elements. The force-deformation behaviour of an isolator is modelled as bi-linear hysteretic behaviour which can be effectively used to model all isolation system in practice. The fixed-base condition is simulated by providing fixity at the basement beam level A. The reinforce concrete floors are modelled using shell elements, in which each floor is assigned by a diaphragm constraint. Masonry walls are modelled using nonlinear layered shell elements [21]. The anisotropic behaviour of masonry is modelled by stress-strain curves for compression, tension and shear behaviour.

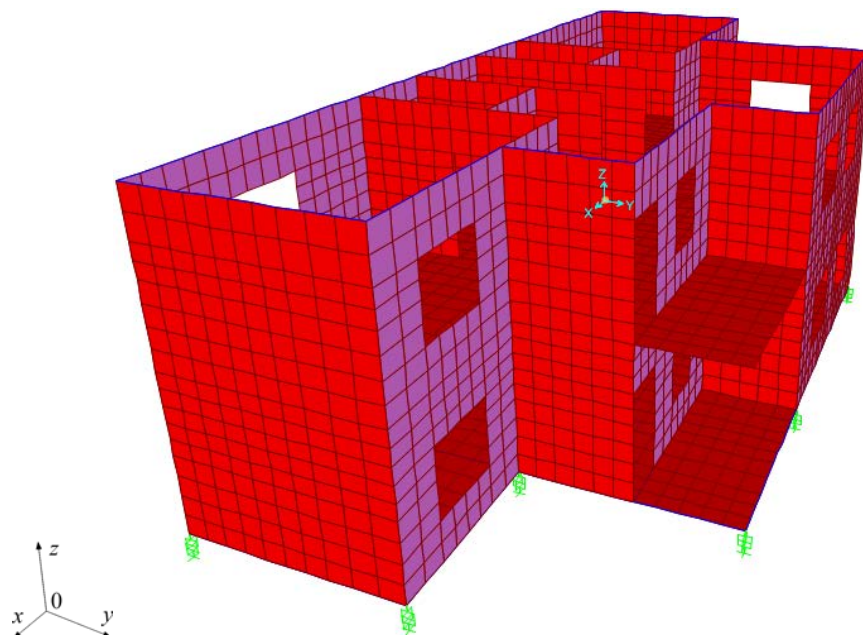


Figure 3. Three-dimensional FE model of the base-isolated masonry building.

Uniaxial compressive and tensile behaviour of masonry prism. Stone masonry building is considered since similar structures are prevalent in the north-eastern zone of India. Material properties are selected to represent the masonry material used in almost all masonry buildings of the zone. In this study, stone masonry with a compressive strength of 7.5 MPa and mortar with a compressive strength of 2.5 MPa are used [17]. Uniaxial compressive and tensile behaviour of masonry prism is defined using the relationship suggested from a number of laboratory tests carried out by [22, 23]. The uniaxial compressive as well as tensile behaviour of masonry prism are shown in Fig. 4.

Stress-strain behaviour of masonry prism in shear. Shear resistance is represented by cohesion and friction between stone (or brick) and mortar, which can be expressed with Mohr-Coulomb friction [24, 25] as

$$\tau = c + \sigma \times \tan \phi, \quad (1)$$

where σ is compressive stress and $\tan \phi$ represents friction between stone and mortar. Numerical analysis is carried out using SAP2000 considering a Mohr-Coulomb failure criterion with a cohesion value of 0.1 MPa and ignoring friction. Thus, the stress-strain behaviour of masonry prism in shear is shown in Fig. 5.

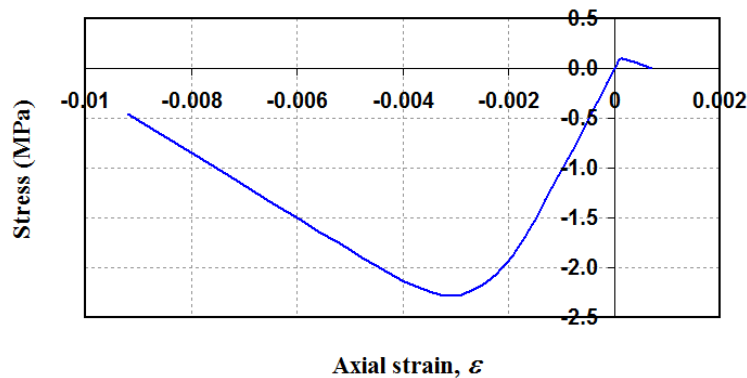


Figure 4. Compressive and tensile behaviour of masonry prism used in the numerical simulation.

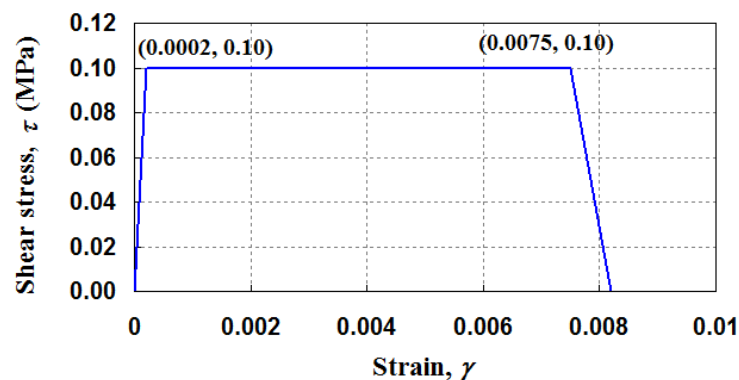


Figure 5. Stress-strain plot for shear of masonry prism.

Boundary condition. The simulation of the building is performed for both FB and BI conditions. For FB building, all nodes at ground level are fixed in all the directions, while for BI building, fourteen isolators placed at locations as per Fig. 2b are modelled by rubber isolator element defined under link type of elements. For simulation of a U-FREI, backbone curves obtained from force-displacement hysteresis loops of typical U-FREIs under horizontal cyclic loading are used to represent the properties of isolator along X and Y-axis. The force-displacement hysteresis loops of all U-FREIs in this study obtained from experimental and numerical analyses can be found in [13, 17]. For modelling of a U-FREI in SAP2000, the nonlinear force-deformation behaviour of its horizontal response is modelled through the bilinear hysteresis loop characterized (Fig. 6, a) by three parameters namely (i) The effective stiffness, K_{eff} , (ii) Initial stiffness K_1 and the post yield to pre-yield stiffness ratio, $n (= K_2/K_1)$, where K_2 is post yield stiffness, and (iii) Yield strength F_y . An idealized bilinear hysteresis loop and idealised as well as actual force-displacement relationship of U-FREI are shown in Fig. 6b. The input parameters for the mechanical properties of the horizontal response of these U-FREIs supported on the prototype building for modelling are presented in Table 1.

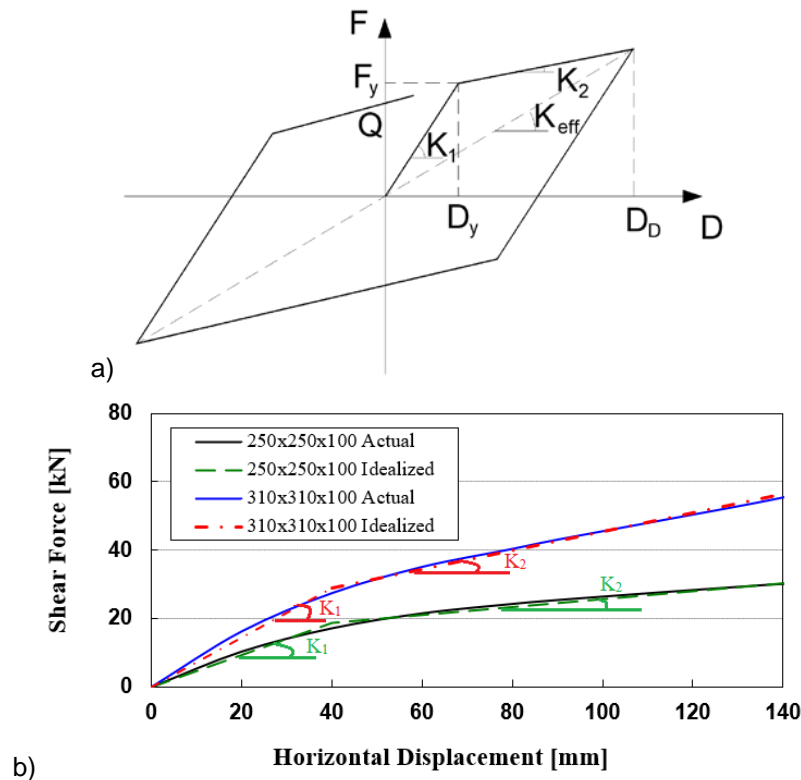


Figure 6. Idealised and actual force-displacement relationship of U-FREIs:
a – Idealised bi-linear force-displacement relationship of isolator;
b – Actual load-displacement curves of U-FREIs with superimposed idealized bi-linear curves.

Table 1. Input mechanical properties of the horizontal response of these U-FREIs for modelling.

Description	250x250x100 mm	310x310x100 mm
K_{eff} (kN/m)	210	395
K_1 (kN/m)	465	725
F_y (kN)	18.5	29.0
n	0.26	0.38

Vertical stiffness (K_V) of a laminated elastomeric isolator is given by [26]

$$K_V = \frac{E_c A}{t_r}, \quad (2)$$

where E_c is the compression modulus of the isolator; A is the full cross-sectional area of the isolator and t_r is the total thickness of elastomer / rubber layers in the isolator. According to [27], the compression modulus, E_c , for a square isolator is $E_c = 6.748 GS^2$, where S is the shape factor of the isolator which is defined as the ratio of the loaded area to load free area of an elastomer / rubber layer. The vertical stiffness of these isolators supported on the building are furnished in Table 2.

Table 2. Vertical stiffness of these U-FREIs for modelling.

Description	250x250x100 mm	310x310x100 mm
Compression modulus, E_c , (MPa)	948.94	1459.09
Vertical stiffness, K_V , (kN/m)	658984.4	1557979.9

Input ground motions of earthquakes. The building is located at Tawang in north-eastern part of India even in the highest seismic zone (zone V). The actual time history data has been carried out specifying closest distance to a known fault that is capable of producing large magnitude events and that has high rate of seismic activity. The recording stations are just near to an active fault, it is likely to be subjected to the near-fault effects. In this study, three time history ground motions with different stations, peak accelerations, frequency contents and durations from actual record earthquakes as Koyna (India, 1967,

Comp – Longitudinal), El-Centro (US, 1940, Comp – N-S) and Victoria (Mexico, 1980, Comp – CPE045) as shown in Fig. 7, are selected. Time history analyses of both FB and BI buildings are carried out along the weaker axis, i.e. Y-axis (Fig. 2).

Numerical analysis. The dynamic response of both FB and BI buildings under the action of various recorded real earthquake time history ground motions above are investigated. Comparison of floor acceleration and inter-storey drift responses of both FB and BI buildings is carried out to evaluate the effectiveness of the BI building. In addition, the hysteresis loops of the U-FREIs under these earthquakes are also investigated.

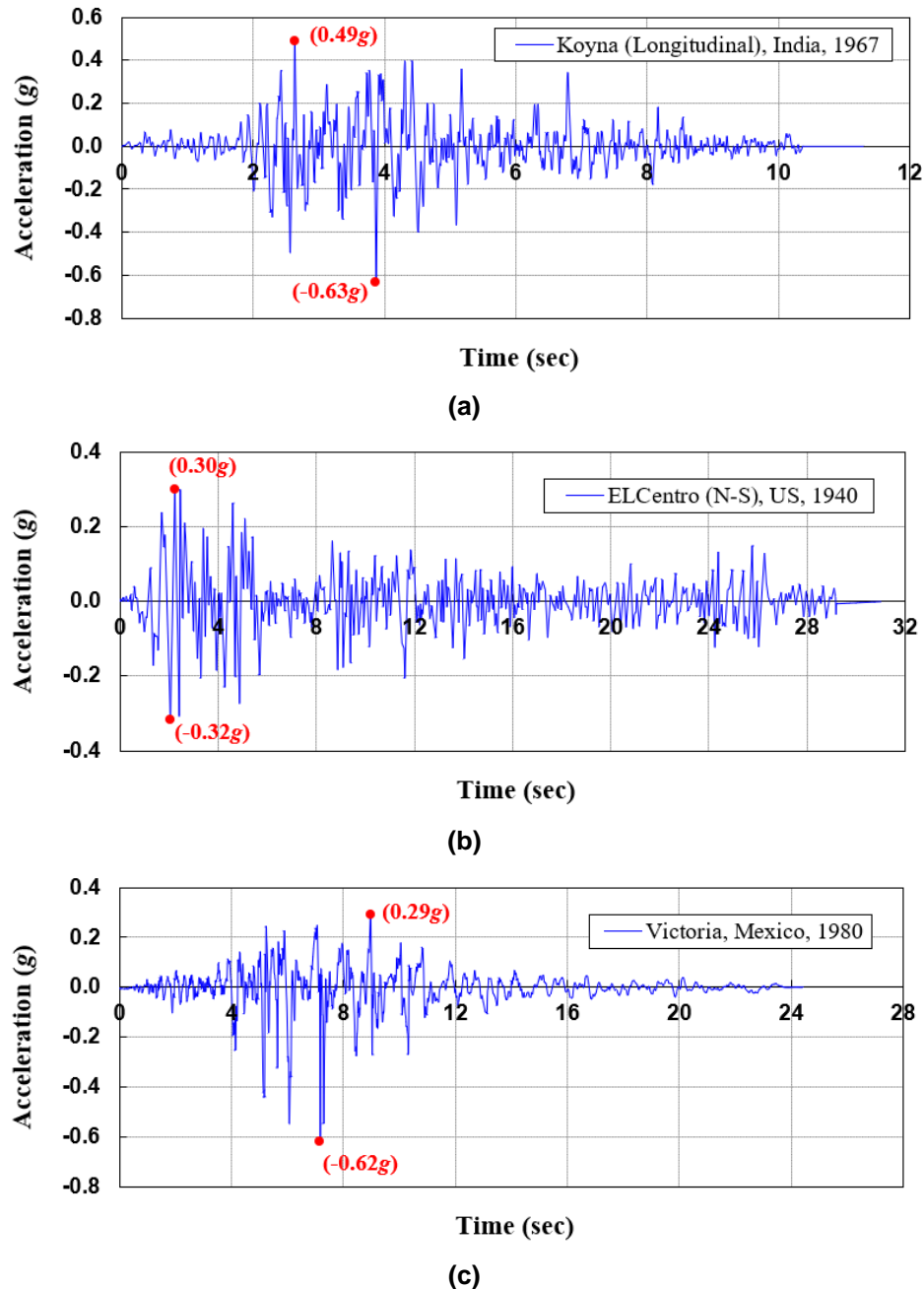


Figure 7. Real time-history record of selected earthquake motions: a – Koyna earthquake; b – ELCentro earthquake; c – Victoria earthquake.

3. Results and Discussion

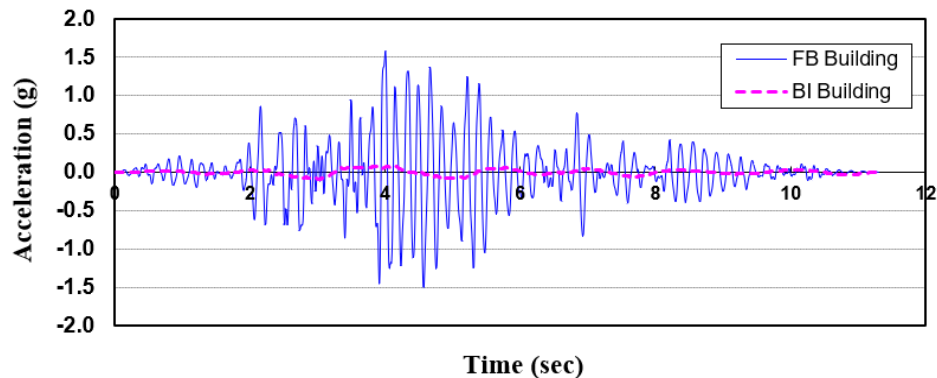
From results of FE analysis, it is found that the dynamic responses (acceleration, inter-storey drift) of BI building are significantly lower than those of FB building. Peak absolute values of floor accelerations and inter-storey drifts of both buildings under various earthquakes are presented in Table 3.

Table 3. Peak values of floor accelerations and inter-storey drifts under various earthquakes.

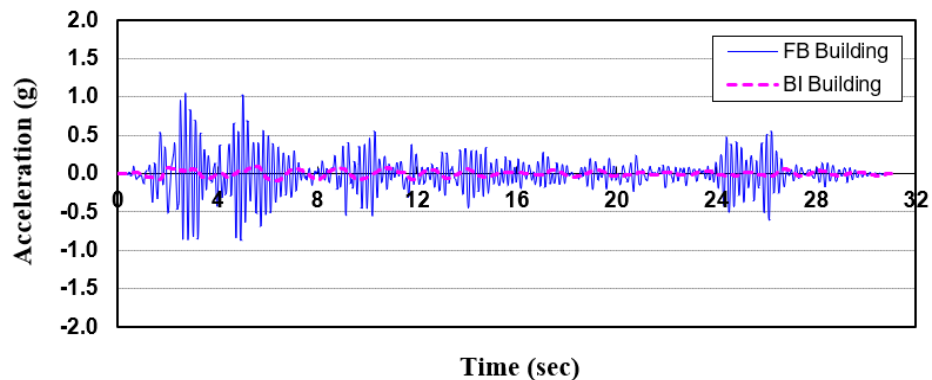
Parameter	FB building			BI building		
	Koyna	EICentro	Victoria	Koyna	EICentro	Victoria
Peak acceleration at 1 st floor level (m/s ²)	1.34g	0.65g	0.76g	0.08g	0.09g	0.12g
Peak acceleration at roof level (m/s ²)	1.57g	1.05g	1.37g	0.09g	0.10g	0.12g
Peak drift at 1 st storey (mm)	8.6	5.0	5.5	0.7	0.7	0.9
Peak drift at 2 nd storey (mm)	4.8	3.0	3.7	0.4	0.4	0.5

g is the acceleration of gravity ($g = 9.81 \text{ m/s}^2$).

It may be seen from Table 3 that significant reduction in magnitude of peak floor accelerations of BI building has taken place as compared to FB building for the sample excitations. Specifically, reduction of peak floor acceleration between FB building and BI building under Koyna earthquake is found from 1.34 *g* to 0.08 *g* (94.0 %) at the 1st floor level and 1.57 *g* to 0.09 *g* (94.3 %) at roof level. Further, the magnitudes of peak acceleration at different floor levels of BI building are almost same under each excitation, which indicates the absence of any noticeable acceleration amplification along the height of the BI building model. Unlike the BI building, the magnitude of peak acceleration of FB building at roof level is significantly higher than that at the 1st floor level as expected. This finding is in agreement with the observation made by [15] based on the shake table testing results of a scaled model of BI un-reinforced brick masonry building supported on U-FREIs. Similar to the acceleration, magnitudes of peak inter-storey drifts of BI building are significantly lesser than that of FB building, thus clearly indicating the lesser possibility of any damage in the superstructure of the BI building. The detailed time history of floor acceleration at roof level (the level has the maximum magnitude of peak acceleration) and the inter-storey drifts at the 1st floor level (the level has the maximum magnitude of peak drift) of both FB and BI buildings under each earthquake excitations are shown in Fig. 8 and 9 respectively.



(a)



(b)

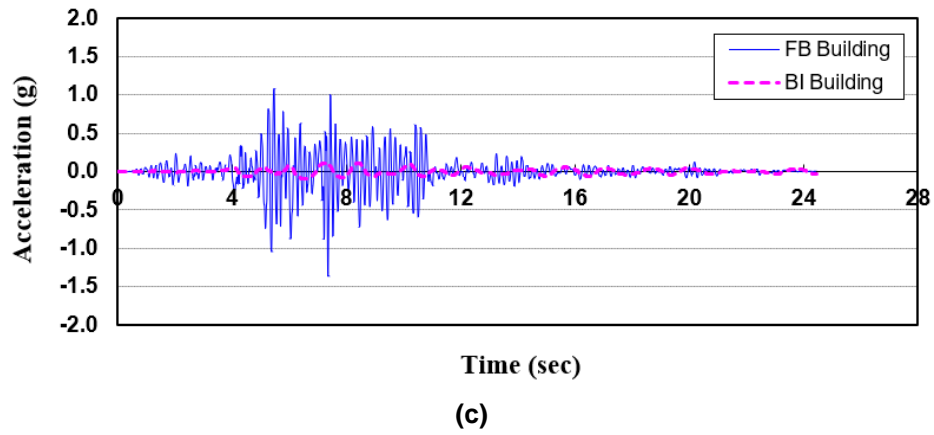


Figure 8. Floor acceleration responses at the roof level of the building under different earthquakes: a – Koyna earthquake; b – ElCentro earthquake; c – Victoria earthquake.

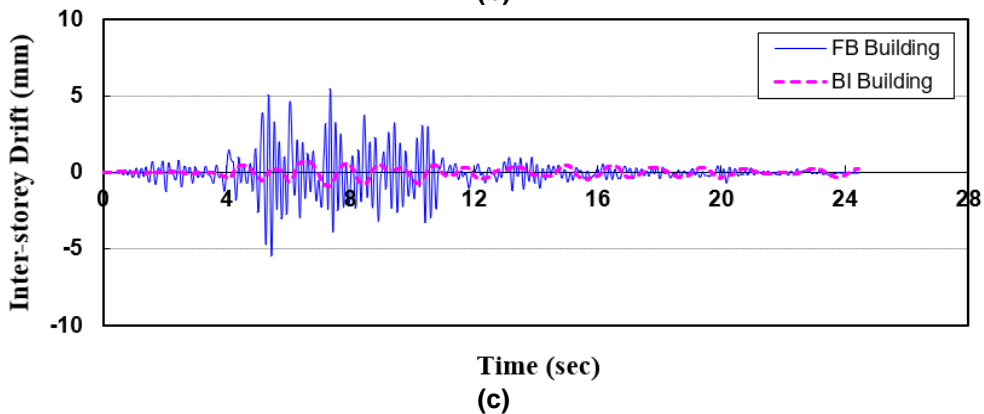
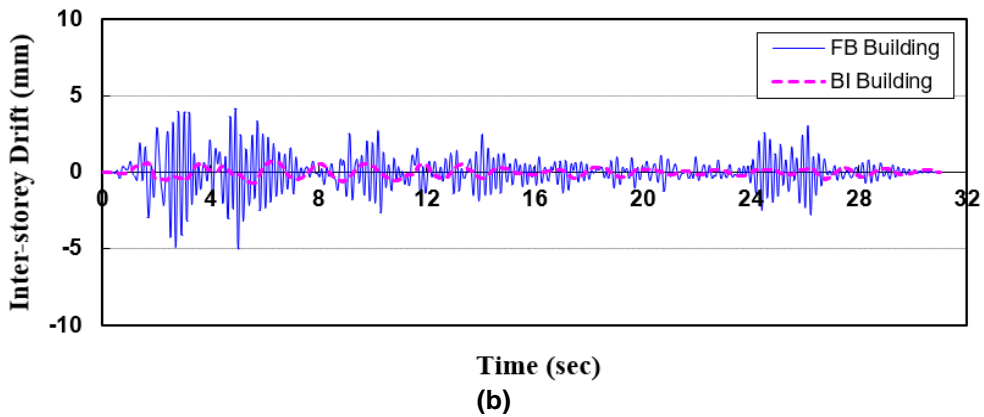
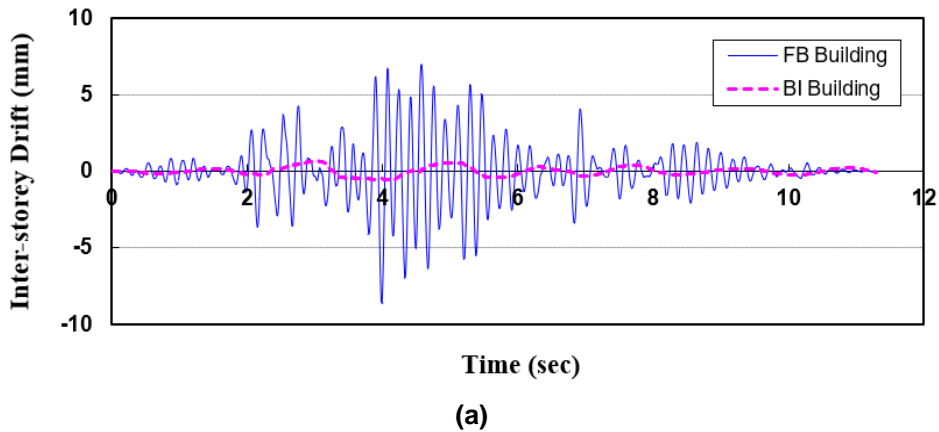


Figure 9. Time history of inter-storey drift at the 1st floor level of the building under various earthquakes: a – Koyna earthquake; b – ElCentro earthquake; c – Victoria earthquake.

Horizontal displacement responses of U-FREIs of the base isolation system under different earthquakes are shown in Fig. 10. It can be seen from the figure that the peak values of horizontal

displacement of U-FREIs under the action of Koyna, ElCentro and Victoria accelerograms are found to be 58, 66 and 104 mm respectively.

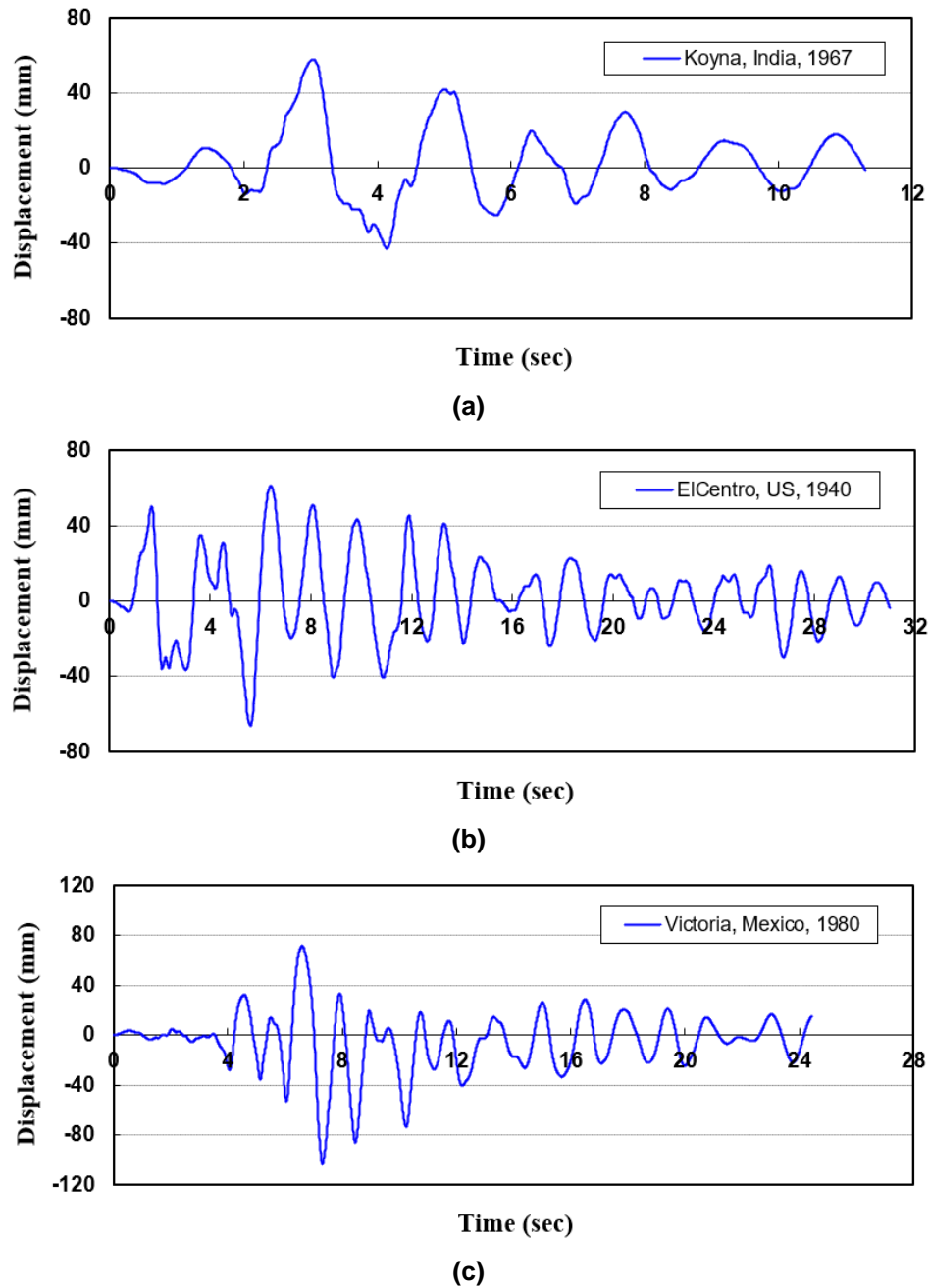
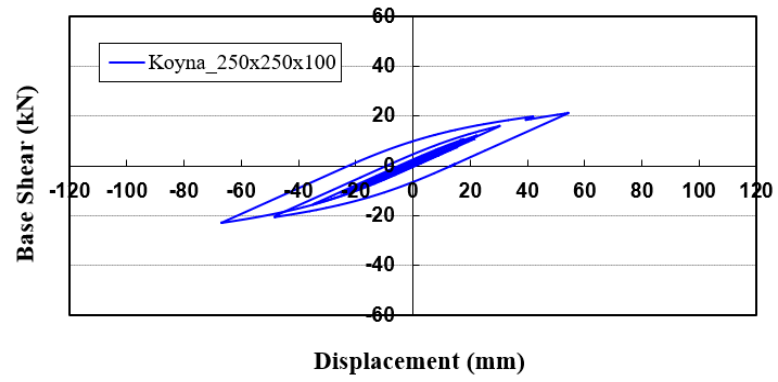


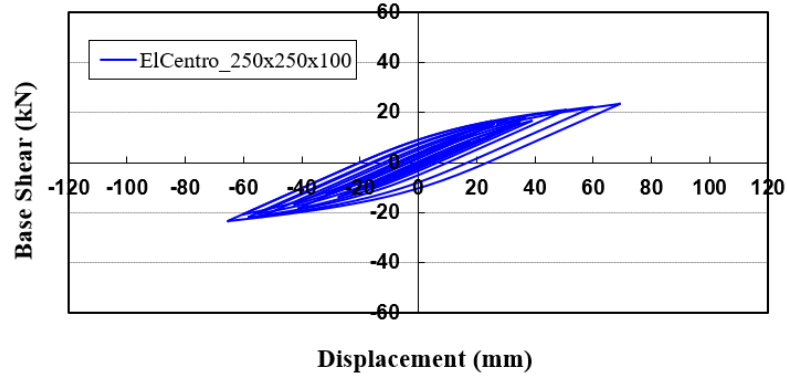
Figure 10. Horizontal displacement responses of U-FREIs under different earthquakes: a – Koyna earthquake; b – ElCentro earthquake; c – Victoria earthquake.

It may further be noted that some standard codes such as [28, 29] specify the performance evaluation of an elastomeric isolator up to a maximum of $1.50 t_r$ (135 mm). According to [9, 17], these U-FREIs in the building are able to maintain stability up to maximum horizontal displacement of $1.70 t_r$ (155 mm). These values are larger than the peak values of horizontal displacement of U-FREIs under the action of Koyna, ElCentro and Victoria accelerograms (Fig. 10). Thus, the adopted base isolation system is capable of ensuring overall safety and stability of the structure under the considered earthquakes induced vibration.

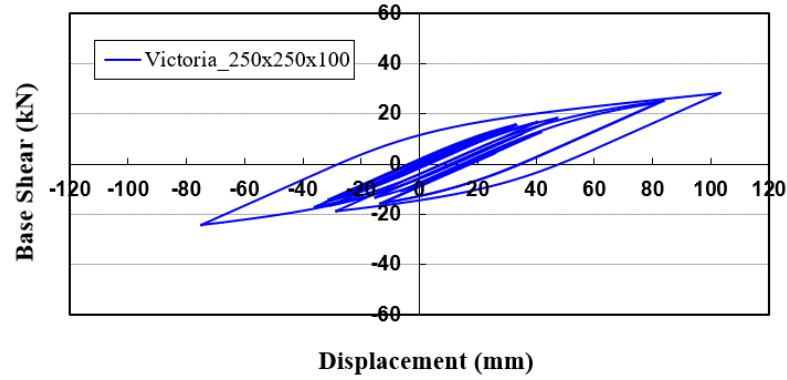
The nonlinear behaviour of any isolator is generally reflected in hysteresis loop. The hysteresis loop of an isolator represents the relationship between shear forces and cyclic horizontal displacements. The hysteresis loops of the U-FREIs supported the prototype BI masonry building under various recorded real earthquake time history ground motions are shown in Fig. 11 and 12 for size of $250 \times 250 \times 100$ mm and $310 \times 310 \times 100$ mm respectively.



(a)

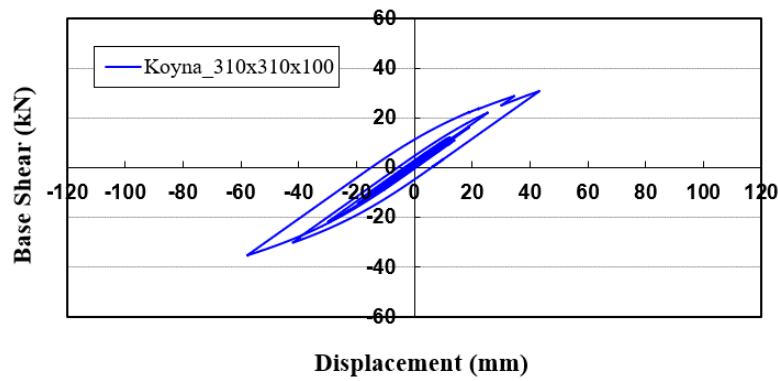


(b)



(c)

Figure 11. Hysteresis loop behaviour of U-FREIs size 250x250x100 mm supported the prototype masonry building under various earthquakes: a – Koyna earthquake; b – ElCentro earthquake; c – Victoria earthquake.



(a)

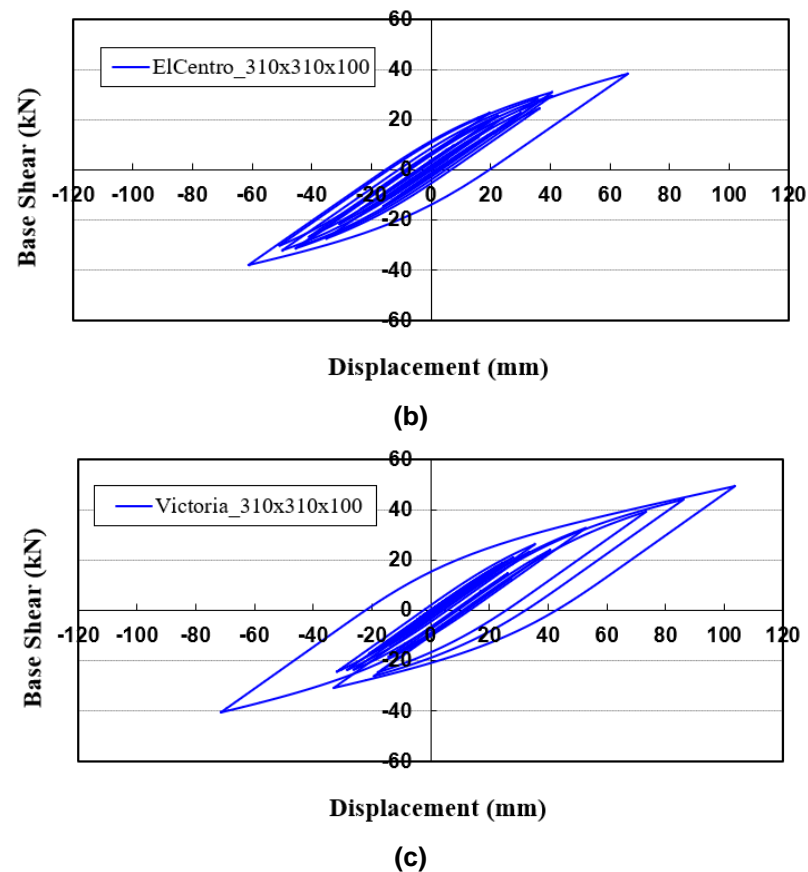


Figure 12. Hysteresis loop behaviour of U-FREIs size 310×310×100 mm supported the prototype masonry building under various earthquakes: a – Koyna earthquake; b – EICentro earthquake; c – Victoria earthquake.

It can be seen from Fig. 11 and 12, the values of shear forces corresponding to the peak value of horizontal displacement of the U-FREIs under various earthquakes are appropriate with the values of input bi-linear behaviour of the U-FREIs in Fig. 6b. A close inspection of the curve shows that the characteristic forces, yield displacement, initial stiffness and post yield stiffness for the U-FREIs appear as modelled. Thus, the results obtained by FE analysis for the BI masonry building supported on square U-FREIs under various recorded real earthquake time history ground motions are be considered as accurate.

4. Conclusion

This study investigates the effectiveness of U-FREIs in controlling seismic response of low-rise masonry building under the action of ground motions of earthquakes. A two-storey stone masonry building supported on fourteen U-FREIs located at Tawang, Arunachal Pradesh State, representative of a common building typology in many parts of north-eastern zone of India is selected to evaluate the effectiveness of the base isolation system using U-FREIs under various ground motions as compared to the corresponding fixed base building. Three-dimensional nonlinear models are simulated for the building in both FB and BI conditions. Dynamic response of both FB and BI buildings subjected to various recorded real earthquake time history ground motions are investigated. The concluding remarks are as follows:

1. Floor acceleration and inter-storey drift responses of BI building under excitations from earthquakes are significantly lesser than those of FB building.
2. While the magnitudes of peak acceleration are amplified along the height of the FB building model under each excitation, those of the BI building are almost same at different floor levels.
3. U-FREIs maintain a stable rollover configuration within the estimated displacement limit.
4. U-FREIs are found to be very effective in reduction of seismic vulnerability of low-rise masonry buildings. U-FREIs are introduced to be use for seismic isolation of low-rise building in remote areas as there are light weight, less expensive and easy to install prototype isolation system.

References

1. Kelly, J.M. Analysis of fiber-reinforced elastomeric isolators. *Journal of Seismology and Earthquake Engineering*. 1999. 2 (1). Pp. 19–34.
2. Zhang, J., Huo, Y. Evaluating effectiveness and optimum design of isolation devices for highway bridges using the fragility function method. *Engineering Structures*. 2009. 31 (8). Pp. 1648–1660. DOI: 10.1016/j.engstruct.2009.02.017
3. Arutunyan, A.R. Modern methods of buildings seismic isolation. *Magazine of Civil Engineering*. 2010. 13 (3). Pp. 56–60. (rus). DOI: 10.18720/MCE.13.1
4. Tavares, D.H., Padgett, J.E., Paultre, P. Fragility curves of typical as-built highway bridges in eastern Canada. *Engineering Structures*. 2012. No. 40. Pp. 107–118. DOI: 10.1016/j.engstruct.2012.02.019
5. Kovaleva, N.V., Rutman, Yu.L., Davydova, G.V. Determination of optimal damping parameters for seismic isolation systems. *Magazine of Civil Engineering*. 2013. 40 (5). Pp. 107–115. (rus). DOI: 10.5862/MCE.40.12
6. Siqueira, G.H., Sanda, A.S., Paultre, P., Padgett J.E. Fragility curves for isolated bridges in eastern Canada using experimental results. *Engineering Structures*. 2014. No. 74. Pp. 311–324. DOI: 10.1016/j.engstruct.2014.04.053
7. Kumar, P., Petwal, S. Seismic performance of secondary systems housed in isolated and non-isolated building. *Earthquakes and Structures, An International journal*. 2019. 16(4). Pp. 401–413. DOI: 10.12989/eas.2019.16.4.401
8. Artar, M., Coban, K., Yurdakul, M., Canb, O., Yilmaz, F., Yildiz, M. Investigation on seismic isolation retrofit of a historical masonry structure. *Earthquakes and Structures, An International journal*. 2019. 16(4). Pp. 501–512. DOI: 10.12989/eas.20-19.16.4.501
9. Toopchi-Nezhad, H., Tait, M.J., Drysdale, R.G. Testing and modeling of square carbon fiber-reinforced elastomeric seismic isolators. *Structural Control and Health Monitoring*. 2008. 15(6). Pp. 876–900. DOI: 10.1002/stc.225
10. Toopchi-Nezhad, H., Tait, M.J., Drysdale, R.G. Lateral response evaluation of fiber-reinforced neoprene seismic isolator utilized in an unbonded application. *Journal of Structural Engineering, ASCE*. 2008. 134 (10). Pp. 1627–1637. DOI: 10.1061/(ASCE)0733-9445(2008)134:10(1627)
11. Toopchi-Nezhad, H., Tait, M.J., Drysdale, R.G. Parametric study on the response of stable unbonded-fiber reinforced elastomeric isolator (SU-FREIs). *Journal of Composite Materials, SAGE*. 2009. 43(15). Pp. 1569–1587. DOI: 10.1177/0021998308106322
12. Dezfuli, F.H., Alam, M.S. Performance of carbon fiber-reinforced elastomeric isolators manufactured in a simplified process: experimental investigations. *Structural Control and Health Monitoring*. 2014. No. 21. Pp. 1347–1359. DOI: 10.1002/stc.1653
13. Ngo, V.T., Dutta, A., Deb, S.K. Evaluation of horizontal stiffness of fibre reinforced elastomeric isolators. *Earthquake Engineering and Structural Dynamics*. 2017. 46(11). Pp. 1747–1767. DOI: 10.1002/eqe.2879
14. Toopchi-Nezhad, H., Tait, M.J., Drysdale, R.G. Shake table study on an ordinary low-rise building seismically isolated with SU-FREIs (Stable Unbonded-Fiber Reinforced Elastomeric Isolators). *Earthquake Engineering and Structural Dynamics*. 2009. 38(11). Pp. 1335–1357. DOI: 10.1002/eqe.923
15. Das, A., Deb, S.K., Dutta, A. Shake table testing of un-reinforced brick masonry building test model isolated by U-FREI. *Earthquake Engineering and Structural Dynamics*. 2016. No. 45. Pp. 253–272. DOI: 10.1002/eqe.2626
16. Losanno, D., Spizzuoco, M., Calabrese, A. Bidirectional shaking table tests of unbonded recycled rubber fiber-reinforced bearings (RR-FRBs). *Structural Control and Health Monitoring*. 2019. 26(9). DOI: 10.1002/stc.2386
17. Ngo, V.T., Deb, S.K., Dutta, A. Mitigation of seismic vulnerability of a prototype low-rise masonry building using U-FREIs. *Journal of Performance of Constructed Facilities, ASCE*. 2018. 32(2). Pp. 04017136-1-13. DOI: 10.1061/(ASCE)CF.1943-5509.0001136
18. Calabrese, A., Losanno, D., Spizzuoco, M., Strano, S., Terzo, M. Recycled rubber fiber-reinforced bearings (RR-FRBs) as base isolators for residential buildings in developing countries: The demonstration building of Pasir Badak, Indonesia. *Engineering Structures*. 2019. No. 192. Pp. 126–144. DOI: 10.1016/j.engstruct.2019.04.076
19. IS 1893 Part 1. Criteria for earthquake resistant design of structures. Bureau of Indian Standard. New Delhi, India. 2002. 45 p.
20. SAP2000 v.15. Computers and Structures Inc., CSI Analysis Reference Manual. Berkeley, California, USA. 2014.
21. Bilgin, H., Korini, O. Seismic capacity evaluation of un-reinforced masonry residential buildings in Albania. *Natural Hazards and Earth System Sciences*. 2012. No. 12. Pp. 3753–3764. DOI: 10.5194/nhess-12-3753-2012
22. Kaushik, H.B., Rai, D.C., Jain, S.K. Stress-strain characteristics of clay brick masonry under uniaxial compression. *Journal of Materials in Civil Engineering, ASCE*. 2007. 19(9). Pp. 728–739. DOI: 10.1061/(ASCE)0899-1561(2007)19:9(728)
23. Akhveissy, A.H., Milani, G. Pushover analysis of large scale unreinforced masonry structures by means of a fully 2D non-linear model. *Construction and Building Materials*. 2013. No. 41. Pp. 276–295. DOI: 10.1016/j.conbuildmat.2012.12.006
24. Milani, G., Lourenco, P.B., Tralli, A. Homogenised limit analysis of masonry walls, Part I: Failure surfaces. *Computers and Structures*. 2006. No. 84. Pp. 166–180. DOI: 10.1016/j.compstruc.2005.09.005
25. Milani, G., Lourenco, P.B., Tralli, A. 3D homogenized limit analysis of masonry buildings under horizontal loads. *Engineering Structures*. 2007. 29(11). Pp. 3134–3148. DOI: 10.1016/j.engstruct.2007.03.003
26. Naeim, F., Kelly, J.M. Design of Seismic Isolated Structures: From Theory to Practice. John Wiley & Sons, Inc. New York, USA. 1999. DOI: 10.1002/9780470172742
27. Kelly, J.M., Konstantinidis, D.A. Mechanics of Rubber Bearings for Seismic and Vibration Isolation. John Wiley & Sons, Ltd, Publication. New Delhi, India. 2011. 222 p.
28. ASCE/SEI 7-10. Minimum Design Load for Buildings and Other Structure. American Society of Civil Engineers. Reston, Virginia, USA. 2013.
29. EN 1337-3. Structural bearings, Part 3: Elastomeric bearings. European Committee for Standardization. CEN/TC250. Brussels. 2005. 94 p.

Contacts:

Van-Thuyet Ngo, thuyet.kcct@tlu.edu.vn



DOI: 10.34910/MCE.108.4

Physical and mechanical properties of construction and demolition waste

S. Manchikanti* , **R. Pavan Kumar**

Gayatri Vidya Parishad College of Engineering (Autonomous), Madhurawada, Visakhapatnam, India,

*E-mail: manchisri@gvpce.ac.in

Keywords: recycled aggregates, construction and demolition waste, concrete, compressive strength

Abstract: Construction and demolition waste is produced every day around the world posing a great disposal problem. Thus, the idea of using wastes in different forms appears to be an effective approach to waste disposal. The various materials that can be reclaimed from construction and demolition waste include recycled concrete aggregates (RCA), crushed brick (CB), reclaimed asphalt pavement (RAP), waste excavation rock (WR), fine recycled glass (FRG). The assessment of the recycled concrete aggregates is identified by performing various tests, which indicate physical, chemical and mechanical properties of the materials. The physical properties test results indicated that the recycled aggregates showed good performance in comparison with the natural ones. The results of the test assessing mechanical performance of concrete with recycled aggregates also indicated better performance when required measures are taken, such as (i) The aggregates to be used are obtained from recycled materials the sizes of the fine aggregates can be controlled as per the requirement during demolition process and by sieving. (ii) The water absorption capacity of the recycled fine aggregates is higher than the natural fine aggregates and this water absorption capacity can be reduced by wetting and drying the aggregates. (iii) The performance of recycled coarse aggregates can be enhanced by removal and separation of the old hardened mortar which adhered to the aggregates obtained post-demolition. (iv) The performance can also be enhanced by the usage of suitable commercially-available plasticiser to reduce the higher water absorption ratio of the recycled aggregates to attain the required strength.

1. Introduction

The study deals with the identification of reusable material salvaged from construction and demolition waste which supports to reduce the usage of natural materials. Previous research has evaluated the sustainability of C&D waste materials in various civil engineering applications such as pavements, ground improvement, pipe backfilling and concrete applications.

The compressive strength of various concrete mixes by using RCA in different replacements with natural aggregates [1] was evaluated and observed loss in compressive strength of concrete is in between 18 % to 39 %. The requirement of cement is more [2] when concrete is produced using recycled aggregates than conventional concrete to obtain the same compressive strength. The loss in strength was evaluated for concrete produced with recycled aggregates [3] and it is found that the negative influence of the use of RCA partially fades over time. The modulus of elasticity of concrete produced from RCA was less than the modulus of elasticity of conventional concrete [4] and a decrease in the elastic modulus was observed. The complete replacement of natural aggregates with RCA keeping the water/cement ratio and cement content constant, a loss in 28-day compressive strength was observed [5]. The compressive strength of various concrete mixes produced using fine aggregate from recycled concrete [5] was found to be similar to the conventional concrete. The use of fine aggregate from recycled concrete was found to be viable [6] since it does not lead to a significant loss in mechanical and durability properties. The performance of construction waste as material for the base of pavement layers [7] was found to be satisfactory and is possible to produce

Manchikanti, S., Pavan Kumar, R. Physical and mechanical properties of construction and demolition waste. Magazine of Civil Engineering. 2021. 108(8). Article No. 10804. DOI: 10.34910/MCE.108.4

© Manchikanti, S., Pavan Kumar, R., 2021. Published by Peter the Great St. Petersburg Polytechnic University



This work is licensed under a CC BY-NC 4.0

the same effect as that of the natural aggregate when the waste material is free from impurities. The influence of superplasticizers on the compressive strength of concrete with fine recycled aggregate was evaluated [8] and it was found that there is an increase in the compressive strength due to the incorporation of superplasticizers. The use of recycled concrete aggregates in pavement applications [9] as a subbase material was found to be satisfactory whereas the usage of crushed brick, recycled asphalt and fine recycled glass requires to be blended with additives for better performance. The usage of recycled materials from C&D waste in embankment fills [10] resulted that the recycled material can be used in the production of mortar and does require washing as long as the recycled material exhibits similar properties to that of natural materials. The performance of concrete produced from recycled aggregates [11, 12] was found to reduce when the ratio of recycled aggregates to the natural aggregates increases and the influencing factors are identified as the source of material and its composition. The mechanical performance of concrete produced using recycled fine aggregate [13] was found to be workable enough to be used in construction and can be used in the construction of members which do not carry much load like walls, hollow bricks etc. The behaviour of recycled aggregates in soil improvement [14] was found to depend on the addition rates of material and needs extensive research to make it a cost effective and sustainable approach. The performance of recycled concrete aggregates and recycled brick aggregates in concrete production [14] was evaluated and found that the performance of recycled concrete aggregates was satisfactory and the performance of recycled brick aggregate can be improved by controlling the particle size distribution.

Recent generation of large amounts of waste produced all over the world has imposed significant pressure on the environment. Waste is being produced from different sources like households, industries, hospitals, construction and demolition of structures which can be categorized into the following:

- Domestic/Municipal waste
- Industrial waste
- Hospital waste
- E-waste
- Construction and demolition (C&D) waste

Construction waste is defined as the waste from the construction, remodeling and repairs of structures i.e., buildings, transport infrastructure and other civil engineering structures.

Demolition wastes are defined as the wastes obtained from the demolition of buildings and roads. The amount of C&D waste being generated all over the world is now gaining concern regarding its production and management.

In India, on an average 28 million tons of C&D waste was produced (as per 2016 estimates), with 11 million tons in the best case and 43 million tons in the worst case scenario. The C&D waste being produced is contributed more from the rural areas ranging between 50 – 80%. The estimates of C&D waste generation in India is shown in the below Table 1.

Table 1. Estimates of C&D waste generation in India [15].

	Estimated volume (million tons)
Metro city demolition	15.0
Industrial demolition	4.0
Demolition waste in Urban locations	3.0
Roads, old highways, old bridges	2.5
Repairs and modifications	1.0
Construction debris	2.0
Miscellaneous unaccounted debris	0.5
Total	28.0

The traditional method of managing C&D waste is to dispose it off in landfills. However, the need to recycle and reuse the C&D waste is a global concern due to the following reasons:

- Environmental pollution being caused due to its disposal.
- Scarcity in the availability of natural materials.

- The increasing proportion of waste materials in landfills and its disposal cost in many countries.

Granite polishing waste (GPW) was used as sand replacement [16] and the results showed that adding a suitable amount of GPW as sand replacement would, apart from reducing waste disposal and sand consumption, also improved mortar performance by filling the voids between sand particles to decrease the voids ratio and porosity and increase the packing density and water film thickness and improve the rheology and impermeability. The physical characteristics of three types of commercially crushed concrete and brick materials [17] were presented two of them being similarly based crushed concrete materials with different degrees of processing and one being crushed brick. Their results showed that there are similarities and differences between the two concrete-based materials and the characteristics of the brick-based materials are significantly different from the crushed concrete materials. The effect of different concentrations of C&D waste (0%, 10%, 20%, 30%, and 50%) as coarse aggregates in concrete as substitute to virgin aggregates on workability, compressive, tensile, and flexural strengths was investigated [18] at the water-to-cement (W/C) ratios of 0.40, 0.45 and 0.50. The strengths were measured at the ages of 7 and 28 days. The results proved that C&D waste has no significant effect on compressive strength, while its negative impact on workability was palpable. With respect to tensile and flexural strength, just 50% of C&D waste led to significant reduction.

The feasibility of using aggregate from recycled C&D waste for urban road embankment applications based on the Sanhuan road construction project in eastern Xi'an (China) was evaluated [19]. The effect of curing on the strength of the C&D waste was investigated using unconfined compression strength (UCS), California bearing ratio (CBR), and deflection tests. The results showed that the C&D waste has the characteristics of high strength and significant stability after simple treatment and further suggest that the use of these materials for paving urban road embankments is feasible.

The feasibility of using aggregate from Recycled Construction and Demolition Waste (RCDW) in pavement applications was evaluated [20] with the help of laboratory experiments. The results revealed that the composition and the compactive effort influenced the physical characteristics of the RCDW aggregates. The compaction process promoted a partial crushing and breakage of RCDW aggregates changing the grain-size distribution and increasing the percentage of cubic grains and this physical change contributed to a better densification of the RCDW aggregates and consequently an improvement in bearing capacity, resilient modulus and resistance to permanent deformation was observed. It was concluded that the RCDW aggregates may be utilized as coarse base and sub-base layer for low-volume roads.

The main difficulties observed with recycled aggregates (RA) in concrete, such as high levels of water demand, porous structure, and low mechanical strength, occur in RA alkali-activated concretes [21]. These are associated with the highly porous nature and defects of RA. It was observed that the high calcium concentration of RA affects the binder gel products, accelerates the hardening rate of the concrete, and reduces the flowability of alkali-activated concretes.

Mortars produced with recycled fine aggregates achieved a compressive strength of 5.20MPa after 28 days [22] which is the minimum requirement for a Type III mortar, consequently they could be used in the manufacturing of masonry mortar. The recycled coarse aggregate originating from pre-cast floor elements could possibly be used in the production of structural concrete for medium and low aggressive environments when concretes were made with 50% and 100% of recycled coarse aggregates in substitution of the natural aggregates. respectively.

The possibility of construction of concrete pavements with a high rate of recycled concrete aggregate [23] was explored. A series of fatigue tests were conducted on concrete. In the first case the coarse natural aggregates were replaced with recycled aggregates, while in the second case all the granular skeleton (sand and coarse particles) were replaced. The tests carried out confirmed that high recycling rates lead only to a slight deterioration in the fatigue behaviour of pavement concretes.

The different applications that are presently [24] practiced to optimize the recovery and/or application of CDW for reuse were summarized, and various measures and strategies to improve the processing of CDW were proposed. It was suggested that to enhance environmental effectiveness, a conscious and comprehensive C&DW management plan should be implemented in each jurisdiction.

Using supplementary cementitious materials and recycled aggregates (from 30 to 50 %) a strength equivalent to natural aggregate concrete was achieved [25].

The core principles were synthesized and the best practices were linked for the management of construction and demolition waste across the entire construction value chain, and it was observed that a systematic implementation of the best practices could dramatically improve resource efficiency [26] and reduce environmental impact by: reducing waste generation, minimizing transport impacts, maximizing re-use and recycling by improving the quality of secondary materials and optimizing the environmental performance of treatment methods.

The economic viability is likely to occur when the cost of landfilling of CDW exceeds the cost of bringing the waste to the recycling centre [27] and the cost of using primary aggregates exceeds the cost of using recycled aggregates. It was demonstrated that recycling centres benefit from economies of scale implying that an increase in the scale of a centre, in turn results in a decrease in recycling costs.

Results of research designed to characterize the physical and chemical properties of fine recycled aggregates for concrete production and their relationship with mineralogical composition and pre-processing were discussed [28]. The constraints of the incorporation of fine aggregates in reinforced concrete were also discussed. It was shown that, unless a developed processing diagram is used, this application is not feasible.

The chemical–mineralogical appraisal of construction and demolition waste indicated that the recycled grain-size fraction 0.60–0.125mm could be directly re-employed [29] in the preparation of new mortar and concrete, while finer fractions could be considered as components for industrial processing in the preparation of cements and bricks/tiles. A study [30] indicated that the use of construction and demolition waste aggregates in percentages of up to 20 % for paving urban roads is feasible.

The analysis of the durability performance of CDW concluded that the use of RA is highly detrimental. This is mostly true when fine RA (recycled aggregates) are used [31]. The carbonation resistance is the property most affected by the use of RA, leading to increase in the carbonation depth between 22.2% and 182.4% for the various RA types. However, the most influencing factor is by far the RA's composition.

A range of case studies undertaken in several countries worldwide were used [32] to highlight the technical viability and appropriateness of using recycled aggregates in a broad range of construction applications.

As approximately 13.71 million tons of C&D waste was generated in 2012 in Shanghai, of which more than 80% of this C&D waste was concrete, bricks and blocks [33], it was suggested to implement proper recycling technologies and measures. And researchers should take it up as an important responsibility of formulating precise policies and specifications to this effect.

A vertical impact crusher was used for the production of high quality recycled sand [34] which resulted in the production of low-porosity sand from construction and demolition waste.

Normalized laboratory tests to assess the performance of standard mortars were used to demonstrate the technical feasibility of recycling the waste produced by the ceramics industry and from the demolition of red-clay bricks or tiles to produce mortars with less/no consumption of natural aggregates [35]. Up to a replacement ratio of sand with ceramic waste of at least 20% the results were encouraging. It is widely accepted that the recycling and reuse of C&D materials will reduce the demand for scarce virgin natural resources and simultaneously reduce the quantity of waste material that is being disposed [36].

The primary aim of this research paper is the identification of gainful utilization of materials which are reclaimed from the waste obtained from construction and demolition sector. It also aims at finding various alternative methods to use the recycled materials to the full extent and what methods can be adopted to meet the expected results.

2. *Methods*

The performance of the materials reclaimed from construction and demolition waste is found by performing various tests. The test results obtained suggest the application of materials in various fields. During the execution of work, the following phases are adopted which are presented in Fig.1 below.

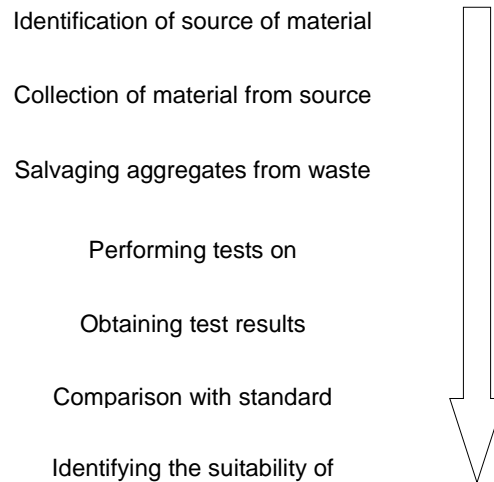


Figure 1. Phases of work

The source of materials was identified and large chunks of concrete from demolished waste was obtained. The concrete chunks were further broken into smaller fragments to reclaim aggregates, both fine and coarse aggregates.

The different tests that were conducted on the aggregates reclaimed are as follows:

- Sieve Analysis
- Specific Gravity
- Water Absorption
- Angularity Number
- Aggregate Impact Value test
- Aggregate Crushing Value test

The results from the above tests performed determine the suitability of materials in transportation and geotechnical perspectives. The suitability of materials in construction field is assessed by studying the behaviour of concrete which include compressive strength, splitting tensile strength and flexural strength of concrete.

The Compressive strength of concrete is found by testing cubes of size 150 mm x 150 mm x 150 mm which are cast and cured for 7 and 28 days. The test on cylinders of size 150 mm in diameter and 300 mm in height reveal the performance of concrete in tension. The behaviour of concrete in flexure can be understood by testing prisms of size 500 mm x 100 mm x 100 mm [37-39]. Review of earlier works indicated that in the study of recycled aggregates from waste, the aggregates used in concrete mix were either coarse aggregates or fine aggregates.

The present study aims at maximum utilization of aggregates reclaimed from waste and adopted the usage of both coarse and fine aggregates in concrete mix which also paves way for the behavioural assessment when both fine and coarse aggregates are used. In this study the concrete behaviour is studied by adopting five different proportions of coarse aggregates. The recycled coarse aggregates are replaced in the following ratios:

- 0 % – all natural coarse aggregates
- 25 %
- 50 %
- 75 %
- 100 %

The recycled concrete sand i.e. the fine aggregate is used at full level i.e. 100 %.

The mix design opted for study is M20 in which the coarse aggregates (CA) are replaced in the above stated percentages and fine aggregate (FA) is replaced completely. As the fine aggregate has a higher

water absorption ratio, the water–binder ratio is fixed as 0.62 with the usage of 1 % superplasticizer Conplast 430.

The different proportions of recycled coarse aggregates (RCA) used are presented in the table below:

Table 2. Representations of different proportions of RCA.

% of RCA	Representation
0	C ₀
25	C _{0.25}
50	C _{0.5}
75	C _{0.75}
100	C ₁

The representation of recycled fine aggregate (RFA) used in the mix is represented as follows:

Table 3. Proportion and representation of RFA.

% of RFA	Representation
0	S ₀
100	S ₁

The representation of the mixes which constitute the various proportions of aggregates specified above are as follows:

Table 4. Composition and representations of different mixes.

% of RCA	% of RFA	Representation
0	0	C ₀ S ₀
0	100	C ₀ S ₁
25	100	C _{0.25} S ₁
50	100	C _{0.5} S ₁
75	100	C _{0.75} S ₁
100	100	C ₁ S ₁

3. Results and Discussion

The results obtained from different tests performed on the materials reclaimed from the construction and demolition waste indicate their behavior and their further usage in various fields. The results also bring a contrast with the standard results so as to identify the effect of re-using the reclaimed material and develop suitable measures to increase their applications.

The results of various tests on aggregates are presented in the Table 5 below:

The values presented in the Table 5 are in close agreement with similar work done by past researchers [11, 36, 40-43].

Table 5. Test Results of aggregates (Natural and Recycled).

Test Conducted	Result
Fineness modulus of NFA	2.68
Fineness modulus of RFA	2.65
Specific Gravity of NCA	2.81
Specific Gravity of RCA	2.70
Specific Gravity of NFA	2.81
Specific Gravity of RFA	2.67
Water Absorption of NCA	0.5%
Water Absorption of RCA	3.15%

Test Conducted	Result
Water Absorption of NFA	1.2%
Water Absorption of RFA	13%
Angularity Number of NCA	7
Angularity Number of RCA	8
Aggregate Impact Value of NCA	14%
Aggregate Impact Value of RCA	18.75%
Aggregate Crushing Value of NCA	18%
Aggregate Crushing Value of RCA	21.86%

3.1. Physical properties

A sample of fine aggregates obtained from crushing of concrete chunks is taken, sieved and grain size distribution curve is plotted which indicated that the material is well graded. On comparison with standards specified by IS 383-1970, the material is categorized under Zone 2.

The figure below shows the grain size distribution curve plotted between grain size (in mm) and % finer.

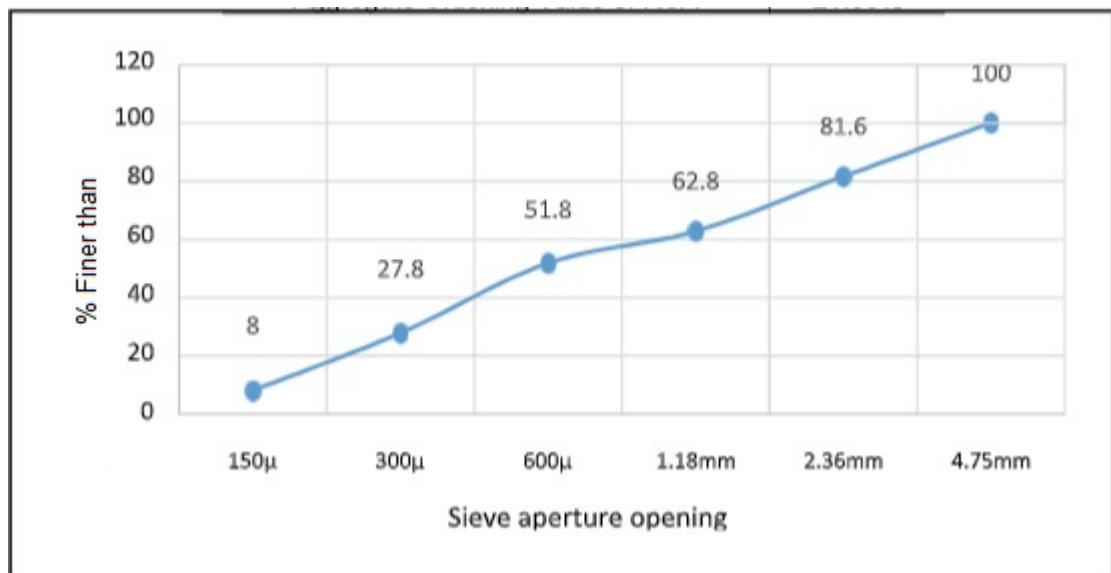


Figure 2. Particle size distribution curve.

The results obtained from specific gravity and water absorption test revealed that the water absorption of recycled aggregates is high [44] and it indicates that the amount of water to be added to the concrete mix to attain suitable workability and strength is more which increases the water–binder ratio than specified by the design code IS 456:2000. And the values of water absorption being high has also been confirmed by many researchers [6,12, 40].

The Aggregate Impact Value Test result indicates that the resistance offered by the reclaimed aggregates from waste is good and the aggregates can be reused in concrete for wearing surface of the pavements. These values are in agreement with the work of past researchers [44] and the code (IS 383:1970).

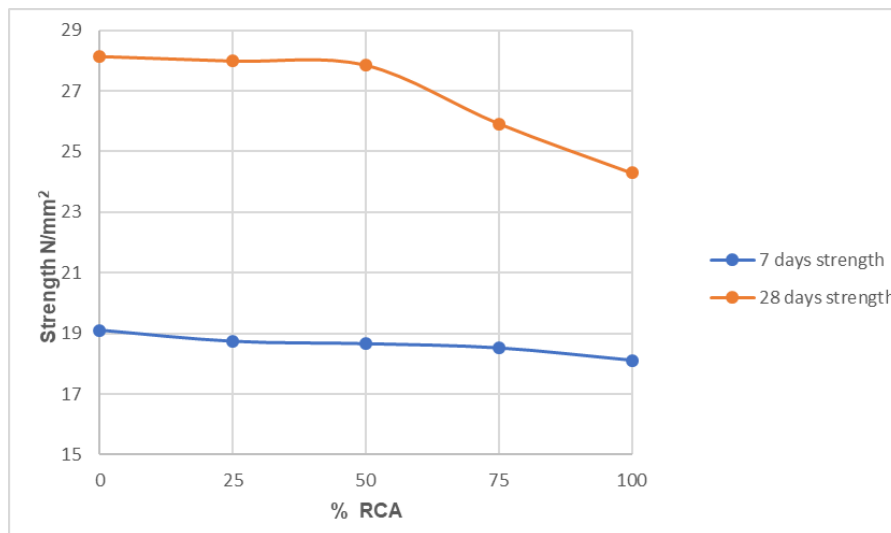
The Aggregate Crushing Value Test result also indicates that the reclaimed aggregates are resistant to compressive load applied gradually and as the value is less than 30 %, it can be used in road construction. These values are in agreement with the work of past researchers [44] and the code (IS 383:1970).

3.2. Mechanical properties

The mechanical behaviour of the aggregates reclaimed from the construction and demolition waste is studied by incorporating the aggregates in concrete mix in various proportions. The strength parameters are observed in compression, tension and flexure. The table below shows the compressive strength of cubes at 7 and 28 days for various replacements of aggregate.

Table 6. Compressive strength of concrete.

Representation	Compressive Strength (MPa)	
	7 days	28 days
C ₀ S ₀	22.5	28.66
C ₀ S ₁	19.11	28.14
C _{0.25} S ₁	18.74	27.99
C _{0.5} S ₁	18.66	27.85
C _{0.75} S ₁	18.52	25.92
C ₁ S ₁	18.11	24.29

**Figure 3. Compressive strength of concrete.**

From Table 6 it is evident that the behaviour of reclaimed aggregates from demolition waste is satisfactory and it is also clear that 3 out of 5 replacements in concrete mix are resulting in the required strength for the design mix opted i.e. M20 and 2 replacements are resulting in strengths which are very close to the required values.

The selection of replacements can be decided based on the results acquired and the replacement of both coarse and fine aggregate can be suggested based on the strength obtained. As concrete is strong in compression and weak in tension, the concrete behavior is also observed in tension by testing cylinders which are cured for 7 and 28 days and the results are compared with that of the conventional cylinders cast using all the natural aggregates. The results are found to be satisfactory. The table below shows the tensile strength of concrete and the values are close to the ones reported by [40, 44].

Table 7. Tensile strength of concrete.

Representation	Tensile Strength(MPa)	
	7 days	28 days
C ₀ S ₀	1.3	3.2
C ₀ S ₁	1.87	2.83
C _{0.25} S ₁	1.85	2.80
C _{0.5} S ₁	2.27	2.73
C _{0.75} S ₁	1.87	2.59
C ₁ S ₁	1.91	2.43

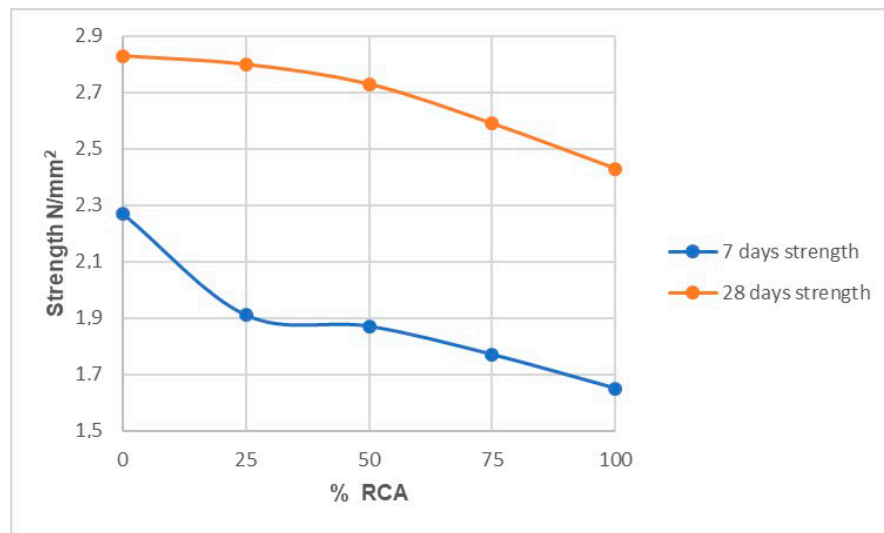


Figure 4. Splitting tensile strength of concrete.

The flexural strength of concrete is found by testing the prisms and the results are satisfactory which are presented in the Table 8 and the values are closer to the values reported by [44].

Table 8. Flexural strength of concrete.

Representation	Flexural Strength (MPa)	
	7 days	28 days
C ₀ S ₀	2.8	3.68
C ₀ S ₁	2.49	3.36
C _{0.25} S ₁	2.29	3.24
C _{0.5} S ₁	2.22	3.09
C _{0.75} S ₁	2.06	2.85
C ₁ S ₁	2.05	2.67

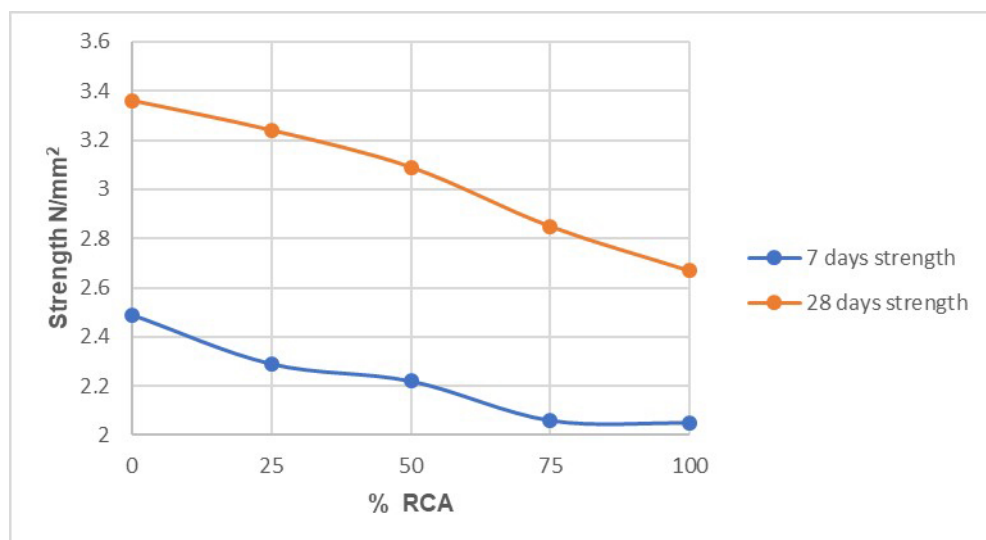


Figure 5. Flexural strength of concrete.

4. Conclusions

1. The behaviour of recycled coarse aggregates is similar to that of natural coarse aggregates.
2. The recycled fine aggregate exhibits a higher water absorption (13%) than natural fine aggregate (1.2%) as it is a by-product of demolition waste which contains cement mortar. The water absorption of recycled fine aggregates is 10 times of water absorption of natural fine aggregate.

3. The water – binder ratio when recycled fine aggregate is used, can be controlled by using plasticizer. The usage of 1% plasticizer to the mix controlled the water – binder ratio by 22.5% (from 0.80 to 0.62).

4. The strength of concrete produced from partial replacement of aggregates i.e. natural coarse aggregates with recycled coarse aggregates and complete replacement of natural fine aggregate with recycled fine aggregate, is high for 0%, 25% and 50% replacements which exhibit 98%, 97% and 96% of strength of concrete produced with natural aggregates.

5. From the above study, it is evident that the usage of recycled aggregates from construction and demolition waste can help in the reduction of usage of virgin materials up to 50% which preserve the virgin materials for future generations.

From the results obtained, it can be concluded that the behaviour of reclaimed coarse aggregates from construction and demolition waste does not show a huge difference in comparison with the natural coarse aggregates and the usage of recycled fine aggregates in comparison with the natural fine aggregate is a bit challenging and proper measures are to be taken to obtain the required result.

Hence the recycled materials when properly brought to reuse they serve various purposes:

- Reduce the usage of natural resources which take a lot of time to replenish.
- Protect the environmental degradation.
- Avoid the inconvenience caused due to its disposal.

References

1. Merlet, J., Pimienta, P. Mechanical and physico-chemical properties of concrete produced with coarse and fine recycled concrete aggregates. Proceedings Demolition and Reuse of Concrete and Masonry, RILEM 23. 1994. Odense, Denmark, Pp. 343–353.
2. Barra, M. Study of the Durability of Concrete with Recycled Aggregates Applied as Reinforced Concrete. Ph.D. thesis in Construction Engineering. Catalonia Polytechnic University. Barcelona. Spain. 1996.
3. Kou, S., Poon, C., Chan, D. Properties of steam cured recycled aggregate fly ash concrete - Use of recycled materials in buildings and structures. International RILEM Conference, Barcelona, Spain, 2004. Pp. 590–599.
4. de Oliveira, M.J., de Assis, C.S., Terni, A.W. Study on compressed stress, water absorption and modulus of elasticity of produced concrete made by recycled aggregate. Proceedings of International RILEM Conference on the Use of Recycled Materials in Buildings and Structures. Barcelona, Spain. 2004. Pp. 636–642.
5. Etxeberria, M., Vazquez, E., Mari, A., Barra, M. Influence of amount of recycled coarse aggregates and production process on properties of recycled aggregate concrete. Cement Concrete Research. 2007. 37(5). Pp. 735–742. DOI:10.1016/j.cemconres.2007.02.002.
6. Evangelista, L., de Brito, J. Durability performance of concrete made with fine recycled concrete aggregates. Cement and Concrete Composites. 2010. 32(1). Pp. 9–14. DOI:10.1016/j.cemconcomp.2009.09.005.
7. Herrador, R., Pérez, P., Garach, L., Ordonez, J. Use of Recycled Construction and Demolition Waste Aggregate for Road Course Surfacing. Journal of Transportation Engineering. 2012. 138(2). Pp.182–190. DOI: 10.1061/(ASCE)TE.1943-5436.0000320.
8. Pereira, P., Evangelista, L., de Brito, J. The effect of superplasticizers on the workability and compressive strength of concrete made with fine concrete aggregates. Construction and Building Materials. 2012. 28(1). Pp. 722–729. DOI: 10.1016/j.conbuildmat.2011.10.050.
9. Arulrajah, A., Piratheepan, J., Disfani, M.M., Winbo, M. Geotechnical and geoenvironmental properties of recycled construction and demolition materials in pavement subbase application. Journal of Materials in Civil Engineering. 2013. 25(8). Pp. 1077–1088. DOI: 10.1061/(ASCE)MT.1943-5533.0000652.
10. Asprone, D., Bilotta, E., Capasso, I., Caputo, D. Reuse of Construction and Demolition waste for geotechnical applications. Geotechnical Engineering for Infrastructure and Development. 2015. Institution of Civil Engineers. Pp.2589–2594. DOI: 10.1680/ecsmge.60678.
11. Bravo, M., de Brito, J., Pontes, J., Evangelista, L. Mechanical performance of concrete made with aggregates from construction and demolition waste recycling plants. Journal of Cleaner Production. 2015. 99(5). Pp. 59–74. DOI: 10.1016/j.jclepro.2015.03.012
12. Evangelista, L., de Brito, J. Mechanical behaviour of concrete made with fine recycled concrete aggregates. Cement Concrete Composites. 2007. 29(5). Pp. 397–401. DOI: 10.1016/j.cemconcomp.2006.12.004.
13. Yadhu, G., Aiswarya Devi, S. An Innovative Study on Reuse of Demolished Concrete Waste, Journal of Civil & Environmental Engineering. 2015. 5(5). Pp. 1–3. DOI: 10.4172/2165-784X.1000185.
14. Henzinger, C., Heyer, D. Soil improvement using recycled aggregates from demolition waste. Proceedings of the Institution of Civil Engineers-Ground Improvement. 2018. 171(2). Pp. 74–81. DOI:10.1680/jgrim.17.00031.
15. Ramanathan, M. Importance of C&D Waste recycling for municipalities. Proc. of 15th Municipalika 2018 Exhibition and Conference, Mumbai. 2018.
16. Chen, J.J., Li, B.H., Ng, P.L., Kwan, A.K.H. Adding granite polishing waste as sand replacement to improve packing density, rheology, strength and impermeability of mortar. Powder Technology. 2020. 364. Pp. 404–415. DOI: 10.1016/j.powtec.2020.02.012
17. O'Flaherty, F., Goodwin, A., Chidiroglou, I., Laycock, E. Physical properties of demolition waste material. Construction Materials. 2008. 161(3). Pp. 97–103. DOI: 10.1680/coma.2008.161.3.9

18. Hadavand, B., Imaninasab, R. Assessing the influence of construction and demolition waste materials on workability and mechanical properties of concrete using statistical analysis. *Innovative Infrastructure Solutions*. 2019. 4. 29. DOI: 10.1007/s41062-019-0214-3
19. Li, Y., Zhou, H., Su, L., Hou, H., Dang, L. Investigation into the Application of Construction and Demolition Waste in Urban Roads. *Advances in Materials Science and Engineering*. 2017. Pp. 12. DOI: 10.1155/2017/9510212
20. da Conceição Leite, F., dos Santos Motta, R., Vasconcelos, K.L., Bernucci, L. Laboratory evaluation of recycled construction and demolition waste for pavements. *Construction and Building Materials*. 2011. 25(6). Pp. 2972–2979. DOI: 10.1016/j.conbuildmat.2010.11.105
21. Abdollahnejad, Z., Mastali, M., Falah, M., Luukkonen, T., Mazari, M., Illikainen, M. Construction and Demolition Waste as Recycled Aggregates in Alkali-Activated Concretes. *Materials (Basel)*. 2019. 12(23). Pp. 4016. DOI: 10.3390/ma12234016
22. Pavón, E., Martínez, I., Etxeberria, M. The production of construction and demolition waste material and the use of recycled aggregates in Havana, Cuba. *Revista Facultad de Ingeniería Universidad de Antioquia*. 2014. 71.
23. Sedran, T., Genesseeux, E. Fatigue behavior of Concrete including Recycled Concrete Aggregate. *Proceedings of XIII International Symposium on Concrete Roads*. Berlin. 2018. Pp 8. URL: <https://hal.archives-ouvertes.fr/hal-02899479>
24. del Río Merino M, Izquierdo Gracia P, Weis Azevedo IS. Sustainable construction: construction and demolition waste reconsidered. *Waste Management & Research*. 2010. 28(2). Pp. 118–129. doi:10.1177/0734242X09103841
25. Akhtar, A., Sarmah, A.K. Construction and demolition waste generation and properties of recycled aggregate concrete: A global perspective. *Journal of Cleaner Production*. 2018. 186. Pp. 262–281. DOI: 10.1016/j.jclepro.2018.03.085
26. Gálvez-Martos, J.-L., Styles, D., Schoenberger, H., Zeschmar-Lahl, B. Construction and demolition waste best management practice in Europe. *Resources, Conservation and Recycling*. 2018. 136. Pp. 166–178. DOI: 10.1016/j.resconrec.2018.04.016
27. Duran, X., Lenihan, H., O'Regan, B. A model for assessing the economic viability of construction and demolition waste recycling—the case of Ireland. *Resources, Conservation and Recycling*. 2006. 46(3). Pp. 302–320. DOI: 10.1016/j.resconrec.2005.08.003
28. Rodrigues, F., Carvalho, M.T., Evangelista, L., de Brito, J. Physical–chemical and mineralogical characterization of fine aggregates from construction and demolition waste recycling plants. *Journal of Cleaner Production*. 2013. 52. Pp. 438–445. DOI: 10.1016/j.jclepro.2013.02.023
29. Bianchini, G., Marrocchino, E., Tassinari, R., Vaccaro, C. Recycling of construction and demolition waste materials: a chemical–mineralogical appraisal. *Waste Management*. 2005. 25(2). Pp. 149–159. DOI: 10.1016/j.wasman.2004.09.005
30. Ossa, A., García, J.L., Botero, E. Use of recycled construction and demolition waste (CDW) aggregates: A sustainable alternative for the pavement construction industry. *Journal of Cleaner Production*. 2016. 135. Pp. 379–386. DOI: 10.1016/j.jclepro.2016.06.088
31. Bravo, M., de Brito, J., Pontes, J., Evangelista, L. Durability performance of concrete with recycled aggregates from construction and demolition waste plants. *Construction and Building Materials*. 2015. 77. Pp. 357–369. DOI: 10.1016/j.conbuildmat.2014.12.103
32. Silva, R.V., de Brito, J., Dhir, R.K. Use of recycled aggregates arising from construction and demolition waste in new construction applications. *Journal of Cleaner Production*. 2019. 236. Pp. 1–16. DOI: 10.1016/j.jclepro.2019.117629
33. Ding, T., Xiao, J. Estimation of building-related construction and demolition waste in Shanghai. *Waste Management*. 2014. 34(11). Pp. 2327–2334. DOI: 10.1016/j.wasman.2014.07.029
34. Ulsen, C., Kahn, H., Hawlitschek, G., Masini, E.A., Angulo, S.C., John, V.M. Production of recycled sand from construction and demolition waste. *Construction and Building Materials*. 2013. 40. Pp. 1168–1173. DOI: 10.1016/j.conbuildmat.2012.02.004
35. Silva, J., de Brito, J., Veiga, R. Recycled Red-Clay Ceramic Construction and Demolition Waste for Mortars Production. *Journal of Materials in Civil Engineering*. 2010. 22(3). Pp. 1–24. DOI: 10.1061/(ASCE)0899-1561(2010)22:3(236)
36. Shrivastava, V., Gettu, R.- Characterisation of recycled aggregates and mortar studies using recycled fine aggregate. [Online]. URL: <http://reports.ias.ac.in/report/19302/characterisation-of-recycled-aggregates-and-mortar-studies-using-recycled-fine-aggregate> (accessed on November 05, 2020).
37. IS 383:1970, Indian Standard Code of specification for coarse and fine aggregate.
38. IS 456-2000, Indian Standard Code of Practice for Plain and Reinforced Concrete.
39. IS 10262:2009, Indian Standard Code of Recommended Guidelines for Concrete Mix Design.
40. Zheng, C., Lou, C., Du, G., Li, X., Liu, Z., Li, L. Mechanical properties of recycled concrete with demolished waste concrete aggregate and clay brick aggregates. *Results in Physics*. 2018. 9. Pp.1317–1322. DOI: 10.1016/j.rinp.2018.04.061.
41. Lye, C., Dhir, R., Ghataora, G. Elastic modulus of concrete made with recycled aggregates. *Proceedings of Institution of Civil Engineers-Structures and Buildings*. 2015. DOI: 10.1680/jstbu.15.00077
42. Akhtar, J.N., Akhtar, M.N. Enhancement in properties of concrete with demolished waste aggregate. *GE-International Journal of Engineering Research*. 2014. 2(9). Pp. 73–83.
43. Arezoumandi, M., Smith, A., Volz, J.S., Khayat, K.M. An experimental study on flexural strength of reinforced concrete beams with 100% recycled concrete aggregate. *Engineering Structures*. 2015. 88. Pp. 154–162.
44. Surya, M., Kanta Rao, V.V.L., Lakshmy, P. Recycled aggregate concrete for Transportation Infrastructure. *Procedia - Social and Behavioral Sciences*. 2013. 104. Pp. 1158–1167. DOI: 10.1016/j.sbspro.2013.11.212

Contacts:

Srinivas Manchikanti, manchisri@gvpce.ac.in

Rangabhatla Pavan Kumar, manchisri@gvpce.ac.in



DOI: 10.34910/MCE.108.5

Properties of recycled aggregate pervious concrete modified with Styrene Butadiene Rubber Latex

Sh. Abdo^{a*} , V.V. Galishnikova^a , A.M. Fawzy^b 

^a Peoples' Friendship University of Russia (RUDN University), Moscow, Russia

^b Alexandria University, Alexandria, Egypt

*E-mail: shamseldin.abdo@outlook.com

Keywords: pervious concrete, recycled aggregate, styrene butadiene rubber latex, water permeability, mechanical properties, degradation.

Abstract. Pervious concrete is a type of concrete mixture that is usually used in pavement with a high range of interconnected voids between large aggregate particles. Herein, an experimental study was conducted in order to figure out the effect of replacing (5%, 10% and 15%) of cement weight by the styrene-butadiene rubber latex (SBRL), in addition to the impact of replacing (0%, 25%, 50%, 75% and 100%) of natural coarse aggregates by recycled ones on the mechanical properties of the pervious concrete. The focused parameters in this experimental study were divided into two parts, permeability indices (density, voids ratio and water permeability) and strength indices (compressive, splitting and flexural tensile strengths and concrete potential to degradation). Additionally, since the water permeability is the most important property in the pervious concrete, relations between water permeability and the other mentioned properties were deduced. Generally, it is noticed that the addition of SBRL positively affects the mechanical properties of the pervious concrete. However, there is a slight decrease in permeability indices. It is observed that the addition of 10% of SBRL to the pervious concrete with 75% recycled aggregate increased the 28 days compressive, splitting tensile and flexural tensile strength by 70.8%, 49.4% and 29.7%, respectively. In addition, the results showed a reduction in the hardened voids content, water permeability and potential to degradation by 13.3%, 11% and 31.7%, respectively.

1. Introduction

Pervious concrete, also called permeable or porous concrete, is a type of concrete mixture with a broad range of interconnected voids between large aggregate particles. These interconnected voids can be achieved by minimizing or eliminating the fine aggregates from the mixture, as well as minimizing the cement paste and water/cement ratio as possible [1–4]. The main property that distinguishes this type of concrete is the high water and air permeability. This high permeability leads to many advantages such as: (a) fast and easy recharge of the water ground level, (b) reduction of the noises from the cars' wheels friction with the roads, (c) elimination of the hot island phenomena in cities [2, 5, 6]. However, this increase in the permeability and porosity leads to a significant reduction in the mechanical strength [6, 7].

Generally, recycling wastes became a matter of concern since it conserves the raw materials for the future generations. However, using the recycled materials in new products consequently affects the products' properties. Regarding pervious concrete, it was found that the use of the recycled coarse aggregates negatively affects the mechanical properties, meanwhile increasing the permeability and porosity [6, 8, 9]. Nonetheless, some researchers found that replacing up to 30% of the raw coarse aggregates with the recycled aggregate produces a negligible effect on the mechanical properties [10–13]. Some researchers even claimed that the percentage that has a non-pronounced impact on the mechanical properties is up to 60% [6, 14, 15]. Meanwhile, there is a research work showing sensitivity of the mechanical properties of pervious concrete to the recycled aggregate percentage [16].

Abdo, Sh., Galishnikova, V.V., Fawzy, A.M. Properties of recycled aggregate pervious concrete modified with Styrene Butadiene Rubber Latex. Magazine of Civil Engineering. 2021. 108(8). Article No. 10805. DOI: 10.34910/MCE.108.5

© Abdo, Sh., Galishnikova, V.V., Fawzy, A.M., 2021. Published by Peter the Great St. Petersburg Polytechnic University



This work is licensed under a CC BY-NC 4.0

Many research works have been done to study and overcome the decay in the mechanical properties occurring either due to high porosity or the addition of the recycled aggregates. It was found that reducing the size of the coarse aggregate, decreasing the water-cement ratio or increasing the cement-to-aggregate ratio subsequently enhance the strength properties of the pervious concrete [1, 15, 17]. Additionally, using pozzolans (silica fume, fly ash, metakaolin, blast furnace slag) in the concrete mix showed remarkable enhancement in the mechanical properties with an acceptable decrease in the pervious concrete porosity and permeability [6, 18, 19]. However, all the mentioned solutions consequently lead to a reduction in the workability of the pervious concrete, where it intrinsically has zero slump. This reduction of the workability will lead to technical problems during the casting [20].

However, one of the best solution to overcome this decay in the mechanical properties, without affecting the workability [21–23], is the addition of styrene-butadiene rubber latex (SBRL). Its addition showed impressive results densifying the microstructure of the cement paste as well as helping in bridging the micro-cracks in the cement paste with a polymer film [24, 25]. It was found that the best dose of the solid latex is up to 10% of the cement weight [4, 15, 24], and even up to 15% in some cases [25]. However, another study noted that when the polymer-cement ratio is above 10%, the mechanical properties are not highly dependent on the apparent bulk density, and the flexural and compressive strength of the mortars are not improved further with more polymer [24].

Here in this research work, an experimental investigation was conducted to observe the impact of replacing 5%, 10% and 15% of cement weight by SBRL on the properties of pervious concrete with different levels of recycled coarse aggregates (0%, 25%, 50%, 75% and 100%). The aim of this research is to observe the permeability indices (density, voids ratio and water permeability) and strength indices (compressive, splitting and flexural tensile strengths and concrete potential to degradation) of this type of concrete. Also, deducing formulas for the water permeability and the other observed properties.

2. Materials and Methods

2.1. Experimental program

Table (1) shows 1m³ concrete components of different 20 mixtures, which were designed according to ACI-522R-10 with a 20% designed porosity. The control mixes are those that are without SBRL. Mixes (6, 11 and 16), (7, 12 and 17), (8, 13 and 18), (9, 14 and 19) and (10, 15 and 20) are compared with 1, 2, 3, 4 and 5, respectively. Due to the high absorption of the recycled aggregate, a proper amount of water that is equal to the first 10 min water absorption of the recycled aggregate during the mixing is added to the water content [9]. Furthermore, the rolling ball test is conducted to make sure that the required workability is achieved [26, 27]. The details of the required specimens for each experiment for each mixture are shown in Table (2).

Table 1. Concrete mixes' components.

Mix number	1	2	3	4	5	6	7	8	9	10	11	12	13	14	15	16	17	18	19	20
Styrene butadiene rubber later (cement replacement ratio by weight)	0%					5%					10%					15%				
Coarse aggregate replacement %	0%	25%	50%	75%	100%	0%	25%	50%	75%	100%	0%	25%	50%	75%	100%	0%	25%	50%	75%	100%
Water content (L/m ³)	105	107	110	112	115	105	107	110	112	115	105	107	110	112	115	105	107	110	112	115
Water/binder ratio	0.3																			
Coarse aggregate content (kg/m ³)	1430																			
Coarse aggregate nominal size (mm)	9.5																			
Fine aggregate content (kg/m ³)	72																			
Cement content (kg/m ³)	350																			

Table 2. Quantity and dimensions of the specimens for each experiment for each mixture.

Experiment	Num. of specimens	Shape and dimensions
Fresh density and voids content	3	Cylinder, D = 20 cm, H = 20 cm
Hardened density and voids content	3	Cylinder, D = 7.5 cm, H = 15 cm
Water permeability test (falling head method)	3	50x50cm ² slab with a 10 cm thickness
Compressive strength	3	Cylinder, D = 15 cm, H = 30 cm
Splitting tensile strength	3	Cylinder, D = 7.5 cm, H = 15 cm
Flexural tensile strength	3	15x15cm ² beam with a 45 cm span
Degradation and potential resistance	9	Cylinder, D = 10 cm, H = 10 cm

2.2. Concrete components

In this research, all the used components in casting the pervious concrete passed the acceptance criteria experiments. Portland cement is categorized as Type I 42.5 N according to ASTM C150 [28], and its properties are presented in Table (3). The natural coarse aggregate is crushed pink limestone with a single size of 9.5 mm, specific gravity of 2.63 and water absorption of 1.4%.

The recycled coarse aggregate was extracted from debris of a 40~50 year old building using a drilling and Los Angeles machine, and then sieved. According to the visual inspection, no visible cracks appeared on the recycled aggregates, and the old mortar covered about 30~40% of the recycled aggregates surface area. The building was in a dry environment during the operation period. The recycled coarse aggregate is also crushed pink limestone with a single size of 9.5 mm, specific gravity of 2.4 and water absorption of 7.1%.

The Natural fine aggregate is siliceous sand with specific gravity of 2.69 and fineness modulus of 2.65.

The styrene butadiene rubber latex is a thick white material in a liquid state with specific gravity of 1.0, low viscosity, 54% liquid content and a P.H. value of 11.0.

Table 3. Properties of the used Portland cement.

Item	Percentage
Calcium oxide (CaO)	63%
Silicon dioxide (SiO ₂)	21.3%
Aluminum oxide (Al ₂ O ₃)	6.2%
Iron oxide (Fe ₂ O ₃)	3.9%
Magnesium oxide (MgO)	2.5%
Sulfur trioxide (SO ₃)	1.7%
Potassium oxide (K ₂ O)	0.7%
Sodium oxide (Na ₂ O)	0.5%
Loss on ignition (LOI)	2.5%

2.3. Methods of testing

2.3.1. Fresh concrete density and voids content

Samples of well-consolidated fresh concrete are placed in the standard measure, then the fresh concrete density and voids content were calculated according to ASTM C1688 [29], as follows:

$$D_f = \frac{M_c - M_m}{V_m}, \quad (1)$$

where D_f represents density of fresh pervious concrete, M_m represents mass of the measure, M_c represents mass of measure filled with pervious concrete and V_m represents volume of the measure;

$$T = \frac{M_s}{V_s}, \quad (2)$$

where T represents the theoretical density, M_s represents the total mass of the pervious concrete components (cement, water, aggregate and SBRL) and V_s is the absolute volume of the concrete components (the sum of mass of each component divided by its specific gravity);

$$V_f = \frac{T - D_f}{T} \times 100, \quad (3)$$

where the V_f represents the voids ration of the fresh state of the pervious concrete.

2.3.2. Hardened concrete density and voids content

The hardened density and voids content were obtained by recording the mass of dried and submerged specimens, then the hardened concrete density and voids content were calculated according to ASTM C1754 [30] as follows:

$$D_h = \frac{K_d \times A}{d^2 \times L}, \quad (4)$$

where D_h represents the density of the concrete, K_d represents a conversion factor that is worth 1273240 in SI units, A represents the dry mass of the specimen and d represents the specimen diameter, and L represents the specimen length;

$$V_h = 1 - \frac{K \times (A - B)}{\rho_w \times D_h^2 \times L}, \quad (5)$$

where V_h represents the voids content of the hardened concrete, B is the submerged mass of the specimen and ρ_w is the water density and the rest of the variables are the same as in Eq. (4).

According to ACI 522R, the upper limit is 2000 kg/m³ and the lower limit is 1600 kg/m³ with voids ratio ranging from 15% to 35%.

2.3.3. Water permeability test (falling head method)

The water permeability is described as the infiltration rate. A 30 cm diameter watertight infiltration ring is placed and fixed on the surface of the concrete as shown in Fig. 1. Then, the consumed time to infiltrate a known mass through the infiltration ring is measured. Afterwards, the infiltrate rate can be calculated according to ASTM C1781 [31] as follows:

$$IR = \frac{K_p \times M}{d^2 \times t}, \quad (6)$$

where IR represents the infiltration rate, M represents the mass of infiltrated water, d represents the inside diameter of the infiltration ring, t is the time required for the designated mass of water to infiltrate through the concrete, and K_p represents a correction factor which is equal to 4 583 666 000 in SI units.

According to ACI 522R, the upper limit is 1.2 cm/s and the lower limit is 0.2 cm/s.

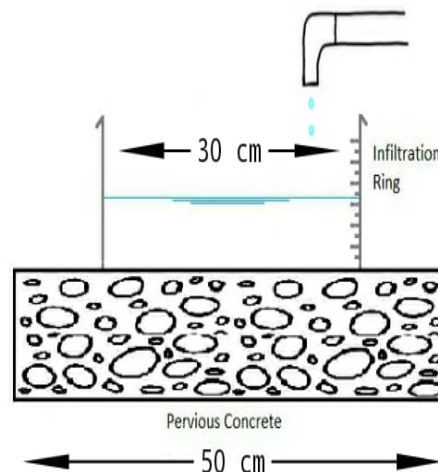


Figure 1. Water Permeability test (falling head method).

2.3.4. Compressive strength

The value of the uniaxial compressive stress that causes the failure of the material is determined, then the ultimate compressive strength can be calculated according to ASTM C 39 [32] as follows:

$$\sigma = \frac{P}{A}, \quad (7)$$

where σ represents the compressive strength, P represents the ultimate loading and A represents the cylinder area.

According to ACI 522R, the compressive strength should not be lower than 3 MPa.

2.3.5. Splitting Tensile strength

The compressing value that causes a compressed concrete cylinder on its side to crack is determined. The splitting tensile strength can be calculated according to ASTM C496 [33] as follows:

$$F_t = \frac{2 \times P}{\pi \times d \times L}, \quad (8)$$

where F_t represents the concrete tensile strength, P represents the maximum loading, d represents diameter of the cylinder and L represents the length of the cylinder.

According to ACI 522R, the splitting tensile strength should not be lower than 1 MPa.

2.3.6. Flexural tensile strength

A $15 \times 15 \text{ cm}^2$ concrete beam with a 45 cm span is loaded at the one-third and two-thirds of its span till failure as shown in Fig. 2. The flexural tensile strength can be calculated according to ASTM C78 [34]. The flexural tensile strength is expressed as modulus of rupture and is calculated as follows:

$$R = \frac{P \times L}{b \times h^2}, \quad (9)$$

where R represents modulus of rupture, P represents maximum applied load, L represents the beam span length, b represents width of beam and h represents depth of beam.

According to ACI 522R, the flexural tensile strength should not be lower than 1 MPa.

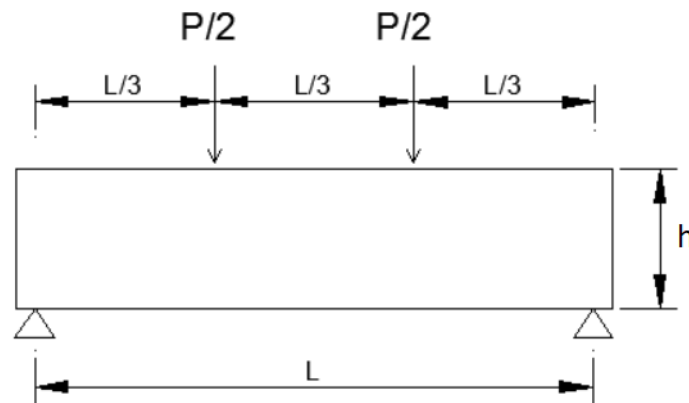


Figure 2. Flexural tensile strength test.

2.3.7. Degradation and potential resistance

The ability of the pervious concrete to resist the degradation occurred from the abrasion and impact is figured out through this test. A known mass of concrete cylinders with 10 cm diameter and 10 cm height are inserted three at a time in the Los Angeles machine without the steel balls, then the Los angles machine rotates 500 cycles. Afterward, the crushed samples are sieved, then the retained concrete on the (1-in.) sieve is weighted. The degradation and potential resistance can be calculated according to ASTM C1747 [35], as follows:

$$Deg = \frac{A - B}{A} \times 100\%, \quad (10)$$

where A is the weight of 3 cylinders and B is the weight of the pervious concrete that retained on sieve size (1-in.) after placing the 3 cylinders in Los Angeles device without balls and perform the test at a speed of 30.33 r/min.

According to ACI 522R, the upper limit is 95% while the lower limit is 19%.

3. Results and Discussion

3.1. Density

Fig. 3.1.1 and 3.1.2 present the relation between the density of the pervious concrete in (kg/cm^3), recycled aggregate proportion and SBRL replacement percentage, respectively. Generally, there is a decrease in the density by the increase in the proportion of the recycled aggregate since the aggregate itself possess more micro cracks because of the extraction process; the attached old mortar decreases the concrete density as well. There is a subsequent increase by the addition of the SBRL. It is noticed that at the fresh state the SBRL has almost a linear effect on the density: the addition of 5% SBRL to the pervious concrete – whether with recycled aggregate or not – increases the density by about 4~5% as shown in Fig. 3.4. Regarding the hardened pervious concrete density, it can be noticed that there is almost no difference between concrete with natural aggregate and 25% recycled aggregate, as shown in Fig. 3.1.2.

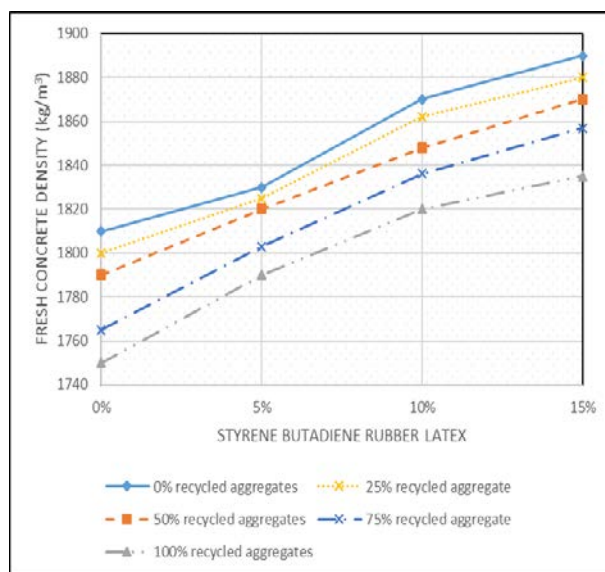


Figure 3.1.1. Density of the fresh pervious concrete.

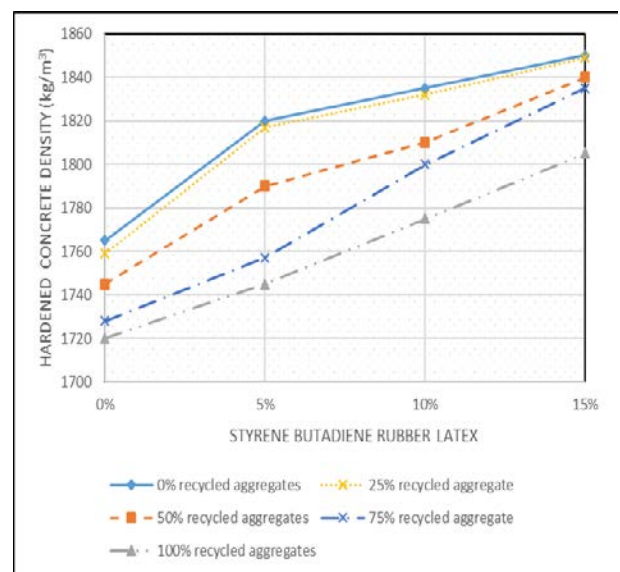


Figure 3.1.2. Density of the hardened pervious concrete.

3.2. Voids content

Figs. 3.2.1 and 3.2.2 show the relation between the voids content of the pervious concrete and recycled aggregate replacement proportion along with the SBRL for the fresh and hardened pervious concrete, respectively. In general, an increase in the voids content is accompanied by the increase of the proportion of the recycled aggregates, which contradicts (Zaetang, Y. et al.), where the authors noticed that the addition of the recycled aggregate has no significant effect [14]. At the same time, there is a decrease in the voids content by the increase of the SBRL percentage. Same as for the density, there is no pronounced difference between the results of pervious concrete with natural aggregate and 25% recycled aggregate. It is observed that replacing 15% of cement weight by SBRL will result in voids ratio less than 15% except for pervious concrete with 100% recycled aggregate, wherein it is recommended in ACI 522R that the voids content should not be less than 15%.

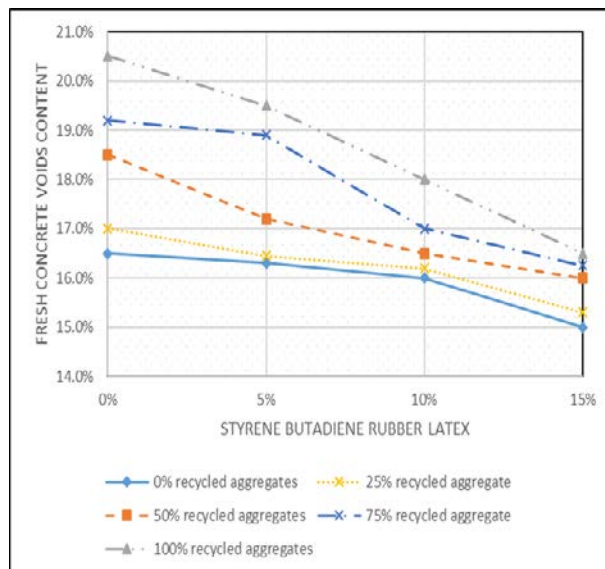


Figure 3.2.1. Voids content in the fresh pervious concrete.

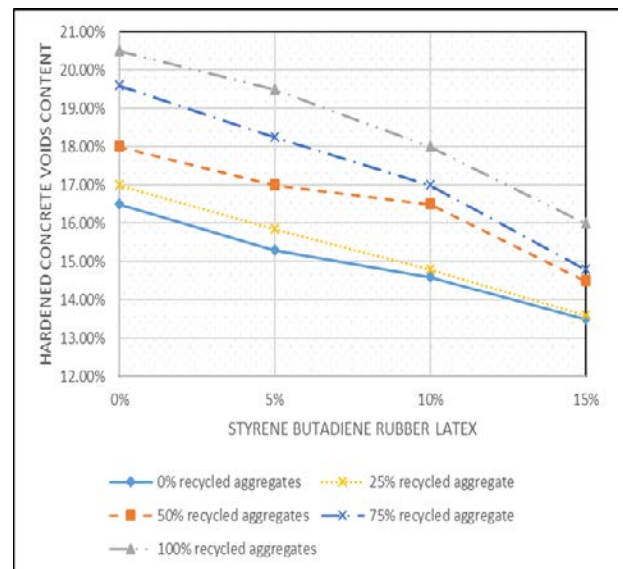


Figure 3.2.2. Voids content in the hardened pervious concrete.

3.3. Water permeability test (falling head method)

Fig. 3.3 shows the relation between the water permeability of the pervious concrete and recycled aggregate replacement proportion along with the SBRL for the fresh and hardened pervious concrete, respectively. It is observed that the SBRL has a negative impact on the water permeability. At the same time, increasing the recycled aggregate percentage in the mixture increases the water permeability. It is observed that the addition of 15% SBRL decreased the water permeability of the pervious concrete with (0%, 25%, 50%, 75% and 100% recycled aggregate) by (10.7%, 14.4%, 14.1%, 16.2% and 11.4%), respectively as shown in Fig. 3.4.

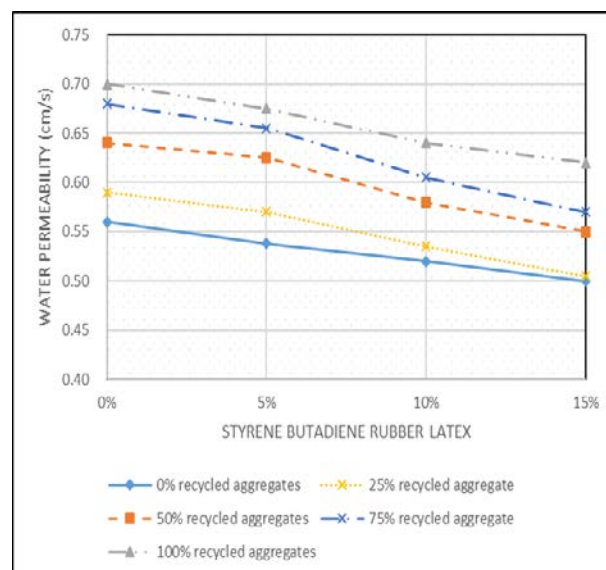


Figure 3.3. Water permeability of the hardened pervious concrete.

3.4. Summary of the effect of styrene butadiene rubber latex on the permeability parameters

Fig. 3.4 highlights the effect of SBRL on the permeability parameters of the recycled aggregate pervious concrete. The figure emphasizes that the addition of the SBRL increases the density while reducing the voids content and the water permeability. For example, replacing 10% of cement weight by SBRL increased the fresh and hardened concrete density by 3.2% and 3.7%, respectively, wherein decreased the hardened voids content and the water permeability by 8.3% and 9.4%, respectively for pervious concrete with 50% recycled aggregate.

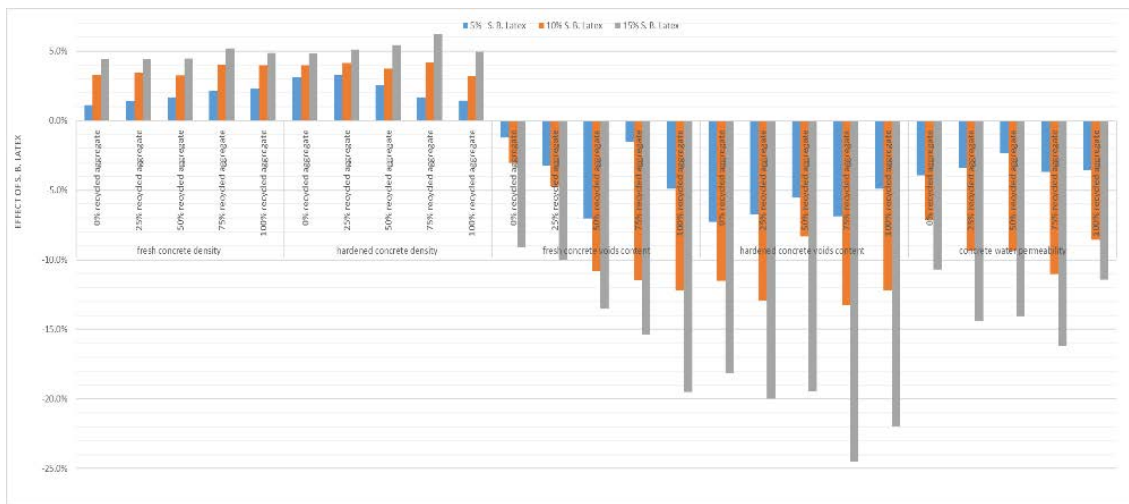


Figure 3.4. Effect of SBRL on the permeability parameters of the recycled aggregate pervious concrete.

3.5. Compressive strength

Fig. 3.5 presents a relation between the 28 days concrete compressive strength (MPa), recycled aggregate replacement percentage and SBRL. Generally, it is observed that by the increase of the dose of the SBRL there is a significant increase in the compressive strength of the pervious concrete. Additionally, it is noticed that when 15% of cement weight is replaced by the SBRL, the difference between the compressive strength of pervious concrete with 50% and 75% recycled aggregate vanishes. This is attributed to the SBRL related densification in the interfacial transition zone between the aggregate and the cement paste [24, 25]. Also, there is no significant deterioration or reduction in the compressive strength of the pervious concrete as a result of replacing 25% of the natural aggregate with recycled ones.

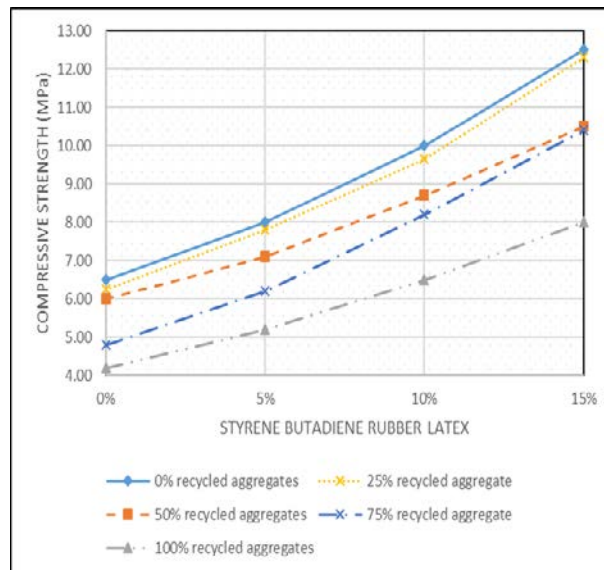


Figure 3.5. 28-day compressive strength of the pervious concrete.

3.6. Tensile strength

Figs. 3.6.1 and 3.6.2 show the impact of the SBRL on the 28 days splitting and flexural tensile strength (MPa) of pervious concrete with different levels of recycled aggregates, respectively. Regarding the splitting tensile strength, it is noticed that the concrete mixtures with 75% and 100% recycled aggregate don't meet the ACI 522R specifications. Additionally, it is observed that the occurred deterioration from the introduction of the recycled aggregates to the concrete mix is reduced by the increase of the SBRL dose.

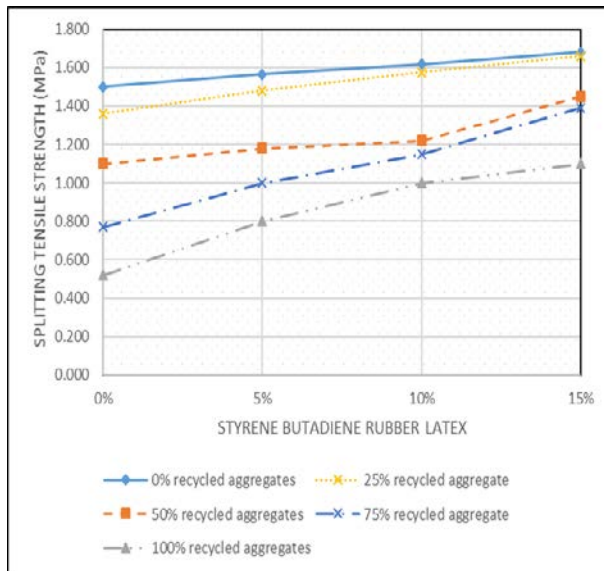


Figure 3.6.1. 28 days splitting tensile strength of the pervious concrete.

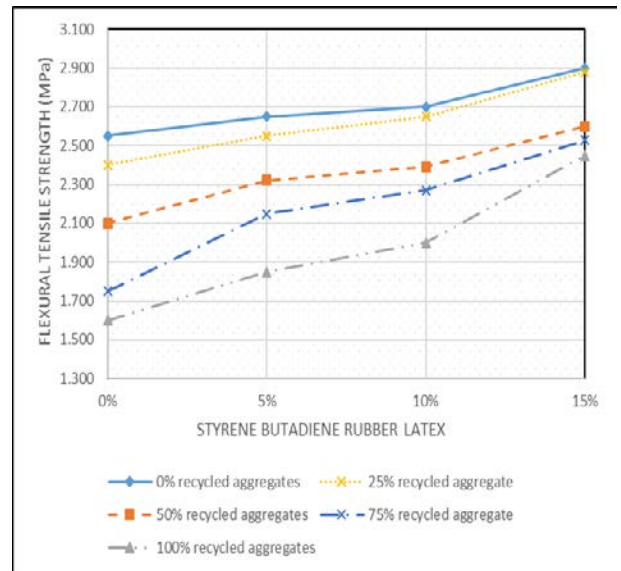


Figure 3.6.2. 28 days flexural tensile strength of the 28 days pervious concrete.

3.7. Degradation and potential resistance

Fig. 3.7 shows the effect of SBRL on the pervious concrete with different levels of recycled aggregates. The figure confirms that SBRL significantly enhances the abrasion resistance of the concrete. Additionally, Fig. 3.8 reveals that when 10% of cement weight is replaced by SBRL, the degradation potential is reduced by 31.7% for the concrete with 75% recycled aggregates.

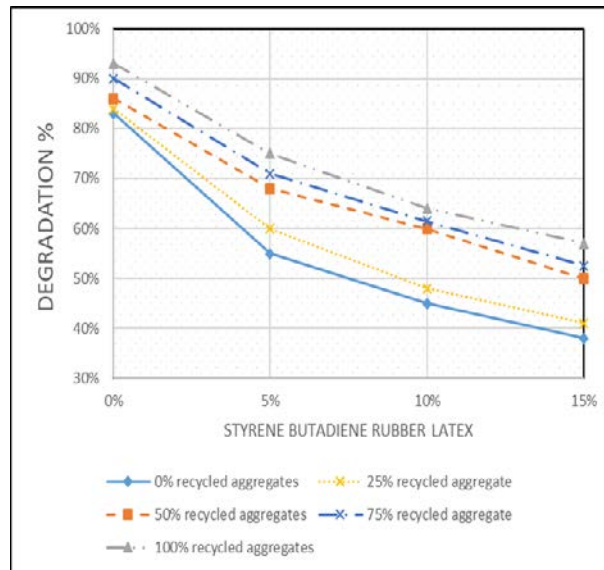


Figure 3.7. Degradation of the pervious recycled aggregate concrete.

3.8. Summary of the effect of styrene butadiene rubber latex on the strength parameters

Fig. 3.8 presents the effect of SBRL on the strength parameters of the pervious concrete with different levels of recycled aggregates. Generally, it is noticed that the addition of the SBRL significantly enhances the mechanical properties even above the 10% dosage which agrees with (Shaker, F.A. et al.) [25] and disagrees with (Wang, Ru. Et al.) [24]. It was noticed that the addition of 15% of SBRL to a pervious concrete with 75% recycled aggregate increased the compressive strength, splitting tensile strength and flexural tensile strength by 116.7%, 80.5% and 40.6%, respectively.

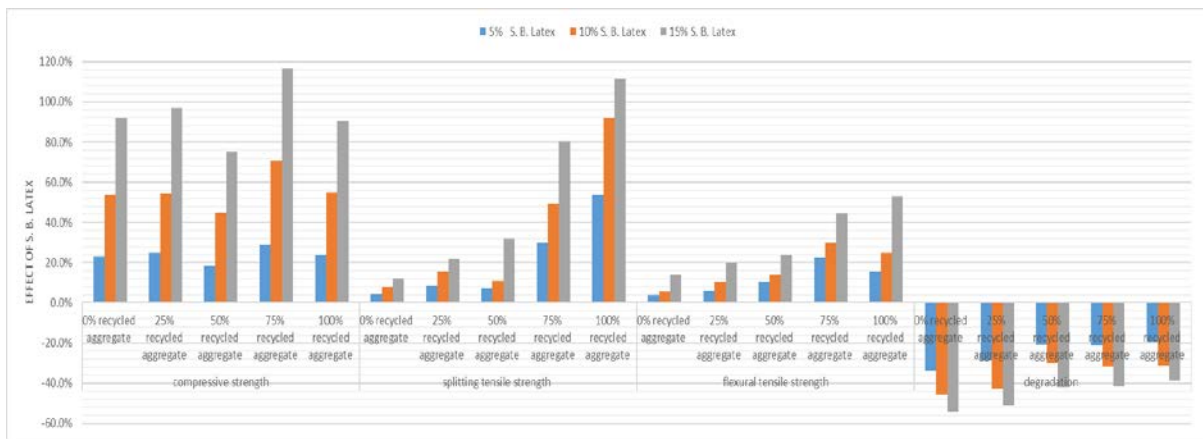


Figure 3.8. Effect of SBRL on the strength parameters of the recycled aggregate pervious concrete.

3.9. General relations between water permeability and other parameters

There are many works establishing relationships between porosity and other parameters [20, 26, 37, 40–41], while there were only a few attempts to find relations between permeability and other properties with a degree of fit (R^2) ranging from 0.53 to 0.91 [20, 36–39].

This section investigates a correlation between water permeability and other parameter, since it is the main parameter in pervious concrete.

It is observed from Fig. 3.9.1 that the increase of the concrete density (D) in (kg/m^3), is accompanied by a consequent decrease in the water permeability (P) in (cm/s). The inferred formula has a very good degree of fit ($R^2 = 0.9245$) and is as follow:

$$D = -550.11P + 2127.9. \tag{11}$$

It is noticed from Fig. 3.9.2 that there is a direct polynomial relationship between the water permeability (P) in (cm/s) and the voids content (V), where the inferred formula has a very good degree of fit ($R^2 = 0.9232$) and is as follow:

$$V = 0.4476P^2 - 0.2151P + 0.1341. \tag{12}$$

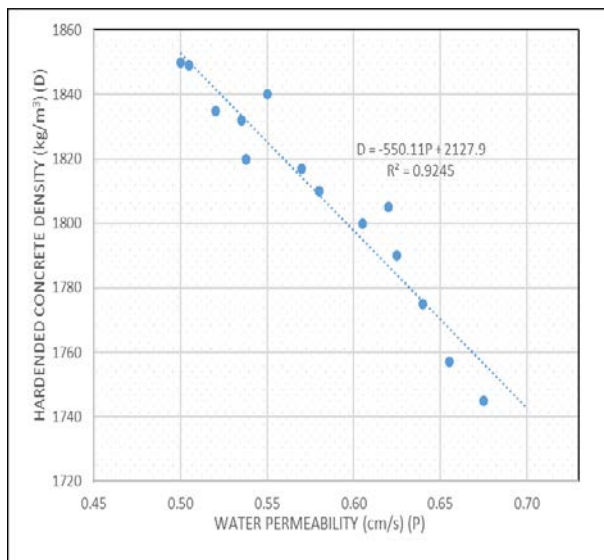


Figure 3.9.1. Correlation between water permeability and hardened concrete density.

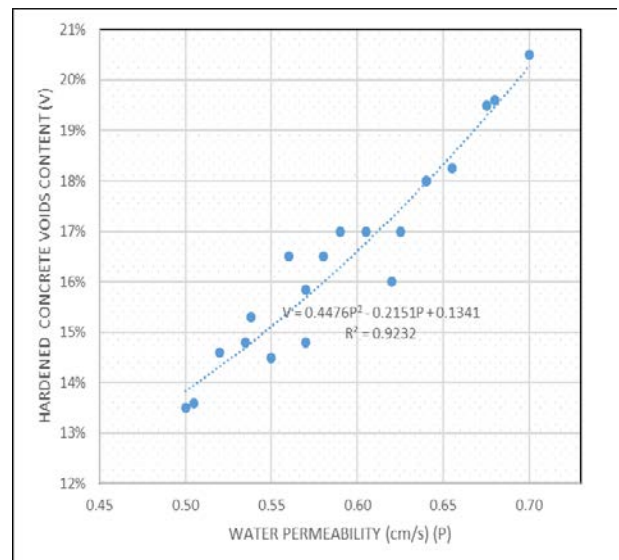


Figure 3.9.2. Correlation between water permeability and hardened concrete voids content.

It is observed from Fig. 3.9.3 that there is an indirect exponential relationship between the water permeability (P) in (cm/s) and the 28 days compressive strength (F_c) in (MPa), where the inferred formula has a good degree of fit ($R^2 = 0.8024$) and is as follow:

$$F_c = 111.32e^{-4526P}. \tag{13}$$

Fig. 3.9.4 presents the inferred relationship between the water permeability in (cm/s) and the 28 days tensile strength in (MPa), whether the splitting tensile strength (F_t) or the flexural tensile strength (F_b). It is observed that there is an indirect exponential relationship between the water permeability (P) and the 28 days tensile strength (F_c), where the inferred formula between the water permeability and the splitting strength has an excellent degree of fit ($R^2 = 0.9684$) and is as shown in Eq. (4). In addition, the inferred formula between the water permeability and the flexural tensile strength has an excellent degree of fit ($R^2 = 0.9491$) and is as shown in Eq. (5).

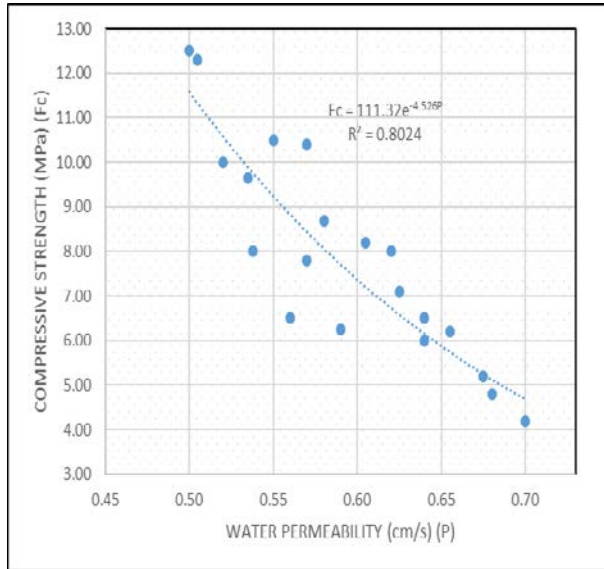


Figure 3.9.3. Correlation between water permeability and pervious concrete compressive strength.

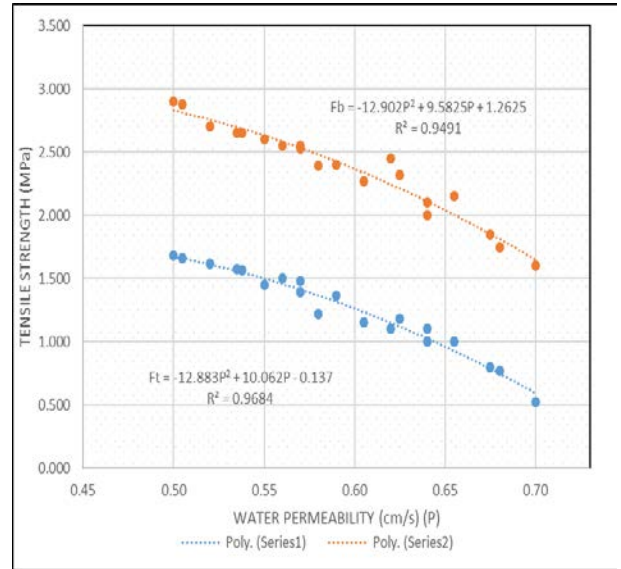


Figure 3.9.4. Correlation between water permeability and pervious concrete tensile strength.

$$F_t = -12.883P^2 + 10.062P - 0.137, \tag{14}$$

$$F_b = -12.902P^2 + 9.5825P + 1.2625, \tag{15}$$

$$Deg = 1.845P - 0.5046. \tag{16}$$

It is observed from Fig. 3.9.5 that there is a direct linear relationship between the water permeability (P) in (cm/s) and the pervious concrete degradation (Deg). The inferred formula has a very good degree of fit ($R^2 = 0.8936$), and is as follow:

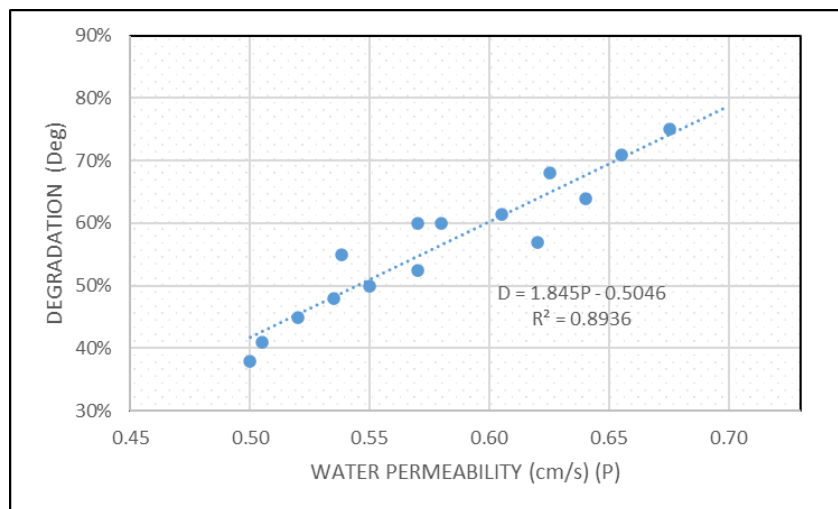


Figure 3.9.5. Correlation between water permeability and pervious concrete degradation.

4. Conclusion

This study focused on the impact of replacing (5%, 10% and 15%) of cement weight by styrene butadiene rubber latex in pervious concrete with different levels of recycled coarse aggregate (0%, 25%, 50%, 75% and 100%).

Thus, it was concluded that:

1. Replacing 25% natural aggregate by recycled aggregates produces next to no negative effect or deterioration in the mechanical properties. Moreover, the deterioration caused by replacing up to 50% of the natural coarse aggregate by the recycled ones is negligible, as the reduction in the mechanical properties is less than 15%.

2. In case of casting mixtures with 75% or more recycled aggregate, it is recommended to use a dose of 10% SBRL in order to meet ACI 522R specifications and to overcome the tensile strength deterioration.

3. High permeability is accompanied by reduced density, compressive strength and tensile strength, but improved voids content and degradation potential.

4. Although a 15% replacement the cement weight by SBRL is the best option, it was found that a 10% replacement is better both in terms of costs and compliance with ACI 522R specifications.

5. In case of using recycled aggregate, it is recommended to increase the mixing water by the amount of the first 10 min absorbed water by the recycled coarse aggregates.

References

- Huang, B., Wu, H., Shu, X., Burdette, E.G. Laboratory evaluation of permeability and strength of polymer-modified pervious concrete. *Construction and Building Materials*. 2010. 24 (5). Pp. 818–823. DOI: 10.1016/j.conbuildmat.2009.10.025.
- Yang, X., Liu, J., Li, H., Ren, Q. Performance and ITZ of pervious concrete modified by vinyl acetate and ethylene copolymer dispersible powder. *Construction and Building Materials*. 2020. 235. Pp. 117532. DOI: 10.1016/j.conbuildmat.2019.117532.
- Nassiri, S., Rangelov, M., Chen, Z. Preliminary Study to Develop Standard Acceptance Tests for Pervious Concrete. 2017. (May). Pp. 1–67.
- Liu, Z., Asce, S.M., Yu, X., Asce, M. Laboratory Evaluation of Abrasion Resistance of Portland Cement Pervious Concrete. *Journal of Materials in Civil Engineering*. 2011. 27 (September). Pp. 1239–1247. DOI: 10.1061/(ASCE)MT
- Yang, J., Jiang, G. Experimental study on properties of pervious concrete pavement materials. *Cement and Concrete Research*. 2003. 33 (3). Pp. 381–386. DOI: 10.1016/S0008-8846(02)00966-3
- Galishnikova, V.V., Abdo, S., Fawzy, A.M. Magazine of Civil Engineering Influence of silica fume on the pervious concrete with different levels of recycled aggregates. *Magazine of civil engineering*. 2020. 93 (1). Pp. 71–82. DOI: 10.18720/MCE.93.7.
- Ćosić, K., Korat, L., Ducman, V., Netinger, I. Influence of aggregate type and size on properties of pervious concrete. *Construction and Building Materials*. 2015. 78. Pp. 69–76. DOI: 10.1016/j.conbuildmat.2014.12.073
- Rizvi, R., Candidate, B., Author, P. Incorporating Recycled Concrete Aggregate in Pervious Concrete Pavements. *Annual Conference of the Transportation Association of Canada*. 2009. Pp. 1–18.
- Yanya, Y. Blending ratio of recycled aggregate on the performance of pervious concrete. *Frattura ed Integrità Strutturale*. 2018. 12 (46). Pp. 343–351. DOI: 10.3221/IGF-ESIS.46.31
- Sonawane, T.R., Pimplikar, P.S.S. Use of Recycled Aggregate Concrete. *Journal of Mechanical and Civil Engineering (IOSR-JMCE)*. 2012. 1 (2). Pp. 52–59.
- Oikonomou, N.D. Recycled concrete aggregates. *Cement and Concrete Composites*. 2005. 27 (2). Pp. 315–318. DOI: 10.1016/j.cemconcomp.2004.02.020
- Etxeberria, M., Marí, A.R., Vázquez, E. Recycled aggregate concrete as structural material. *Materials and Structures/Materiaux et Constructions*. 2007. 40 (5). Pp. 529–541. DOI: 10.1617/s11527-006-9161-5
- Poh, S., Zhao, P., Chen, C., Goh, Y., Adebayo, H., Hung, K., Wah, C. Characterization of pervious concrete with blended natural aggregate and recycled concrete aggregates. *Journal of Cleaner Production*. 2018. 181. Pp. 155–165. DOI: 10.1016/j.jclepro.2018.01.205. URL: <https://doi.org/10.1016/j.jclepro.2018.01.205>
- Zaetang, Y., Sata, V., Wongsu, A., Chindaprasit, P. Properties of pervious concrete containing recycled concrete block aggregate and recycled concrete aggregate. *Construction and Building Materials*. 2016. 111. Pp. 15–21. DOI: 10.1016/j.conbuildmat.2016.02.060.
- Aliabdo, A.A., Elmoaty, A., Elmoaty, M.A., Fawzy, A.M. Experimental investigation on permeability indices and strength of modified pervious concrete with recycled concrete aggregate. *Construction and Building Materials*. 2018. 193. Pp. 105–127. DOI: 10.1016/j.conbuildmat.2018.10.182.
- El-hassan, H., Kianmehr, P., Zouaoui, S. Properties of pervious concrete incorporating recycled concrete aggregates and slag. *Construction and Building Materials*. 2019. 212. Pp. 164–175. DOI: 10.1016/j.conbuildmat.2019.03.325.
- Fu, T.C., Yeih, W., Chang, J.J., Huang, R. The Influence of Aggregate Size and Binder Material on the Properties of Pervious Concrete. 2014.
- Saboo, N., Shivhare, S., Kori, K.K., Chandrappa, A.K. Effect of fly ash and metakaolin on pervious concrete properties. *Construction and Building Materials*. 2019. 223. Pp. 322–328. DOI: 10.1016/j.conbuildmat.2019.06.185.
- Kim, H.H., Kim, C.S., Jeon, J.H., Park, C.G. Effects on the physical and mechanical properties of porous concrete for plant growth of blast furnace slag, natural jute fiber, and styrene butadiene latex using a dry mixing manufacturing process. *Materials*. 2016. 9(2). Pp. 1–11. DOI: 10.3390/ma9020084

20. Bhutta, M.A.R., Tsuruta, K., Mirza, J. Evaluation of high-performance porous concrete properties. *Construction and Building Materials*. 2012. 31. Pp. 67–73. DOI: 10.1016/j.conbuildmat.2011.12.024.
21. Yang, Z., Shi, X., Creighton, A.T., Peterson, M.M. Effect of styrene-butadiene rubber latex on the chloride permeability and microstructure of Portland cement mortar. *Construction and Building Materials*. 2009. 23 (6). Pp. 2283–2290. DOI: 10.1016/j.conbuildmat.2008.11.011
22. Beeldens, A., Van Gemert, D., Schorn, H., Ohama, Y., Czarnecki, L. From microstructure to macrostructure: An integrated model of structure formation in polymer-modified concrete. *Materials and Structures/Materiaux et Constructions*. 2005. 38(280). Pp. 601–607. DOI: 10.1617/14215
23. Shu, X., Huang, B., Wu, H., Dong, Q., Burdette, E.G. Performance comparison of laboratory and field produced pervious concrete mixtures. *Construction and Building Materials*. 2011. 25 (8). Pp. 3187–3192. DOI: 10.1016/j.conbuildmat.2011.03.002.
24. Wang, R., Wang, P.M., Li, X.G. Physical and mechanical properties of styrene-butadiene rubber emulsion modified cement mortars. *Cement and Concrete Research*. 2005. 35 (5). Pp. 900–906. DOI: 10.1016/j.cemconres.2004.07.012
25. Shaker, F.A., El-Dieb, A.S., Reda, M.M. Durability of Styrene-Butadiene latex modified concrete. *Cement and Concrete Research*. 1997. 27 (5). Pp. 711–720. DOI: 10.1016/S0008-8846(97)00055-0.
26. Sriravindrarajah, R., Wang, N.D.H., Ervin, L.J.W. Mix Design for Pervious Recycled Aggregate Concrete. *International Journal of Concrete Structures and Materials*. 2012. 6 (4). Pp. 239–246. DOI: 10.1007/s40069-012-0024-x
27. Rasiah, S. Environmentally Friendly Pervious Concrete for Sustainable Construction Environmentally Friendly Pervious Concrete for Our World in Concrete & Structures Environmentally Friendly Pervious Concrete for Sustainable Construction. 2010. (September).
28. ASTM C 150. Standard Specification for Portland Cement. ASTM International. 2015. (June 1999). Pp. 1–6. DOI: 10.1520/C0010
29. ASTM C1688/C1688M. Standard Test Method for Density and Void Content of Freshly Mixed Pervious Concrete. ASTM International. 2014. Pp. 1–4. DOI: 10.1520/C1688
30. ASTM C1754/C1754M-12. Standard Test Method for Density and Void Content of Hardened Pervious Concrete. ASTM International. 2012. P. 3. DOI: 10.1520/C1754
31. ASTM C1781/C1781M. Standard Test Method for Surface Infiltration Rate of Permeable Unit Pavement. ASTM International. 2015. Pp. 1–6. DOI: 10.1520/C1781. URL: <http://compass.astm.org/download/C1781C1781M.8914.pdf>
32. ASTM C39/C39M-14. Standard Test Method for Compressive Strength of Cylindrical Concrete Specimens. ASTM International. 2014. Pp. 1–8. DOI: 10.1520/C0039. URL: <http://www.astm.org/cgi-bin/resolver.cgi?C39C39M-17b>
33. ASTM C496/C496M-11. Standard Test Method for Splitting Tensile Strength of Cylindrical Concrete Specimens. *Annual Book of ASTM Standards Volume 04.02*. 2011. Pp. 1–5. DOI: 10.1520/C0496. URL: [http://www.c-s-h.ir/wp-content/uploads/20-15/01/C-496.pdf%0Aftp://ftp.astmtmc.cmu.edu/docs/diesel/cummins/procedure_and_ils/ism/Archive/ISM Procedure \(Draft 10\).doc](http://www.c-s-h.ir/wp-content/uploads/20-15/01/C-496.pdf%0Aftp://ftp.astmtmc.cmu.edu/docs/diesel/cummins/procedure_and_ils/ism/Archive/ISM Procedure (Draft 10).doc)
34. ASTM Standard C78/C78M. Standard Test Method for Flexural Strength of Concrete (Using Simple Beam with Third-Point Loading). ASTM International. 2010. C78-02 (C). Pp. 1–4. DOI: 10.1520/C0078
35. ASTM C1747. Standard Test Method for Determining Potential Resistance to Degradation of Pervious Concrete by Impact and Abrasion 1. ASTM International. 2015. (c). Pp. 5–7. DOI: 10.1520/C1747
36. Tho-In, T., Sata, V., Chindapasirt, P., Jaturapitakkul, C. Pervious high-calcium fly ash geopolymer concrete. *Construction and Building Materials*. 2012. 30 (325). Pp. 366–371. DOI: 10.1016/j.conbuildmat.2011.12.028.
37. Ibrahim, A., Mahmoud, E., Yamin, M., Patibandla, V.C. Experimental study on Portland cement pervious concrete mechanical and hydrological properties. *Construction and Building Materials*. 2014. 50. Pp. 524–529. DOI: 10.1016/j.conbuildmat.2013.09.022.
38. Kayhanian, M., Anderson, D., Harvey, J.T., Jones, D., Muhunthan, B. Permeability measurement and scan imaging to assess clogging of pervious concrete pavements in parking lots. *Journal of Environmental Management*. 2012. 95 (1). Pp. 114–123. DOI: 10.1016/j.jenvman.2011.09.021.
39. Aliabdo, A.A., Abd Elmoaty, A.E.M., Fawzy, A.M. Experimental investigation on permeability indices and strength of modified pervious concrete with recycled concrete aggregate. *Construction and Building Materials*. 2018. 193. Pp. 105–127. DOI: 10.1016/j.conbuildmat.2018.10.182.
40. Chen, Y., Wang, K., Wang, X., Zhou, W. Strength, fracture and fatigue of pervious concrete. *Construction and Building Materials*. 2013. 42. Pp. 97–104. DOI: 10.1016/j.conbuildmat.2013.01.006.
41. Yahia, A., Kabagire, K.D. New approach to proportion pervious concrete. *Construction and Building Materials*. 2014. 62. Pp. 38–46. DOI: 10.1016/j.conbuildmat.2014.03.025.

Contacts:

Shamseldin Abdo, shamseldin.abdo@outlook.com

Vera Galishnikova, galishnikova-vv@rudn.ru

Ahmed Fawzy, engahmedfawzy90@yahoo.com



DOI: 10.34910/MCE.108.6

Mechanical properties of slag sand mixture used in road pavements

H. Cherfa^a, A. Nechnech^b, N. Saoudi^c, K. Ait Mokhtar^b

^aUniversity of Sciences and Technology Houari Boumediene, Algiers, Algeria

^bLaboratory of Environment, Water Geomechanics and Structures LEEGO / University of Sciences and Technology Houari Boumediene (USTHB)

^cDépartement of Civil Engineering, Akli Mohand Oulhadj University Bouira (UAMOB), Bouira, Algeria

*E-mail: ha_cherfa@yahoo.fr

Keywords: mechanical properties, local materials, slag, dune sand, pavement, road engineering

Abstract. Today the road has become a necessity and an important factor in the economic and social development of nations. Algeria knows the realization of many grandiose road projects that required large quantities of noble materials such as aggregates and crushed sands and which unfortunately are becoming increasingly rare. The inability of Algerian quarries to supply these materials is a reason for the valorization of industrial waste and local materials that are in abundance. Among these materials, we find granulated slag and dune sand. Our study presents valorization of these two materials through a formulation and characterization of slag sand mixture composed of dune sand treated with different percentages of granulated blast furnace slag, which acts as a hydraulic binder. The results obtained show that this treatment improves the cohesion and mechanical properties of sand dune, which allows its use in road engineering, particularly in the pavement layers.

1. Introduction

The industrial wastes valorization is work that aims on the one hand the protection of the environment and on the other hand the rational and economic use of these materials in the field of civil engineering. Among these wastes we find granulated blast furnace slag (GBFS) which serve to stabilize and improve the mechanical properties of several soils including dune sands (DS) which present local materials without resistance. Algeria has a large iron and steel complex that generates large quantities of granulated slag. For example, the annual production of granulated slag is 430 000 tons [1].

The vast desert area of Algeria contains priceless quantities of dune sands. These sands cover about 60 % the surface of Algeria [2]. Granulated blast furnace slag (GBFS) is a by-product of the manufacture of cast iron in blast furnaces, obtained by rapid cooling, and has been used as a building material since the 17th century [3]. Several research works were carried out for the valorization of (GBFS) and DS in the field of civil engineering.

GBFS are used for soil stabilization [4–7] and for flexible and semi-rigid pavement layers [8–10]. The GBFS is mixed with one or more sands to obtain slag sand (SS) intended especially for the base and foundation road and highway layers. This slag sand can be manufactured in several countries which have steel complexes which produce granulated slag such as India, China, USA, Japan, Russia, UK, Iran, France, Turkey, Brazil,...etc.

In the cement industry, granulated slag is considered as an industrial by product with zero CO₂ emissions because its substitution with clinker allows direct emission reduction of between 65 % and 95 % [11], knowing that CO₂ accounts for 82 % of the total greenhouse gas which is responsible of climate

Cherfa, H., Nechnech, A., Saoudi, N., Ait Mokhtar, K. Mechanical properties of slag sand mixture used in road pavements. Magazine of Civil Engineering. 2021. 108(8). Article No. 10806. DOI: 10.34910/MCE.108.6

© Cherfa, H., Nechnech, A., Saoudi, N., Ait Mokhtar, K., 2021. Published by Peter the Great St. Petersburg Polytechnic University



This work is licensed under a CC BY-NC 4.0

change [12]. For the concrete manufacture, Granulated Slag was widely used compared to others wastes [13], it has been used as a basis material to improve the concrete strength [14]. Many researchers, in their studies, have shown that the strength of the granulated slag-based concrete is less affected by chemicals product than the conventional concrete when exposed to an aggressive environment [15–20]. Granulated blast furnace slags therefore have many qualities that make them interesting in several application fields.

Dune sands are generally treated and stabilized by cement and lime according to the literature [2]. However, very limited studies have focused on treating and stabilizing these sands with granulated slag for use in road engineering.

This work is concerned with the technique of treating the dune sand by adding different percentages of GBFS as hydraulic binders (GBFS+1 % lime). Initially, the materials used were identified and characterized by conventional geotechnical tests and by mineralogical and chemical analyses. Then in a second step, the study focused on the effect of hydraulic binders on the mechanical behavior in order to determine the optimal mixture which presents the best mechanical properties making it potential candidate for use in pavements layers.

2. Materials and methods

2.1. Materials

2.1.1. Granulated blast furnace slag GBFS

GBFS used in this study is a granulated blast furnace slag of fresh production and 0/5 mm granulometry (Fig. 1) coming from the steel complex of El-Hadjar (Annaba, Algeria), obtained by rapid cooling. It presents the main characteristics given in Table 1. Its reactivity coefficient α is 39. It satisfies the criteria set by the Algerian catalog which specifies a minimum value greater than 20 [21]. Its X-ray diffraction (XRD) analysis and Scanning Electron Microscopy (SEM) image are given in Fig. 2.



Figure 1. Granulated blast furnace slag.

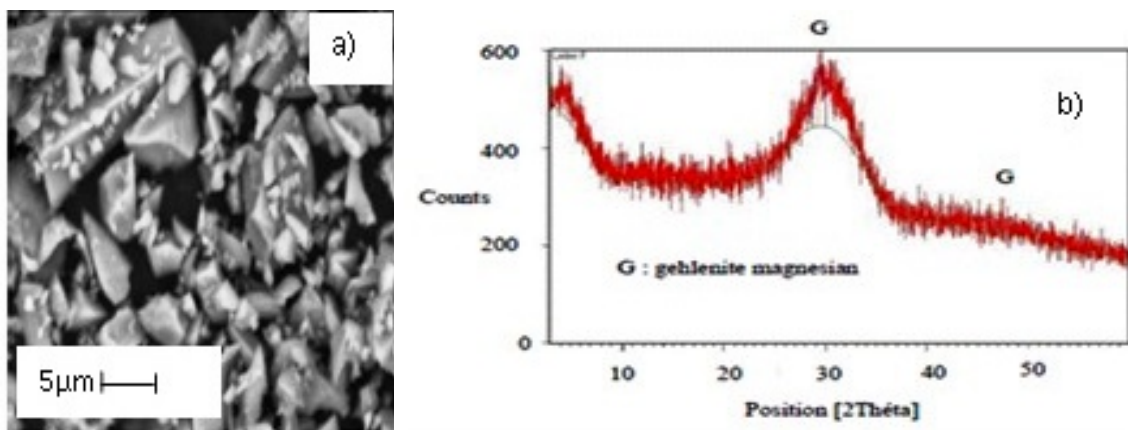


Figure 2. Scanning Electron Microscopy (a) and X-ray diffraction analysis (b) of GBFS

Figure 2 shows that the granulated slag is amorphous and it presents an amorphous halo angle of around $2\theta = 30^\circ$ which shows that GBFS is typically glassy. A small quantity of gehlenitemagnesian (G) presents in the glass. This result is consistent with the results found in the literature [22–25]. It was also observed from the SEM picture that the GBFS particles were angular in shape and the surface of slag is rough.

2.1.2. Dune Sand DS

The dune sand used is a fine sand of 0/1 mm granulometry from Boussaâda region (Msila, Algeria). It is siliceous considering its content of silica (SiO₂) which is 97.10 %. According to the GTR 2000 soil classification [26], dune sand belongs to class D1. It is characterized as permeable, incoherent, and poorly graded sand. This suggests that dune sand alone will not be sufficiently compact, and subsequently its immediate bearing index is not adequate [27, 28]. Therefore, a treatment of this sand with hydraulic binders will be essential. The X-ray analysis shown in Fig. 3 reveals its very high quartz content.

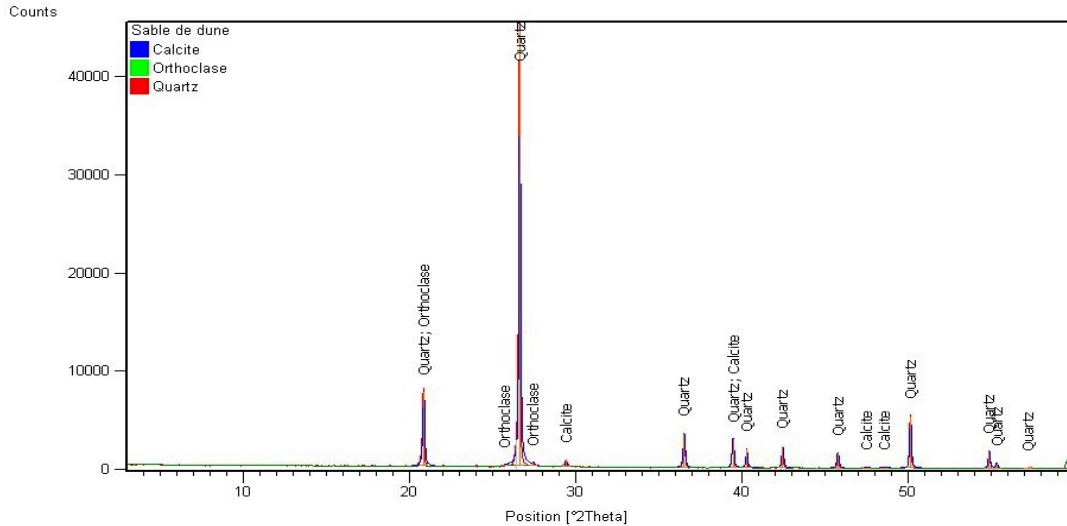


Figure3. DS X-ray analysis.

2.1.3. Crushed Sand CS

CS used is crushed quarry sand with a particle size of 0/6 mm; it is calcareous with carbonate content (CaCO₃) of 89 %.

2.1.4. Lime

The lime used in our study is a slaked lime which has a role of basic activator of the slag. It's coming from the region of Ghardaïa, Algeria. Its CaO content is greater than 50 %, it verifies the specifications for its use for roads.

The physico-chemical characteristics of the different study materials are given in Table 1, their particle size curves are represented in Fig. 4.

Table 1. Physico-chemical analysis of the used materials.

Material	GBFS	DS	CS	Lime
Density [g/cm ³]	2.8	2.65	2.81	2.58
Friability (%)	19	–	40	–
Blaine specific surface (cm ² /g)	2057	–	–	10165
Pistonsandequivalent (%)	–	73.79	94	–
Methylenebluevalues	–	0.4	0.5	–
Basicitymodulus	1.3	–	–	–
Finenessmodulus	3.21	0.88	4.2	–
CoefficientofuniformityCu ¹	3.39	1.97	14.75	–
CoefficientofcurvatureCc ²	1.17	0.86	1.99	–

$${}^1 Cu = D_{10} / D_{60}$$

$${}^2 1 \leq Cc = (D_{30})^2 / D_{10} \times D_{60} \leq 3, \text{ where } D_{10}, D_{30} \text{ and } D_{60} \text{ are diameters (in mm) corresponding respectively to 10, 30 and 60 \% passing percentages.}$$

Material	GBFS	DS	CS	Lime
CaO (%)	45.78	0.54	40.61	64.27
SiO ₂ (%)	34.99	97.10	5.94	2.85
CaCO ₃ (%)	–	3.39	89.65	–
Al ₂ O ₃ (%)	9.79	0.71	8.85	0.56
MgO (%)	3.92	0.06	3.56	0.45
Fe ₂ O ₃ (%)	0.67	0.39	3.25	0.27

The methylene blue values of crushed sand and dune sand indicates the absence of noxious clay particles in these sands.

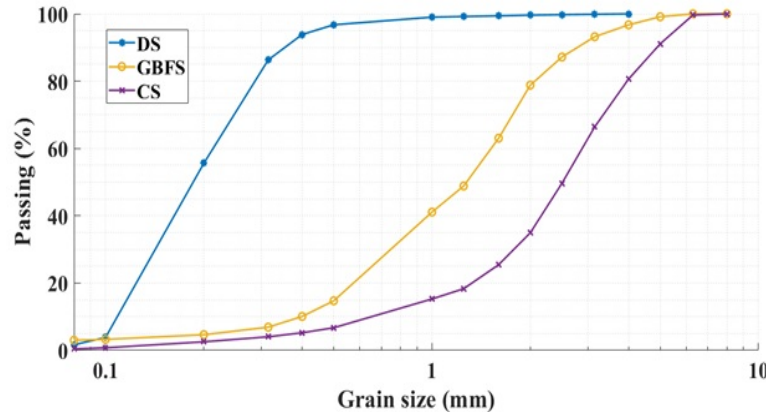


Figure 4. Particle size distribution curves of the used materials.

According to the granulometric curves, we find that our crushed sand is clean, well-graded sand and its grain size curve reflects a continuous dimensional distribution, the uniformity coefficient ($C_u > 2$) confirms the spread out curve of the granularity. On the other hand, the granulometric curve of dune sand represents a tight granularity which is confirmed by the coefficient of uniformity value ($C_u < 2$), so the dune sand is clean sand as Sm class according to the GTR 2000 Soil Classification [26].

2.2. Methods

The present study deals with the effect of the addition of hydraulic binders (GBFS + 1 % lime) on the mechanical properties of the studied sand. The different mixtures (DS+CS + GBFS + 1 % lime) called slag sands (SS) were formulated, in the laboratory, with percentages of granulated slag (GBFS) ranging from 10 % to 30 %. In order to determine the optimal mixtures, various tests such as; compaction test, CBR test, simple compression test and triaxial shear test were carried out to study the mechanical behavior of the above-mentioned slag sand mixtures.

2.1.5. Slags and mixtures formulation methodology

A slag sand can be defined as the mixture (Fig. 5), carried out in a mixing plant, of one (or more) sand (s), a certain percentage of slag (granulated or pelletized) and a basic activator such as lime at a dosage generally around 1 %. It is mainly used for pavement foundations. The choice of the compositions of the SS mixes is essentially based on the following two criteria:

1. The stability before compaction (immediate stability) of the mixtures is appreciated by their coefficients of uniformity and curvature, the aim of which is to have continuous particle size curves. We must verify that:

$$C_u = D_{10} / D_{60} \geq 6, \quad (1)$$

$$1 \leq C_c = (D_{30})^2 / D_{10} \times D_{60} \leq 3. \quad (2)$$

2. The stability of compacted mixtures is assessed by the immediate bearing test. According to the value of the immediate bearing index (IBI), we can classify the stability of our mixture:

$$IBI \leq 25, \text{ unstable mixture;}$$

$$25 \leq IBI \leq 50, \text{ medium stability;}$$

$$IBI > 50, \text{ stable mixture.}$$



Figure 5. Slag sand mixture.

Table 2 recapitulates the formulations adopted while respecting the conditions of immediate stability.

Table 2. The Cu and Cc values of the different SS mixtures.

Formulation	GBFS (%)	CS (%)	DS (%)	Lime (%)	Cu	Cc
1	0	20	80	0	4.8	1.7
2	10	30	60	1	6	1.7
3	15	37	48	1	6.4	1
4	20	33	47	1	6	1.2
5	25	27	48	1	6	1.12
6	20	22	48	1	8.4	1.15

2.1.6. Compaction test

The compaction is widely used in many geotechnical applications for improving soil compactness [29]. The purpose of compaction is to increase the density of a soil. This consequently reduces its rate of deformation and improves its bearing capacity.

In this respect, the different mixtures that have been formulated by combination of dune sand with different percentages of GBFS were compacted to different water content in order to determine the optimal water content and the maximum dry density by the modified Proctor test according to standard NFP94-093 [30].

2.1.7. Californian Bearing Ratio (CBR) test and simple compression test

The CBR tests were carried out on samples of a mixture of slag sand, compacted in CBR molds, under Proctor conditions, according to standard NF P94-078 [31]. The aim of this test is to assess the ability of a soil to support the traffic load. The test consists of punching slag sand mixtures compacted with energy of 56 blows per layer in a CBR mold and at water contents corresponding to the optimum of the Modified Proctor test. The test CBR is carried out in a CBR press (Fig. 6) without overload, to determine the immediate bearing indices (IBI) of the mixtures.



Figure 6. CBR press.

Cylindrical SS samples (Fig. 7) obtained by static compaction, where the mixture is put in a single layer in a cylindrical mold with 50 mm in diameter and 100 mm in height with double piston, then statically compacted at a speed of 1.14 mm/min, according to the standard EN 13286-53 [32]. This method of compaction leads to a homogeneous distribution of compaction stress [33]. The samples were then preserved in bags at a temperature of 20 ± 2 °C until the date of the compression tests according to the standard NF EN 13286-41 [34]. These tests were performed at age of 0, 7, 14, 28, 60 and 90 days.



Figure 7. Cylindrical slag sand samples

The compression test is widely used in pavement and soil stabilization applications [2, 33]. This test is carried out, according to the standard EN 13286-41 [34], on cylindrical slag sand samples.

2.1.8. *Unconsolidated undrained triaxial test*

Triaxial shear tests were performed on non-treated sand (0 % GBFS) and slag- treated sand (SS) samples. Triaxial shear tests have been used in most of the experimental programs reported in the literature in order to access the influencing factors on the shear strength of treated soils, which simulated the general construction conditions of a lot of engineering projects [35]. All slag sand mixtures were statically compacted at the Proctor optimum prior their placement in triaxial apparatus (Fig. 8). The test is carried out with a fast speed of 1 mm/min corresponding to an unconsolidated undrained test (UU) according to the standard NF P94-074 [36]. The measurement of the axial strain was conducted with a vertical displacement sensor located on the top of pressure cell. The axial deviatoric force was measured by axial load sensor. Three confining pressures σ_3 (100 kPa, 200 kPa, and 300 kPa) were applied.



Figure 8. The triaxial cell.

3. Results and Discussions

3.1. Determination of Proctor characteristics

The results obtained by the modified Proctor test are shown in Fig. 9a. The evolution of the optimum water content and the maximum dry density is shown in Fig. 9b.

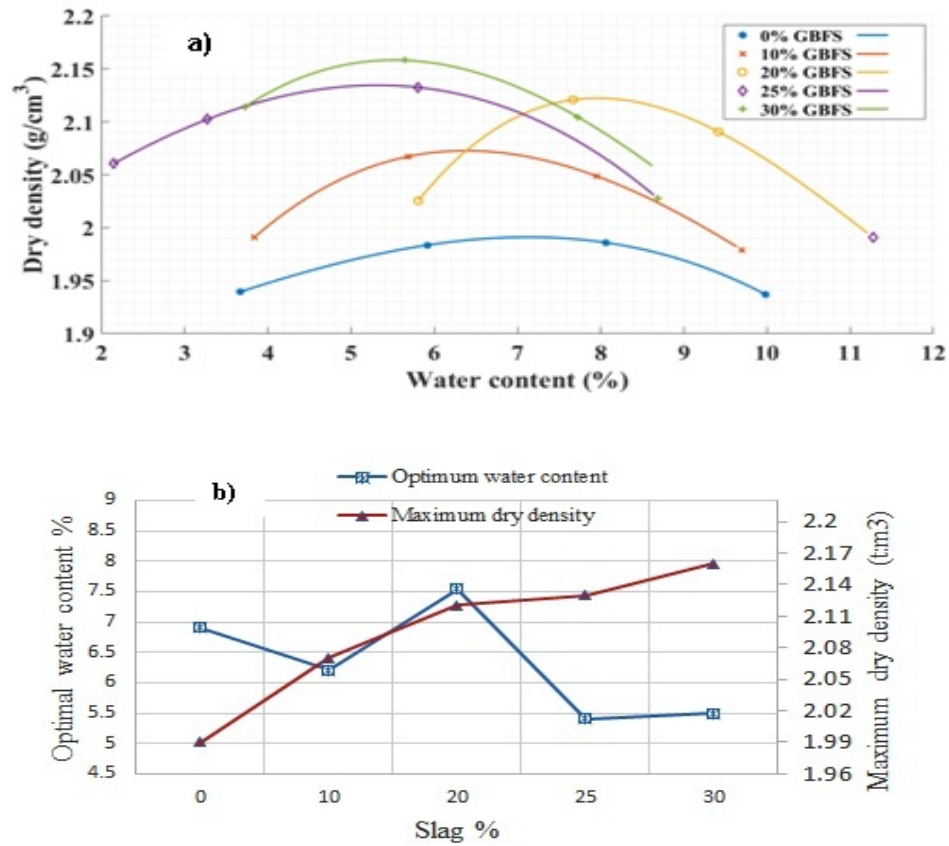


Figure 9. a) Modified Proctor curves according to the percentage of GBFS, b) maximum dry density and optimum water content according to the percentage of slag (GBFS).

From Fig. 9b the density increases while increasing the GBFS content contrary to the optimal water content which reaches it's maximum for 20 % slag and then decreases beyond this value. A similar result was observed by [1].

3.2. Determination of the immediate bearing index (IBI)

Fig. 10 shows the increase of the immediate bearing index (IBI) with increasing of the percentage of GBFS up to the value of 25 % then decreased. According to this result, we can say that our optimal mixture is obtained for 25 % of GBFS added with respect to the bearing capacity of this sand.

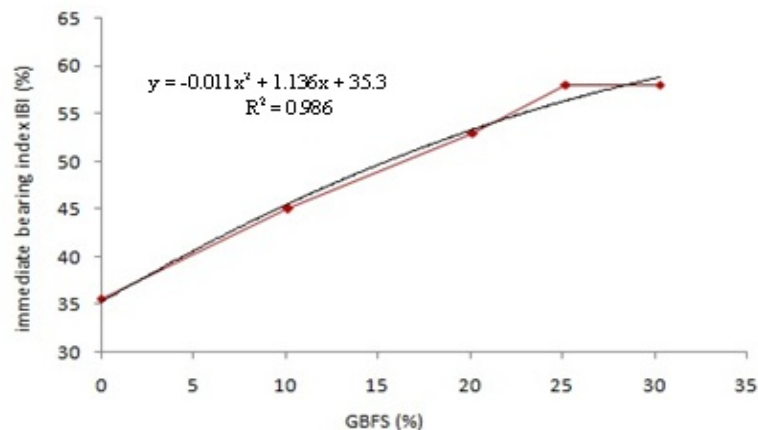


Figure 10. Immediate bearing index (IBI) according to GBFS content.

3.3. Effect of GBFS on the compressive strength of SS

Fig. 11 illustrates the evolution of the compressive strength as a function of the percentages of the binder (GBFS) for different curing times (0, 7, 28, 60 and 90 days).

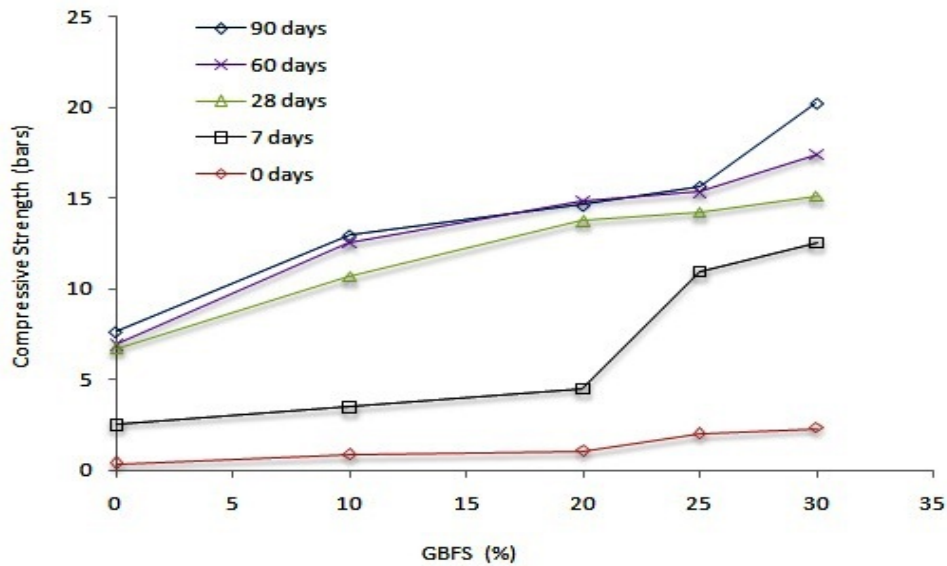


Figure 11. Compressive strength according to GBFS content and curing times.

According to Fig. 11 the compressive strength increases proportionally to the percentages of the added GBFS over time, without reaching a maximum. This result is similar to the result found by smaida and al [2] on the treatment of dune sand with hydraulic binders. These remarkable mechanical performances are due to the chemical role of the slag which consists in improving the microstructure of the SS mixture by fixing the Portlandite ($\text{Ca}(\text{OH})_2$) released by the hydration of the slag. This hydraulic reaction gives rise to a second additional calcium silicate hydrate (CSH), the phase responsible for the hardening of slag sand over time.

3.4. The stress- strain behavior of SS

The deviatoric stress ($q = \sigma_1 - \sigma_3$) versus axial strain (ϵ_1) curves obtained from the triaxial shear tests on sand samples treated with 20 % GBFS are shown in Fig. 12. It was found that SS reveals a peaked stress-strain curves with a peak strength increased with the increase in confining pressure.

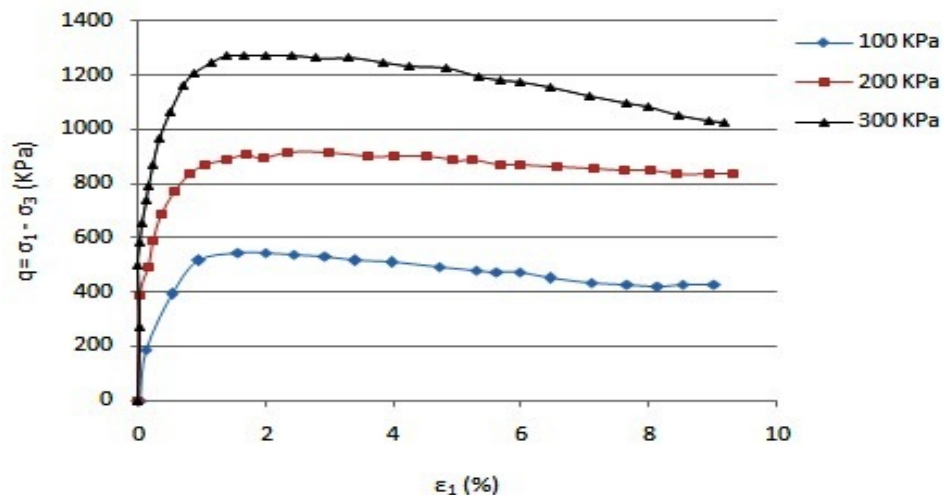


Figure 12. Deviatoric stress versus axial strain curves at 20 % GBFS.

The stress- strain behavior of slag sand can be described as initially rigid, linear up to a well-defined limit point, beyond which the sand undergoes increasingly plastic deformations until failure. The same behavior was observed in the result of Daheur [33].

Fig. 13 shows the maximum deviatoric principal stress (q_{max}) according to GBFS content with various confining pressures 100, 200 and 300 kpa.

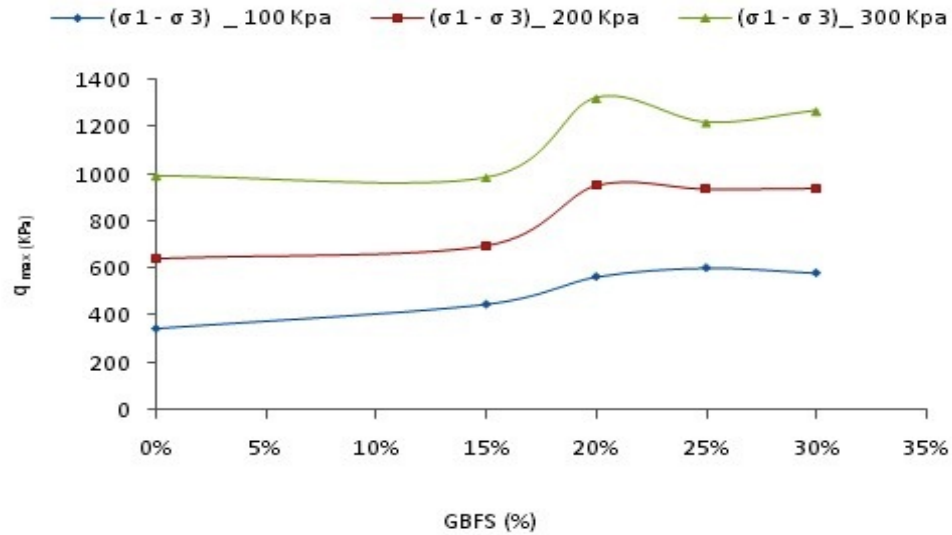


Figure 13. The maximum deviatoric principal stress according to GBFS content with various confining pressures 100, 200 and 300 kpa.

By inspecting the curves presented in Fig. 13, it can be noted that the maximum constraint deviator stress increases with the increase of the dosage in GBFS up to a value of 20 % then decreased.

3.5. Effect of GBFS on the friction angle and the cohesion of SS

Given the cohesive-frictional nature of soils treated with hydraulic binders, the shear strength can be expressed as a function of the internal friction angle and of the cohesion. Table 3 gives the friction angle and the cohesion as a function of the GBFS content. According to this result, the friction angle oscillates between 35.7° and 41.4°. Given the value of the friction angle 38.9° for untreated sand (0 % GBFS) and the value of 38.8° for sand treated with 30 %, we can say that the friction angle is not strongly influenced by the GBFS content. On the other hand the cohesion increases with the increase in percentage of GBFS and reaches a maximum value of 73.5 kpa for 25 % slag added.

Table 3. The cohesion and friction angle values as a function of GBFS.

GBFS (%)	friction angle (°)	Cohesion (kpa)
0	38.9	0
15	35.7	39.9
20	41.4	42.8
25	37.5	73.5
30	38.8	61.4

3.6. Use of slag sand in the foundation layer of a semi-rigid pavement

According to the comparative sizing study carried out on two types of pavement structure, the first with an untreated sand foundation layer and the second with slag sand, we see that by using the slag sand in the foundation layer (Fig. 14), we obtained a gain of 2 cm in thickness at the level of the gravel bitumen base layer. This gain confirms the economic role of our material.

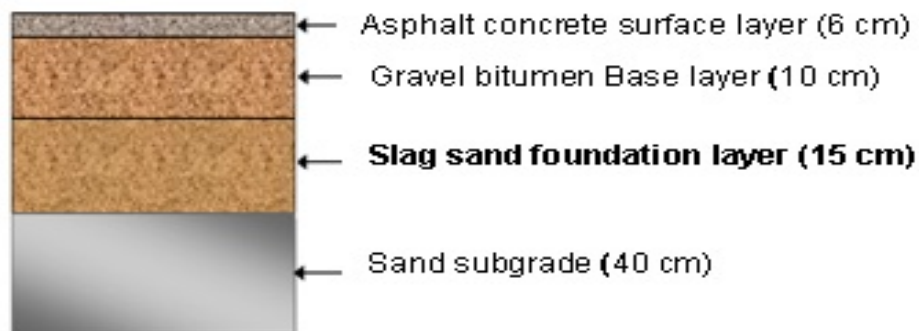


Figure 14. Pavement structure made up of slag sand foundation layer.

4. Conclusion

This article presents a feasibility study on the manufacture of a composite material based on dune sand (DS) treated with granulated blast furnace slag (GBFS). It aims to characterize and to study the mechanical properties of slag sand (SS) mixture prepared in the laboratory. The following conclusions can be drawn from this study:

1. The results of our study allow to conclude that dune sand, which is a local material of low mechanical performance can be improved with treatment with the recycled granulated slag to obtain high resistances while increasing the percentage of slag.
2. Dune sand treatment with GGBF increases the density, bearing capacity, compression strength and shear strength of the slag sand mixture which is suitable for road pavements; the percentages of added GBFS play the role of a hydraulic binder which results in good compactness in the mixtures and subsequently improves mechanical characteristics.
3. With the increase in the percentage of GBFS, the maximum dry density increases. This result is considered to be an indication of the improvement in the compaction characteristics of the sand stabilized with activated slag.
4. The bearing capacity of the sand treated with GBFS is always better than those of untreated sand (0 % of GBFS) and the maximum value of IBI is obtained for 25 % of GBFS which is 58.34 %.
5. The compressive strength of the slag sand mixture increases with increasing GBFS content over time without reaching the maximum; the value of the compressive strength increases from 10.94 bars at 7 days to 15.65 bars at 180 days and it increases from 7.66 bars for untreated sand (0 % of GBFS) to 20.56 bars for 30 % of GBFS at 180 days of cure. These results indicate that sand mixed with GGBS has the potential to be used in road construction, such as in highway and road foundation layer materials.
6. These remarkable mechanical performances are due to the chemical role of the slag which consists in improving the microstructure of the SS mixture by fixing the Portlandite ($\text{Ca}(\text{OH})_2$) released by the hydration of the slag. This hydraulic reaction gives rise to a second additional calcium silicate hydrate (CSH), the phase responsible for the hardening of slag sand.
7. According to the triaxial shear test, our material has an elastoplastic behavior with a maximum deviatoric principal stress for 20 % of slag.
8. The friction angle is not strongly influenced by the GBFS content. On the other hand the cohesion increases with the increase in percentage of GBFS and reaches a maximum value of 73.5 kpa for 25 % slag added.
9. Based on the results mentioned above, GBFS activated with hydraulic lime may be the recommended additive for stabilizing the dune sands intended for use in roadways. A percentage of 20 % and 25 % of activated slag are recommended to improve the mechanical properties of dune sand.
10. Finally, two optimal mixtures were determined to improve the characteristics of dune sand in order to adopt it for use in pavement foundations. These mixtures are: (20 % GBFS +1 % lime +33 % CS+47 % DS) and (25 % GBFS +1 % lime +27 % CS+48 % DS). Given the low cost of GBFS which is approximately 3 \$ per ton and DS which is in abundance, these mixtures have a double advantage of better performance and lower cost.

5. Acknowledgments

The authors gratefully acknowledge the support of the laboratory CTPP (Technical Inspection of Public Works) which allows us to carry out triaxial tests. They acknowledge the research team of the LEEGO and LBE laboratory of USTHB University for their support to this study as a PhD thesis. Without forgetting the steel complex of El Hadjar (Annaba, Algeria) which provides us with a quantity of granulated slag for our study.

References

1. Zemouli, S., Chelghoum, N. Use of ground granulated blast furnace slag in soils stabilization. *Rev. Sci. Technol.* 2018. Synthèse. Vol. 36. Pp. 103–114.
2. Smaida, A., Haddadi, S., Nechnech, A. Improvement of the mechanical performance of dune sand for using in flexible pavements. *Constr Build Mater.* 2019. 208. Pp. 464–471. <https://doi.org/10.1016/j.conbuildmat.2019.03.041>
3. Tarun Yadav, Jatin Singh, Sandeep Panchal, Md. Mohsin Khan, Shilpa Pal. Analysis of Effect of Ground Granulated Blast Furnace Slag (GGBFS) on the Mechanical Properties of Concrete using Destructive and Non-destructive Tests. *J. Mech. cont. & Math. Sci.* 2019. Vol. 14. No. 1. Pp. 78–90. <https://doi.org/10.26782/jmcms.2019.02.00006>
4. Ashish, K.P., Pandey, V., Krishna, M., Singh, J.P. Soil Stabilisation Using Ground Granulated Blast Furnace Slag. *Int. Journal of Engineering Research and Applications.* 2014. Vol. 4. No. 5 (Version 2), Pp.164–171.

5. Sharma, A.K., Sivapullaiah, P.V. Ground granulated blast furnace slag amended fly ash as an expansive soil stabilizer. *Soils and Foundations*. 2016. 56(2). Pp. 205–212. <https://doi.org/10.1016/j.sandf.2016.02.004>
6. Jiawei, D., Yuhuan, B., Shenglai, G., Leiju, T., Zhonghou, S. Effects of epoxy resin on ground-granulated blast furnace slag stabilized marine sediments. *RSC Adv*. 2017. 7. 36460. DOI: 10.1039/c7ra06460h
7. Mohd, A.R., Farhat, H., Lohani, T.K. An experiment on stabilization of soil by using waste product like fly ash, GGBS and CCR. *International Journal for Technological Research in Engineering*. 2019. Vol. 6.No. 7.
8. Cherfa, H. Stabilisation des sols et des couches de chaussée par des résidus industriels – application au laitier de haut fourneau. Thèse de Magister. Université des Sciences et de technologie Houari Boumediene. Alger, 2010. 145 p.
9. Piratheepan, J., Gnanendran, C.T., Lo, S.C.R. Characterization Of Cementitiously Stabilized Granular Materials for Pavement Design Using Unconfined Compression and Idt Testings with Internal Displacement Measurements. *Journal of Materials in Civil Engineering*. 2010. 22(5). Pp. 495–505. DOI: 10.1061/(ASCE)MT.1943-5533.0000051
10. Du, J., Bu, Y., Guo, S., Tian, L., Shen, Z. Effects of epoxy resin on ground-granulated blast furnace slag stabilized marine sediments. *RSC Adv*, 2017, 7, 36460–36472. DOI: 10.1039/C7RA06460H
11. Divet, L., Le Roy, R. Étude de la durabilité vis-à-vis de la corrosion des armatures des bétons formulés avec des ciments à forte teneur en laitier de haut fourneau. *Bulletin des Laboratoires des Ponts et Chaussées*, 2013, pp. 63–84. (hal-00985729)
12. Damtoft and al. cited by Adewumi, A.A., Ismail, M., Ariffin, M.A.M., Yusuf, M.O., Maslehuddin, M., Mohamed, H.D. Strength and microstructure of alkali-activated natural pozzolan and limestone powder mortar. 2019. *Magazine of Civil Engineering*. 92(8). Pp. 36–47. DOI: 10.18720/MCE.92.3
13. Bhavik kumar B. Patel, Jayesh kumar Pitroda, A Review of Geo Polymer Concrete by Using Various Industrial Waste Materials. *International Journal of Constructive Research in Civil Engineering (IJCRCE)*. 2017. Volume 3, Issue 4. Pp.121–131. DOI: <http://dx.doi.org/10.20431/2454-8693.0304011>
14. Yusuf, M.O., Johari, M.A.M., Ahmad, Z.A., Maslehuddin, M. Evolution of alkaline activated ground blast furnace slag–ultrafine palm oil fuel ash based concrete. *Materials & Design*, 2014. 55, Pp. 387–393. <http://dx.doi.org/10.1016/j.matdes.2013.09.047>
15. Ashish, D.K., Singh, B., Verma, S.K. The effect of attack of chloride and sulphate on ground granulated blast furnace slag concrete. *Advances in Concrete Construction*. 2016. Vol. 4, No. 2. Pp. 107–121 <http://dx.doi.org/10.12989/acc.2016.4.2.107>
16. Dave, N., Misra, A.K., Srivastava, A., Sharma, A.K., Kaushik, S.K. Study on quaternary concrete micro-structure, strength, durability Considering the influence of multi-factors. *Construction and Building Materials*. 2017. 139. Pp. 447–457. <http://dx.doi.org/10.1016/j.conbuildmat.2017.02.06>
17. Makhloufi, Z., Bouziani, T., Hadjoudja, M., Bederina, M. Durability of limestone mortars based on quaternary binders subjected to sulfuric acid using drying immersion cycles. *Const. Build. Mater*. 2014. Pp. 579–588. <http://dx.doi.org/10.1016/j.conbuildmat.07.05017>
18. Osborne, G.J. Durability of Portland blast-furnace slag cement concrete. *Cem Concr Compos*. 1999. 21, Pp.11–21. (98) 00032-8 Osborne GJ. <https://doi.org/10.1016/S0958-9465>
19. Yeau, K., Kim, E. An experimental study on Corrosion resistance of concrete with ground granulated blast-furnace slag. *Cement Concrete Res*. 2005. 35. Pp. 1391–1399. <https://doi.org/10.1016/j.cemconres.11.010>
20. Lurkowski, P., Salih, A. Durability of mortars containing ground granulated blast-furnace slag in acid and sulphate environment. *Procedia Engineering*. 2015. 108. Pp. 47–54.
21. Catalogue Algérien de dimensionnement des chaussées neuves – Fascicule 1», Ministère des travaux publics-direction des routes, Novembre (2001).
22. Neto, A.A.M., Cincotto, M.A., Repette, W. Mechanical properties, drying and autogenous shrinkage of blast furnace slag activated with hydrated lime and gypsum. *Cement & Concrete Composites*. 2010. 32. Pp.312–318. <https://doi.org/10.1016/j.cemconcomp.2010.01.004>
23. Cao, R., Li, B., You, N., Zhang, Y., Zhang, Z. Properties of alkali-activated ground granulated blast furnace slag blended with ferronickel slag. *Construction and Building Materials*. 2018. 192. Pp. 123–132. <https://doi.org/10.1016/j.conbuildmat.2018.10.112>
24. Nguyen, H.-A., Chang, T.-P., Lee, P.-H., Shih, J.-Y. Experimental Investigation of Bond-Slip Performance of Reinforcement in Two Green Concretes. 2020. *Journal of Materials in Civil Engineering*. 32(3). 04020014. DOI: 10.1061/(asce)mt.19435533.0003029.
25. Nguyen, H.A., Chang, T.P., Chen, C.T., Yang, T.R., Nguyen, T.D. Physical-chemical characteristics of an eco-friendly binder using ternary mixture of industrial wastes. *Materiales de Construcción*. 2015. Vol. 65. No. 319. <http://dx.doi.org/10.3989/mc.2015.07414>
26. SETRA-LCPC. GTR. Technical guide for the realization of embankments and layers of form. SETRA-LCPC Editions, Papers I & II. 2000. 98 p. and 102 p.
27. Venkatarama, R.B.V., Ajay, G. Influence of sand grading on the characteristics of mortars and soil–cement block masonry. *Constr. Build. Mater*. 2008. 22 1614–1623. <https://doi.org/10.1016/j.conbuildmat.2007.06.014>
28. Haach, V.G., Vasconcelos, G., Lourenço, P.B. Influence of aggregates grading and water/cement ratio in workability and hardened properties of mortars. *Constr. Build. Mater*. 2011. Vol. 25. Pp.2980–2987. <https://doi.org/10.1016/j.conbuildmat.2010.11.011>
29. Ören, A.H. Estimating compaction parameters of clayey soils from sediment volume test. *Applied Clay Science*. 2014. 101. Pp. 68–72. <https://doi.org/10.1016/j.clay.2014.07.019>
30. AFNOR NF P94-093: Soils: recognition and tests – Determination of the compaction references of a material – Normal Proctor test – Modified Proctor test. October 2014.
31. AFNOR, NF P94-078. Sols: reconnaissance et essais – Indice CBR après Immersion-Indice CBR immédiat-Indice Portant immédiat. (1997).
32. AFNOR NF EN 13286-53. Mélanges traités et mélanges non traités aux liants hydrauliques – Partie 53: méthode de confection par compression axiale des éprouvettes de matériaux traités aux liants hydrauliques. 2005.
33. Daheur, E.G., Goual, I., Taibi, S., Mitiche-Kettab, R. Effect of Dune Sand Incorporation on the Physical and Mechanical Behaviour of Tuff: (Experimental Investigation). *Geotech Geol Eng*. 2019. 37. Pp.1687–1701 <https://doi.org/10.1007/s10706-018-0715-4>
34. AFNOR, NF EN 13286-41. Mélanges traités et mélanges non traités aux liants hydrauliques – Partie 41: méthode d'essai pour la détermination de la résistance à la compression des mélanges traités aux liants hydrauliques. 2003.

35. Gueddouda, M.K., Lamara, M., Abou-bekr, N., Taibi, S. Hydraulic behaviour of dune sand bentonite mixtures under confining stress. *Geomechanics and Engineering*. 2010. 2(3). Pp. 213–227.
36. AFNOR NF P94-074 Sols: Reconnaissance et essais – Essais à l'appareil triaxial de révolution – Essai (UU) non consolidé non drainé – Essai (CU +u) consolidé non drainé avec mesure de pression interstitielle – Essai (CD) consolidé drainé. 1994.

Contacts:

Hayet Cherfa, ha_cherfa@yahoo.fr

Ammar Nechnech, nechnech_a@yahoo.fr

Nacira Saoudi, saoudinacira@gmail.com

Khedidja Ait Mokhtar, k.aitmokhtar@laposte.net



DOI: 10.34910/MCE.108.7

Effect of irregularity on seismic design parameters of RC-infilled structures

M. Shendkar^a , H. Beiraghi^b , S. Mandal^a

^aDepartment of Civil Engineering, Indian Institute of Technology (BHU), India

^bDepartment of Civil Engineering, Mahdshahr Branch, Islamic Azad University, Mahdshahr, Iran

*E-mail: mangesh.shendkar94@gmail.com

Keywords: masonry walls, adaptive pushover analysis, response reduction factor, ductility, irregularity, seismic performance

Abstract. A four-storey reinforced concrete (RC) building is seismically evaluated with the incorporation of different irregularities. Three model systems have been considered, i.e., model I: (RC-infilled regular frame in X and Y direction), model II: (RC-infilled plan irregular frame in X and Y direction), and model III: (RC infilled vertical + plan irregular frame in X and Y direction). Adaptive pushover analyses have been carried out to evaluate the seismic performance of the structure by using seismostruct software incorporating inelastic material behaviour for concrete, steel, and infill walls. Infill walls have been modelled as “double strut nonlinear cyclic models”. The most up-to-date seismic design includes the nonlinearity in the structure through a response reduction factor (R). The ductility reduction factor and overstrength factor are the main components of the response reduction factor. These seismic design parameters were computed from the adaptive pushover analysis, and finally, the response reduction factor has been calculated for all models and compared with the value recommended by IS 1893 part-1 (2016). The result shows that the evaluated R-factors are higher than the value recommended by the BIS code. However, it is observed that R-values are higher than the corresponding values recommended in the BIS code when the irregularity present in the structures.

1. Introduction

Buildings with masonry infill wall RC frames are the most common type of structures used for multistory constructions all over the world. The presence of the infill walls increases the lateral stiffness considerably. Due to the change in stiffness and mass of the structural system, the dynamic characteristics change as well. In several moderate earthquakes, such buildings have shown excellent performance during an earthquake. In the recent era, the earthquake loads imposed in the structure are typically greater than the loads considered in the design. Most of the seismic design codes include the nonlinear response of a structure through a response reduction factor/behavior factor (R). The majority of the structures are designed using the equivalent static method, which is based on the use of the response reduction factor. Different codes and guidelines specify the ‘R’ value for different types of moment-resisting frame structures. However, IS 1893 Part-1: (2016) code does not give any specific explanation on different issues namely, irregularities, structural & geometrical configuration, etc. Thus, the primary focus of the present study is to investigate the actual response reduction factor of regular and irregular structures.

Alghane et al. [1] presented a study about an existing RC building in Madinah that is seismically evaluated with and without an infill wall. Four model systems have been considered i.e. model- I (no infill), model- IIA (strut infill-update from field test), model- IIB (strut infill- ASCE/SEI 41), and model- IIC (strut infill-Soft storey- ASCE/SEI 41). The response modification factor (R) for the 5 story RC building was evaluated from capacity and demand spectra (ATC-40) for the studied models. From this study, the

Shendkar, M., Beiraghi, H., Mandal, S. Effect of irregularity on seismic design parameters of RC-infilled structures. Magazine of Civil Engineering. 2021. 108(8). Article No. 10807. DOI: 10.34910/MCE.108.7

© Shendkar, M., Beiraghi, H., Mandal, S., 2021. Published by Peter the Great St. Petersburg Polytechnic University



This work is licensed under a CC BY-NC 4.0

authors concluded that the R factor increase due to the presence of infill and it satisfy the requirement of the code (SBC 301) but in the case of the bare frame, does not satisfy the requirement of the response modification factor. Chaulagain H. et al. [2] studied the response reduction factor of existing reinforced concrete buildings in Kathmandu valley. They concluded that the calculated R values of the buildings are less than the values given by the BIS code. From the extracted results, the R-value is highly dependent on the "column to beam capacity ratio". Motiani R. et al. [3] worked on the calculation of the response modification factor for realistic RC moment frame buildings by using pushover analysis. In this research study, they modeled 4, 8 & 12 storey reinforced concrete buildings as per guidelines provided by IS 456:(2000). The static pushover analysis has been used in SAP2000 software. From the detailed study, the authors concluded that ultimately response reduction factor decreases with increases in the height of the structure. The value of R is given by IS 1893 (2002) is improperly estimated. The actual value of R is lesser than the values given by BIS code because, irregularity in structure, torsional effect, poor workmanship, etc.

Brahmavathan D. and Arunkumar C. [4] worked on the evaluation of the response reduction factor of irregular i.e., stepped reinforced concrete frames. The stepped building form means the incorporation of vertical irregularity. In this paper, three types of reinforced concrete three-dimensional framed structures having an equal number of bays, but a different number of stories are considered. They modeled 3, 6, and 9 stories for both OMRF and SMRF cases. The non-linear static pushover analysis of the three stepped RC building models was carried out by using SAP 2000 software for both cases. The authors concluded that the actual values of response reduction factor of stepped RC buildings are lesser than the values recommended by the BIS code, the values of R decreases as the storey number increases. Due to vertical irregularity R values decreases significantly so there is a need to consider the irregularity in IS 1893 code and ductility factor depends on the optimum percentage of steel reinforcement beyond its limit range of R values in decreasing trend.

Smyrou et al. [5] described the implementation of the "inelastic infill panel element" for masonry infill panels within a fiber-element-based SeismoStruct program. They assessed analytical results compared with experimentally obtained from the pseudo-dynamic test and also defined characteristic values for material and geometrical properties of infill. Mohamed S. Issa and Heba M. Issa [6] worked on the evaluation behavior factor of reinforced concrete moment resisting frame by using pushover analysis. According to the researcher's statement, nonlinear dynamic analysis consumes more time and it's a complex process but pushover analysis is the more popular and simple method to calculate the behavior factor. In this research three different RC frames were studied i.e., 3 storey, 5 storey and 7 storey RC frame with each of four different bays like 2 bays, 3bays, 4 bays, and 5 bays, and static pushover analysis have been performed in the SesimoStruct program. From the effective study, the authors concluded that Static pushover analysis is an efficient and practical method to study the nonlinear behavior of RC structures as compared to other methods. As the height of the structure increases the behavior factor decreases. The most suitable method to calculate the behavior factor is Uang 1991.

Many researchers did work on this important response reduction factor of the different RC frames. From the analytical study, the value of R is more when the infill is considered in the frame so the R-value is sensitive to the material & geometrical configuration of the structure. Also, the evaluated values of R for the bare frames are lesser than the recommended value by the BIS code. The R-factor significantly decreases by considering the opening in masonry infills, the height of the structure increases, and as the seismic zone increases. The evaluated R-factor based on the "Miranda & Bertero relationship (1994) is the most realistic as compared to other methods [7–18]. In strong earthquakes, the structures experience nonlinear behavior [19, 20].

In this study, the following principal objectives are adopted.

1. To evaluate the actual response reduction factor of RC-infilled regular and irregular frames.
2. To compare the response reduction factor of different RC-infilled frames with the values recommended by the BIS code.

List of abbreviations:

R is the response reduction factor;

R_d is the ductility reduction factor;

R_o is the Overstrength factor;

R_R is the redundancy factor;

V_d is the design base shear;

V_y is the ideal yield base shear;

Δ_{\max} is maximum displacement;

Δ_y is the yield displacement;

μ is the ductility;

X_{oi} is the horizontal offsets;

Y_{oi} is the vertical offsets;

d_m is the diagonal strut length;

λ_h is the dimensionless parameter;

h_z is the equivalent contact length.

2. Methodology

2.1. Adaptive pushover analysis

This is the advanced version of pushover analysis in which the applied load is updated at every single step of analysis. Researchers (Kalkan & Kunnath [21] and Gupta & Kunnath [22]) proposed to consider higher mode effects in the seismic analysis. So this adaptive pushover analysis considers the variation of dynamic properties & the applied load is updated with respect to input ground motion. In this advanced pushover method, the spectral amplification part is used for updating the load vectors. In the present study, the accelerogram time-history of the IS 1893 response spectrum & Chi-Chi earthquake have been considered for spectral amplification as shown in Fig. 1 and Fig. 2 respectively. Source: Pacific Earthquake Engineering Research Center (PEER) Strong Motion Database.

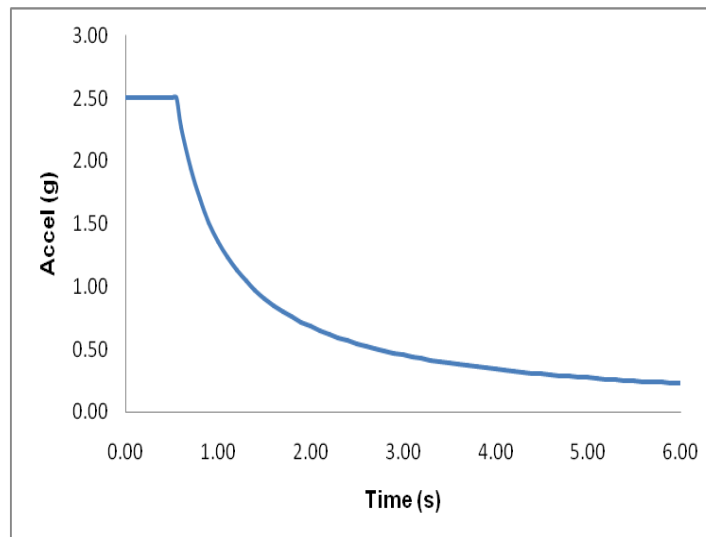


Figure 1. IS: 1893 Response Spectrum Curve.

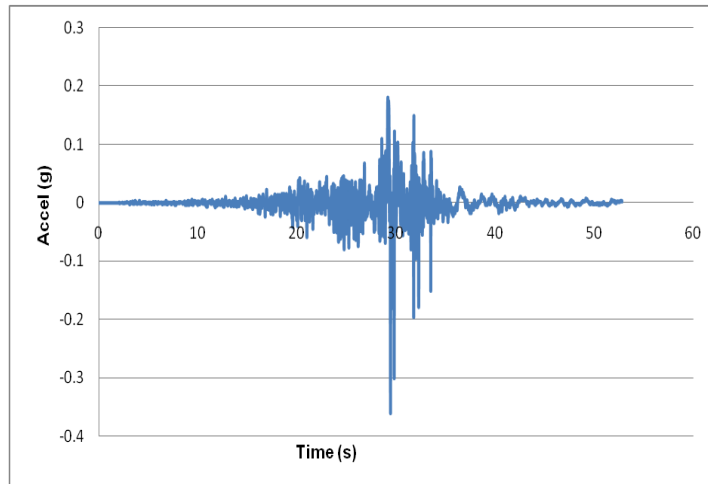


Figure 2. Chi-Chi Earthquake (date: 20 September 1999).

2.2. Response reduction factor

The response reduction factor is defined as the ratio of elastic strength to inelastic design strength. In other word, R-factor is the seismic design tool which shows the level of non-linearity in the structure. The recommended values of response reduction factor by IS: 1893 (Part-1) – 2016 as shown in Table 1. According to ATC-19 [23] the parameters related to the R factor can be mathematically expressed as:

$$R = R_d \times R_o \times R_R, (1)$$

where, R is the Response reduction factor, R_d is the ductility reduction factor, R_o is the overstrength factor and R_R is redundancy. But according to Indian seismic code provision, the response reduction factor can be presented as shown in Fig. 3 and mathematically expressed in equation- 2 [2,9,14].

$$2R = R_d \times R_o. (2)$$

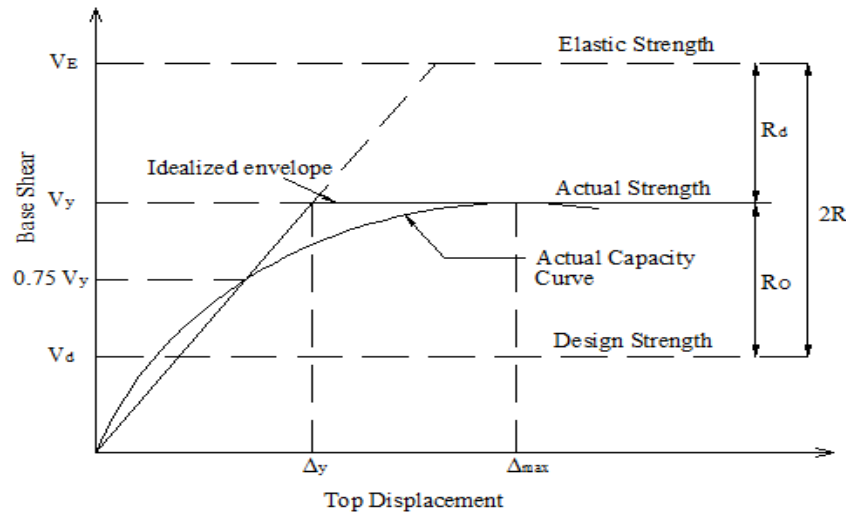


Figure 3. Relationship between Response reduction factor (R), over-strength factor (R_o), and ductility reduction factor (R_d).

Here the ductility is the ratio of maximum displacement (Δ_{max}) to the yield displacement (Δ_y) and it has been calculated based on the reduced stiffness method [24, 25]. The ductility reduction factor has been calculated based on the expressions of Newmark and Hall (1982) [26]. The overstrength factor is the ratio of the ideal yield base shear (V_y) to design base shear (V_d). In this study, redundancy is incorporated into the overstrength factor.

Table 1. Recommended values of Response reduction factor by IS: 1893 (Part-1) – 2016 [27].

Frame System	Response Reduction Factor
Ordinary moment-resisting frame	3
Special moment-resisting frame	5

3. Results and Discussion

3.1. Model Description

In this study, three-dimensional 4-storey building with 3 bay frames in both directions i.e., X and Y direction. Models are studied for regular and irregular structures with considered openings in masonry infill. The buildings are designed for seismic zone 'IV' and it has been modeled in SeismoStruct software as follows:

1. RC-infilled regular frame in X and Y direction;
2. RC-infilled plan irregular frame in X and Y direction;
3. RC infilled vertical + plan irregular frame in X and Y direction.

The plan of the building is shown in Fig. 4 and Fig. 5 shows the models of the building. Material and sectional properties are as shown in Table 2. Column & beam dimensions have shown in Table 3, 4.

These special moment resisting frames are rigidly connected at beam-column junction. Also foundation of the structure assumed as a rigid connection in the present study.

The total seismic weight of the three models has been calculated manually as per the BIS code and the design base shear has also been evaluated according to IS 1893 Part-1:2016 as:

$$V_b = \frac{Z}{2} \frac{I}{R} \frac{S_a}{g} \times W, \quad (3)$$

where V_b is the design base shear, Z is the seismic zone factor, I is the importance factor, $\frac{S_a}{g}$ is the design acceleration coefficient, W is the seismic weight of the structure.

The seismic weight of the RC-infilled regular frame is 9617.77 kN. Similarly, the seismic weight of the RC-infilled plan irregular frame and RC infilled vertical + plan irregular frame is 7898.88 kN & 6041.25 kN respectively.

The time period of building with masonry infill is $\frac{0.09 \times h}{\sqrt{d}}$ as per IS 1893 Part-1:2016 (4)

Where, h is the height of building, and d is the base dimension of the building in the direction earthquake shaking.

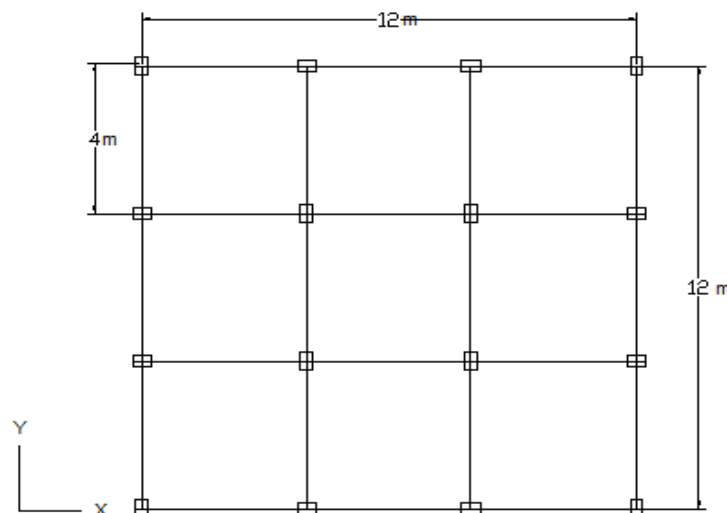


Figure 4. a – Regular Plan of the building.

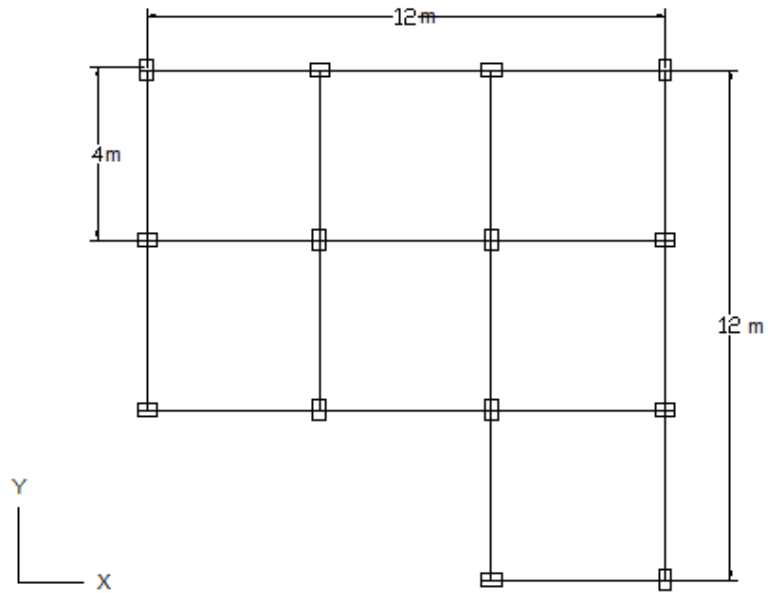


Figure 4.b – Irregular Plan of the building.

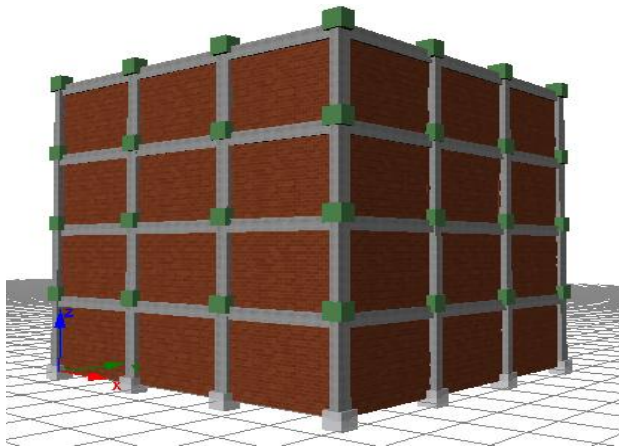


Figure 5.a – RC-infilled regular frame.

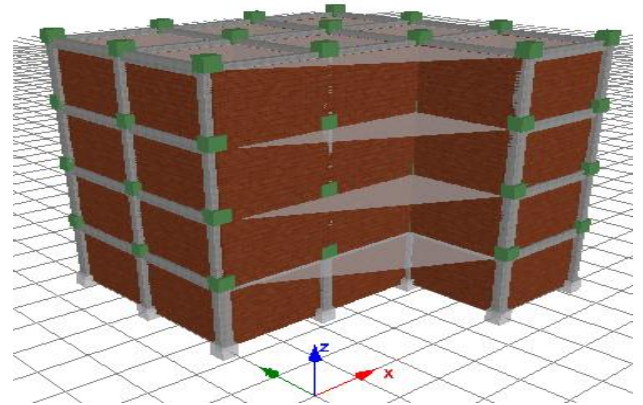


Figure 5.b – RC-infilled plan irregular frame.

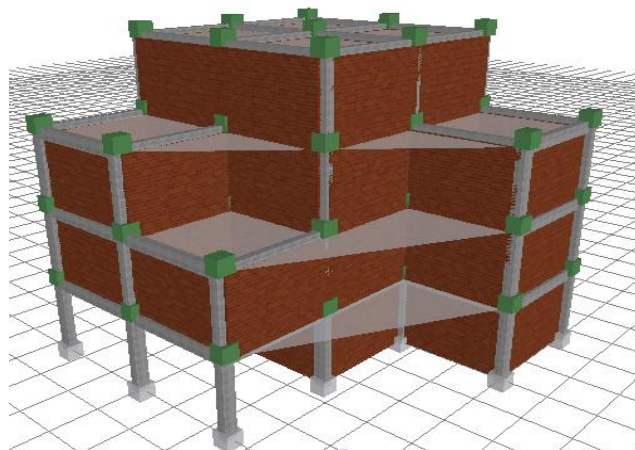


Figure 5.c – RC infilled vertical + plan irregular frame.

Table 2. Structural details of building.

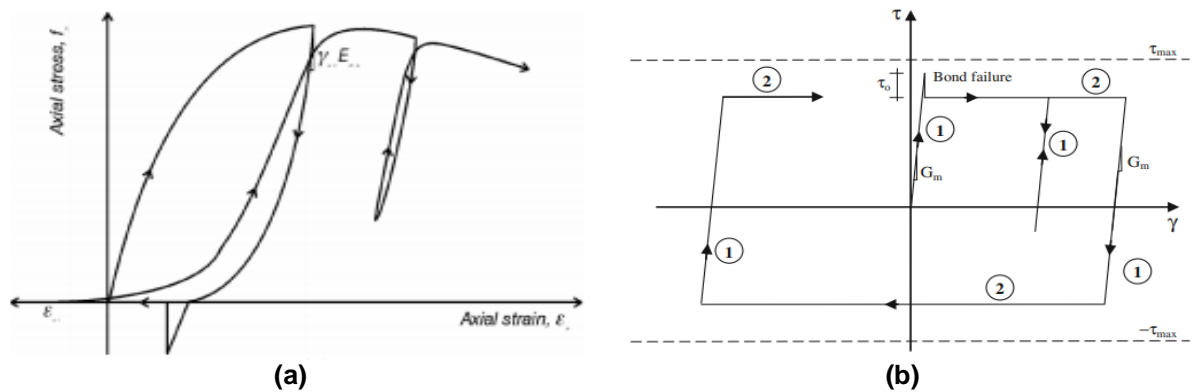
Frame structure	Special moment-resisting frame
Number of storey	4
Seismic zone	IV
Floor Height	3 m
Bay length	4 m in both direction
Infill wall	230 mm
Comp. strength of masonry	3 MPa
Modulus of Elasticity of masonry	1650 MPa
Width of a strut with the opening in infill	262 mm
Area of strut	60,260 sq. mm
Equivalent contact length (hz)	20.37 %
Horizontal offset (X_o)	5.62 %
Vertical offset (Y_o)	7.5 %
Type of soil	Medium stiff soil
Column size (mm)	300 X 450
Beam size (mm)	250 X 450
Slab Depth (mm)	150
Live load (kN/m^2)	3
Material	M -25 grade concrete and Fe-415 reinforcement
Damping	5 %
Importance factor	1.2

3.2. Inelastic Infill Panel Element (infill)

Each infill panel element is represented by four axial struts and two shear springs, as shown in Fig. 6. "Double strut nonlinear cyclic model" was developed by the Crisafulli (1997) [28]. It accounts for separately compressive and shears behavior of masonry and adequately represents the hysteretic response. The presence of an opening in infill will directly affect the seismic performance of the structures; the effect can be incorporated by minimizing the width (diagonal strut).

$$W_{do} = (1 - 2.5A_r) \cdot X \cdot W_d, \quad (5)$$

Where W_{do} is the width of the diagonal strut with an opening in infill, W_d the width of the diagonal strut, and A_r is the ratio of opening area to face area of infill. The Eq. 5 is valid for openings in walls ranging from 5 % to 40 % [8]. In this paper, the opening size in infill is considered as 2.44 sq. m, this implies that approximately 20 % opening area is considered in the infill.



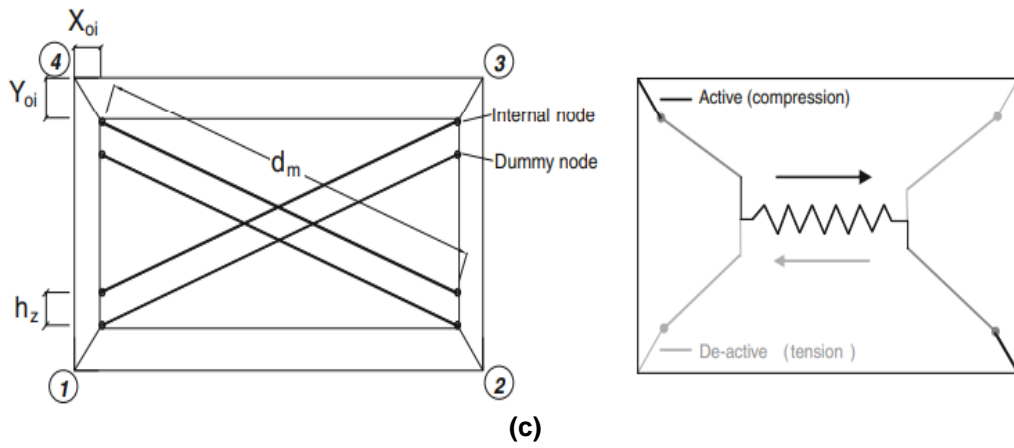


Figure 6.(a) Masonry strut hysteresis, (b) Shear cyclic relationship, and (c) Infill panel element configuration [28, 29].

Here, X_{oi} and Y_{oi} represent horizontal and vertical offsets respectively, d_m is the diagonal strut length, and h_z is the equivalent contact length.

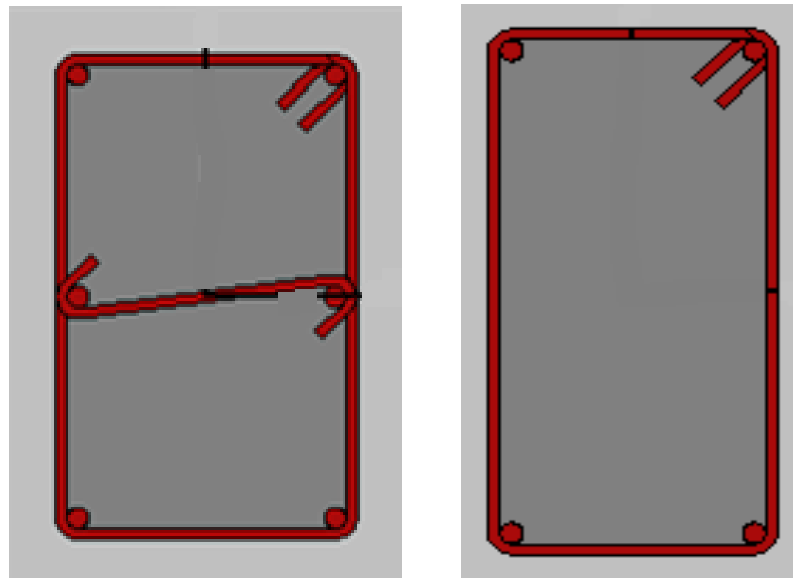


Figure 7.a Column Detailing.

Figure 7.b Beam Detailing.

Table 3. Column dimensions and detailing.

Column	Size(mm)	Main Reinforcement	Shear Reinforcement
All columns of the building	300 × 450	4 nos. of 16 mm dia. at the corner and two nos. of 16 mm on the longer side.	8 mm Dia. @ 100 mm c/c

Table 4. Beam dimensions and detailing.

Beam	Size(mm)	Main Reinforcement	Shear Reinforcement
All beams of the building	250 × 450	2 nos. of 16 mm diameter @ top as well as the bottom	8 mmDia. @ 100 mm c/c

3.3. Verification of masonry infill through experimental and analytical by pseudo-dynamic loading

This example describes the modeling of a full-scale, four-storey building, which was designed according to initial versions of Eurocode 8 (CEN, 1995) and Eurocode 2 (CEN, 1991). The structure was tested at the ELSA laboratory under pseudo-dynamic loading using an artificial accelerogram derived from the 1976 Friuli earthquake.

The analytical results, obtained with the FE analysis program SeismoStruct, are compared with the experimental results.



Figure 8. Four-storey 3D infilled frame tested by Negro et al. (1996) [29].

Structural Geometry: The model consists of eight (exterior) RC columns (0.4×0.4 m), one (interior) RC column (0.45×0.45), T-section RC beams with different dimensions and infill panels.

Material Properties: The Mander et al. concrete model is employed for defining the concrete material used for columns and beams. Menegotto-Pinto steel model is employed for defining the steel material with the following properties: $E_s = 200000000$ kPa; $f_y = 555000$ kPa, $\mu = 0.02$.

3.4. Modeling and Loading

The RC columns and beams are modeled through 3D force-based inelastic frame elements (infrmFB) with 4 integration sections. The number of fibers used in section equilibrium computations is set to 200. The infill panels are modeled through a four-node masonry panel element (inelastic infill panel element).

In order to run a nonlinear static time-history analysis, four time-history curves (one for each floor) are loaded in the time-history curves.

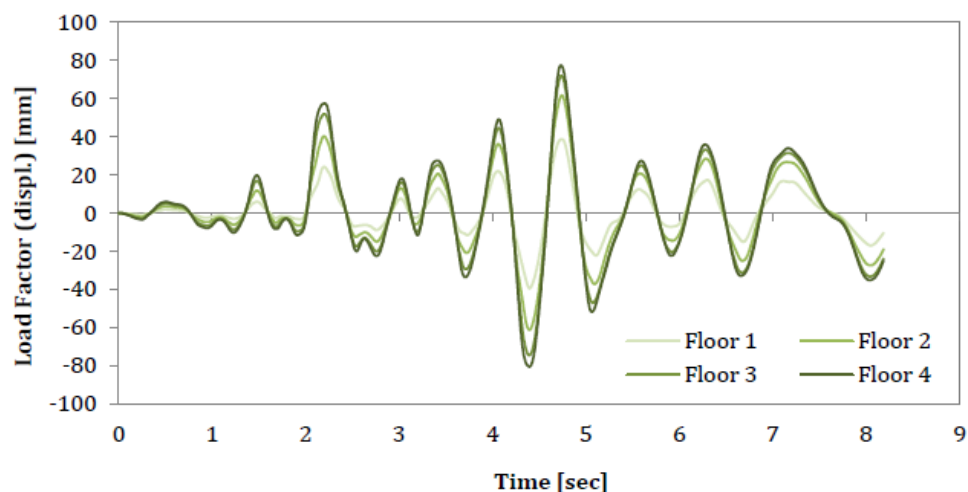


Figure 9. Artificial record generated from Friuli accelerogram – displacement histories.

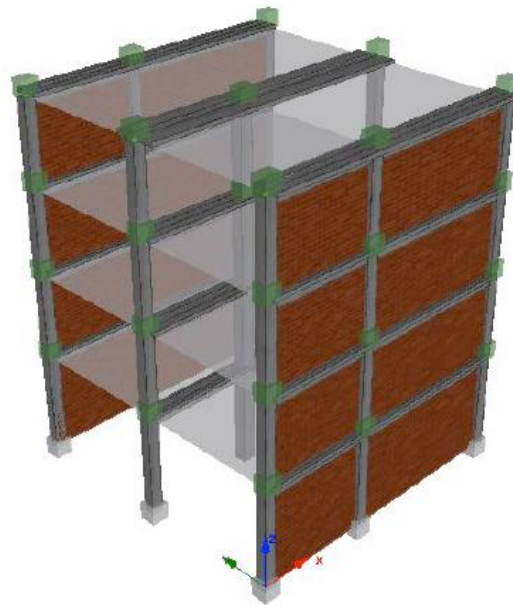


Figure 10. Model of building.

3.5. Results comparison

The comparison between experimental and analytical results is shown Fig. 11.

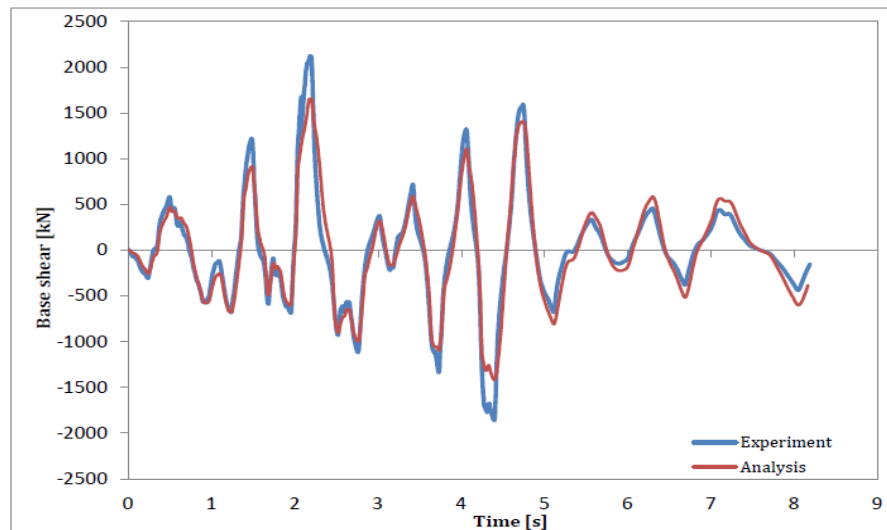


Figure 11. Experimental vs. Analytical results.

3.6. Pushover Curves

The several seismic design parameters namely; strength, ductility, response reduction factor, etc. are evaluated from pushover curves. The significance of masonry infills which play an important role in the RC frame has been quantified. These pushover curves are as shown in Fig.12.

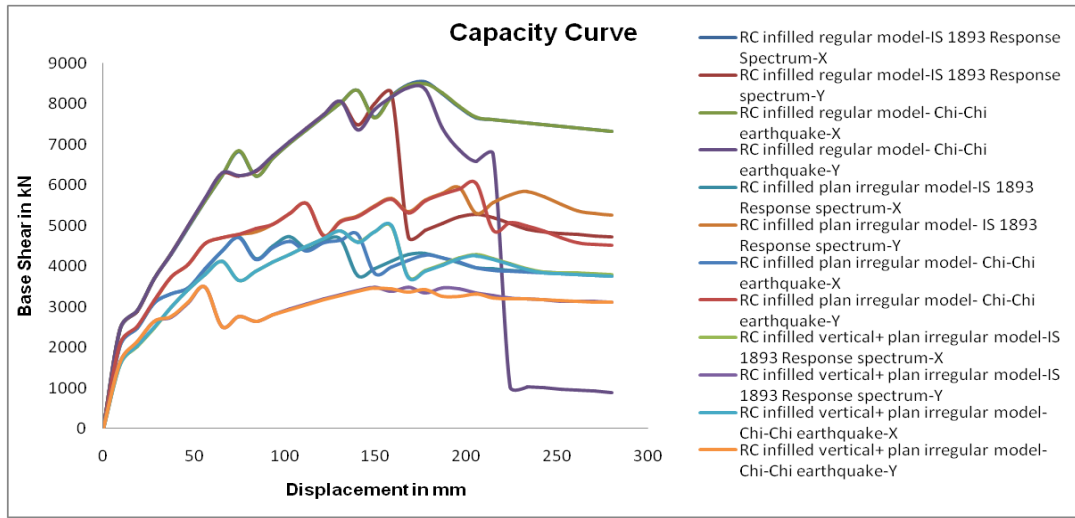


Figure 12. Comparisons of Pushover Curves.

3.7. Base Shear

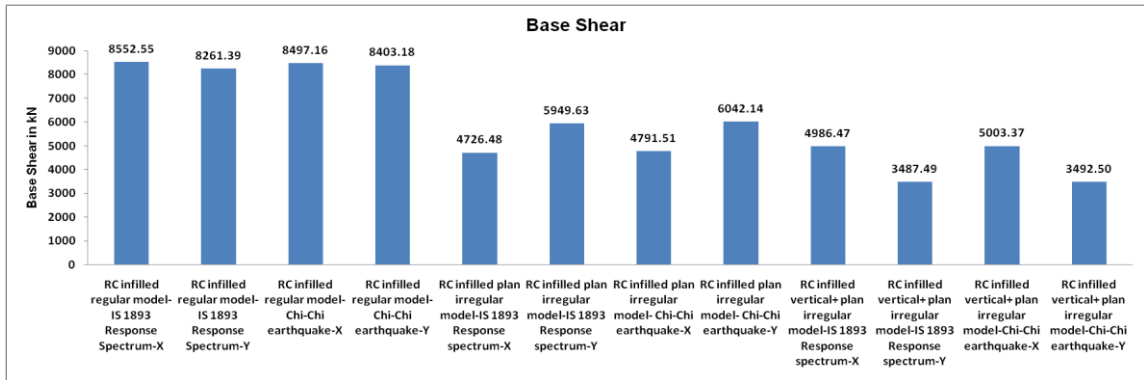


Figure 13. Comparison of Base Shear.

As per the Fig. 13, base shear is lower in RC-infilled vertical +plan irregular frame as compared to other frames. Averagely 25.98 % and 27.51 % base shear increases in RC-infilled plan irregular frame as compared to RC-infilled vertical + plan irregular frame for IS-1893 response spectrum and Chi-Chi earthquake respectively. In the case of RC-infilled regular frame in x and y direction, there is a small variation of base shear due to more symmetry as compared to others. The base shear is more in RC-infilled regular frame as compared to other irregular frames due to the presence of regularity in the structure.

3.8. Ductility

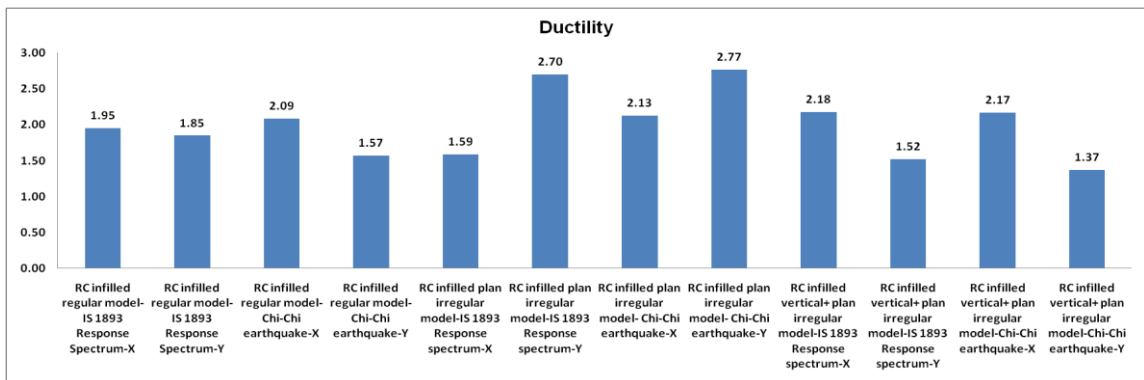


Figure 14. Comparison of Ductility.

As per the Fig. 14, the average ductility obtained is higher in RC-infilled plan irregular frame as compared to other frames. Averagely 12.63 % and 33.87 % ductility increases in RC-infilled plan irregular frame as compared to RC-infilled regular frame for IS-1893 response spectrum and Chi-Chi earthquake

respectively. In the case of both irregular frames, there is an average variation of ductility by 15.67 % and 38.41 % for IS-1893 response spectrum and Chi-Chi earthquake respectively.

3.9. Ductility Reduction Factor

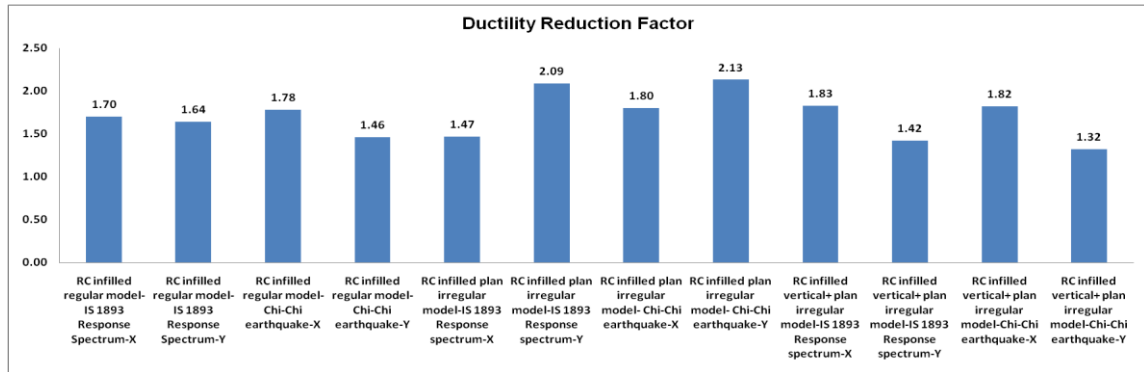


Figure 15. Comparison of Ductility Reduction Factor.

The ductility reduction factor is evaluated based on the “Newmark & Hall” theory. As per the Fig. 15, averagely 6.58 % and 20.98 % ductility reduction factor increases in RC-infilled plan irregular frame as compared to the RC-infilled regular frame for IS-1893 response spectrum and Chi-Chi earthquake respectively. In the case of both irregular frames, there is an average variation of ductility reduction factor by 9.53 % and 24.84 % for IS-1893 response spectrum and Chi-Chi earthquake respectively.

3.10. Overstrength Factor

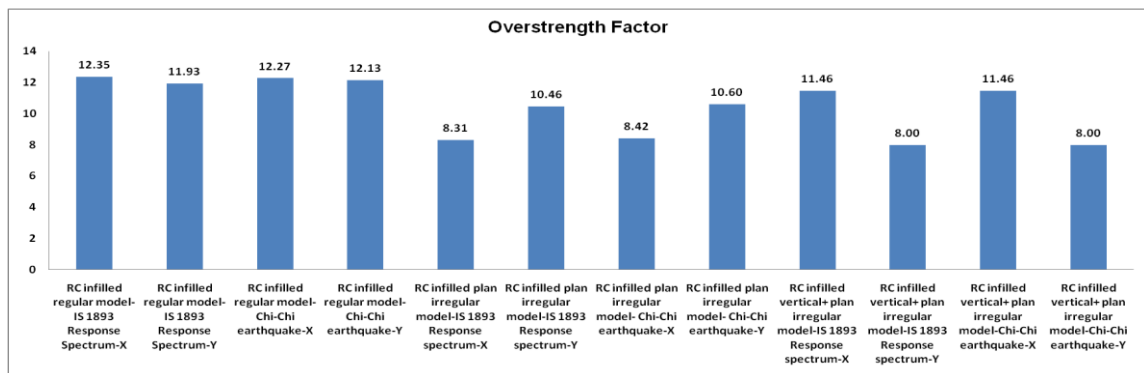


Figure 16. Comparison of Overstrength Factor.

As per the Fig. 16, the overstrength factor is higher in the RC-infilled regular frame as compared to other frames due to less irregularity. Averagely 24.76 % and 25.38 % overstrength factor increases in RC-infilled regular frame as compared to RC-infilled vertical + plan irregular frame for IS-1893 response spectrum and Chi-Chi earthquake respectively. In the case of irregular frames, there is an average variation of overstrength factor by 3.73 % and 2.31 % for IS-1893 response spectrum and Chi-Chi earthquake respectively.

3.11. Response Reduction Factor

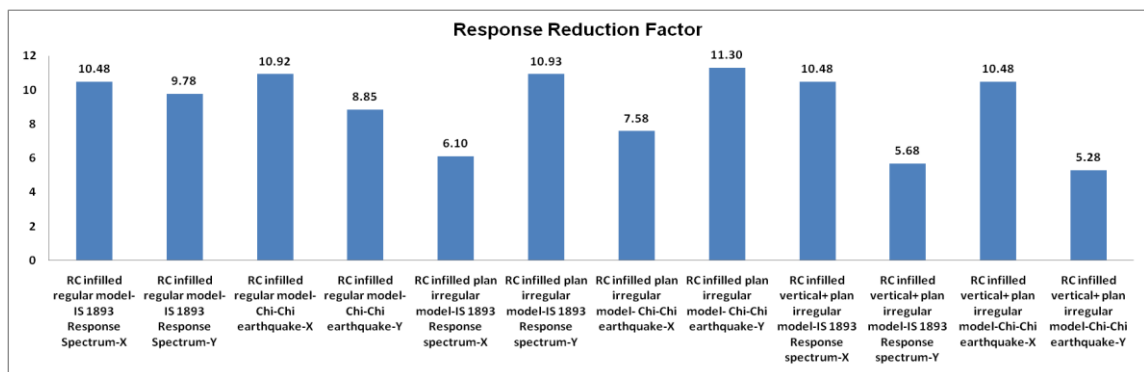


Figure 17. Comparison of Response Reduction Factor.

Using Equation (2) the R factor has been evaluated. As per Fig. 17, the response reduction factor is higher in the RC-infilled regular frame as compared to other frames similar to the overstrength factor. Averagely 25.37 % and 25.38 % R- factor increases in RC-infilled regular frame as compared to RC-infilled vertical + plan irregular frame for IS-1893 response spectrum and Chi-Chi earthquake respectively. In the case of irregular frames, there is an average variation of R-factor by 5.32 % and 19.79 % for IS-1893 response spectrum and Chi-Chi earthquake respectively. Similarly, Alguhane T.M. et al. [1] presented the study about an existing RC building (irregular in plan and elevation) in Madinah city that is seismically evaluated with and without an infill wall. In which the response reduction factor of the bare frame is lesser than the specified code value (R-value- 2.5, Ω factor-3 according to Saudi Building Code SBC 301) by 18.4 %. However, including an infill wall in the frame system, increase the value of the response modification factor (4.55) by 82 % and Over-strength factor (4.55) by 51.66 % as compared to specific code value i.e., satisfying the code requirements.

4. Conclusions

After the interpretation of analytical results and comparison of values, the conclusions drawn from this study are as summarized below:

1. The base shear values are larger in regular RC-infilled frames as compared to other irregular frames.
2. Average ductility and ductility reduction factor are higher in RC-infilled plan irregular frame as compared to other frames because there is no infill and structural members in some part of the frames, so it allows higher drift.
3. The over-strength factor is significantly influenced by the redundancy of the frame. Also, as a result of it, the response reduction factor of the RC-infilled regular frame is higher than the other irregular frames.
4. The computed values of 'R' for regular and irregular RC-infilled frames evaluated by adaptive pushover analysis are more than the value suggested by the BIS code. To note, after the incorporation of different irregularities in the frames the computed values of 'R' also are more than the values given by BIS code, because, infill plays an important role to maintain the overall structural integrity of the frames.
5. As per the present study, in the case of both irregular frames, the R-factor is more influenced by the ductility reduction factor as compared to the overstrength factor due to maximum variation in the ductility & ductility reduction factor.
6. Generally, the R-factor indirectly depends on the redundancy of structure. In the case of irregular frames, R-factor is less in RC-infilled vertical + plan irregular frame as compared to RC-infilled plan irregular frame due to less redundancy.
7. According to the present study, the evaluated response reduction factor (R) of different RC-infilled frames is more as compared to the value given by BIS code.
8. As per the present study, R-factor is sensitive to material, geometrical & structural configuration of the structure.

References

1. Alguhane, T.M., Ayman H.K., Fayed, M.N., Ismail, A.M. Seismic assessment of old existing RC buildings with masonry infill in Madinah as per ASCE. International Journal of Civil, Environmental, Structural, Construction, and Architectural Engineering. 2015. 9 (1). Pp.52–63.
2. Chaulagain, H., Rodrigues, H., Spacone, E., Guragain, R., Mallik, R., Varum, H. Response reduction factor of irregular RC buildings in Kathmandu valley. Earthquake engineering and engineering vibration. 2014.13. Pp. 455–470. <https://doi.org/10.1007/s11803-014-0255-8>
3. Motiani, R., Kunal, J.R., Gahrana, S., Nambiar, A., Desai, M. Evaluation of response reduction factor by pushover analysis. Int. J. Structural Engineering. 2018.9(2). Pp. 116–129.
4. Brahmavathan, D., Arunkumar, C. Evaluation of response reduction factor of irregular reinforced concrete framed structures. Indian Journal of Science and Technology.2016.9(23).DOI: 10.17485/ijst/2016/v9i23/95981
5. Smyrou, E., Blandon, C., Antoniou, S., Pinho, R., Crisafulli, F. Implementation and verification of a masonry panel model for nonlinear dynamic analysis of infilled RC frames. Bulletin of Earthquake Engineering. 2011. 9. Pp. 1519–1534. DOI: <https://doi.org/10.1007/s10518-011-9262-6>
6. Mohamed, S.I., Heba, M.I. Application of Pushover Analysis for the calculation of Behavior Factor for Reinforced Concrete Moment-Resisting Frames. International Journal of Civil and Structural Engineering. 2015.5(3). Pp.216–226. DOI: 10.6088/ijcser.2014050021
7. Goud, S.S., Pradeep kumar, R. Rationalizing Response Reduction Factor (R) for better Performance of Reinforced Concrete Framed Buildings. National Conference on Recent Research Advances in Civil Engineering, Tamilnadu, India, 2014. <https://www.researchgate.net/publication/268805699>

8. Shendkar, M., Pradeep Kumar, R. Influence of opening in infill on R factor of RC infilled frame structures. Indian Concrete Institute Journal. 2018.October-December 2018. Pp. 1–6.
9. Shendkar, M.R., Mandal, S., Pradeep Kumar, R. Effect of lintel beam on response reduction factor of RC-infilled frames. Current Science. 2020.118(7). Pp. 1077–1086. DOI:10.18520/cs/v118/i7/1077-1086
10. Mandal, S., Shendkar, M.R. Evaluation of response reduction factor of RC-infilled frames. 17th World Conference on Earthquake Engineering.17WCEE Sendai. Japan, 2020. Pp. 1–12.
11. Shendkar, M., Pradeep Kumar, R. Response Reduction Factor of RC framed structures with Semi-interlocked masonry and Unreinforced masonry infill. Indian Concrete Institute (ICI) Journal. 2018. Jan-Mar 2018.Pp. 24–28.
12. Shendkar, M., Mandal, S., Pradeep Kumar, R., Maiti, P.R. Response Reduction Factor of RC-infilled frames by using different methods. Indian Concrete Institute (ICI) Journal. 2020. April-June 2020.Pp.14–23.
13. Shendkar, M.R., Pradeep Kumar, R., Maiti, P.R. Effect of aspect ratio on response reduction factor of RC framed structures with semi-interlocked masonry and unreinforced masonry infill.The Indian Concrete Journal.2020.94(12). Pp.7–16.
14. Shendkar, M.R., Kontoni, D.-P.N., Mandal, S., Maiti, P.R., Gautam, D. Effect of lintel beam on seismic response of reinforced concrete buildings with semi-Interlocked and unreinforced Brick Masonry Infills. Infrastructures. 2021.6(6). Pp.1–18. <https://doi.org/10.3390/infrastructures6010006>
15. Nishanth, M., Visuvasam, J., Simon, J., Packiaraj, J.S. Assessment of seismic response reduction factor for moment-resisting RC frames. IOP Conf. Series: Materials Science and Engineering.2017. Pp. 1–11. <https://doi:10.1088/1757-899X/263/3/03-2034>
16. Mwafy, A.M., Elnashai, A.S. Calibration of Force Reduction Factors of RC buildings. Journal of Earthquake Engineering.2002.6(2). Pp. 239–273. <https://doi.org/10.1080/13632460209350416>
17. Maheri, M.R., Akbari, R. Seismic behaviour factor, R, for steel X-braced and knee-braced RC buildings. Eng. Struct. 2003.25. Pp.1505–1513.
18. Chaulagain, H., Guragain, R., Mallik, R.K. Assessment of response reduction factor of RC buildings in Kathmandu valley using nonlinear pushover analysis. ME thesis. Purbanchal University. Nepal, 2010.
19. Beiraghi, H. Earthquake effect on the concrete walls with shape memory alloy reinforcement. Smart Structures and Systems. 2019. 24(4). Pp. 491–506.
20. Beiraghi, H. Fragility assessment of shear walls coupled with buckling restrained braces subjected to near-field earthquakes. Steel and Composite Structures. 2019.33(3). Pp. 389–402.
21. Kalkan, E., Kunnath, S.K. Adaptive modal combination procedure for nonlinear static analysis of building structures. Journal of Structural Engineering ASCE.2006.132(11). Pp.1721–1731. [https://doi.org/10.1061/\(ASCE\)0733-9445\(2006\)132:11\(1721\)](https://doi.org/10.1061/(ASCE)0733-9445(2006)132:11(1721))
22. Gupta, B., Kunnath, S.K. Adaptive spectra-based pushover procedure for seismic evaluation of structures. Earthquake Spectra. 2000.16(2). Pp.367–391.<https://doi.org/10.1193/1.1586117>
23. ATC 19 Seismic response modification factors. Applied Technical Council. California Seismic Safety Commission. Redwood City. California, 1995.
24. Park, R. Ductility evaluation from laboratory and analytical testing. Proceedings of the 9th World Conference on Earthquake Engineering. University of Tokyo. Japan, 1988. Pp.605–616.
25. Pauley, T., Priestley, M.J.N. Seismic design of reinforced concrete masonry buildings. Wiley Interscience. New York. USA, 1992.
26. Uang, C.M. Establishing R and Cd Factors for Building Seismic Provisions. Journal of Structural Engineering ASCE.1991.117(1). Pp. 19–28. DOI: [https://doi.org/10.1061/\(ASCE\)0733-9445\(1991\)117:1\(19\)](https://doi.org/10.1061/(ASCE)0733-9445(1991)117:1(19))
27. IS 1893 Criteria for Earthquake Resistant Design of Structures-Part-1 General Provisions and Buildings (sixth Revision).Bureau of Indian Standards.New Delhi, 2016.
28. Crisafulli, F.J. Seismic behavior of reinforced concrete structures with masonry infills (Doctoral Thesis) University of Canterbury. New Zealand, 1997.<https://ir.canterbury.ac.nz/handle/10092/1221>
29. Seismosoft-Seismostruct, A computer program for static and dynamic nonlinear analysis of framed structure,seismostruct user manual.2020.<http://www.seismosoft.com>: SeismoSoft

Contacts:

Mangeshkumar Shendkar, mangesh.shendkar94@gmail.com

Hamid Beiraghi, h.beiraghi@msh-iau.ac.ir

Sasankasekhar Mandal, smandal.civ@itbhu.ac.in



DOI: 10.34910/MCE.108.8

Behavior of CFT steel columns damaged by thermal shock

R. Al-Rousan 

Jordan University of Science and Technology, Irbid, Jordan

E-mail: rzalrousan@just.edu.jo

Keywords: cyclic lateral loads, fiber reinforced polymer, nonlinear, finite element analysis

Abstract. Experimental evaluation of the structural behavior of concrete-filled tubular (CFT) circular steel columns under the combined effects of axial and cyclic lateral loads is costly and challenging. Therefore, this study provides a nonlinear finite element analysis (NLFEA) of fourteen models for thermal shock damaged CFT circular steel columns wrapped with various layers of carbon fiber reinforced polymer (CFRP) composites at its end region, which represents the critical location in terms of the lateral load capacity. Firstly, the column axial load was applied as the first loading step, and then the horizontal load was applied at the top of the column as displacement-controlled loading to guarantee the descending part of the load-displacement behavior. The intent is to confine the column end to avoid outward local buckling of the CFT column and thus developing high strength, larger net drift and more energy dissipation. The NLFEA models were properly calibrated and validated with reputable experimental results, followed by conducting a parametric study to assess the influence of the number of CFRP layers and the impact of thermal shock on the CFT circular steel column performance. For the modeled CFT circular steel column, the use of five to ten layers of CFRP composites resulted in a significant performance enhancement. However, the performance enhancements using 9 and 10 CFRP layers were comparable with 8 CFRP layers. In addition, it was found that the column axial load level significantly affects the CFT circular steel column behavior under lateral loading; better behavior as the axial load level increased. Strengthening of any CFT circular steel column must be optimized through proper NLFEA modeling and the findings of this study represent useful guidelines and methodology for the similar strengthening of CFT steel columns damaged by thermal shock.

1. Introduction

In the outward direction, the local buckling has been a source of disturbance for practitioners in the field of concrete-filled tubular (CFT) steel columns. In addition, such columns are always exposed, aside from the axial load, to seismic forces and/or sideways winds, resulting in generating moments close to the columns' ends, in particular. That makes that region- the columns end- a risky one. Therefore, it is essential to design highly-ductile, resistant-to-moment columns, able to in a way that is capable of undergoing lateral, plastic deformation. Several researchers have investigated the performance of the steel CFT columns [1–2].

Overloading structures and exceeding their ultimate loads, such as heavy trafficking on a bridge or increasing the number of stories in a building, necessitates the structural elements to be reinforced and repaired. To resolve the issue of overloading, the structural elements can be either reconstructed or retrofitted, aiming to enhance the element's load capacity. However, the reconstruction process is not so preferable because it is time-consuming and costly; this process may harm the nearby elements when knocking down a structure due to the generated vibratory force. In contrast, the retrofitting process saves time and more cost-effective, particularly for real old buildings. In some countries, such as India, the design of most of the buildings does not abide by the standard seismic codes; therefore, such structures cannot withstand strong earth shakes. So, these structures need to be retrofitted to increase their seismic capacity.

Al-Rousan, R. Behavior of CFT steel columns damaged by thermal shock. Magazine of Civil Engineering. 2021. 108(8). Article No. 10808. DOI: 10.34910/MCE.108.8

© Al-Rousan, R., 2021. Published by Peter the Great St. Petersburg Polytechnic University



This work is licensed under a CC BY-NC 4.0

There are many retrofitting columns; the steel and concrete jacketing and the fiber-reinforced polymer (FRP). The FRP has been widely adopted worldwide because high in tensile capacity, not costly, non-corrosive, and easy to shape and erect. There are many types of FRP materials available, namely: carbon fiber-reinforced polymers (CFRP), glass fiber, reinforced polymer (GFRP), and aramid fiber-reinforced polymer (AFRP). However, the FRP materials have a setback; as its mode of failure is de-bonding, the FRP-concrete bond is sudden and brittle. A number of studies related to this field were conducted to investigate the reinforced concrete (RC) columns' performance when they were subjected to loads, concentrically and eccentrically [3]. It has been found that it is urgent to strengthen the damaged and deteriorated RC columns due to the additional loads from earthquakes and other environmental situations. The techniques of steel plate jackets and the RC jackets have been broadly used in strengthening the RC columns. However, it has been observed that these techniques have several problems: they are time consumers because of the slowness of the curing; they are material consumers because they require the columns to be bigger, in addition to the material characteristics. To avoid such obstacles, a new method was introduced at the beginning of the eighties of the last decade, which was to externally confine the concrete columns with wraps of CFRP composite material. This technique has improved the strengthened columns' ductility and load capacity because the CFRP materials are: cost-effective, time-saving, easy to shape and erect, non-corrosive, and have an ultra-strength-to-weight ratio. To find a way to strengthen the CFT columns further and avoid the outward local buckling, Alrousan et al. [4] suggested to confine the ends of the columns with FRP. Furthermore, confining the ends of columns has enhanced the performance quality of the internal concrete, particularly in the ends at which high stresses develop [4–6]. The method of confining the CFT steel columns with FRP has been the focus of a number of experimental and investigatory researches [7–13]. Among those, they were investigating the behavior of circular CFT columns, confined with glass FRP, when exposed to 1) axial compression with the monotonic application [6], and 2) cyclic axial compression [14, 15]. On the other hand, very few researches have been showing to investigate the seismic behavior of FRP confined CFT steel columns [7, 8, 11]. These studies showed a remarkable enhancement in the circular-shaped and square-shaped CFT steel columns' behavior quality when confined with FRP.

It is common knowledge that the RC elements are subjected to severe harms or damages when encountering very high temperatures. RC beams, for instance, when RC beams are exposed to excessive degrees of temperatures beyond 250 °C, the concrete's and the steel's mechanical characteristics will be altered, causing stresses to be redistributed; In consequence, their stiffness and toughness are lessened, and they will suffer big deformations, permanently [16, 17]. At present, the CFRP sheets are being widely utilized to rehabilitate the heat-damaged RC beams. That is because these sheets are non-corrosive, time-saving, cost-effective, easy to shape, very applicable, and simple to install on the structural elements. Several studies stated that the heat-damaged beams could- to an extent- re-gain their flexural capacity and improve their behavior when they were bonded, from the external side, with sheets of CFRP. Nevertheless, this is governed by a number of factors, namely: the element's resistivity to fire [18], the structure's ability to withstand very high temperatures [19, 20], the type of fiber used [21–24], the type of analysis [25–29], the energy integrity resistance [30], the utilized method of anchoring [31], the conditions of heating [32, 33], the severity of the damage, the beam's geometry, and the utilized type of fiber sheet [34], in addition to the adopted safety factors when reinforcing the bridges by CFRP [35].

RC structures (e.g., near-to-furnace, chimneys, rocket launcher sites, power plants) are frequently exposed to consistent heating-cooling cycles. Such cycles endanger the structural stability and demand certain requirements upon designing [36, 37]. It is of common knowledge that concrete can withstand heat till 250-300 °C before it begins to weaken. Beyond 500 °C, the mechanical features of concrete decrease, to a great extent. In addition, another cause of concrete weakening is rapid cooling, e.g., putting out a fire attack with cool water, as this method produces a big difference in the temperature between the concrete surface and its core, causing cracking of concrete due to the development of high superficial tensile stresses. This is another form of damage of structures caused by the weakening of the aggregates' quality and the adjoining paste due to the frequent, incompatible expansions and contractions. It must be mentioned that several factors determine the severity of the damage, such as the structure's size, the sort of the utilized cement and aggregates, the amount of moisture contained in concrete, the time and the frequency the structure is exposed to heat, the cooling mechanism, and the attained maximum degree of temperature [38]. To modify and strengthen the already standing concrete structures, various methods have been utilized, for example RC jacketing, bolting steel plates, prestressed external tendons, and the newly-developed FRP materials. The FRP composites technique has been adopted in various parts of the world for its many features, namely: highly strong, ductile, resistant to corrosion, easy to shape and erect, viable in many applications, high strength-to-weight ratio; keeping in mind that the majority of concrete structures are subjected to damage because of steel corrosion, frequent cycles of freezing and thawing, and dynamic loads [39, 40].

For the past two decades, using CFRP materials to repair and strengthen the RC structures has been a focus worldwide. Many researchers studied RC structures' behavior, CFT columns in particular when externally reinforced by laminates of CFRP. It is worth noting that it is very complicated to examine CFT columns' behavior when exposed to both axial and cyclic lateral loadings. This experiment requires a high-capacity testing machine and a specially-designed setup, which are not easy to attain. The nonlinear finite analysis (NLFEA) method has been utilized to validate the obtained test results, as this method can produce close-to-real results. With adequate validation, the NLFEA method can be employed to examine the reinforced-by-external-CFRP elements impacted by many parameters, such as the thickness of the CFRP layers. What has made it urgent to conduct the study in hand is the severe shortage of information about CFT columns' behavior damaged by thermal shock, which hinders further expansions in this field. In this study, the NLFEA program was used to investigate the influence of externally confining the heat-damaged CST columns, with CFRP materials, on the columns ductility and strength, aiming to obtain out-of-the-box results.

Testing CFT columns under combined axial and cyclic lateral loading is a challenge since it requires a special setup and testing machine with unique capacities. The availability of sound experimental test results is considered priceless and can be used to create and validate robust NLFEA simulating the actual ones. Therefore, this study presents an advanced NLFEA model for predicting seismic behavior and mode of failure of CFRP-confined CFT circular steel columns. To simulate the real behavior of CFT circular steel columns, experimentally obtained relationships for the mechanical characteristic of concrete were incorporated in the simulating process [41], along with suitable models for the various components of the CFT circular steel columns, including concrete, steel tube, and testing conditions. The first step, in this paper, includes the validation of the CFT circular steel model against the published experimental results by Yu et al. [41] and then was expanded to consider the effect of the number of CFRP layers (zero (control), five, six, seven, eight, nine and ten layers) subjected to room temperature (un-damaged) and thermal shock (damaged). The theoretically generated data included stress contours, horizontal load-displacement hysteretic loops, lateral load, net drift capacities, horizontal displacement-steel strain responses, horizontal displacement-CFRP strain responses, stiffness degradation, performance enhancement factor, and energy dissipation. In all simulations, realistic constitutive laws for materials, reasonable interface models, and the reliable verified factors were adopted.

2. Methods

2.1. Experimental Work Review

Fig. 1 shows the specimen's geometric details and a schematic diagram of the experimental test set-up [41]. The CFT column is 318 mm in diameter and 1625 mm in the height of 1625 mm connected rigidly to a stiff, reinforced concrete footing that is 1500 mm long, 1400 mm wide, and 550 mm thick. The steel tube used in all specimens is 3 mm thick with a diameter to thickness ratio of 106. The confinement at the column end (500 mm) was provided using a CFRP jacket to allow full plastic hinge formation and developing a high toughness and ductility.

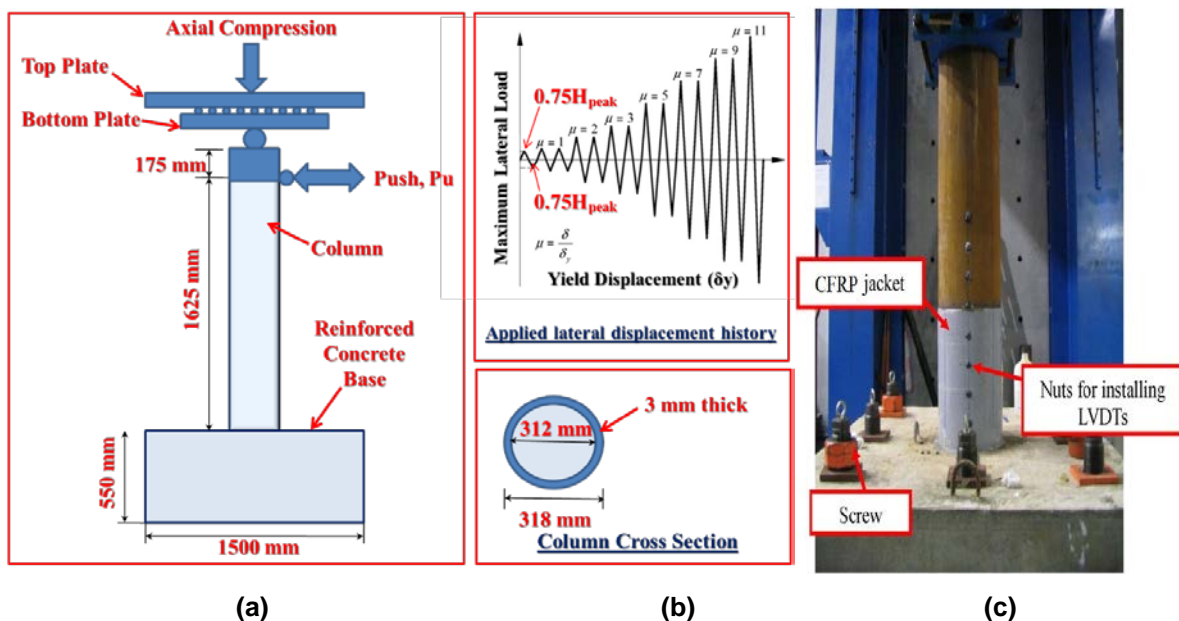


Figure 1. Test set-up details (dimensions are in mm) [41]: (a) Schematic diagram of test set-up, (b) Cross-section and lateral displacement history, and (c) Column wrapped with a CFRP jacket.

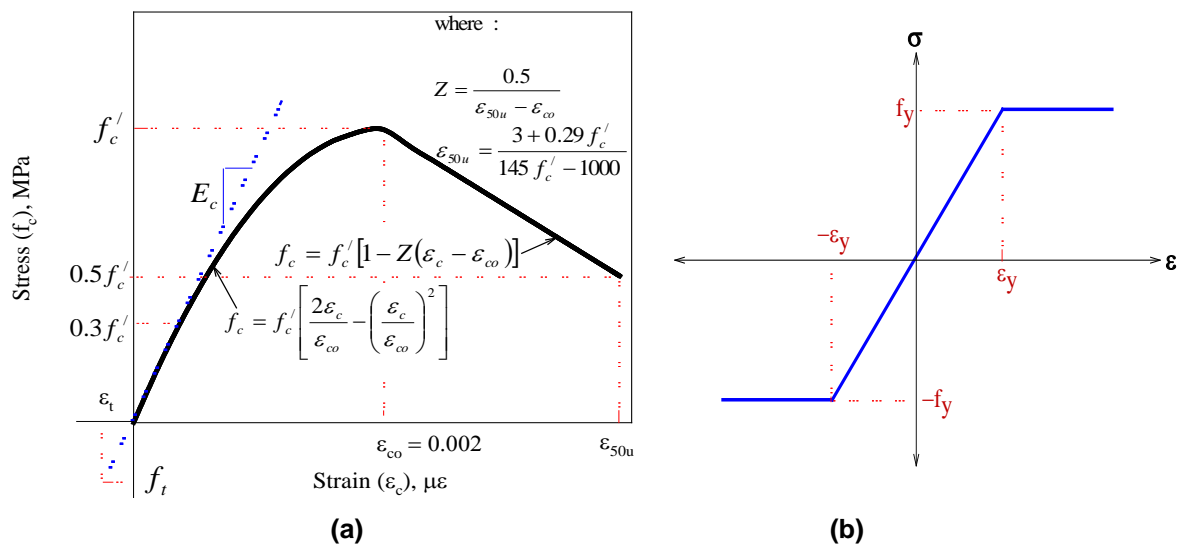
2.2. Description of NLFEA Program

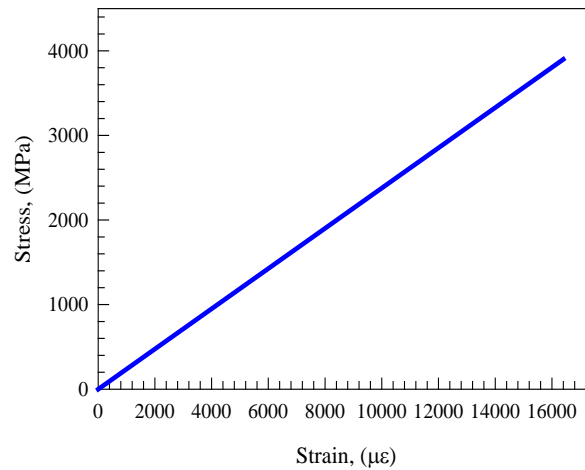
Nonlinear finite element analysis (NLFEA) has been used in this study for its reliability and efficiency in analyzing complicated structures before being executed, saving by that costs, effort, and time. This method also detects design error, assesses the structural stresses and strains at various loads in addition to the resultant deflections, and permits the possibility of making any necessary modifications. Also, the NLFEA facilitates the ability to examine the effectiveness of a given parameter on the structure. To fulfill the purposes of this study, fourteen full-scale, strengthened-with-CFRP models were constructed and examined. The support was roller at the top of the column to allow for relative drift while kept fixed at the other end. Firstly, the column axial load was applied as the first loading step, and then the horizontal load was applied at top of the column as displacement-controlled loading to guarantee the descending part of the load-displacement behavior. In order to avoid sudden failure or on other word solution divergence as well as obtain stable analysis process, this loading was applied incrementally by providing more load sub-steps within a loading step. The steps can be divided automatically by ANSYS but the number of sub-steps must be previously inserted.

2.2.1. Description of Non-linear Finite Element Analysis (NLFEA)

The concrete material is not homogenous, brittle, and does not exhibit the same behavior in compression and tension. The SOLID 65 element has the capability to predict the concrete's response by employing a smeared crack approach in terms of ultimate uniaxial compression and tensile. In the cylinders, the compressive strength before the thermal shock was 36.6 MPa, while it was 9.8 MPa after the cylinder was thermally shocked and damaged [42]. The cylinder's tensile strength before being thermally shocked was 3.75 MPa, while it was 1.25 MPa for the damaged-by-thermal-shock ones. For this study, the Poisson's ratio was set to 0.2, and so was the shear transfer coefficient. Fig. 2(a) shows the stress-strain relationship for unconfined concrete, which describes the post-peak stress-strain behavior.

Also, the SOLID45 element has been used for its capability to interpret all directions and its efficiency in the simulation of the circular tubes of steel and the steel plates. In addition, the elastic, linear stress-strain behavior was utilized with the following settings: The Young's modulus of 203 GPa, ultimate stress of 353 MPa, the yield stress of 271 MPa, and a Poisson's ratio of 0.30. In the specimens that had been simulated, the steel was presumed to have the same fully elastic-plastic behavior in both tension and compression. The steel, used for reinforcement, had: A Poisson's ratio of 0.3, the yield stress of undamaged beams of 410 MPa, damaged beams' yield stress of 0.78 of the yielding stress, an elastic modulus of undamaged beams of 200 GPa, and 0.6 of the elastic modulus for the damaged ones [43]. Fig. 2(b) demonstrates the relationship between the stress and the strain in its ideal form. The steel plates' material was presumed linear and elastic, having a Poisson ratio of 0.3 and an elastic modulus of 200 GPa. On the other side, the CFRP material was presumably orthotropic material, having: a thickness of 0.17 mm, tensile strength of 3800 MPa, the elastic modulus of 230 GPa, and an ultimate tensile strain of 0.0169, as illustrated in Fig. 2(c).





(c)

Figure 2. Stress-strain curves for: (a) unconfined concrete [42], (b) steel reinforcement [43], and CFRP composite.

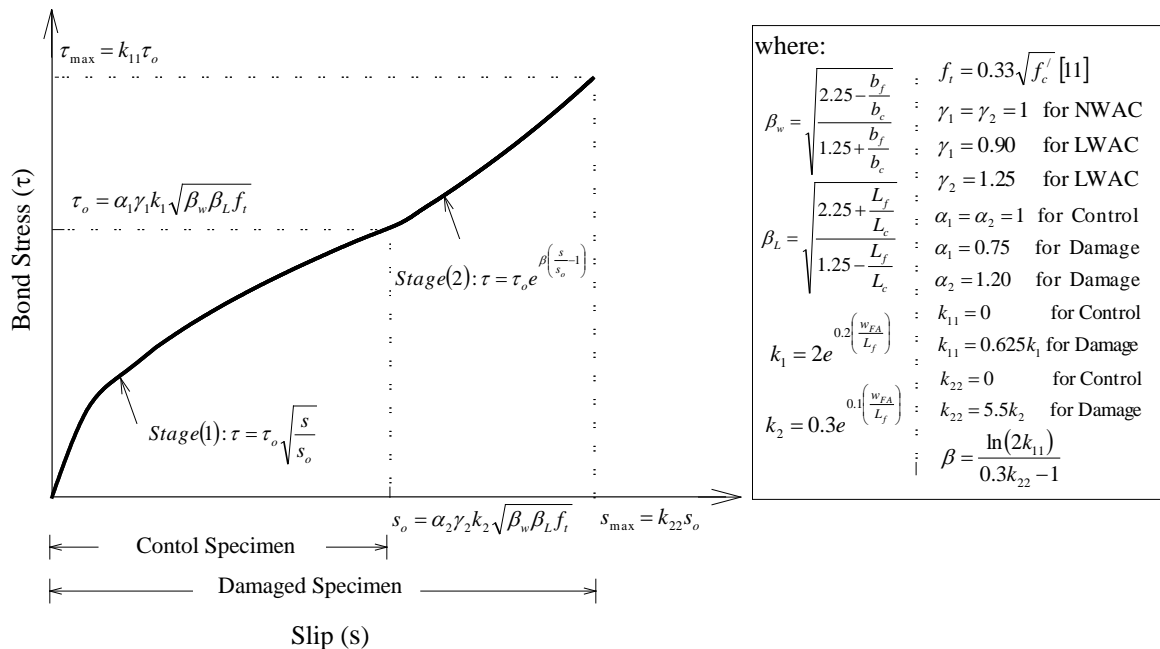


Figure 3. CFRP to concrete bond-slip model [42].

The CONTA174 element had been employed to design the zone of contact between the CFRP laminates and concrete. In this study, the utilized model of the stress-slip bonding, located between the heat-damaged concrete and the CFRP plates, had been suggested by Haddad and Al-Rousan [42], as depicted in Fig. 3. In order to investigate the performance of the RC control specimen, a simulation of a full-scale column was carried out, as illustrated in Fig. 4. Also, the density of the mesh was specified by conducting a convergence study. For more accuracy, the CFRP-concrete bonding was presumed Perfect. Fig. 4 illustrates a FEM of the meshing of the CFT specimens. The applied load had been split into a group of increments, or steps, of the load. The Newton-Raphson equilibrium iterations were employed to avail convergence at each load step's end, between the tolerance limits, with a value of 0.001 for a load increment of 0.35 kN.

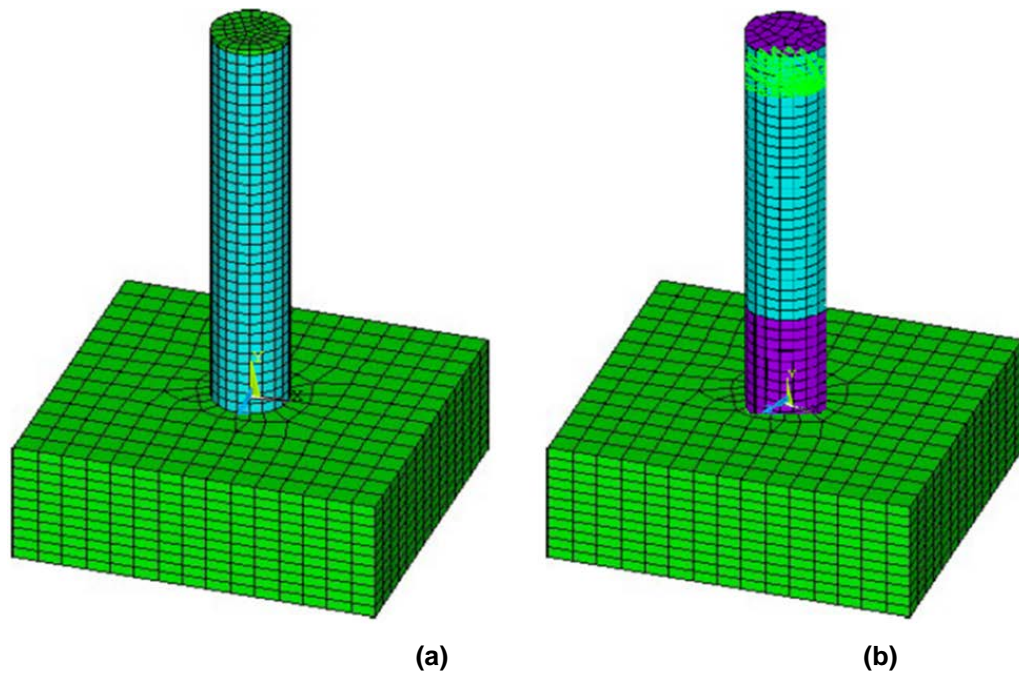


Figure 4. Typical finite element meshing of the Column:
(a) Without CFRP jacket and (b) With CFRP jacket.

Table 1. NLFEA configuration of confined CFT columns with CFRP composites.

Group Number	Number of CFRP layers	Column number	Un-damaged/ Damaged	CFRP strengthening configuration
1	0	CFT0-UD	Un-damaged	None
	5	CFT5-UD		five layers of CFRP
	6	CFT6-UD		six layers of CFRP
	7	CFT7-UD		seven layers of CFRP
	8	CFT8-UD		eight layers of CFRP
	9	CFT9-UD		nine layers of CFRP
2	10	CFT10-UD	Damaged	ten layers of CFRP
	0	CFT0-D		None
	5	CFT5-D		five layers of CFRP
	6	CFT6-D		six layers of CFRP
	7	CFT7-D		seven layers of CFRP
	8	CFT8-D		eight layers of CFRP
	9	CFT9-D	nine layers of CFRP	
	10	CFT10-D	ten layers of CFRP	

Note: C: Column, UD: un-damaged, D: Damaged

2.2.2. Investigated Parameters

In Table 1, different configurations of strengthening techniques are illustrated. All the columns were labeled as follows: CFTXX-UD/D, where: CFT for the type of column, the XX stand for the number of CFRP layers installed, and UD/D (un-damaged/damaged). Two control CST columns were included: an un-damaged one designated as (CFT0-UD) and a damaged one labeled as (CFT0-D). The remaining specimens, 12 CFT columns, were reinforced-in-shear with sheets of CFRP, as follows: CFT5-UD and CFT5-D had five layers of CFRP (with a thickness of 0.85 mm); the CFT6-UD and CFT6-D had six layers of CFRP (thickness of 1.02 mm); the CFT7-UD and CFT7-D had seven layers of CFRP (thickness of 1.19 mm); the CFT8-UD and CFT8-D had eight layers of CFRP (thickness of 1.36 mm); CFT9-UD and CFT9-D had nine layers of CFRP (thickness of 1.53 mm), and the CFT10-UD and CFT10-D had ten layers of CFRP (thickness of 1.7 mm). The finite element modeling groups are detailed in Table 1.

2.2.3. Validation Process

By inspecting Fig. 5, a remarkable agreement has been noticed between the results of the load-drift hysteresis obtained from the NLFEA and Yu et al. [41]. A confined-by-six-CFRP-layers CFT column (labeled as LCFT-6C-106-F, according to Yu et al. [42]) was examined. Again, there was a significant agreement in

the results regarding the modes of failure and the deformed shapes (Fig. 6). The NLFEA is recommended, by many designers, to conduct additional testing and analysis to enhance the awareness of the behavior of the circular, damaged-by-thermal-shock, confined-by-CFRP CFT steel columns when undergoing simultaneous axial and lateral cyclic loading. Consequently, fourteen NLFEA models were constructed using calibrated models, aiming to assess the impact of the number of the erected CFRP layers (5 to 10 layers) and the existence of the thermal shock (with/ without).

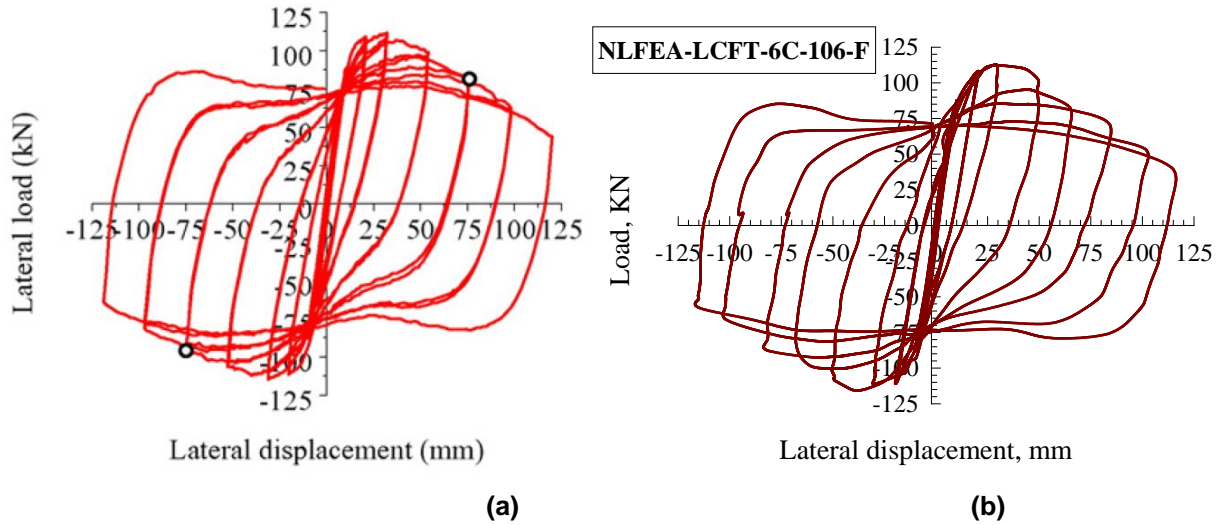


Figure 5. Validation of the FEA results: (a) Yu et al. [41] test result and (b) LCFT-6C-106-F.

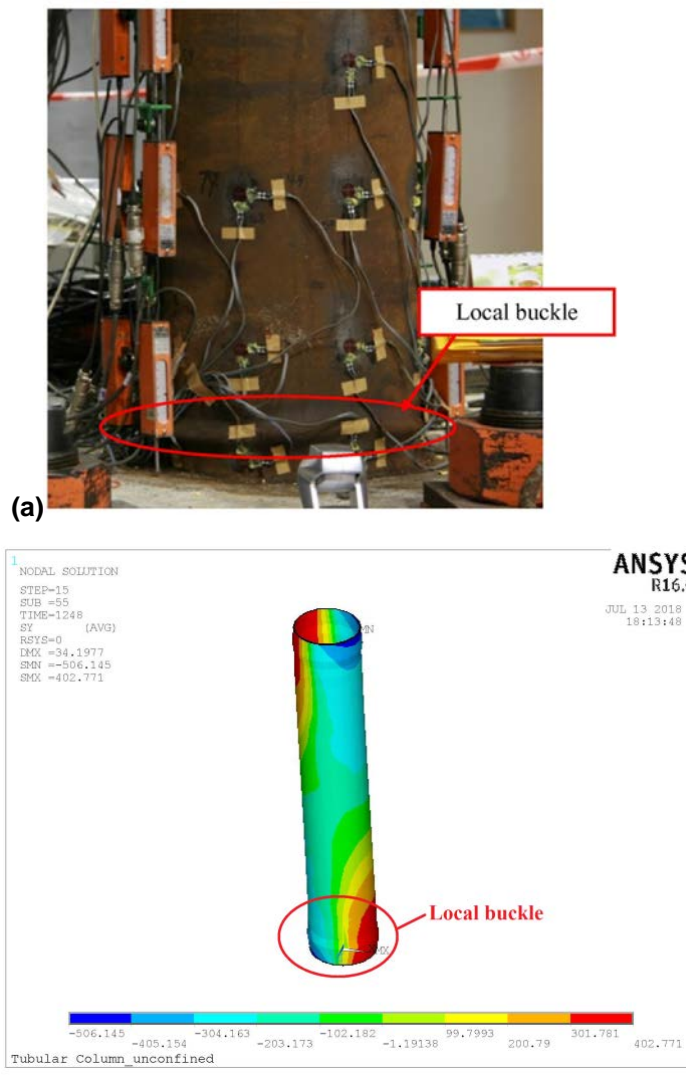


Figure 6. Deformed shapes of the FEA: (a) Yu et al. [41] test Result and (b) LCFT-6C-106-F.

3. Results and Discussion

In brief, Table 2 demonstrates the experimental results obtained from testing fourteen NLFEA models and how the study parameters have impacted them. The designation of the specimens has been explained in section 2.3. The obtained results included: the net drift, the maximum horizontal load, the strain of steel, the strain of the CFRP laminates, the degradation of stiffness, the enhancement factor of performance, and the amount of energy dissipated.

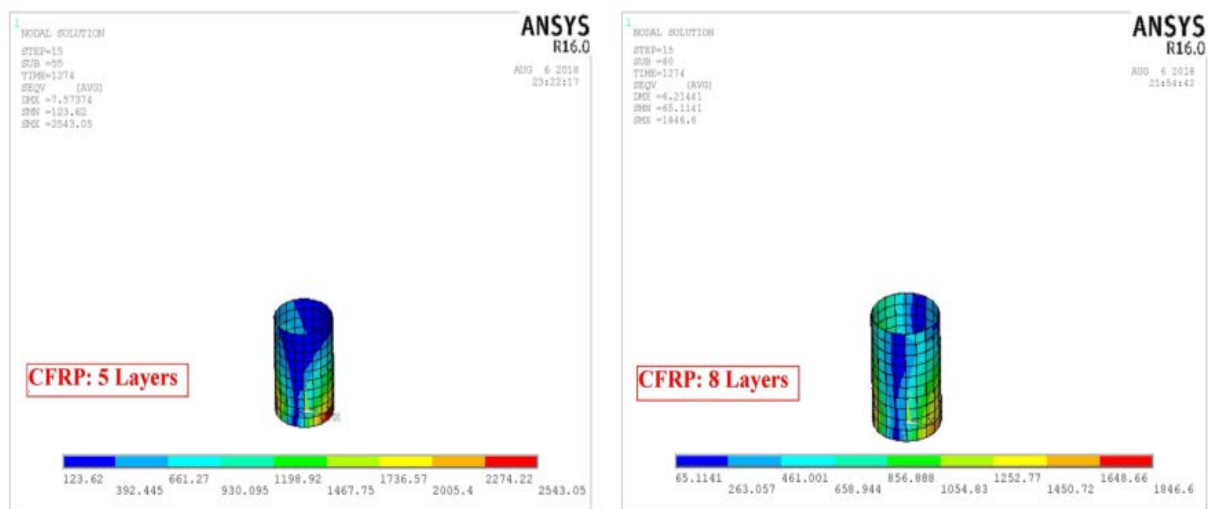
Table 2. NLFEA results of all models.

Group Number	Specimen Designation	Maximum horizontal net drift, mm	Maximum horizontal load, kN	Maximum steel strain, $\mu\epsilon$	Maximum CFRP strain, $\mu\epsilon$
1	CFT0-UD	102.8	102.5	1623	---
	CFT5-UD	115.8	113.9	1648	Rupture
	CFT6-UD	121.9	119.3	1674	8245
	CFT7-UD	131.7	127.8	1700	8093
	CFT8-UD	138.7	134.5	1719	7380
	CFT9-UD	144.0	138.4	1734	6786
	CFT10-UD	147.7	140.8	1745	6269
	CFT0-D	56.6	87.1	1392	---
	CFT5-D	63.7	96.0	1432	Rupture
	CFT6-D	67.1	104.4	1460	7191
2	CFT7-D	72.4	112.5	1496	6814
	CFT8-D	76.3	118.9	1526	6089
	CFT9-D	79.2	122.4	1551	5482
	CFT10-D	81.2	125.7	1560	4953

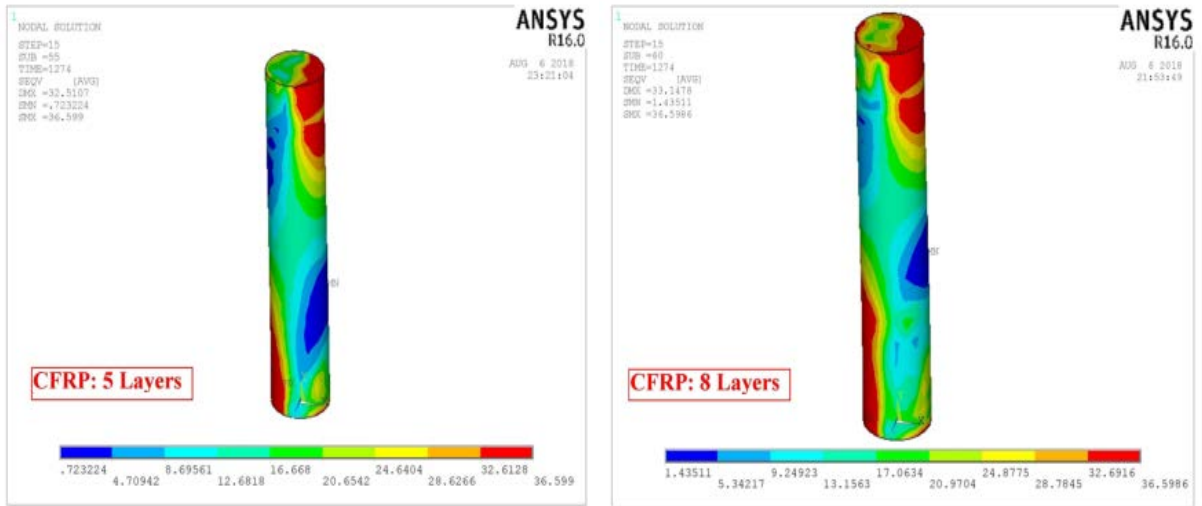
Note: yielding strain for steel is 1335 $\mu\epsilon$, and CFRP ultimate strain is 8500 $\mu\epsilon$.

3.1. Horizontal load-displacement hysteretic loops

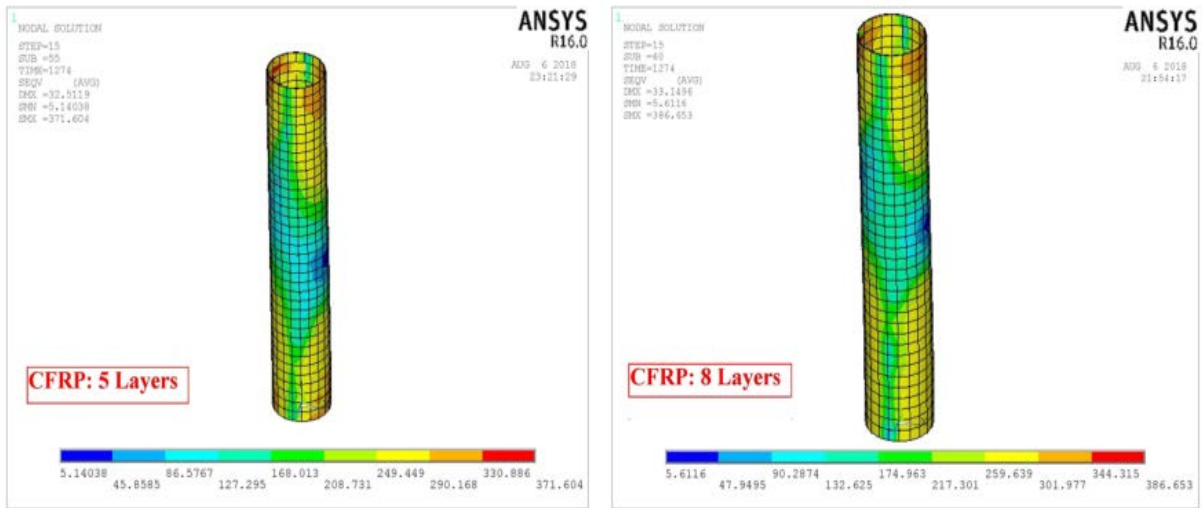
Each model's stresses (of the concrete, CFRP, and steel) had been attained. Fig. 7 contours of the specimens' stresses are demonstrated for CST0-UN (control beam) and CST08-UN (un-damaged, 8 CFRP layers), showing the spots at which the stresses were condensed, particularly at the specimen's bottom end. Fig. 8 illustrates the horizontal load-displacement hysteretic loops for the un-damaged columns, while the loops of the damaged ones are depicted in Fig. 9. Both figures showed, explicitly, the influence of the layers of CFRP in improving the behavior of the CFT column and enhancing its: capacities of lateral load and net drift, in addition to the increase in the energy dissipation.



(a)

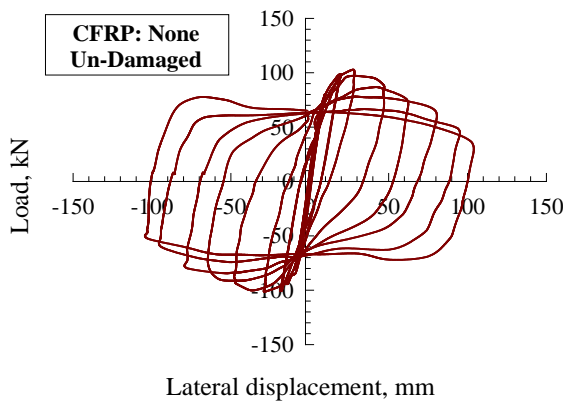


(b)

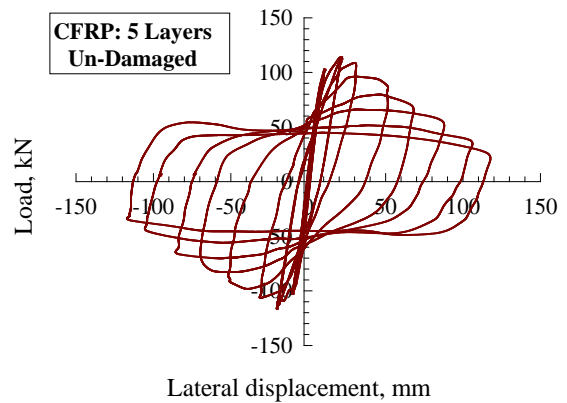


(c)

Figure 7. Sample stress contours: (a) CFRP, (b) Concrete, and (c) Steel tube.



(a)



(b)

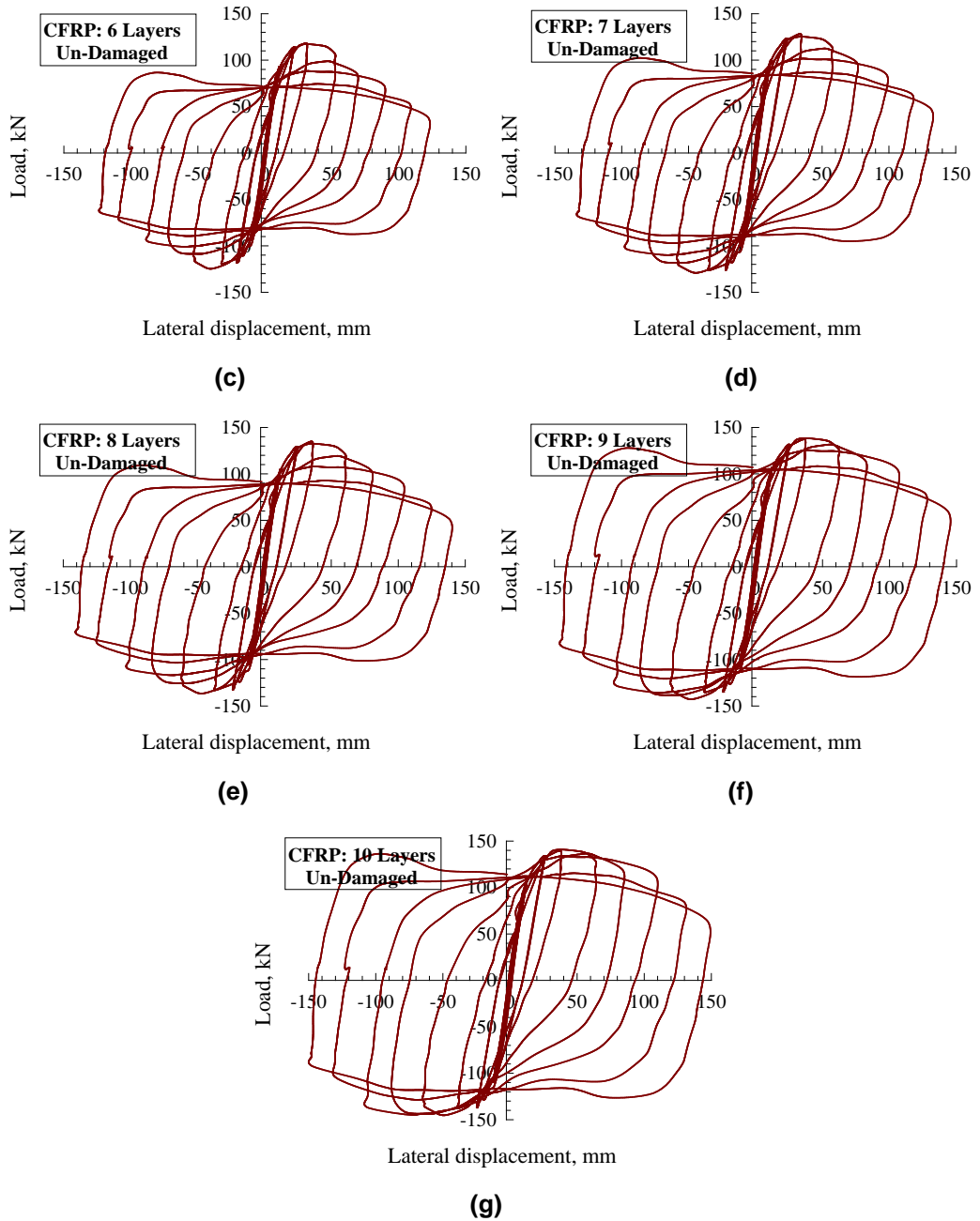
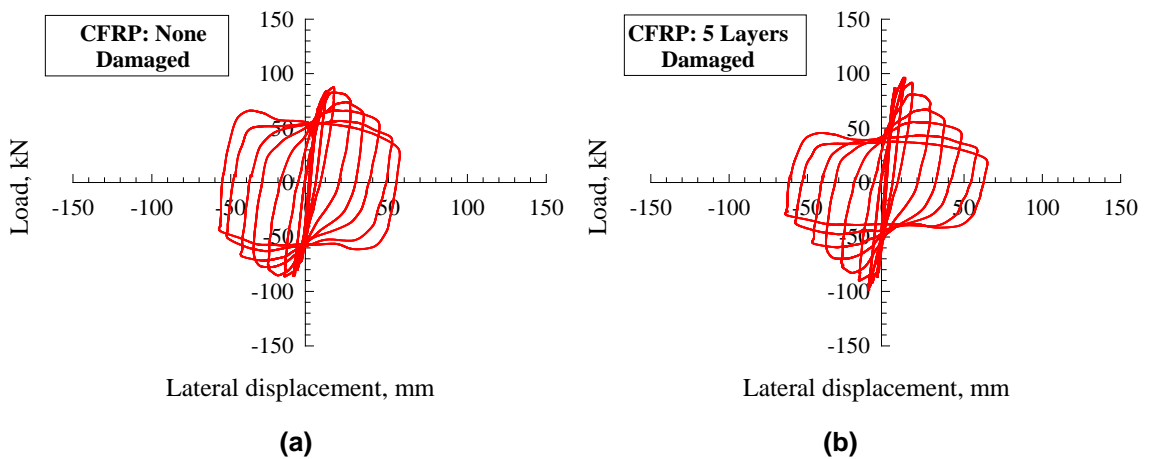


Figure 8. Horizontal load-net drift hysteresis loops for the un-damaged CFT column strengthened with (a) without CFRP, (b) 5 Layers of CFRP, (c) 6 Layers of CFRP, (d) 7 Layers of CFRP, (e) 8 Layers of CFRP, (f) 9 Layers of CFRP, and (g) 10 Layers of CFRP.



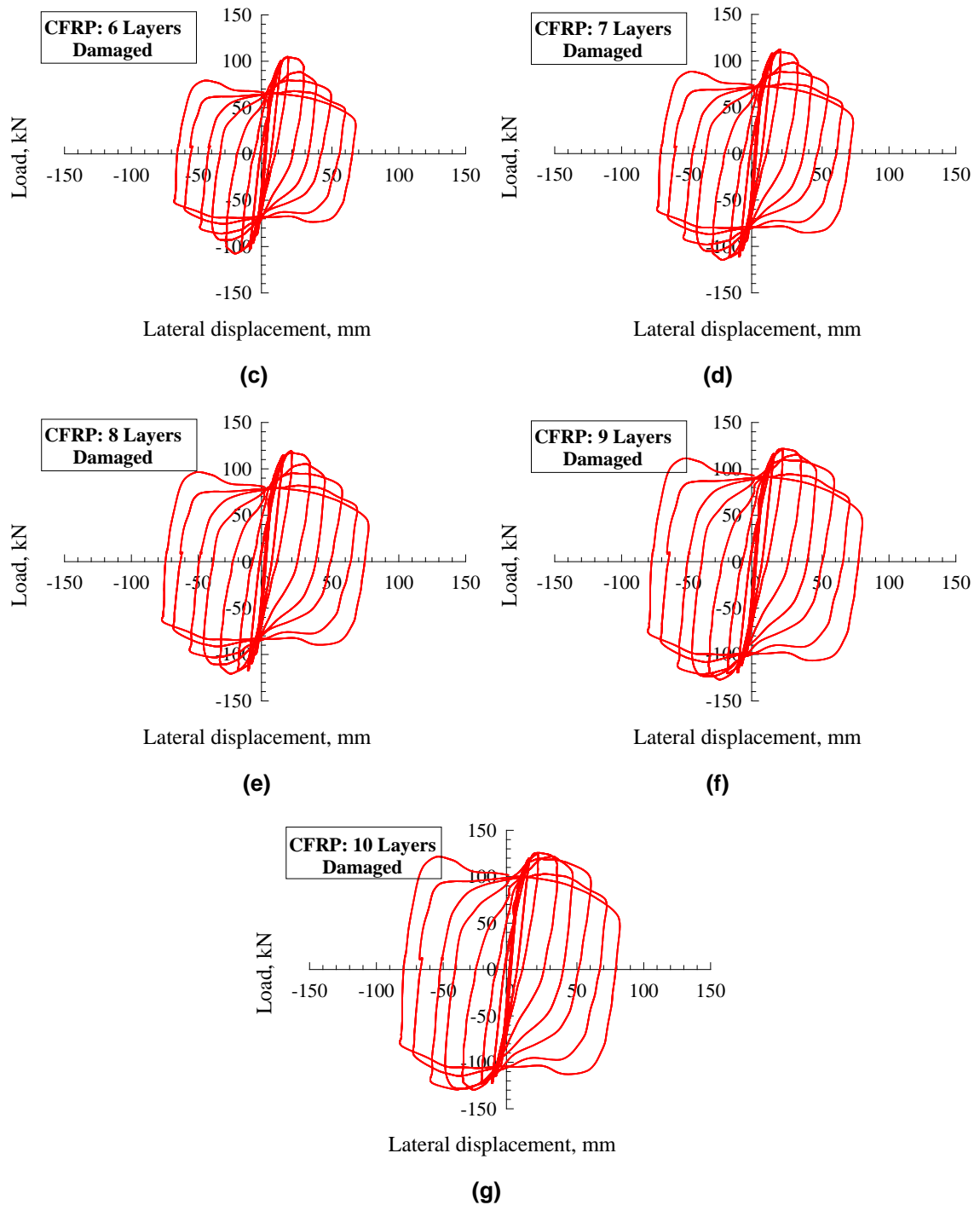


Figure 9. Horizontal load-net drift hysteresis loops for the damaged CFT column strengthened with (a) without CFRP, (b) 5 Layers of CFRP, (c) 6 Layers of CFRP, (d) 7 Layers of CFRP, (e) 8 Layers of CFRP, (f) 9 Layers of CFRP, and (g) 10 Layers of CFRP.

3.2. Lateral Load and Net Drift Capacities

Referring to Table 2 and Fig. 10 and 11, the following points have been noticed: 1) a considerable, disproportionate increase in the lateral net-drift of the un-damaged columns, while it was not as much in the lateral load capacity; 2) the number of installed CFRP layers has a considerable, positive impact on the capacities of lateral load and lateral net-drift; as installing more layers of CFRP increased both capacities, though not with the same rates; 3) the CFRP layers had no significant effect when installing less than 5 layers of them; 4) installing 8, 9, or 10 layers of CFRP had the same influence on the column behavior; 5) the maximum strain of the steel tube was slightly affected by each of the numbers of CFRP layers and the thermal shock; and, lastly, 6) the maximum strain of the CFRP reduced when the number of its layers was increased. Hence, it can be concluded that installing 5 to 8 layers of CFRP strengthened the CFT circular steel column, resulting in improving the lateral load capacity and the net drift.

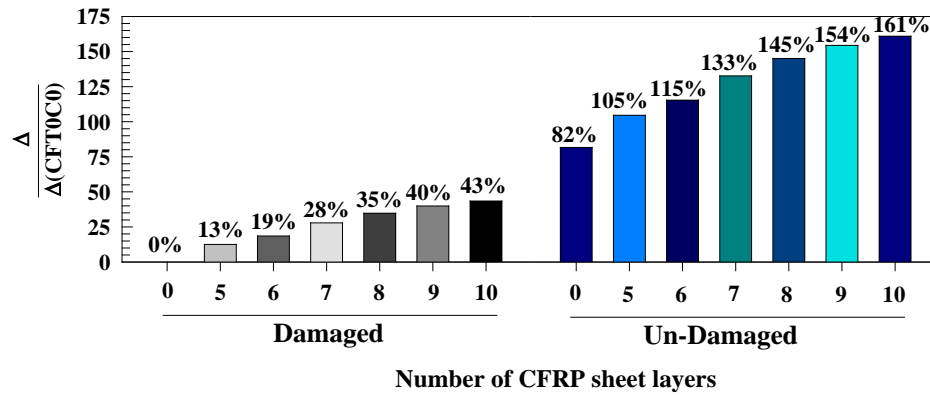


Figure 10. Effect of number of CFRP layers on the maximum horizontal net drift.

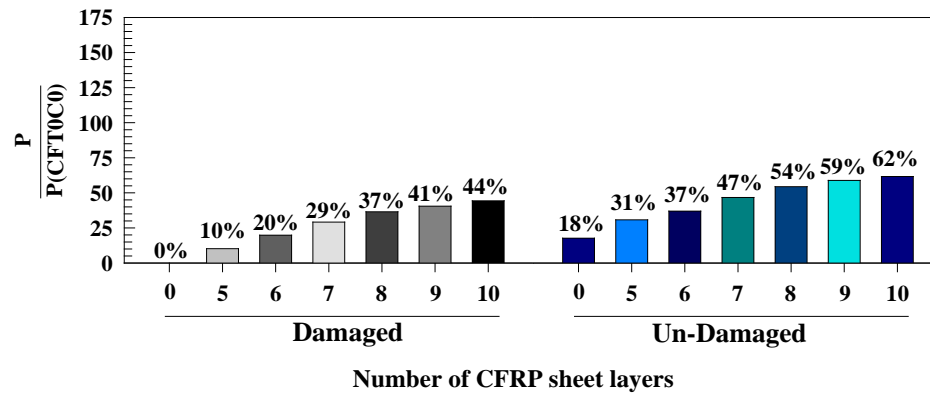


Figure 11. Effect of number of CFRP layers on the maximum horizontal load capacity.

3.3. Horizontal displacement-steel strain responses

The behavior of the CFT columns had been examined by utilizing the data of the steel tube strain. The graph of the steel tube strain vs. the emerging deflections is plotted in Fig. 12. It is worth mentioning that un-damaged CFT columns have a higher steel tube strain capacity than the damaged ones, as depicted in Table 2 and Fig. 12. To examine the influence of the study parameters on the steel strain, the steel reinforcement was modified as per the yielding value of strain, as illustrated in Fig. 13. Considering Fig. 13, it is apparent that the increase in the number of CFRP strips results in enhancing the strain of thermally-damaged steel tubes enhanced by 5 % for 0 strips, 8 % for 5 layers, 10 % for 6 layers, 12 % for 7 layers, 15 % for 8 layers, 16 % for 9 layers, and 17 % for 10 layers of CFRP. As for the un-damaged columns, the increase was: 22 % for 0 layers, 24 % for 5 layers, 26 % for 6 layers, 28 % for 7 layers, 29 % for 8 layers, 30 % for 9 layers, and 31 % for 10 CFRP layers. Also, the increase in the number of the CFRP layers from 5 to 8 layers enhanced the strain of the steel tubes proportionally. However, increasing the layers from 8 to 10 had no significant effect. So, it can be concluded that 8 layers of CFRP are the best configuration.

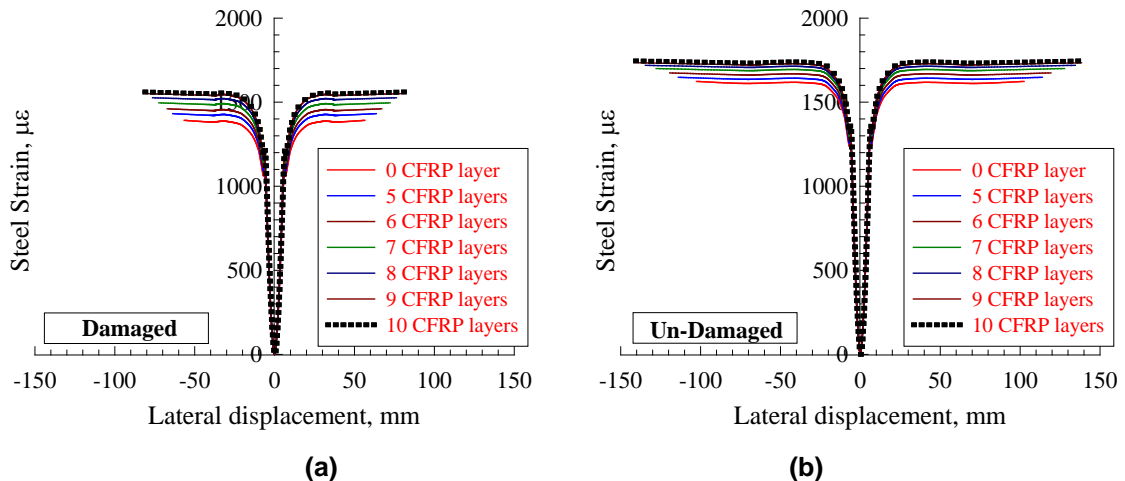


Figure 12. Steel strain CFT column: (a) Damaged and (b) Un-damaged.

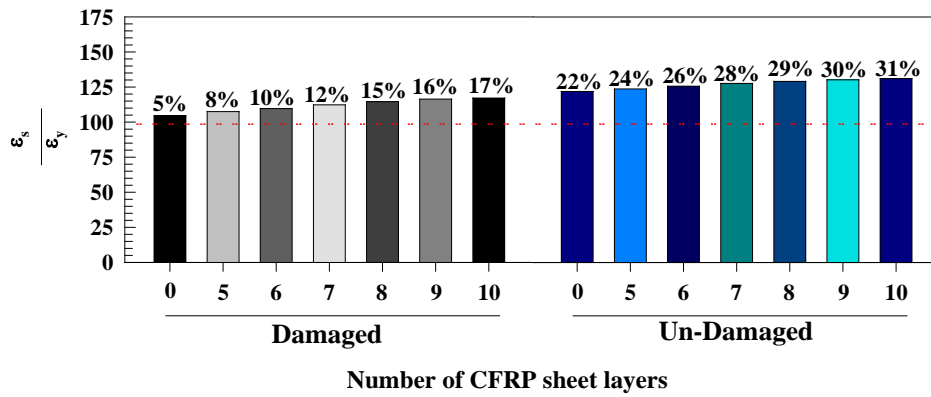


Figure 13. Effect of investigated parameters on maximum steel strain.

3.4. Horizontal displacement-CFRP strain responses

Figure 14 illustrates the graphical representation of the horizontal displacement in the reinforced-with-CFRP CST columns against the CFRP material's strain responses. The graph has two parts: 1) covers the horizontal displacements range from 0 to 10 mm, 2) is from 10 mm to failure. Fig. 14 indicates that a slight increase in the horizontal displacement results in a rapid boost in the CFRP strain. Nevertheless, a big boost in the horizontal displacement has resulted in a very slight increase in the CFRP strain. Fig. 15 also indicates that increasing the number of CFRP layers in damaged columns has resulted in a reduction in the CFRP strain, by 0 % (rupture) for 0 layers, 15 % for 5 layers, 20 % for 6 layers, 28 % for 7 layers, 64 % for 8 layers, and 42 % for 10 layers. All the percentages are of the ultimate strain value of the CFRP composite, provided by the supplier (ϵ_{fu}), for damaged columns. As for the un-damaged columns, the minimum reduction percentages in the CFRP strain were: 3 % for 5 layers, 5 % for 6 layers, 13 % for 7 layers, 20 % for 8 layers, and 26 % for 10 layers. Further, increasing the CFRP layers from 5 to 8 enhanced the strain of the steel tube in a proportional manner; whereas, the use of 9 or 10 layers had the same influence of 8 layers. That explicitly means that 8 layers is the best number of CFRP layers. On the other side, the thermal shock reduced the strain of CFRP material by 28 %. Finally, less than 5 layers of CFRP did not affect the strain behavior of CFRP.

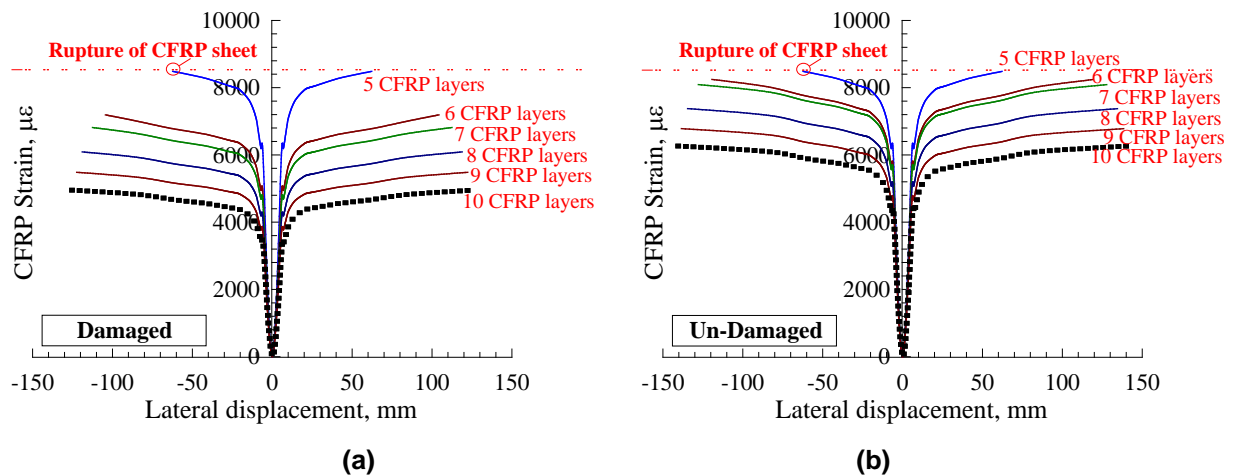


Figure 14. CFRP strain CFT column: (a) Damaged and (b) Un-damaged.

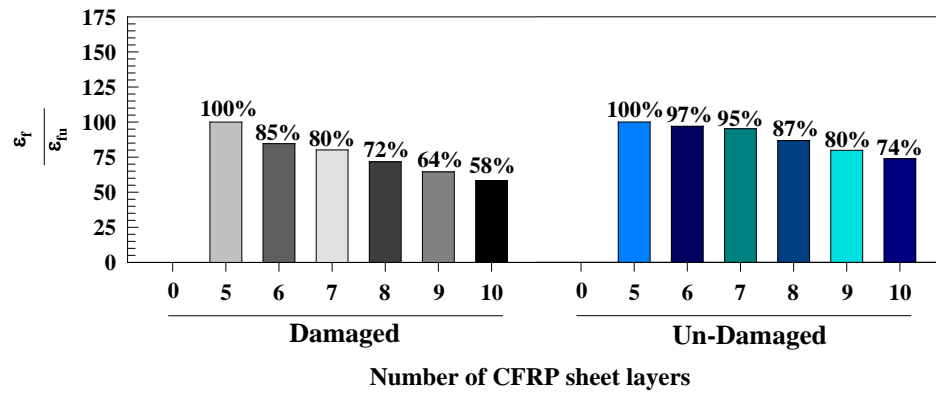


Figure 15. Effect of tested parameters on maximum CFRP strain.

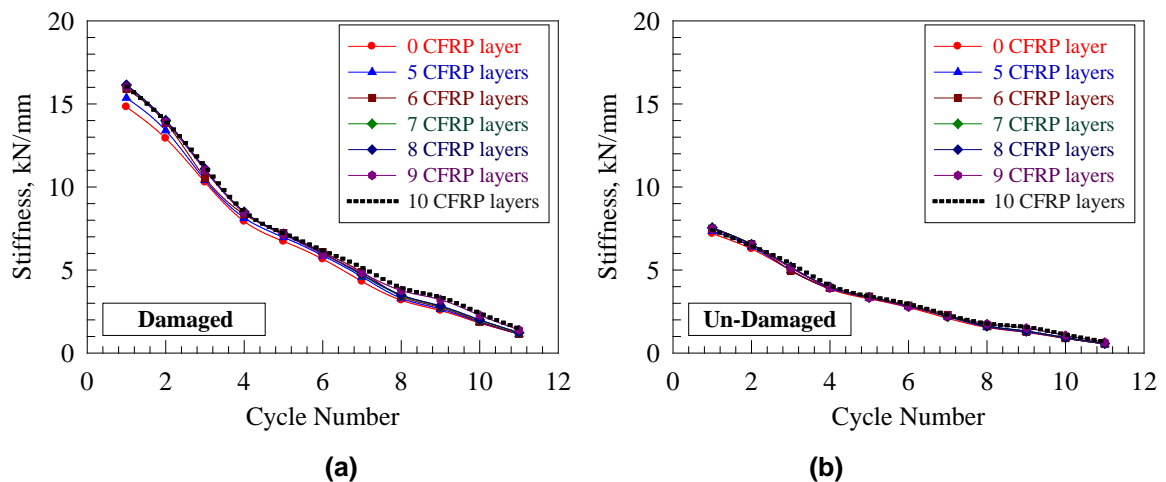


Figure 16. Stiffness degradation: (a) Damaged and (b) Un-damaged.

3.5. Stiffness degradation

In every cycle, the stiffness values were computed to determine the degradation; then, the obtained values were plotted graphically against the number of cycles of the CFT column (Fig. 16). Considering Fig. 16, the graph shows a very sharp slope for the damaged columns, where it became less and less sharp for the un-damaged ones because the intact concrete fully confined the footing-column zone. Also, neither the stiffness nor the number of cycles was significantly affected by the CFRP reinforcement technique. On the other side, the thermal shock reduced the initial stiffness, the number of cycles, while it enhanced the sharpness of stiffness degradation because of the rise of the column's compressive stress. Further, the thermal shock reduced the stiffness degradation by approximately 60 %, with respect to un-damaged columns.

3.6. Performance Enhancement Factor and Energy Dissipation

Table 3 demonstrates the increase in the lateral load capacity and net drift, referred to as load and displacement factors. They were modified in accordance to the control column CFT0-D. Every specimen's performance factor was computed by using the expression (load factor \times displacement factor), to obtain a more accurate evaluation of the improvement. Compared to CFT0-D, the damaged models had a performance factor of nearly 1.25 when using 5 CFRP layers. By raising the number of the CFRP layers from 5 to 10, the performance factor increased, in a proportional manner, by almost 0.20. On the other hand, the obtained results showed no significant effect on less than 5 layers. Energy dissipation is a critical factor in seismic design. It is defined as the quantity of the energy dispersed by a structural element. It is strongly related to ductility, as they are directly proportional to each other.

As illustrated in Table 2, increasing the number of CFRP layers in un-damaged models resulted in a significant rise in the dissipated energy, where the increase was not as much in the damaged ones. It is noted that the modified energy dissipation gets along, to a limit, with the majority of the experimented cases, in terms of the performance enhancement factor. This is perfectly logical because when the performance factors have been computed, both the strength of the samples and their displacement are given the same weight. It must be stated, at this point, that it is possible to compute for the performance enhancement factor, in some cases, by assigning different ratios of weight to ductility and strength. To elaborate, when

focusing on ductility, it can be given a ratio of 0.75 % of weight, while the strength is given a ratio of 0.25 % of the weight and the other way around.

Table 3. Performance improvement factor and energy dissipation.

Group Number	Specimen Designation	Strength Factor (SF)	Displacement Factor (DF)	Performance Factor (SF*DF)	Energy dissipation, kN.mm	Normalized Energy Dissipation
1	CFT0-UD	1.82	1.18	2.14	12020	2.14
	CFT5-UD	2.05	1.31	2.68	13120	2.33
	CFT6-UD	2.15	1.37	2.95	16604	2.95
	CFT7-UD	2.33	1.47	3.41	19656	3.51
	CFT8-UD	2.45	1.54	3.78	21918	3.89
	CFT9-UD	2.54	1.59	4.04	24721	4.41
	CFT10-UD	2.61	1.62	4.22	26364	4.69
	CFT0-D	1.00	1.00	1.00	5619	1.00
	CFT5-D	1.13	1.10	1.24	6086	1.08
	CFT6-D	1.19	1.20	1.42	7995	1.42
2	CFT7-D	1.28	1.29	1.65	9511	1.69
	CFT8-D	1.35	1.37	1.84	10654	1.90
	CFT9-D	1.40	1.41	1.97	12019	2.14
	CFT10-D	1.43	1.44	2.07	12941	2.30

The models that had been reinforced with the same number of CFRP layers were subjected to a comparative study to be able to measure the impact of the axial load level on the behavior of CFT circular steel columns. The un-damaged columns had a performance enhancement factor of 2.16 with 5 CFRP layers, 2.08 with 6 layers, 2.07 with 7 layers, and 2.05 with 8 layers, 2.05 with 9 layers, and 2.04 with 10 layers. Checking these numbers shows that the value of the enhancement factor of performance, for the un-damaged columns, was around 2.0, and it was almost constant, regardless of the number of the installed CFRP layers.

3.7. Comparison of NLFEA with other results

Comparing the results obtained from NLFEA with Valipour and Foster [2], both methods showed a close resemblance of the results when subjecting concrete-filled steel (CFS) specimens to the nonlinear static and cyclic analysis. Further, the experimenting methods employed the modified fiber element technique and the total stiffness of secant to consider the material nonlinearity at section level and force interpolation concept. The impact, of each of the size and the confinement of steel tubes, on the ductility and the strength of concrete has been considered, too. Furthermore, the modeling methods had investigated the impact of local buckling, in steel tubes, on the structural strength and had the same findings.

4. Conclusions

This study presents an advanced NLFEA model for predicting seismic behavior and mode of failure of CFRP-confined CFT circular steel columns. The numerical results obtained by NLFEA model were firstly verified using experimental results obtained by Yu et al. [41]. Then, a parametric study was carried out using this NLFEA model to investigate effect of the number of CFRP layers (zero (control), five, six, seven, eight, nine and ten layers) subjected to room temperature (un-damaged) and thermal shock (damaged). The following conclusions are drawn based on the findings of this study:

1. For the modeled CFT circular steel column, the use of 5 to 10 layers of CFRP composites resulted in an increase in the lateral load and drift capacities and consequent performance factor and energy dissipation.
2. The structural lateral performance of CFT circular steel columns can be significantly enhanced through wrapping with CFRP composites.
3. The use of 9 and 10 CFRP layers did not add measurable enhancement over what was achieved with 8 CFRP layers, indicating that the optimum number of CFRP layers for the studied CFT circular steel column is 8.

4. The influence of the un-damaged column is significant and indicates a better performance than damaged columns.

5. The performance enhancement is dependent on the CFT steel column properties, thermal shock, and the number of wraps of CFRP composites, but in a non-proportional fashion. This dictates that the strengthening of any CFT circular steel column must be optimized through proper FEA modeling.

6. The findings of this study represent useful guidelines and methodology for a similar strengthening of CFT steel columns.

References

- Han, L.H., Yang, Y.F. Cyclic performance of concrete-filled steel CHS columns under flexural loading. *Journal of Construction Steel Research*. 2005. 61 (4). Pp. 423–452. DOI: 10.1016/j.jcsr.2004.10.004
- Valipour, H.R., Foster, S.J. Nonlinear static and cyclic analysis of concrete-filled steel columns. *Journal of Construction Steel Research*. 2010. 66 (6). Pp. 793–802. DOI: 10.1016/j.jcsr.2009.12.011
- Mohsen, A. Issa, Rajai Z. Alrousan, Moussa A. Issa. Experimental and Parametric Study of Circular Short Columns Confined with CFRP Composites. *Journal of Composite Construction*. 2009. 13 (2). Pp. 135–147. DOI: 10.1061/(ASCE)1090-0268(20-09)13:2(135)
- Al-Rousan, R.Z., Issa, M.A. Stress-strain model and design guidelines for CFRP-confined circular reinforced concrete columns. *Polymer Composites*. 2016. 39 (8). Pp. 2722–2733. DOI: 10.1002/pc.24262
- Khairidin, M. Abdalla, Rajai Al-Rousan, Mohammad A. Alhassan, Nikos D. Lagaros. Finite-element modelling of concrete-filled steel tube columns wrapped with CFRP. *Proceedings of the Institution of Civil Engineers: Structures and Buildings*. 2020. 173 (11). Pp. 844–857. DOI: 10.1680/jstbu.19.00011
- Mao, X.Y., Xiao, Y. Seismic behavior of confined square CFT columns. *Engineering Structures*. 2006. 28 (10). Pp. 1378–1386. DOI: 10.1061/(ASCE)0733-9445(2005)131:3(488)
- Xiao, Y., He, W.H., Choi, K.K. Confined concrete-filled tubular columns. *ASCE Journal of Structural Engineering*. 2005. 131 (3). Pp. 488–497. DOI: 10.1061/(ASCE)0733-9445(2005)131:3(488)
- Qin, P., Xiao, Y., Zhou, Y., Zhang, G. Research on CFRP confined circular concrete-filled steel tubular columns subjected to cyclic lateral forces. *Journal of Earthquake Engineering, Engineering Vibrations*. 2013. 33 (5). Pp. 190–196. DOI: 10.131-97/j.eeev.2013.05.190.qinp.024
- Tao, Z., Han, L.H., Zhuang, J.P. Axial loading behavior of CFRP strengthened concrete-filled steel tubular stub columns. *Advances in Structural Engineering*. 2007. 10 (1). Pp. 37–46. DOI: 10.1260/136943307780150814
- Park, J.W., Hong, Y.K., Choi, S.M. Behaviors of concrete filled square steel tubes confined by carbon fiber sheets (CFS) under compression and cyclic loads. *Steel Composite Structures*. 2010. 10 (2). Pp. 187–205. DOI: 10.12989/scs.2010.10.2.187
- Abdalla, S., Abed, F., Alhamaydeh, M. Behaviour of CFSTs and CCFSTs under quasi-static axial compression. *Journal of Construction Steel Research*. 2013. 90 (1). Pp. 235–244. DOI: 10.1016/j.jcsr.2013.08.007
- Wang, Z.B., Yu, Q., Tao, Z. Behaviour of CFRP externally-reinforced circular CFST members under combined tension and bending. *Journal of Construction Steel Research*. 2015. 106 (1). Pp. 122–137. DOI: 10.1016/j.jcsr.2014.12.007
- Hu, Y.M., Yu, T., Teng, J.G. FRP-confined circular concrete-filled thin steel tubes under axial compression. *ASCE Journal of Composites in Construction*. 2011. 15 (5). Pp. 850–860. DOI: 10.1061/(ASCE)CC.1943-5614.0000217
- Yu, T., Hu, Y.M., Teng, J.G. FRP-confined circular concrete-filled steel tubular columns under cyclic axial compression. *Journal of Construction Steel Research*. 2014. 94 (1). Pp. 33–48. DOI: 10.1016/j.jcsr.2013.11.003
- Teng, J.G., Hu, Y.M., Yu, T. Stress-strain model for concrete in FRP-confined steel tubular columns. *Engineering Structures*. 2013. 49 (1). Pp. 156–167. DOI: 10.1016/j.engstruct.2012.11.001
- Kodur, V., Agrawal, A. An approach for evaluating residual capacity of reinforced concrete beams exposed to fire. *Engineering Structures*. 2016. 110 (1). Pp. 293–306. DOI: 10.1016/j.engstruct.2015.11.047
- Al-Ostaz, A., Irshidat, M., Tenkhoff, B., Ponnappalli, P.S. Deterioration of bond integrity between repair material and concrete due to thermal and mechanical incompatibilities. *Journal of Materials in Civil Engineering*. 2010. 22 (2). Pp. 136–144. DOI: 10.1061/(ASCE)0899-1561(2010) 22:2(136)
- Nedviga, E., Beresneva, N., Gravit, M., Blagodatskaya, A. Fire Resistance of Prefabricated Monolithic Reinforced Concrete Slabs of "Marko" Technology. *Adv. Intell. Syst. Comput.* 2018. 692 (1). Pp. 739–749. DOI: 10.1007/978-3-319-70987-1_78
- Hezhev, T.A., Zhurlov, A.V., Tsipinov, A.S., Klyuev, S.V. Fire resistant fibre reinforced vermiculite concrete with volcanic application. *Magazine of Civil Engineering*. 2018. 80 (1). Pp. 181–194. DOI: 10.18720/MCE.80.16
- Goremikins, V., Blesak, L., Novak, J., Wald, F. Experimental investigation on SFRC behaviour under elevated temperature. *Journal of Structural Fire Engineering*. 2017. 8 (1). Pp. 287–299. DOI: 10.1108/JSFE-05-2017-0034
- Goremikins, V., Blesak, L., Novak, J., Wald, F. To testing of steel fibre reinforced concrete at elevated temperature. *Applications of Structural Fire Engineering*. 2017. 1 (1). Pp. 48–54. DOI: 10.14311/asfe.2015.055
- Blesak, L., Goremikins, V., Wald, F., Sajdlova, T. Constitutive model of steel fibre reinforced concrete subjected to high temperatures. *Acta Polytechnica*. 2016. 56 (1). Pp. 417–424. DOI: 10.14311/AP.2016.56.0417
- Korsun, V., Vatin, N., Franchi, A., Korsun, A., Crespi, P., Mashtaler, S. The strength and strain of high-strength concrete elements with confinement and steel fiber reinforcement including the conditions of the effect of elevated temperatures. *Procedia Engineering*. 2015. 117 (1). Pp. 970–979. DOI: 10.1016/j.proeng.2015.08.192
- Goremikins, V., Blesak, L., Novak, J., Wald, F. Experimental method on investigation of fibre reinforced concrete at elevated temperatures. *Acta Polytechnica*. 2016. 56 (1). Pp. 258–264. DOI: 10.14311/AP.2016.56.0258
- Selyaev, V.P., Nizina, T.A., Balykov, A.S., Nizin, D.R., Balbalin, A.V. Fractal analysis of deformation curves of fiber-reinforced fine-grained concretes under compression. *PNRPU Mechanics Bulletin*. 2016. 1 (1). Pp. 129–146. DOI: 10.155-93/perm.mech/2016.1.09

26. Bily, P., Fladr, J., Kohoutkova, A. Finite Element Modelling of a Prestressed Concrete Containment with a Steel Liner. Proceedings of the Fifteenth International Conference on Civil, Structural and Environmental Engineering Computing. Civil-Comp Press. 2015. DOI: 10.4203/ccp.108.1
27. Bílý, P., Kohoutková, A. Sensitivity analysis of numerical model of prestressed concrete containment. Nuclear Engineering and Design. 2015. 295 (1). Pp. 204–214. DOI: 10.1016/j.nucengdes.2015.09.027
28. Al-Rousan, R. Behavior of two-way slabs subjected to drop-weight. Magazine of Civil Engineering. 2019. 90(6). Pp. 62–71. DOI: 10.18720/MCE.90.6
29. Al-Rousan, R. The impact of cable spacing on the behavior of cable-stayed bridges. Magazine of Civil Engineering. 2019. 91 (7). Pp. 49–59. DOI: 10.18720/MCE.91.5
30. Krishan, A., Rimshin, V., Erofeev, V., Kurbatov, V., Markov, S. The energy integrity resistance to the destruction of the long-term strength concrete. Procedia Engineering. 2015. 117 (1). Pp. 211–217. DOI: 10.1016/j.proeng.2015.08.143
31. Korsun, V., Vatin, N., Korsun, A., Nemova, D. Physical-mechanical properties of the modified fine-grained concrete subjected to thermal effects up to 200°S. Applied Mechanics and Materials. 2014. 633–634. Pp. 1013–1017. DOI: 10.4028/www.scientific.net/AMM.633-634.1013
32. Korsun, V., Korsun, A., Volkov, A. Characteristics of mechanical and rheological properties of concrete under heating conditions up to 200°C. MATEC Web Conference. 2013. 6 (1). Pp. 07002. DOI: 10.1051/mateconf/20130607002
33. Petkova, D., Donchev, T., Wen, J. Experimental study of the performance of CFRP strengthened small scale beams after heating to high temperatures. Construction and Building Materials. 2014. 68 (1). Pp. 55–61. DOI: 10.1016/j.conbuildmat.2014.06.014
34. Ji, G., Li, G., Alaywan, W. A new fire resistant FRP for externally bonded concrete repair. Construction and Building Materials. 2013. 42 (1). Pp. 87–96. DOI: 10.1016/j.conbuildmat.2013.01.008
35. Trentin, C., Casas, J.R. Safety factors for CFRP strengthening in bending of reinforced concrete bridges. Composite Structures. 2015. 128 (1). Pp. 188–198. DOI: 10.1016/j.compstruct.2015.03.048
36. Ferrari, V.J., Hanai, J.B. de, Souza, R.A. de. Flexural strengthening of reinforcement concrete beams using high performance fiber reinforcement cement-based composite (HPFRCC) and carbon fiber reinforced polymers (CFRP). Construction and Building Materials. 2013. 48 (1). Pp. 485–498. DOI: 10.1016/j.conbuildmat.2013.07.026
37. Attari, N., Amziane, S., Chemrouk, M. Flexural strengthening of concrete beams using CFRP, GFRP and hybrid FRP sheets. Construction and Building Materials. 2012. 37 (1). Pp. 746–757. DOI: 10.1016/j.conbuildmat.2012.07.052
38. Kara, I.F., Ashour, A.F., Körog̃lu, M.A. Flexural behavior of hybrid FRP/steel reinforced concrete beams. Composite Structures. 2015. 129 (1). Pp. 111–121. DOI: 10.1016/j.compstruct.2015.03.073
39. Rajai, Z., Al-Rousan, I., Abo-Msamh. Bending and torsion behaviour of CFRP strengthened RC beams. Magazine of Civil Engineering. 2019. 92 (8). Pp. 48–62. DOI: 10.18720/MCE.92.4
40. Rajai, Z., Al-Rousan. The shear behavior of CFRP strengthened RC beams. Magazine of Civil Engineering. 2020. 98 (6). Art. No. 9810. DOI: 10.18720/MCE.98.10
41. Yu, T., Hu, Y.M., Teng, J.G. Cyclic lateral response of FRP-confined circular concrete-filled steel tubular columns. Journal of Constructional Steel Research. 2016. 124 (1). Pp. 12–22. DOI: 10.1016/j.jcsr.2016.05.006
42. Rajai, Z., Al-Rousan, I. Behavior of CFRP strengthened columns damaged by thermal shock. Magazine of Civil Engineering. 2020. 97 (5). Art. No. 9708. DOI: 10.18720/MCE.99.10
43. Rajai, Z., Al-Rousan. Behavior of strengthened concrete beams damaged by thermal shock. Magazine of Civil Engineering. 2020. 94 (2). Pp. 93–107. DOI: 10.18720/MCE.94.8

Contacts:

Rajai Al-Rousan, rzalrousan@just.edu.jo



DOI: 10.34910/MCE.108.9

Effective seismic response control of buildings with sliding bearings

A. Dushimimana^{a*} , E. Singirankabo^b, L. Kathumbi^b 

^a Ondokuz Mayıs University, Körfez, Turkey

^b Pan African University Institute for Sciences, Technology and Innovation, Juja, Nairobi

*E-mail: chenkodu432@gmail.com

Keywords: Seismic isolation, friction pendulum bearing, flat surface slider, restoring force, energy dissipation, superstructure acceleration, story drift, shear force, near and far-fault ground motion

Abstract. A complete response investigation on behavior of conventional sliding bearings applicable to seismic-isolated structures has not yet been fully realized, while use of such bearings is a common practice. A Full Structural Response Investigation (FSRI) comprising energy dissipation, bearing's effective and post-yield stiffness, displacements, story drifts, shear forces, accelerations and time instants for peak responses has been carried out on a ten-story RC building model with varied superstructure stiffness, and isolated by flat and curved surface sliders under different types of earthquakes. Disregarding some of the responses mentioned above FSRI can result in poor control of seismic isolation, since all the responses are observed to be affected by the type of earthquake and bearing's slider surface. Furthermore, the findings demonstrate that seismic isolation may not provide all desired responses, and in some situations, some responses may need to be of first priority owing to their beneficial effects.

1. Introduction

Seismic isolation is about decoupling a structure from the ground so that seismic loads cannot be transmitted to the superstructure when an earthquake occurs. Since twentieth century, seismic isolation has been adopted as a strategy and accepted design technique for protecting structures against earthquake hazards. Isolators decouple a superstructure from its substructure that is in turn resting on the ground and reduce the superstructure's natural frequency by dissipating energy from seismic load. Existing seismic isolators include mainly elastomeric and sliding bearings. The latter has greater durability feature and is more preferred for large deformations, and more attractive due to its mechanism to restore force by gravity action and ability to be designed independent of the superstructure's effective mass, hence easy to model [1–3]. Sliding bearing systems are displacement dependent for passive energy dissipation, and are based on simple principle of friction. The main advantage of these isolation systems is the possibility to control a wide range of frequencies and the maximum acceleration transmitted to the superstructure using the coefficient of friction [2–4].

The sliding bearing systems are subdivided into pure friction (PF) systems, flat surface sliding bearings and Friction Pendulum Systems (FPS). PFs are the first innovations in isolation by friction: they depend on friction coefficient with sliding occurring when excitation force exceeds the frictional force [5, 6]. PFs have been reported to be effective for buildings with no overturning moments [6]. Flat surface sliding bearings are free sliding with no restoring force, simple and economical [7–10]. Furthermore, these bearings have low coefficient of friction that ranges from 0.1 to 0.15 and less than 0.02 for unlubricated and lubricated bearings, respectively [11]. Flat sliding bearings differ from the curved surface bearings in that their restoring force is provided by adding springs in the system, while

Dushimimana, A., Singirankabo, E., Kathumbi, L.K. Effective seismic response control of buildings with sliding bearings. Magazine of Civil Engineering. 2021. 108(8). Article No. 10809. DOI: 10.34910/MCE.108.9

© Dushimimana, A., Singirankabo, E., Kathumbi, L.K., 2021. Published by Peter the Great St. Petersburg Polytechnic University



This work is licensed under a CC BY-NC 4.0

the spherical surface provides restoring force for the curved FPS [12]. FPS were invented in order to solve the problems exhibited in pure friction systems regarding permanent displacement by provision of a restoring force mechanism [13, 14]. FPS operate based on the principle of the pendulum motion and like PF systems, they also depend on the friction coefficient [15].

Over the last years, innovations in various FPS have been developed to enable multiple performance of the bearing system in seismic isolation using curved surface bearings and identified by the number of effective pendula and sliding regimes. The first being the single FPS invented back in 1980s [16, 17]. Later on, authors in [18] modified equation of single FPS to describe a smooth transition of breakaway to minimum sliding coefficient of friction. This bearing is characterized by a single sliding surface, but it is challenged by resonance, thus rendering it ineffective for some structures as the isolated structure can collapse [14, 19, 20]. To solve this problem, double FPS was invented with two effective pendula and three sliding regimes to improve relative displacement capacity and isolator flexibility [12, 21]. Researchers in [22] modified the double FPS by developing triple FPS with three effective pendula and five sliding regimes. A significant number of researchers have additionally reported various advantages of triple FPS over double FPS such as greater strength and stiffness in response to change in displacement and velocities, increased energy dissipation capacity and adaptive behavior [22–28]. The latest innovation is the quintuple friction pendulum isolator, an innovation of Lee et al. [29], with five effective pendula and nine sliding regimes. The added number of pendula as well as the sliding regimes have added advantage of adaptability, but made its behavior too complex to model [29]. These systems have been reported to show great performance, though not fully developed as they still lack experimental studies [3]. The study of Mokha et al. [7] on flat sliding bearings showed a good agreement between numerical and experimental results when experimentally derived parameters of $\mu_{\max} = 0.12$, $\mu_{\min} = 0.0389$, and $\alpha = 15.75$ s/m under bearing pressure of 3.45 MPa were adopted. Also a study by Xu et al. [18] on static friction of curved sliders under low to moderate earthquakes showed that for isolators with low friction coefficients, an increase of breakaway-to-minimum ratio from 1 to 4 induced moderate changes in bearing shear forces, superstructure drift and floor accelerations, while for moderate and high isolators' friction the breakaway-to-minimum ratio of 2 introduced no significant changes.

Poornima and Babu [30] reported that for a 15 story RC building, FPS were the best in seismic isolation in comparison with Lead Rubber Bearings (LRB) and high damping rubber bearings. They concluded that FPS with damping ratio of 0.05 and friction coefficient from 0.03 to 0.06 could increase isolated building period by 37.97 % and top floor displacement by 29.05 %, while decreasing story acceleration, story shear and story drifts by 56.31 %, 63.828 % and 44.15 %, respectively. However, previous study on a 5 story RC building by Pokhrel et al. [31] had reported that both LRB and FPS can reduce base shear force, inter-story drifts and top floor acceleration by 50 %, and adding that while LRBs were the best in reducing elastic base shear as well as inter-story drifts, FPS showed greater control of isolator displacement for adopted bearing characteristics and wider hysteresis loop under far-fault earthquakes.

To date, there have been appreciable modifications of sliding bearings, and a substantial number of existing researches seem to have been mainly focusing on modified bearings (double, triple, and quintuple FPS), with less literature on the conventional (flat and single curved) bearings despite of their greater economic advantages [7, 9], and hence their potential applicability in developing countries. Furthermore, the existing literature on conventional sliding bearings seem to have been partially developed in terms of Full Structural Response Investigation (FSRI) on the behavior of both bearings and isolated superstructure when exposed to near and far-fault ground motions. Most importantly, studies that fully examine seismic isolation behavior in terms of FSRI (energy dissipation, top and base floor displacements, story drifts, superstructure accelerations, base shear force and accelerations, isolator's effective and post-yield stiffness variation, optimal control of bearing's hysteretic behavior, and control on the time instants for the occurrence of structural peak responses) under different types of earthquakes seem to have not yet been conducted. The authors of this study believe that in order to gain insights on effective performance of seismic isolation under different types of seismic loads, it is necessary to conduct studies that are pertinent to FSRI. In this regard, the main purpose of this study was to control the responses of a 10 story RC building model isolated by conventional sliding bearings and exposed to both near and far-fault earthquake ground motions, by applying FSRI to ensure a full seismic response control on the above building. In addition to the governing equations for flat and single-curved surface sliders, the study also attempted to formulate an improved equation for curved slider having its stiffness as a tenth of the first story structure and compared its results with ones from the existing curved slider equation.

2. Methods

In order to achieve the objectives of this study, equations governing the dynamic behavior of superstructure and substructure were first defined. Furthermore, a numerical study on seismic response control of a 10 story RC building model isolated by flat and curved surface sliding bearings was conducted by using the aforementioned equations.

2.1. Governing Equations

The equation governing a dynamic motion of any structure that is fixed at its base and exposed to a dynamic load can be written as:

$$M_{n \times n} \ddot{U}_{n \times 1} + C_{n \times n} \dot{U}_{n \times 1} + K_{n \times n} U_{n \times 1} = -M_{n \times n} R_{n \times 1} \{\ddot{U}_g\}. \quad (1)$$

For a dynamic motion of a structure isolated at its base, the governing differential equations can be expressed as:

$$\begin{pmatrix} [I] & [\Phi^T MR] \\ [R^T \Phi] & [R^T MR + M_b] \end{pmatrix}_{(m+1)(m+1)} \begin{Bmatrix} \ddot{U}^* \\ \ddot{U}_b \end{Bmatrix} + \begin{pmatrix} [2\xi_i \omega_i] & 0 \\ 0 & [C_b] \end{pmatrix}_{(m+1)(m+1)} \begin{Bmatrix} \dot{U}^* \\ \dot{U}_b \end{Bmatrix} + \begin{pmatrix} [\omega_i^2] & 0 \\ 0 & [K_b] \end{pmatrix}_{(m+1)(m+1)} \begin{Bmatrix} U^* \\ U_b \end{Bmatrix} = - \begin{bmatrix} \Phi^T MR \\ R^T MR + M_b \end{bmatrix}_{(m+1) \times 1} \ddot{U}_g \quad (2)$$

Where $U_n = \phi_{n \times m} U_{m \times n}^*$ and ϕ is the modal matrix of fixed base superstructure normalized with respect to mass, and is used to find the diagonal matrices: $\Phi^T M \Phi = I$, $\Phi^T K \Phi = \omega^2$, $\Phi^T C \Phi = 2\xi\omega$, where ω is diagonal matrix of natural frequencies of fixed base structure, ξ is diagonal matrix of damping ratio of fixed base structure, U^* , \dot{U}^* , \ddot{U}^* are model displacement, velocity and acceleration vectors relative to the base, m is the number of eigenvectors retained in the analysis, ξ_i is modal damping ratio and ω_i is natural frequency of fixed base structure for mode i , M is the diagonal superstructure mass matrix, C is superstructure damping matrix, K is the superstructure stiffness matrix, R is influence matrix, M_b is diagonal mass matrix of rigid base, K_b is resultant stiffness matrix of elastic isolation elements, C_b is resultant damping matrix of viscous isolation element, U_b , \dot{U}_b , \ddot{U}_b are vectors of base displacement, velocity and accelerations relative to the ground respectively, \ddot{U}_g is vector of ground acceleration, f is vector containing forces mobilized in the nonlinear elements of the isolation system. Equation (2) has been adopted in 3D-BASIS Software by Tsopelas et al. [32]. However, for simplicity and easy solution by 4th order Runge-Kutta algorithm, this equation can also be expressed as shown below:

a) The equation governing a dynamic motion of superstructure can be written as:

$$M_{n \times n} \ddot{U}_{n \times 1} + C_{n \times n} \dot{U}_{n \times 1} + K_{n \times n} U_{n \times 1} = -M_{n \times n} R_{n \times 1} \{\ddot{U}_g + \ddot{U}_b\}, \quad (3)$$

Where n is the number of floors, $M_{n \times n}$ is the diagonal superstructure mass matrix, $C_{n \times n}$, $K_{n \times n}$ are the superstructure damping and stiffness matrices respectively, and $U_{n \times 1}$, $\dot{U}_{n \times 1}$, $\ddot{U}_{n \times 1}$ are vectors of superstructure displacement, velocity, and acceleration for n floors, respectively.

From equation (3), $\ddot{U}_{n \times 1}$ can be expressed as:

$$\ddot{U}_{n \times 1} = - \left(M_{n \times n} R_{n \times 1} (\ddot{U}_g + \ddot{U}_b) + C_{n \times n} \dot{U}_{n \times 1} + K_{n \times n} U_{n \times 1} \right) / M_{n \times n}. \quad (4)$$

Then, Equation (4) yields

$$\ddot{U}_{n \times 1} = - (\ddot{U}_g + \ddot{U}_b) - (C_{n \times n} \dot{U}_{n \times 1} + K_{n \times n} U_{n \times 1}) / M_{n \times n}. \quad (5)$$

- b) The equation governing a unidirectional dynamic motion of base structure can be expressed as:

$$R_{1 \times n}^T M_{n \times n} \left\{ \left\{ \ddot{U} \right\}_{n \times 1} + R_{n \times 1} \left\{ \ddot{U}_b + \ddot{U}_g \right\}_{1 \times 1} \right\} + M_{b \ 1 \times 1} \left\{ \ddot{U}_b + \ddot{U}_g \right\}_{1 \times 1} + C_{b \ 1 \times 1} \left\{ \dot{U}_b \right\}_{1 \times 1} + K_{b \ 1 \times 1} \left\{ U_b \right\}_{1 \times 1} + \left\{ f \right\}_{1 \times 1} = 0, \quad (6)$$

Where, $R_{1 \times n}^T$ is the transpose of the influence matrix, 1×1 is the index representing a one by one matrix or simply a single value (for each time step) when unidirectional motion is considered.

Rearranging Equation (6),

$$R_{1 \times n}^T M_{n \times n} \ddot{U}_{n \times 1} + R_{1 \times n}^T M_{n \times n} R_{n \times 1} \left\{ \ddot{U}_b + \ddot{U}_g \right\}_{1 \times 1} + M_{b \ 1 \times 1} \ddot{U}_{b \ 1 \times 1} + M_{b \ 1 \times 1} \ddot{U}_{g \ 1 \times 1} + C_{b \ 1 \times 1} \dot{U}_{b \ 1 \times 1} + K_{b \ 1 \times 1} U_{b \ 1 \times 1} + f_{1 \times 1} = 0. \quad (7a)$$

Equation (7a) can be rearranged such that $\ddot{U}_{b \ 1 \times 1}$ is easily obtained:

$$\ddot{U}_{b \ 1 \times 1} \frac{\left(R_{1 \times n}^T M_{n \times n} R_{n \times 1} + M_{b \ 1 \times 1} \right)}{A_b} = \frac{-\left(R_{1 \times n}^T M_{n \times n} \ddot{U}_{n \times 1} + R_{1 \times n}^T M_{n \times n} R_{n \times 1} \ddot{U}_{g \ 1 \times 1} + M_{b \ 1 \times 1} \ddot{U}_{g \ 1 \times 1} + C_{b \ 1 \times 1} \dot{U}_{b \ 1 \times 1} + K_{b \ 1 \times 1} U_{b \ 1 \times 1} + f_{1 \times 1} \right)}{B_b}. \quad (7b)$$

Then, the base floor acceleration for each time step can be solved as:

$$\ddot{U}_{b \ 1 \times 1} = A_b^{-1} * B_b. \quad (7c)$$

The superstructure mass, stiffness and damping matrices can be formulated as:

$$[M_{n \times n}] = \begin{bmatrix} m_1 & 0 & 0 & 0 & 0 & 0 \\ 0 & m_2 & 0 & 0 & 0 & 0 \\ 0 & 0 & m_3 & 0 & 0 & 0 \\ 0 & 0 & 0 & \dots & 0 & 0 \\ 0 & 0 & 0 & 0 & \dots & 0 \\ 0 & 0 & 0 & 0 & 0 & m_n \end{bmatrix}, \quad (8)$$

$$[K_{n \times n}] = \begin{bmatrix} k_1 + k_2 & -k_2 & 0 & 0 & 0 & 0 \\ -k_2 & k_2 + k_3 & -k_3 & 0 & 0 & 0 \\ 0 & -k_3 & k_3 + k_4 & -k_3 & 0 & 0 \\ 0 & 0 & \dots & \dots + \dots & \dots & 0 \\ 0 & 0 & 0 & \dots & \dots + \dots & -k_n \\ 0 & 0 & 0 & 0 & -k_n & k_n \end{bmatrix}. \quad (9)$$

In this study, the superstructure damping matrix $[C_{n \times n}]$ was calculated from $[M_{n \times n}]$ and $[K_{n \times n}]$ based on Rayleigh formula [4, 33], which is defined as shown in Equation (10).

$$[C_{n \times n}] = \alpha_0 [M_{n \times n}] + \alpha_1 [K_{n \times n}]. \quad (10)$$

To obtain the coefficients α_0 and α_1 , Equation (11) can be used [34].

$$\frac{1}{2} \begin{bmatrix} \frac{1}{w_i} & w_i \\ \frac{1}{w_j} & w_j \end{bmatrix} \begin{Bmatrix} \alpha_0 \\ \alpha_1 \end{Bmatrix} = \begin{Bmatrix} \xi_i \\ \xi_j \end{Bmatrix}, \tag{11}$$

where w_i, w_j and ξ_i, ξ_j are natural frequencies and damping ratios of the non-isolated structure with i^{th} and j^{th} modes respectively. The damping ratios at i^{th} and j^{th} can be assumed as shown in [4].

The hysteretic behavior of sliding bearings has been modelled by a substantial number of researchers using Bouc-Wen model for dynamic analysis of bilinear and non-linear hysteretic systems [6, 32]. This model is adopted in this study for hysteretic force (f) of flat and curved bearings.

For flat surface sliding bearings:

$$f_x = \mu W Z_x. \tag{12}$$

For single curved surface sliding bearings:

$$f_x = \frac{w}{R_{eff}} U_b + \mu W Z_x. \tag{13}$$

Apart from Eq. (12) and (13), a new formulation typical to Eq. (13) is formulated as shown in Eq. (14) where the isolator stiffness is directly related to the first story stiffness through the value K_c . Eq. (12)–(14) are all adopted and compared to examine their effectiveness. Particularly, Eq. (14) is compared with the existing Eq. (13) to examine its possible applicability for other structures with same properties as one investigated in this study.

$$f_x = K_c U_b + \mu W Z_x. \tag{14}$$

Where:

$$\mu(\dot{u}) = \mu_{\max} - (\mu_{\max} - \mu_{\min}) e^{-\alpha|\dot{u}|}, \tag{15}$$

f_x is hysteretic force in x -direction, μ is the coefficient of friction, α is a constant and the parameters μ_{\min} and μ_{\max} describe the friction coefficients at essentially zero and high velocities, respectively, R_{eff} is the radius of curvature, W is the total weight of the structure calculated as: $W = (\sum_{i=1}^{10} m_i + M_b) \times g$, where, g is the gravity acceleration and m_i is the mass at the i^{th} floor; K_c is the tenth of the first story stiffness, and Z_x is a hysteretic component of the unidirectional Wen's non-linear model and can be derived from Equation (16).

$$\dot{Z}_x = \left[A \dot{U}_{bx} - \dot{U}_{bx} Z_x^2 \left(\gamma \text{sign}(\dot{U}_{bx} Z_x) + \beta \right) \right] / U_y, \tag{16}$$

where A, γ, β are dimensionless quantities, x stands for the base motion in x -direction, U_y is the yield displacement. The idealized hysteretic behavior of the aforementioned bearings is shown in Fig. 1.

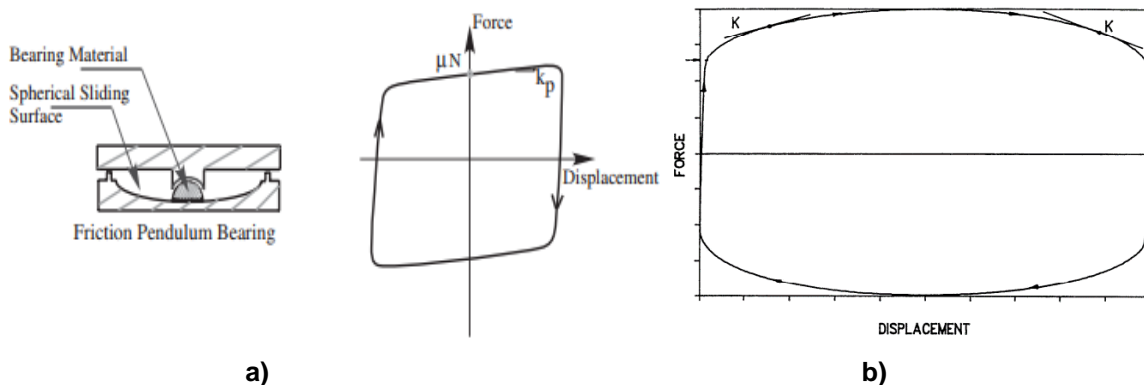


Figure 1. Idealized force-displacement relations: a) curved, b) flat surface sliding bearings.

In this study, Eq. (5) and (7c) derived from the general equations of superstructure and base motion respectively, and Eq. (12) through (16) were solved by 4th order Runge-Kutta algorithm in MATLAB environment. The detailed procedures involved in this algorithm can be found in [34].

2.2. Numerical Study

Responses of 10 story structure model under four input parameters and three earthquake ground motions were investigated with respect to flat and curved surface sliding bearings defined by Equations (12)–(14). The earthquakes were sourced from PEER strong ground motions [35], then filtered and corrected using Seismosignal Software(SS). The characteristics of these earthquakes are summarized in Table 1. It is important to mention that various kinds of excitations have been proposed to investigate dynamic behavior of isolated structures, such as the use of blasts [36] and micro tremors [37], however, this study focused on the use of near and far-fault earthquakes occurred in the past. The engineering data used for the above structure are shown in Table 2. Additionally, structural masses lumped at each floor, story height of 3 m for each floor and overall damping ratio of 5 percent are assumed for the investigated structure. The values of K_b , M_b and C_b are assumed equal to ones of the first story stiffness, mass and damping, respectively. K_c is taken as the tenth of the first story stiffness, for each input. Yield strength of the isolator is computed as $U_y = F_y / K_b$, and the friction parameters adopted are: $\mu_{\min} = 0.02$, $\mu_{\max} = 0.15$, $R_{\text{eff}} = 0.435$ m, $A = 1$, $\beta = 0.1$, and $\gamma = 0.9$. It is important to note that these friction parameters and data shown in Table 2 for Input 2 have been previously adopted in [23]. The response quantities of interest investigated are: Energy Dissipation Capacity (EDC), Maximum Isolator Displacement (MID), Maximum Isolator Force (MIF), top floor displacements, story drifts, base floor shear force and accelerations, isolator's effective and post-yield stiffness variation, peak story accelerations, peak story shear forces, optimal control of bearing's hysteretic behavior (by checking the relationship among MID, MIF and EDC), and control on the Time Instants (TIs) for the occurrence of structural peak story displacements under the aforementioned earthquakes.

Table 1. Characteristics of used earthquakes.

Earthquake	Component	PGA (m/s ²)	PGV(m/s)	PGD(m)	Te(s)	Type	Duration (s)
Elcentro	NS	3.42	0.32	0.09	2.88	LP	56.52
Düzce	EW	8.05	0.63	0.12	0.96	NF	55.85
Kobe	NS	8.03	0.92	0.18	1.10	NF	49.93

PGA, PGV, and PGD are peak ground acceleration, velocity and displacement respectively, Te: predominant period, NF: Near Fault, LP: Long period, NS: North-South direction, EW: East-West direction

Table 2. Input parameters.

		Story 1	Story 2	Story 3	Story 4	Story 5	Story 6	Story 7	Story 8	Story 9	Story 10
Input 1	m	400000	520000	520000	520000	520000	520000	520000	520000	520000	520000
	k	2187e5	800e5								
Input 2	m	8385063	8285063	8285063	8285063	8285063	8285063	8285063	8285063	8285063	8285063
	k	10.75e9	8.78e9	6.80e9	5.65e9	4.90e9	4.38e9	4.01e9	3.12e9	3.50e9	3.33e9
Input 3	m	8385063	8285063	8285063	8285063	8285063	8285063	8285063	8285063	8285063	8285063
	k	10.75e11	8.78e11	6.80e11	5.65e11	4.90e11	4.38e11	4.01e11	3.12e11	3.50e11	3.33e11
Input 4	m	8385063	8285063	8285063	8285063	8285063	8285063	8285063	8285063	8285063	8285063
	k	10.75e12	8.78e12	6.80e12	5.65e12	4.90e12	4.38e12	4.01e12	3.12e12	3.50e12	3.33e12

Abbreviations: m: mass of superstructure (in Kg), k: stiffness of superstructure in (in N/m)

Insights on the inputs shown in Table 2 demonstrate that both mass and stiffness values are kept equal under Input 1 for all floors except for 1st story floor. On the other hand, Input 2 has the same story mass but varied story stiffness. Furthermore, Input 3 and 4 are of similar trend as Input 2 except that their story stiffness are 10^2 and 10^3 times the story stiffness of Input 2, respectively. Existing literature demonstrates that superstructure stiffness can be increased through retrofitting and strengthening [38–40], use of shear walls and braced frames [41, 42], as well as central core, tube and double tube systems. That is, increasing superstructure stiffness is important because the current building industry is toward larger floors, longer spans and taller buildings, all of which may require sufficient structural stiffness against both axial and dynamic loads. In this regard, the story stiffness was increased to examine the effect of superstructure stiffening on behavior of the used bearings.

3. Results and Discussion

3.1. Top Floor Displacements

Floor displacement control is vital, as very large and dangerous superstructure displacements can occur in earthquake-prone areas [43], hence damaging sensitive equipment in buildings, especially those located in NF zones where long period earthquakes can occur [44]. Under moderate earthquakes like Elcentro, the top floor relative displacements (U_{top}) are observed to be equal for all equations under each input as can be seen in Fig. 2. That is, (U_{top}) are observed to be approximately 0.28, 0.13, 0.0041 and 0.00044 m for Inputs 1, 2, 3 and 4 respectively.

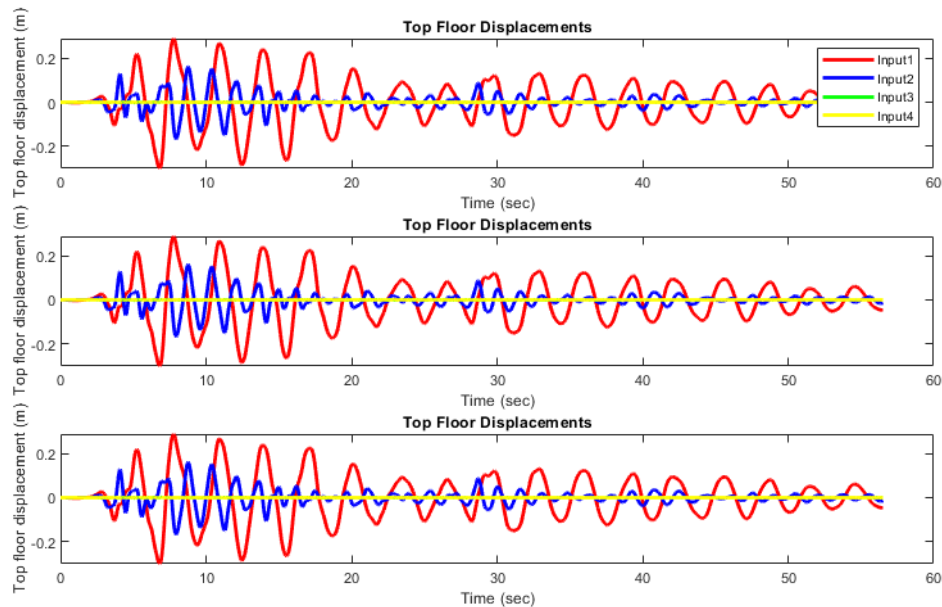


Figure 2. Top floor displacements under equations (12) to (14) (from top to bottom) – Elcentro.

Similar trends are also observed for Kobe earthquake, where (U_{top}) of approximately 0.4, 0.5, 0.0075, and 5.78×10^{-4} m are obtained for Input 1, 2, 3 and 4, respectively under Equations (12)–(14). Based on this observation, Input 1 is the most favourable as it results in reasonably reduced (U_{top}) for a 10 story structural model compared to other inputs. This shows the importance of using equal stiffness for all floors in reduction of (U_{top}) under strong earthquake by approximately 10 %.

Like Elcentro and Kobe earthquake, Duzce is also observed to result in similar trend of (U_{top}) with approximately 0.2, 0.2, 0.0073, and 6.0279×10^{-4} m for Input 1, 2, 3 and 4, respectively. However, using similar story stiffness values under Duzce and Elcentro result in unwanted long-lasting (U_{top}) peaks over nearly the entire duration of each earthquake (Fig. 2, 4), which can cause substantial cracks in structural components of the superstructure. Deep insights on this unwanted behavior can be found referring to Table 4, where the time instants of the occurrence of maximum story peaks are observed to alter significantly between story 5 to 6 and 9 to 10 under Duzce and 7 to 8 and 8 to 9 under Elcentro, and hence outlining that use of similar superstructure stiffness may be unreliable in controlling superstructure displacements when such earthquakes occur. Furthermore, the pronounced long-lasting (U_{top}) peaks over the entire duration of Elcentro and Duzce lead to suggesting that PGA alone may not characterize the earthquake severity, since those two earthquakes have significantly different PGA values as can be seen in Table 1.

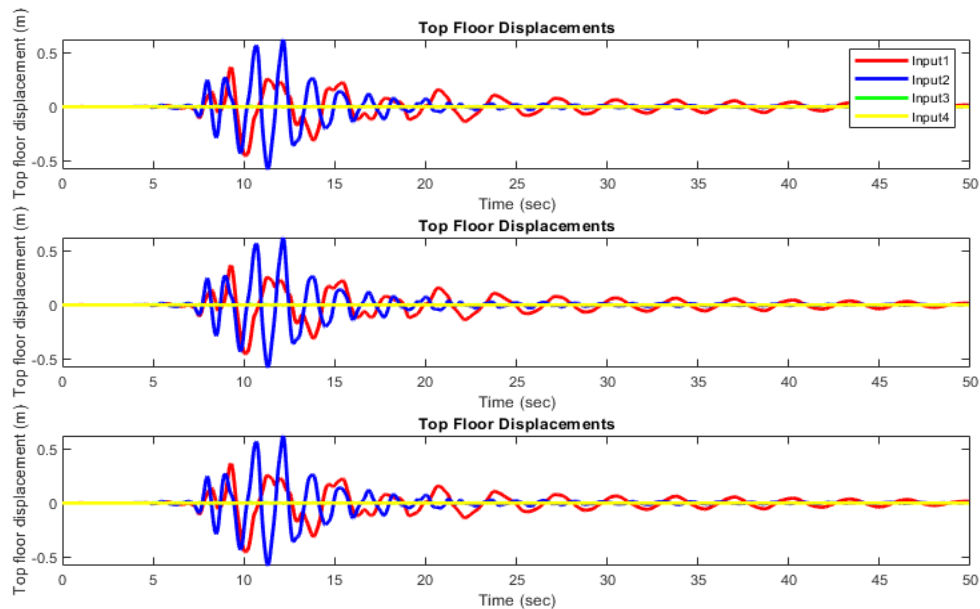


Figure 3. Top floor displacements under equations (12) to (14) (from top to bottom) – Kobe.

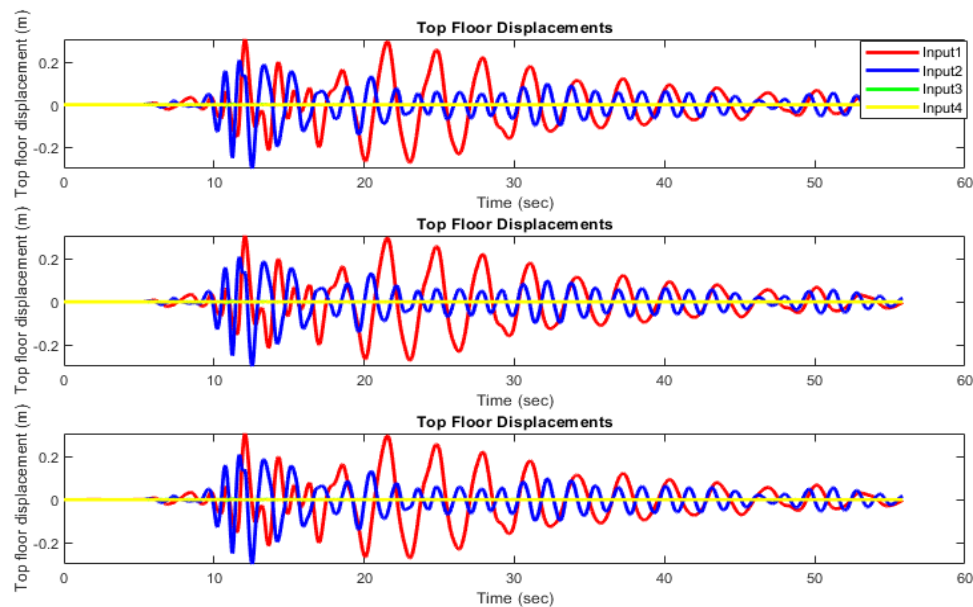


Figure 4. Top floor displacements under equations (12) to (14) (from top to bottom) – Duzce.

From the above results, it can be noted that Equations (12)–(14) perform similarly and equally in reducing top floor displacement (U_{top}) for each used input. Besides, under all three earthquakes it is seen that the resulting (U_{top}) are smaller when moderate LP earthquakes like Elcentro are used, rather than strong NF ones like Kobe. However, though Duzce is also classified as a strong NF earthquake, this earthquake and Elcentro are observed to result in comparable (U_{top}) as can be seen in Fig. 2 and 4. This may be interpreted as Duzce having a single PGA at around 10 s, followed by a sharp decrease in PGA and thereafter levelling off all along until its final duration time, a nature that is far different from Kobe's which has successive peak fluctuations over 8-13 s interval of time. Additionally, this shows that some NF earthquakes may behave like LP moderate ones, regardless of their PGA.

Under all earthquakes, the increase in stiffness leads to decrease in (U_{top}), and all the earthquakes tend to result in approximately similar displacement profiles as stiffness becomes large, which indicate that (U_{top}) of very stiff superstructure may not significantly be affected by the magnitude of the earthquake. Further observation shows that LP moderate & NF with smaller PGV earthquakes tend to cause the structure with varied story stiffness perform better than the structure with Dushimimana, A., Singirankabo, E., Kathumbi, L.K.

constant story stiffness in terms of (U_{top}) reduction, contrary to NF with higher PGV earthquakes where the effect is less pronounced. Looking at the resulting maximum (U_{top}) , it can be seen that Equation (12) results in the smallest (U_{top}) under all earthquakes for Inputs 1 and 2, thus making flat slider the most effective in terms of (U_{top}) reduction for less stiffened superstructure.

Table 3. Structural responses under all inputs and all earthquakes.

EARTHQUAKE	SLIDER	KOBE			DUZCE			ELCENTRO		
		Eq.(12)	Eq.(13)	Eq.(14)	Eq.(12)	Eq.(13)	Eq.(14)	Eq.(12)	Eq.(13)	Eq.(14)
Input1	$\ddot{U}_{b\max}$	3.6113	3.2088	3.5292	3.6556	2.7416	3.09	1.0847	0.9479	0.9804
	U_{top}	0.3746	0.403	0.3792	0.209	0.2682	0.235	0.2743	0.2825	0.2771
	$F_{sb\max}$	1.44e06	1.28e6	1.41e6	1.45e6	1.10e6	1.24e6	4.34e5	3.79e5	3.92e5
Input2	$\ddot{U}_{b\max}$	11.8702	9.3349	15.5153	8.1562	6.3273	7.5064	5.8244	3.9769	5.0927
	U_{top}	0.4881	0.5276	0.5067	0.2227	0.2443	0.2382	0.1224	0.1386	0.1288
	$F_{sb\max}$	9.26e7	7.83e7	9.05e7	6.76e7	5.31e7	6.29e7	4.56e7	3.33e7	4.13e7
Input3	$\ddot{U}_{b\max}$	0.9279	0.9252	1.3921	4.067	4.0562	3.4225	2.4584	2.448	1.9813
	U_{top}	0.0075	0.0075	0.0076	0.0073	0.0073	0.0075	0.0041	0.0041	0.0041
	$F_{sb\max}$	7.63e6	7.63e6	7.22e6	3.20e7	3.19e7	2.62e7	1.99e7	1.99e7	1.58e7
Input4	$\ddot{U}_{b\max}$	0.1731	0.1728	0.1701	0.7988	0.7974	0.6317	0.8018	0.8031	0.7074
	U_{top}	5.78e-4	5.78e-4	5.84e-4	6.03e-4	6.03e-4	6.08e-4	4.38e-4	4.36e-4	4.4e-4
	$F_{sb\max}$	1.45e6	1.45e6	1.42e6	6.70e6	6.69e6	5.30e6	5.78e6	5.79e6	5.57e6

Abbreviations: $\ddot{U}_{b\max}$ is base floor acceleration, U_{top} is top floor displacement, $F_{sb\max}$ is base shear force.

3.2. Base Floor Accelerations and Base Shear Forces

Looking at the resulting maximum base shear forces ($F_{sb\max}$) in Table 3, it can be seen that for very high stiffness all the used equations result in approximately equal $F_{sb\max}$ values of $1.9e^7$ and $5.7e^6$ N for Elcentro, $7.6e^6$ and $1.4e^6$ N for Kobe, $3.2e^7$ and $6.677e^6$ N for Duzce under Inputs 3 and 4, respectively. Similarly, approximately equal $\ddot{U}_{b\max}$ values of 2 and 0.8 m/s² for Elcentro, 1 and 0.2 m/s² for Kobe, 4 and 0.7 m/s² for Duzce are observed under the respective inputs. On the other hand, it can be seen that for all the used equations, the smaller the base acceleration the smaller the shear force, as expected [45]. Focusing on moderate stiffness, Input 1 is observed to result in smaller $F_{sb\max}$ than that from Input 4 for all the equations and earthquakes. Besides, Input 2 results in the highest value of $F_{sb\max}$ for all used equations and earthquakes, whereas Input 1 results in the least. This reveals that Input 1 can be the most effective in terms of $F_{sb\max}$ reduction compared to other inputs. Additionally, it can be seen that Equation (13) results in the smallest base shear force for Input 1 and 2, whereas Equation (14) results in the smallest force in all other inputs and earthquakes.

Focusing on the resulting maximum base accelerations ($\ddot{U}_{b\max}$) in Table 3 and Fig. 5, it can be seen that all equations perform equally in reducing or increasing accelerations for each input. It is clear that all equations result in $\ddot{U}_{b\max}$ of approximately 1, 2 and 0.8 m/s² for Inputs 1, 3, and 4 respectively, except for Input 2 where Equation (13) reduces $\ddot{U}_{b\max}$ more than the other equations.

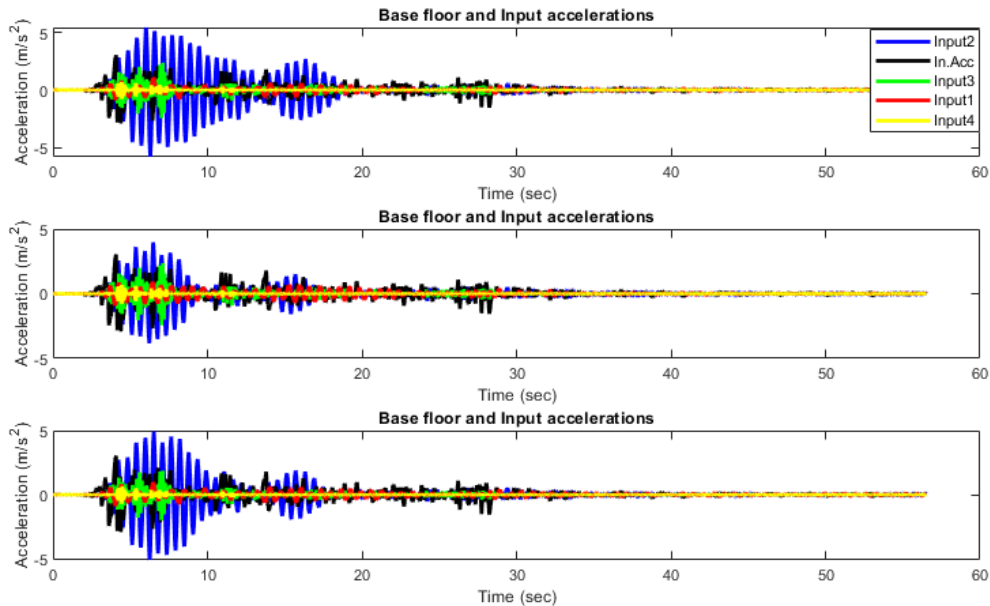


Figure 5. Base floor & Input accelerations under equations (12) to (14) (top to bottom) –Elcentro.

On the other hand, Input 1 results in slightly smaller $F_{sb\max}$ than that of Input 4 for all equations, and when Input 1 and 3 are used, Equation (13) tends to result in the smallest $F_{sb\max}$ compared to both Equation (12) and (14) as seen in Table 3. This indicates that Equation (13) can be more effective for structures with moderate stiffness than Equation (12) under NF earthquake ground motions. Further observation from Fig. 5 and 6 shows that Input 2 amplifies $\ddot{U}_{b\max}$ under both Kobe and Elcentro earthquakes while keeping $\ddot{U}_{b\max}$ from Duzce approximately equal to Duzce acceleration, except for Equation (12) where a slight amplification of nearly 0.1 m/s² is observed as can be seen in Table 3 and Fig. 7. Contrarily to Input 2, Input 1 is observed to result in the most desirable $\ddot{U}_{b\max}$ values of approximately 3.6113, 3.2088 and 3.5292 m/s²; 3.6556, 2.7416, and 3.09 m/s²; 1.0847, 0.9479 and 0.9804 m/s² from Equations (12), (13), and (14) under Kobe, Duzce and Elcentro earthquakes, respectively. This makes Input 2 less viable in terms of $\ddot{U}_{b\max}$ reduction, though was proven to perform better than Input 1 in terms of superstructure story displacements control.

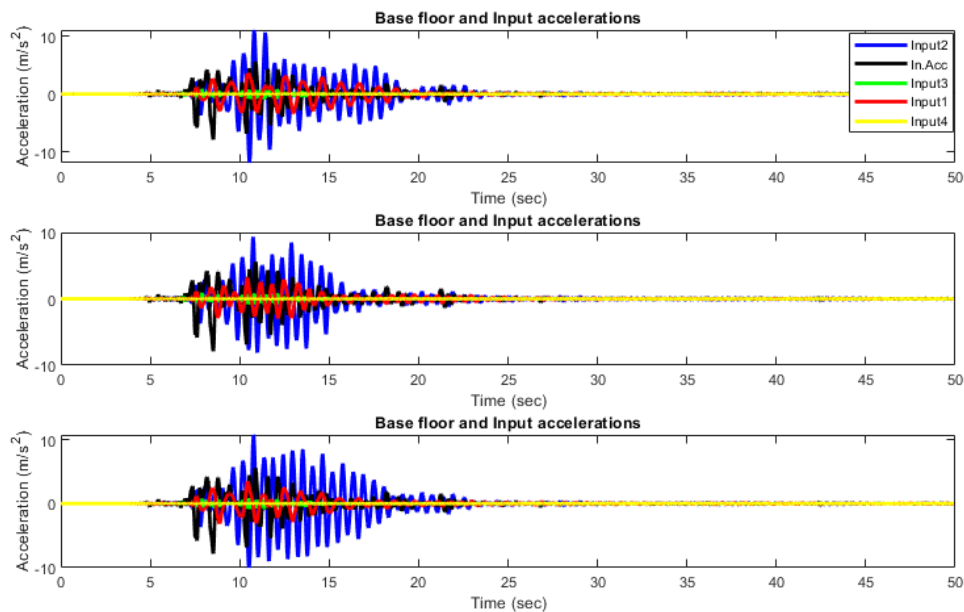


Figure 6. Base floor & Input accelerations for equations (12) to (14) (top to bottom) – Kobe.

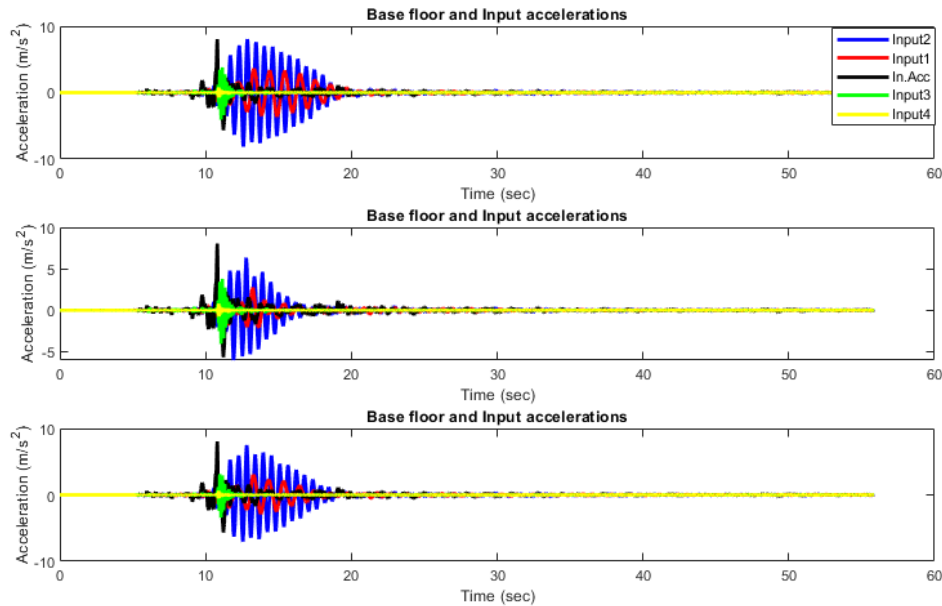


Figure 7. Base floor & Input accelerations for equations (12) to (14) (top to bottom) – Duzce.

On the other hand, a drastic increase in stiffness of the superstructure leads to drastic decrease in relative $\ddot{U}_{b\max}$ up to a value smaller than 1 m/s^2 as seen under Input 3 and 4 in Table 3. However, increasing stiffness can hinder reasonable isolator displacement as shown in Fig. 5, 6, 7, and Table 3. This is also confirmed by observing a substantial reduction of EDC, despite of the resulting reduced accelerations, hence indicating that stiffer systems can perform well in reducing the relative base shear forces and accelerations but poorly in dissipating sufficient energy as it will be shown in section 3.4. Overall, Input 1 and 3 can result in more benefits when considering shear forces, energy dissipation and base acceleration, but the former input can lead to large displacements for some earthquakes as explained in the previous section 3.1.

In order to make the isolator perform effectively by reducing $\ddot{U}_{b\max}$ and dissipating sufficient energy, Input 1 can be adopted for all investigated equations over other inputs. By prioritizing Input 1, it is clear from Table 3 that Equation (13) results in the smallest $\ddot{U}_{b\max}$ of approximately 3.2088, 2.7416, 0.9479 m/s^2 under Kobe, Duzce, and Elcentro, respectively, as compared to Equations (12) and (14) which result in 3.6113 and 3.5292 m/s^2 , 3.6556 and 3.09 m/s^2 , and 1.0847 and 0.9804 m/s^2 , under the same respective earthquakes, thus making Equation (13) the most effective for the investigated structure. For example, deep insights under Duzce earthquake show that approximately 55.8, 65.5 and 61.6 % $\ddot{U}_{b\max}$ reduction are observed from Equation (12), (13), and (14), respectively, making Equation (13) the most effective.

3.3. Time Instant for the occurrence of story floor displacements

The Time Instants (TIs) for which the maximum floor displacements take place are examined and the observed values are shown in Table 4. Investigating the TIs for which the peak responses take place can provide insights on the rigid body motion behavior of the superstructure. For instance, authors in [20] observed that under Elcentro earthquake, a six story building isolated by FPS resulted in a TI of 4.51 s for the superstructure displacements. In this study, under NF earthquakes like Kobe with Inputs 1 and 4, the maximum displacements from all used equations are observed to simultaneously occur at nearly 10 and 8.5 s, respectively. Besides, the displacements under Inputs 2 and 3 are observed to result in negligible differences of approximately 1 s in the first four floors and 2 s in the last three floors, respectively. Under Elcentro, Input 2 results in TIs of approximately 8 s. Similarly, Inputs 3 and 4 result in TIs of approximately 3.66 and 4.4 s. However, Input 1 tend to alter TIs significantly with a difference of 6s longer for 8th floor compared to other floors, thus showing lack of rigid motion behavior and making this input ineffective for the studied 10 story building when moderate LP earthquake occurs. Similar trends when Input 1 is adopted are observed even when strong earthquake like Duzce (NF, but with smaller PGV than Kobe's) is used with a substantial difference in TI between the first and last five floors, whereas the remaining Inputs 2, 3, and 4 cause the TIs to happen at reasonable values for all floors of nearly 12, 11, and 11 s respectively. Overall, the type of earthquake ground motion and input parameter are observed to influence the TIs, and therefore, for full control of structural responses under dynamic loads, TIs should be investigated.

Table 4. Time Instants for the occurrence of story floor displacements.

Earthquake		KOBE			DUZCE			ELCENTRO		
Slider	ST	Eq.(12)	Eq.(13)	Eq.(14)	Eq.(12)	Eq.(13)	Eq.(14)	Eq.(12)	Eq.(13)	Eq.(14)
Input 1	ST1	10.3	10.3	10.3	12.6	12.6	12.6	6.3	6.3	6.3
	ST2	10.3	10.3	10.3	13.1	13.1	13.1	6.4	6.4	6.4
	ST3	10.3	10.3	10.3	13.2	13.2	13.2	6.4	6.4	6.5
	ST4	10.3	10.3	10.3	13.2	13.2	13.2	6.5	6.5	6.5
	ST5	10.4	10.4	10.4	13.2	13.2	13.2	6.5	6.5	6.5
	ST6	10.3	10.3	10.3	21.4	21.4	21.4	6.5	6.5	6.5
	ST7	10.3	10.3	10.3	21.4	21.4	21.4	6.5	6.5	6.5
	ST8	10.2	10.2	10.2	21.5	21.5	21.5	12.5	12.5	12.5
	ST9	10.1	10.1	10.1	21.5	21.5	21.5	6.8	6.8	6.8
	ST10	10.1	10.1	10.1	12.1	12.1	12.1	6.8	6.8	6.8
Input 2	ST1	10.5	10.5	10.5	11.8	11.8	11.8	8.1	8.1	8.1
	ST2	10.5	10.5	10.5	11.8	11.8	11.8	8.1	8.1	8.1
	ST3	10.5	10.5	10.5	11.8	11.8	11.8	8.1	8.1	8.1
	ST4	10.5	10.5	10.5	11.9	11.9	11.9	8.1	8.1	8.1
	ST5	12.1	12.1	12.1	11.9	11.9	11.9	8.1	8.1	8.1
	ST6	12.1	12.1	12.1	11.9	11.9	11.9	8.1	8.1	8.1
	ST7	12.1	12.1	12.1	12.5	12.5	12.5	8.0	8.0	8.0
	ST8	12.1	12.1	12.1	12.5	12.5	12.5	8.0	8.0	8.0
	ST9	12.1	12.1	12.1	12.5	12.5	12.5	8.0	8.0	8.0
	ST10	12.2	12.2	12.2	12.5	12.5	12.5	7.9	7.9	7.9
Input 3	ST1	8.5	8.5	8.5	10.8	10.8	10.8	3.7	3.7	3.7
	ST2	8.5	8.5	8.5	10.8	10.8	10.8	3.7	3.7	3.7
	ST3	8.5	8.5	8.5	10.8	10.8	10.8	3.7	3.7	3.7
	ST4	8.5	8.5	8.5	10.8	10.8	10.8	3.7	3.7	3.7
	ST5	8.5	8.5	8.5	10.8	10.8	10.8	3.7	3.7	3.7
	ST6	8.6	8.6	8.6	10.8	10.8	10.8	3.7	3.7	3.7
	ST7	8.6	8.6	8.6	10.8	10.8	10.8	3.7	3.7	3.7
	ST8	10.5	10.5	10.5	10.8	10.8	10.8	3.7	3.7	3.7
	ST9	10.5	10.5	10.5	10.8	10.8	10.8	3.7	3.7	3.7
	ST10	10.5	10.5	10.5	10.8	10.8	10.8	3.7	3.7	3.7
Input 4	ST1	8.5	8.5	8.5	10.8	10.8	10.8	4.4	4.4	4.4
	ST2	8.5	8.5	8.5	10.8	10.8	10.8	4.4	4.4	4.4
	ST3	8.5	8.5	8.5	10.8	10.8	10.8	4.4	4.4	4.4
	ST4	8.5	8.5	8.5	10.8	10.8	10.8	4.4	4.4	4.4
	ST5	8.5	8.5	8.5	10.8	10.8	10.8	4.4	4.4	4.4
	ST6	8.5	8.5	8.5	10.8	10.8	10.8	4.4	4.4	4.4
	ST7	8.5	8.5	8.5	10.8	10.8	10.8	4.4	4.4	4.4
	ST8	8.5	8.5	8.5	10.8	10.8	10.8	4.4	4.4	4.4
	ST9	8.5	8.5	8.5	10.8	10.8	10.8	4.4	4.4	4.4
	ST10	8.5	8.5	8.5	10.8	10.8	10.8	4.4	4.4	4.4

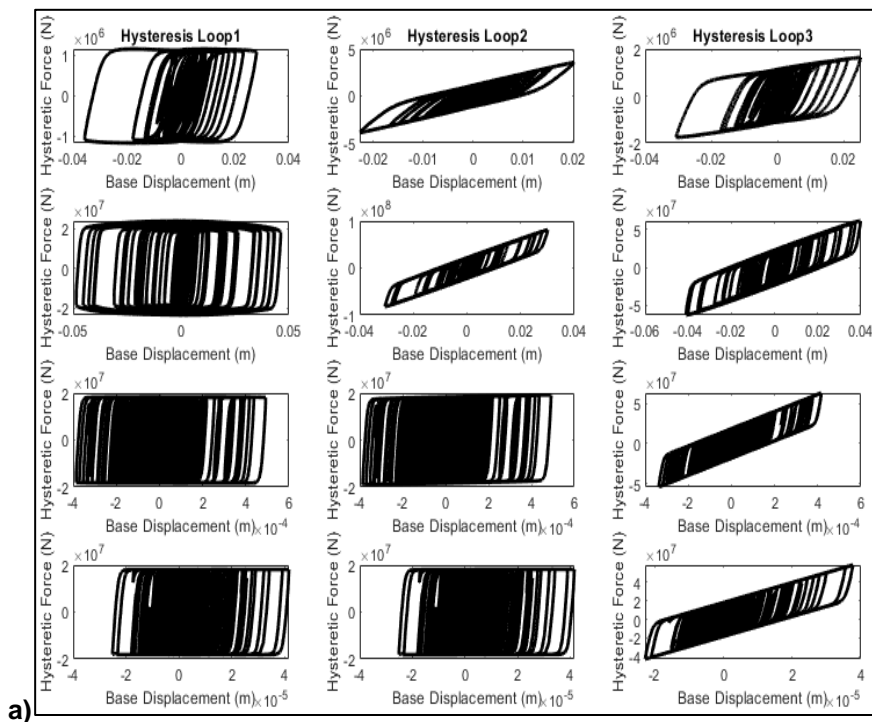
3.4. Force-Displacement Relationship of Flat and Curved Sliding Bearings (EDC, MID, & MIF)

Control on the hysteretic loop shape and size and parameters of the isolator is vital as it has been reported that these mainly affect the responses of base-isolated structure [46]. Looking at Elcentro, EDCs from all equations vary significantly for Inputs 1 and 2. For instance, EDCs resulting under Input 2 from Equation (12), (13) and (14) are $5.13e^7$, $2.30e^7$ and $3.61e^7$ J, respectively. Furthermore, under the same inputs and equations, maximum isolator force (MIF) are approximately $2.39e^7$, $8.08e^7$, and $6.13e^7$ N respectively. From this observation and considering the fact that high EDC

with small MIF leads to effective performance of the bearing [47], it is clear that flat slider defined by Equation (12) has the highest performance followed by Equation (14) and lastly the Equation (13). On the other hand, owing to very high superstructure stiffness from Inputs 3 and 4, approximately similar behavior is observed for Equations (12) & (13), except for Equation (14) which results in smaller EDC and higher MIF, performing seemingly poor as compared to other equations.

Focusing on the combined hysteresis loops from Inputs 1 and 2 in Fig. 8b, 9b, 10b, it can be observed that smaller superstructure stiffness used for Input 1 causes the isolator to similarly result in smaller isolator stiffness, whereas larger superstructure stiffness from Input 2 similarly results in larger isolator stiffness. That is, the more the superstructure stiffness is the more the isolator stiffness. This observation is used to compare the behavior of Equations (13) and (14) defined for curved surface slider, and in order to have deep insights, Inputs 2, 3, and 4 are shown in the same Figure. Referring to the above stiffness variation trend under Inputs 1 and 2, it can be observed from Inputs 2, 3, and 4 that Equation (13) tends to deviate from the expected behavior (i.e. the more the superstructure stiffness the more the isolator stiffness) by resulting in hysteresis with almost similar isolator stiffness as one of Equation (12). However, the reality is that Equation (13) was expected to continue increasing isolator stiffness as superstructure stiffness increases but it is observed to underestimate isolator stiffness for higher superstructure stiffness from Inputs 3 & 4, whereas Equation (14) keeps its conservative behavior, hence rendering the latter equation more effective. In this way, priority is given to Equation (14) rather than Equation (13) in the rest of discussions related to stiffened superstructure (Inputs 3 & 4).

Looking at EDC from Table 5 and Fig. 8 for Elcentro earthquake, Input 2 results in the highest EDC and MIF followed by Input 3. Similar to Elcentro, EDCs under Kobe from all sliders governed by Equations (12), (13) and (14) are observed to vary significantly based on both the slider and input type. For instance, under Input 2 EDCs of $7.84e^7$, $5.84e^7$, and $8.72e^7$ J are observed from Equations (12), (13) and (14), respectively as shown in Table 5 and Fig. 9. This indicates that the proposed Equation (14) can result in more energy dissipation than other equations, thus rendering it more effective than the existing curved slider formula denoted by Equation (13). However, similarly to Elcentro, for structures requiring high story stiffness (represented by Inputs 3 and 4), the proposed formula can perform better than the existing equation as can be seen in Fig. 9. Furthermore, under Input 2 the MIFs are observed to be $2.98e^7$, $2.14e^8$, and $1.42e^8$ N for Equations (12), (13) and (14), respectively. This indicates that flat slider can perform better in reducing MIF. A comparative perspective on both EDC and MIF demonstrates that flat surface slider can be the most effective for the studied building in terms of EDC and earthquake force reduction during NF Kobe earthquake. Considering other inputs, it is seen that for all equations, Input 2 results in the highest EDC followed by Inputs 1, 3 and 4, respectively. Duzce earthquake is, furthermore, observed to have similar trends as the ones from the previously investigated Kobe and Elcentro earthquakes (see Table 5 and Fig. 10).



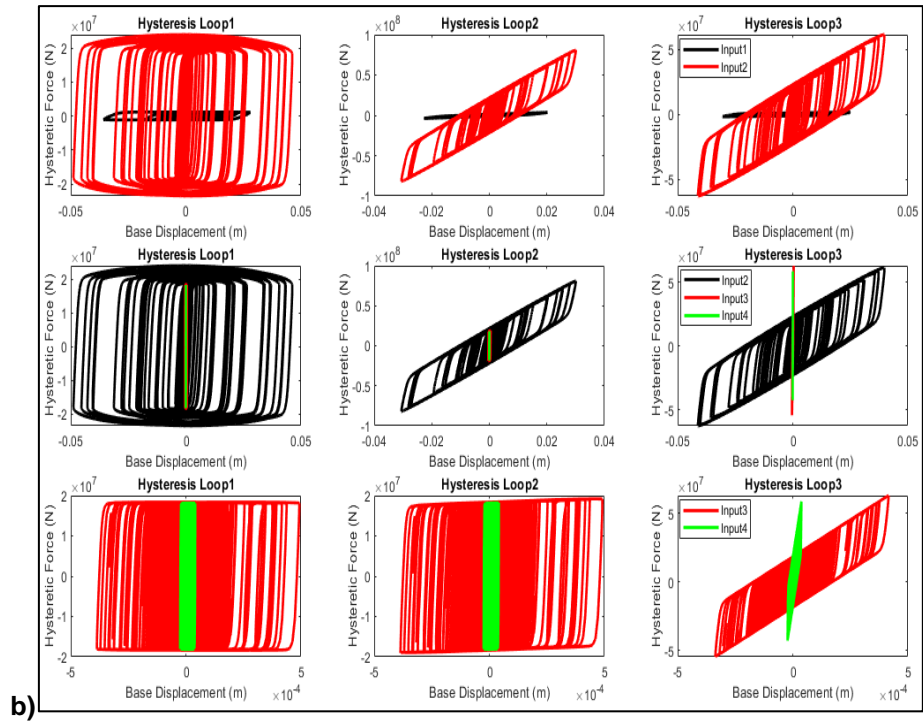
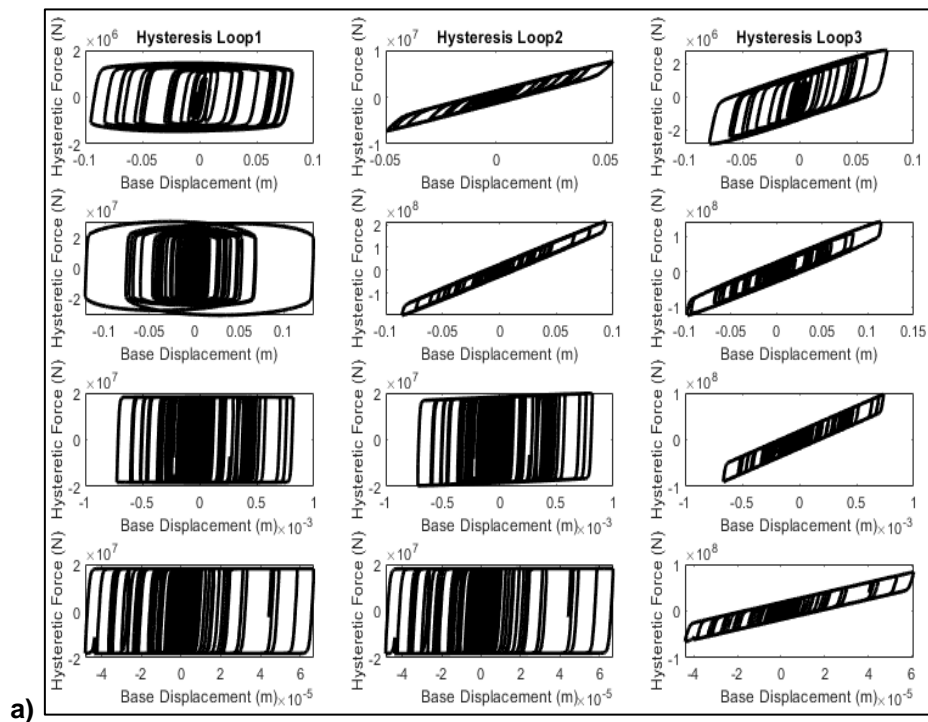


Figure 8. Force-displacement relations under Elcentro: a) Inputs 1 to 4 (top to bottom), and Hysteretic Loop1 to 3 (Equations (12) to (14)) for both a) and b).



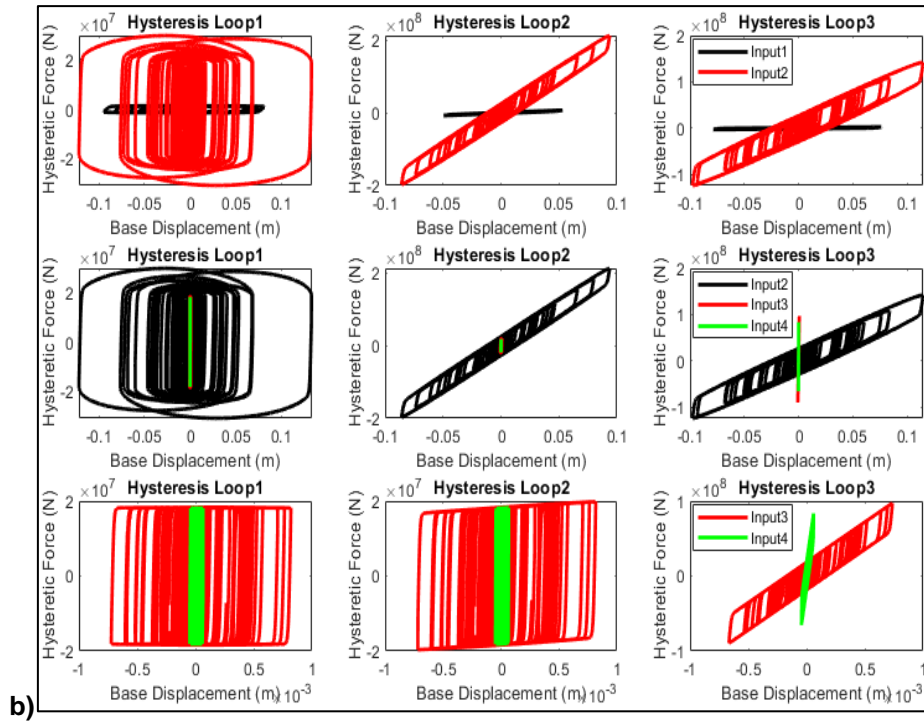
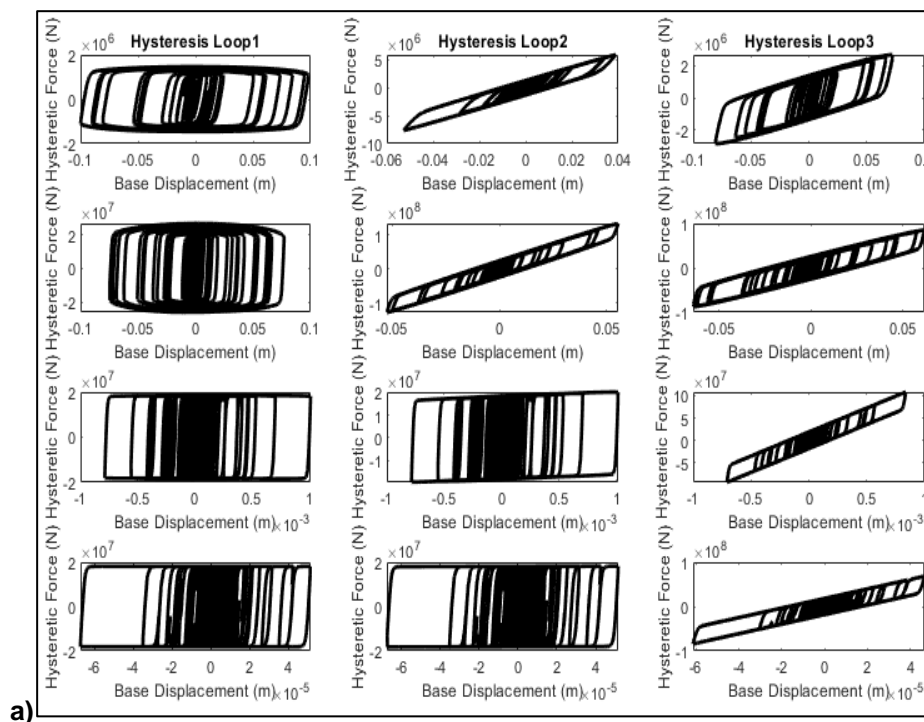


Figure 9. Force-displacement relations under Kobe: a) Inputs 1 to 4 (top to bottom), and Hysteresis Loop1 to 3 (Equations (12) to (14)) for both a) and b).

However, it is important to note that for all earthquakes, Equation (14) resulted in higher EDC than Equation (13) for Input1 and 2, and approximately similar EDC for Input 3 and 4, indicating that under the former inputs Equation (14) overestimates EDC as can be seen in Table 5. From this observation, the proposed formula can be reliable only when the increase in superstructure stiffness is expected. On the other hand, Equation (12) is observed to result in higher EDC than Equation (13) for Input 1 and 2, and nearly equal EDC for Input 3 and 4, indicating that under the former inputs, flat surface slider defined by Equation (12) can have better performance than curved one. Furthermore, a comparative perspective on EDC and MIF indicates that Input 1 and 2 can perform better as these inputs are capable of keeping both EDCs and MIF in a comparable range, while EDC and MIF from Inputs 3 and 4 are observed to differ significantly as seen in Fig. 8, 9, 10 and Table 5.



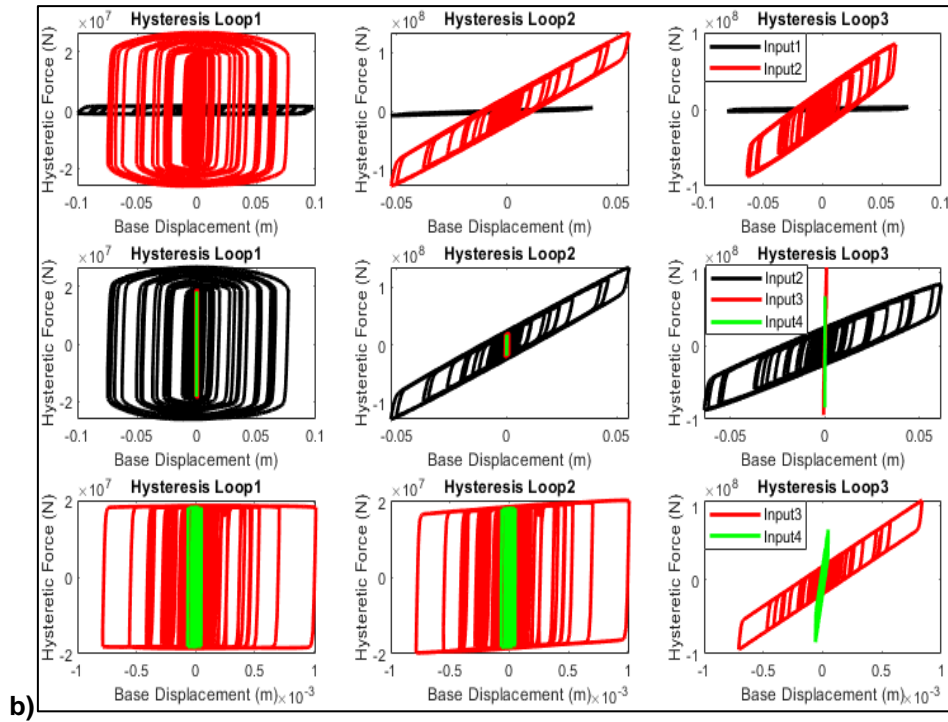


Figure 10. Force-displacement relations under Duzce: a) Inputs 1 to 4 (top to bottom), and Hysteresis Loop1 to 3 (Equations (12) to (14)) for both a) and b).

Further observations demonstrate that Equations (12) and (14) result in conservative hysteresis loop shapes from all inputs and earthquakes even when the story stiffness is increased up to e11 and e12, contrarily to curved surface slider defined by Equation (13), which tends to lose its stiffness trend as superstructure stiffness increases as can be seen Fig. 8b, 9b, 10b. In fact, curved slider from Equation (13) is observed to almost act as flat slider as the superstructure stiffness becomes large under Inputs 3 and 4. Similar observations are also made when NF earthquakes with high PGA like Kobe and Duzce are used, thus demonstrating that the conservative behavior of Equations (14) remains true under different types of earthquakes. Overall, for all earthquakes, flat slider is observed to be the most effective in both EDC and MIF reduction under all input parameters, followed by curved slider defined by Equation (14) under Inputs 3 and 4 or the curved slider defined Equation (13) under Input 1 and 2 in both EDC and MIF reduction.

Table 5. Energy Dissipation Capacity, Maximum Isolator Force and Displacement.

EARTHQUAKES	SLIDER TYPE	KOBE			DUZCE			ELCENTRO		
		Eq.(12)	Eq.(13)	Eq.(14)	Eq.(12)	Eq.(13)	Eq.(14)	Eq.(12)	Eq.(13)	Eq.(14)
Input1	EDC (J)	3.25e6	1.29e6	1.99e6	3.02e6	7.34e5	1.85e6	5.39e5	4.00e5	4.72e5
	MIF (N)	1.45e6	7.66e6	2.79e6	1.47e6	5.90e6	2.69e6	1.15e6	3.58e6	1.63e6
	MID (m)	0.08	0.05	0.08	0.09	0.04	0.07	0.03	0.02	0.03
Input2	EDC (J)	7.84e7	5.84e7	8.72e7	6.02e7	2.74e7	4.62e7	5.13e7	2.30e7	3.61e7
	MIF (N)	2.98e7	2.14e8	1.42e8	2.67e7	1.34e8	8.47e7	2.39e7	8.08e7	6.13e7
	MID (m)	0.13	0.09	0.11	0.08	0.06	0.06	0.05	0.03	0.04
Input3	EDC (J)	6.97e5	6.95e5	6.15e5	4.26e5	4.24e5	3.39e5	9.95e5	9.92e5	8.30e5
	MIF (N)	1.85e7	7.99e7	9.73e7	1.87e7	2.03e7	1.08e8	1.86e7	1.92e7	6.28e7
	MID (m)	8.19e-4	8.18e-4	7.36e-4	0.001	0.001	8.4e-4	4.93e-4	4.92e-4	4.17e-4
Input4	EDC (J)	3.73e4	3.73e4	3.34e4	1.95e4	1.95e4	1.68e4	4.52e4	4.52e4	3.84e4
	MIF (N)	1.81e7	1.82e7	8.36e7	1.82e7	1.82e7	6.83e7	1.83e7	1.83e7	5.85e7
	MID (m)	6.70e-5	6.70e-5	6.09e-5	5.16e-5	5.15e-5	4.7e-5	4.16e-5	4.16e-5	3.77e-5

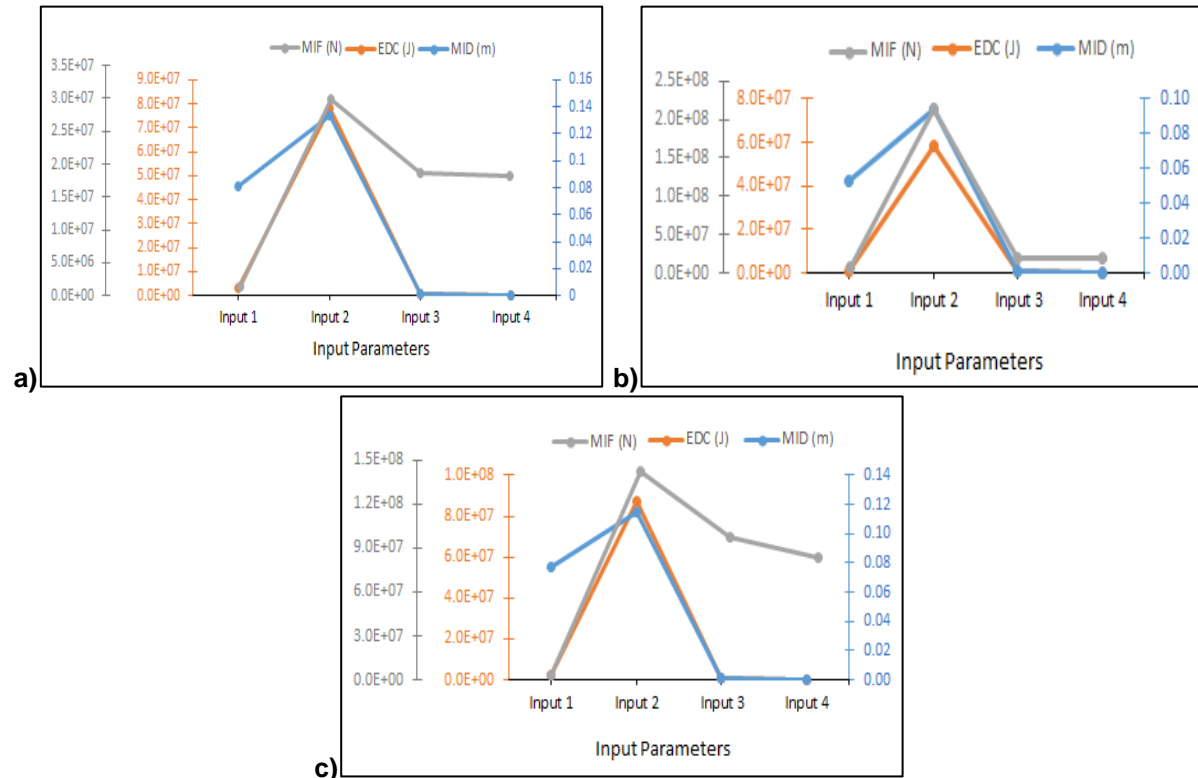
Looking at Fig. 11 and Table 5, Input 1 results in MID of approximately 0.03 m for both Equation (12) and (14), while for the same equations Input 2 results in MID of approximately 0.04 m under Elcentro. Additionally, Equation (13) results in approximately 0.02 and 0.03 m under Input 1 and 2, respectively. From this observation together with the observed base shear forces and base accelerations, Equation (13) can be the more effective than Equation (12) under Elcentro earthquake as it results in the smaller MID and reasonable $\ddot{U}_{b\max}$ under Input 1 and 2. Similar suggestions can Dushimimana, A., Singirankabo, E., Kathumbi, L.K.

also be made for Duzce which is observed to result in MID of 0.09, 0.04 and 0.07 m under Input 1, and 0.08, 0.06 and 0.06 m under Input 2 for Equation (12), (13) and (14) respectively. Overall, curved slider defined by Equation (13) results in the smaller MID under Input 1 and 2, while flat slider results in the highest values followed by the proposed Equation (14) under all earthquakes, thus making Equation (13) the most reliable in terms of MID reduction under Inputs 1 & 2.

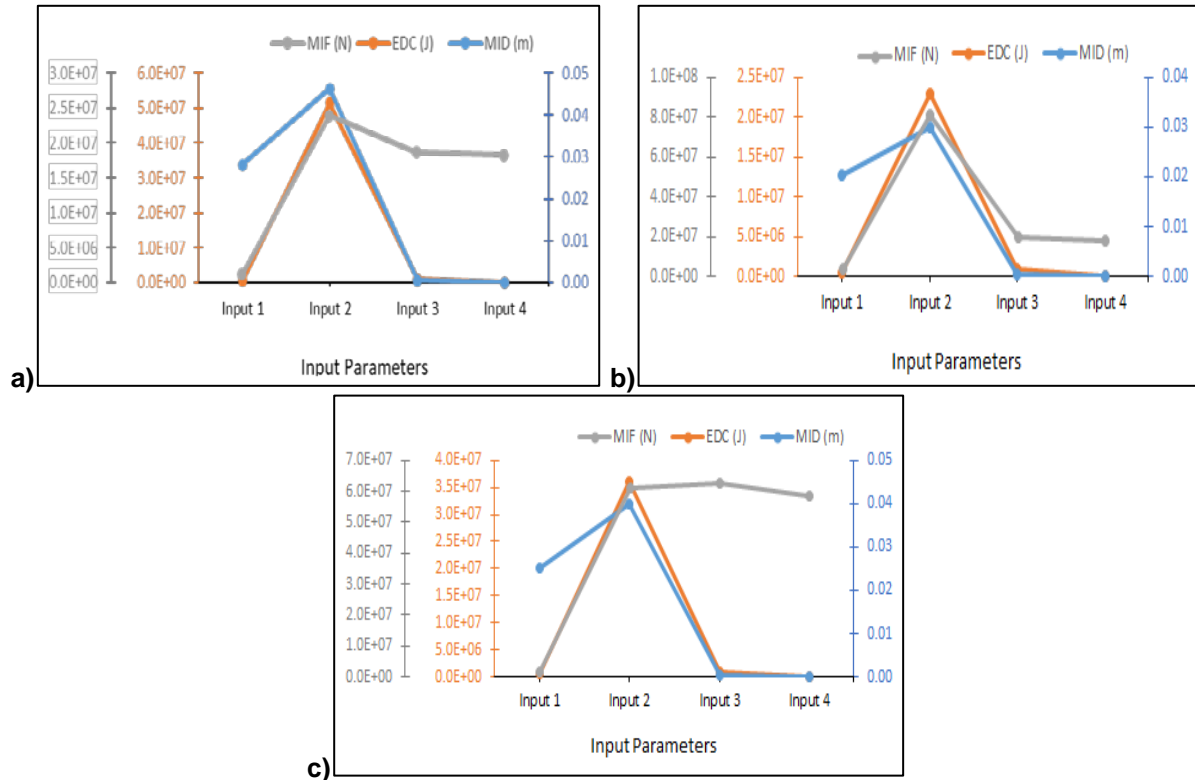
On the other hand, it can be seen that under Inputs 1, 2, 3 and 4, Kobe earthquake resulted in approximately 3,3,2,1.6; 2.6,2,1.6,1.6; and 3,3,1.8,1.6 times larger MID than Elcentro's under Equation (12), (13) and (14), respectively. Not surprisingly, strong earthquake results in higher MID than moderate earthquake as expected. Furthermore, as story stiffness increases, differences in MID from the two earthquakes become less pronounced; demonstrating that MID of conventional sliding bearings used to isolate stiffened superstructure may not significantly be affected by the earthquake magnitude.

Focusing on stiffened systems, Inputs 3 and 4 are observed to result in approximately equal values for both Equation (12) and (13) with nearly $8e^{-4}$ and $7e^{-5}$ m, respectively, whereas under Duzce nearly equal MID are observed for all equations of approximately 0.00005 and 0.001 m, respectively. On the other hand, under Elcentro these inputs result in approximately similar MID values of $4.9e^{-4}$ and $4.2e^{-5}$ m for Equation (12) and (13), while (14) results in slightly smaller MID of approximately $4.2e^{-4}$ and $3.8e^{-5}$ m under Inputs 3 and 4 respectively. These small displacements explain the inefficiency of the isolator to dissipate much energy, though their corresponding base floor accelerations and shear forces were observed to reduce significantly in Section 3.2. It is, therefore, necessary to mention that in situations where reduced base accelerations and shear forces are of first priority, stiffened superstructure can be adopted.

Kobe earthquake



Elcentro earthquake



Duzce earthquake

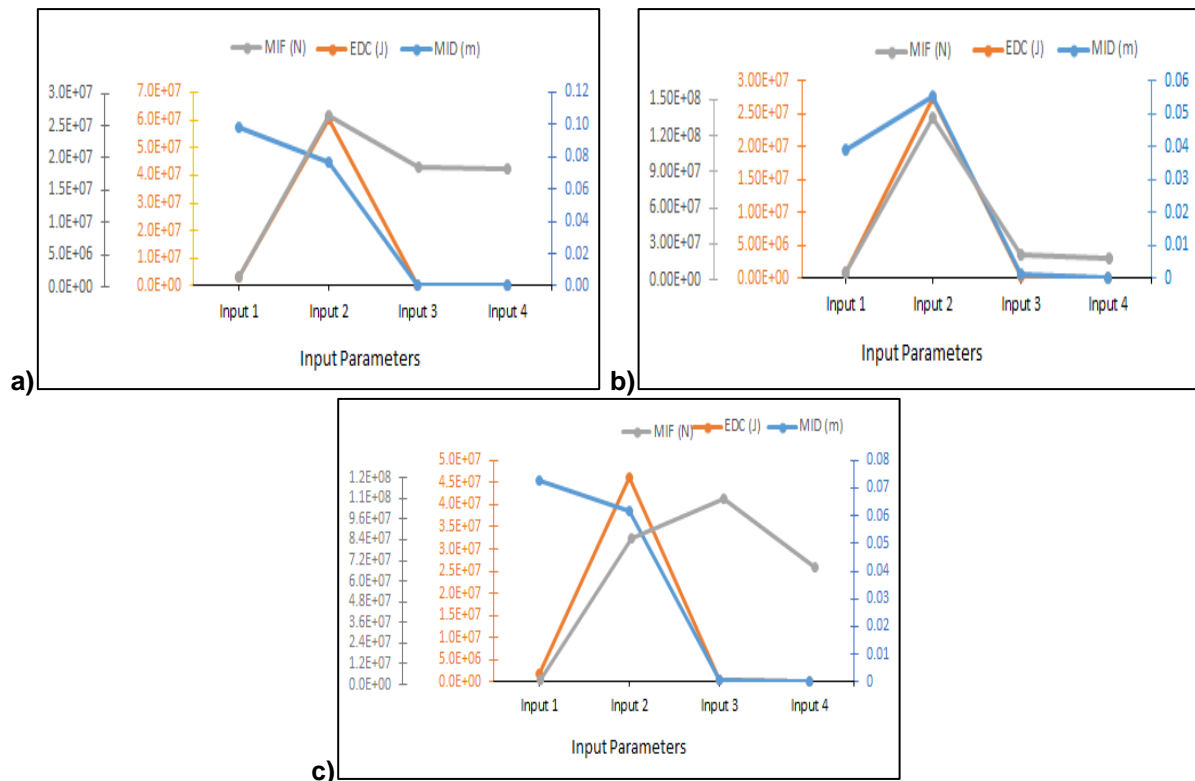


Figure 11. Variation of EDC, MIF, and MID under Equations: a) (12), b) (13), c) (12).

Looking at the results of EDC, MIF, and MID in Fig. 11 under all inputs, all earthquakes tend to result in similar trends for each equation. Additionally, Equations (12) and (13) demonstrate that, for all types of earthquakes, the increase in superstructure stiffness decreases MIF to a certain value, thereafter levelling off such that further increase leads to negligible changes in MIF. The same holds for Equations (14) under Kobe and Elcentro, except under Duzce where an increase in MIF is observed as stiffness increases from Input 2 to 3, and further increase leading to decrease in MIF. Further observations show that increase in story stiffness leads to decrease in both MID and EDC for all

earthquakes as can be seen particularly considering Inputs 2, 3 and 4, where only story stiffness is increased while keeping the same story mass.

Overall, a comparative perspective from Fig. 11 demonstrates that Input 2 has higher EDC than Input 1 while the latter has smaller MIF, thus making the former possess desirable properties than the latter when dissipation is prioritized. Besides, both Input 1 and 2 can perform better as these inputs are capable of keeping EDC, MIF and MID responses in a comparable range while these responses from Inputs 3 and 4 are observed to alter significantly, with almost zero values of MID and EDC as can be seen in Fig.11 and Table 5.

3.5. Effective and Post-yield Stiffness

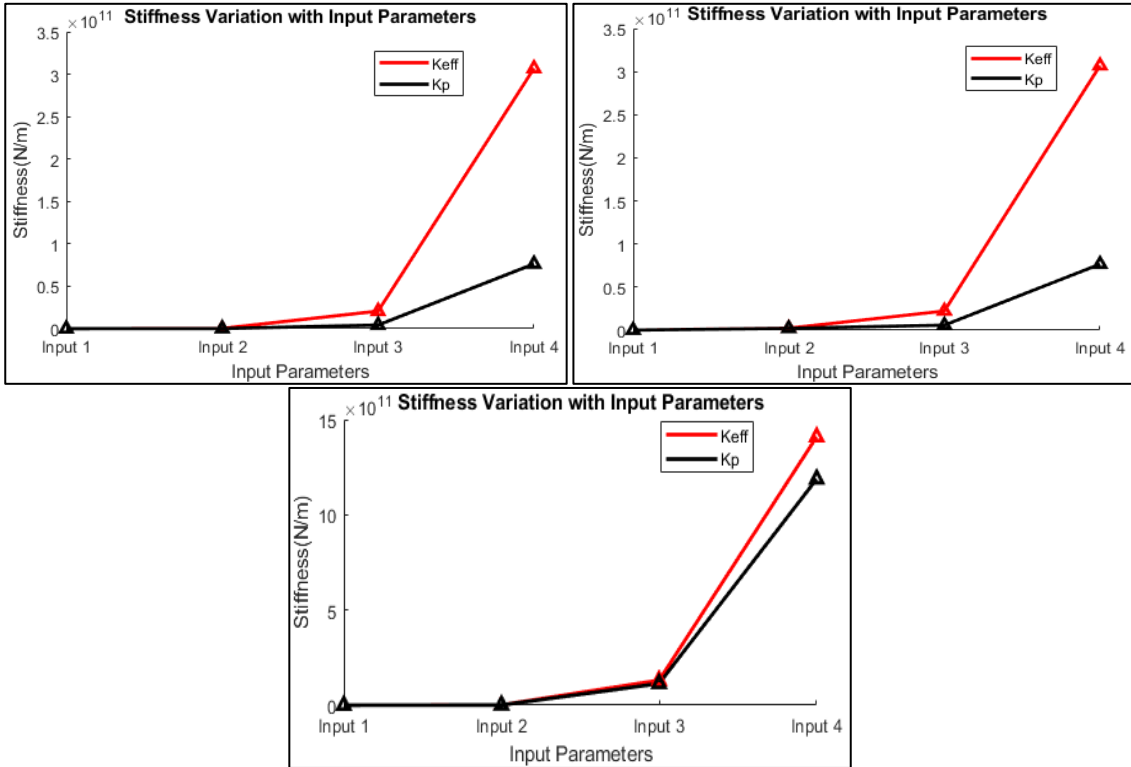
In order to maintain the hysteretic behavior of the bearing and define the isolation period in such a way that resonance is avoided, it is important to control the stiffness of the isolator. Effective stiffness (K_{eff}) and post-yield stiffness (K_p) of the isolator are compared for each input and equation to provide insights on the behavior of isolator in terms of its consistency in keeping desirable hysteretic behavior under horizontal loading. Looking at the isolator stiffness variation under Kobe earthquake, it can be seen from Table 6 and Fig. 12 that Input 1 results in K_{eff} and K_p of approximately 1.65e7 and 7.69e6, 1.45e8 and 1.38e8, and 3.62e7 and 2.65e7 N/m; while K_{eff} and K_p under Input 2 are 2.38e8 and 1.17e8, 2.28e9 and 2.15e9, and 1.25e9 and 1.13e9 N/m, for Equation (12), (13) and (14), respectively.

Table 6. Effective and post-yield stiffness under various sliding bearings and earthquakes.

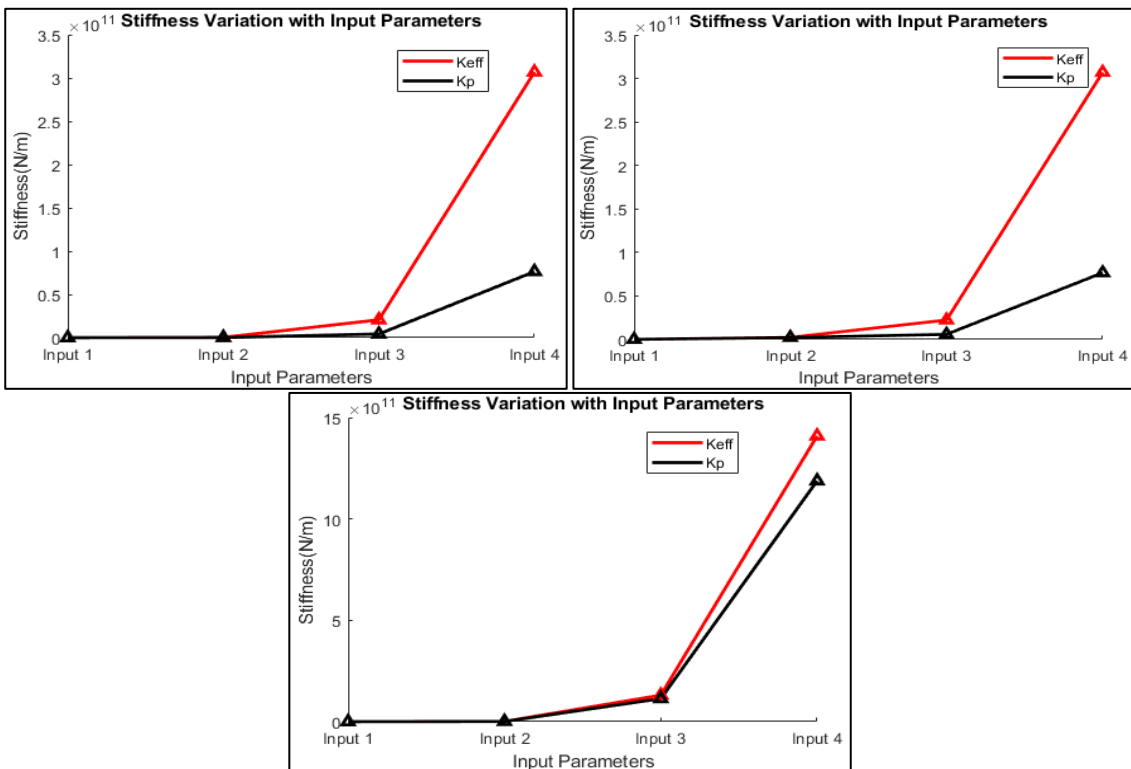
EARTHQUAKES		KOBE			DUZCE			ELCENTRO		
TYPE OF SLIDERS		Eq.(12)	Eq.(13)	Eq.(14)	Eq.(12)	Eq.(13)	Eq.(14)	Eq.(12)	Eq.(13)	Eq.(14)
Input1	K_{eff}	1.65e7	1.45e8	3.62e7	1.47e7	1.47e8	3.63e7	3.62e7	1.74e8	6.07e7
	K_p	7.69e6	1.38e8	2.65e7	6.51e6	1.44e8	2.68e7	1.22e7	1.67e8	3.66e7
Input2	K_{eff}	2.38e8	2.28e9	1.25e9	3.47e8	2.42e9	1.37e9	4.99e8	2.68e9	1.53e9
	K_p	1.17e8	2.15e9	1.13e9	1.62e8	2.21e9	1.17e9	2.12e8	2.31e9	1.22e9
Input3	K_{eff}	2.39e10	2.57e10	1.33e11	2.07e10	2.23e10	1.31e11	4.20e10	4.34e10	1.56e11
	K_p	5.15e8	6.88e9	1.15e11	4.27e9	5.92e9	1.14e11	8.79e9	1.01e10	1.20e11
Input4	K_{eff}	3.14e11	3.15e11	1.42e12	3.07e11	3.07e11	1.41e12	5.46e11	5.49e11	1.67e12
	K_p	5.67e10	5.86e10	1.16e12	7.64e10	7.67e10	1.19e12	9.63e10	9.64e10	1.21e12

With similar interpretation as above for other earthquakes, it can be observed that K_p is consistently less than K_{eff} as expected for all equations and earthquakes. Additionally, both K_p and K_{eff} are observed to increase as the stiffness of the superstructure increases. Thus, Input 1 has the least values of K_{eff} and K_p due to its lowest superstructure stiffness while Input 4, which has the highest superstructure stiffness, has the highest isolator stiffness.

Duzce earthquake



Kobe earthquake



Elcentro earthquake

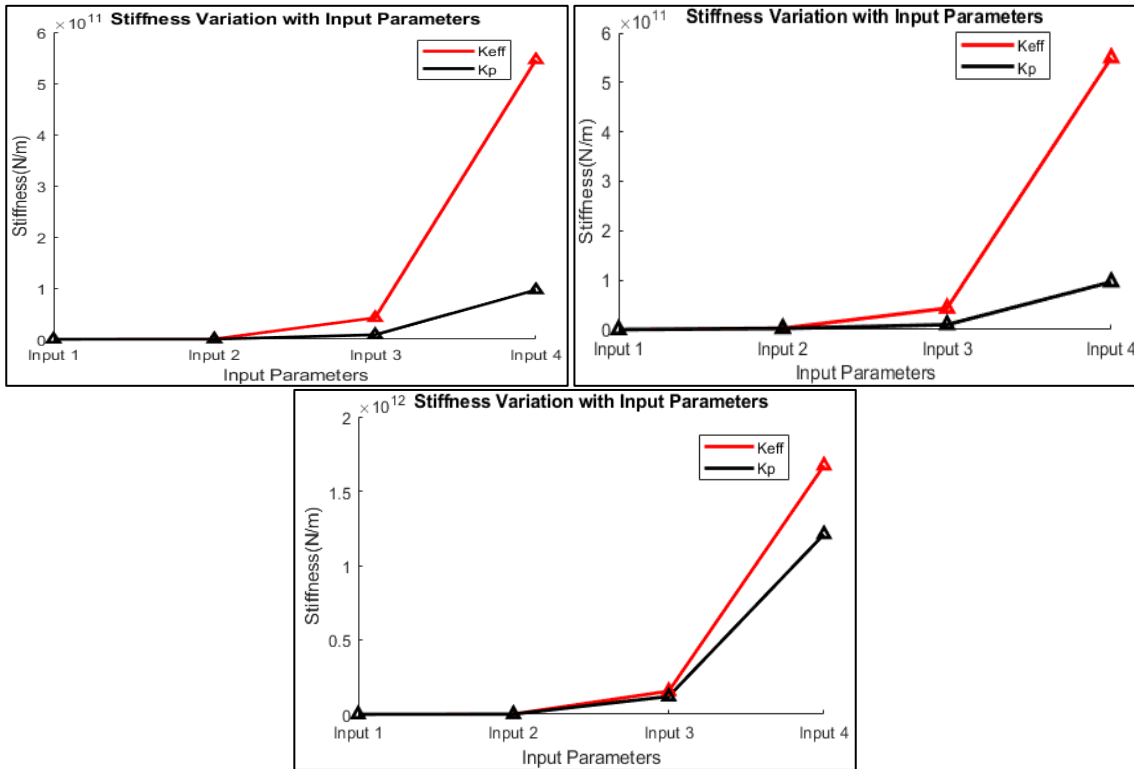


Figure 12. Effective and post-yield stiffness variation under various bearings and inputs.

The above observations are in agreement with the previously observed isolator displacement trends, which are found to be smaller for Inputs 4 and 3 compared to other inputs due to the presence of very high K_{eff} and K_p that prevent and limit the isolator flexibility, and hence leading to small MID. It is, furthermore, of paramount importance to indicate that this prevention of isolator flexibility results in small EDC as previously discussed. Under all studied earthquakes and inputs, it is also important to note that Equation (12) results in the smallest K_{eff} and K_p , followed by Equation (14) and Equation (13), respectively. This makes flat surface slider possess the best performance in terms of minimizing K_{eff} and K_p , as well as providing desirable MIDs, followed by curved slider defined by Equation (14) and lastly by (13). This shows again that Equation (14) can be more effective than (13) in terms of isolator stiffness control, particularly for stiffened superstructure where the proposed equation has previously shown tremendous behavior over the existing equation (13). On the other hand, comparing Elcentro results with Kobe's, it can be seen that the latter earthquake results in smaller stiffness values indicating that NF earthquakes will lead to larger MID, owing to their ability to reduce the isolator stiffness as compared to moderate earthquakes like Elcentro. Furthermore, authors in [46] reported that high isolator stiffness can increase superstructure accelerations for NF earthquake, and high post-yield stiffness leads to limited lateral displacement capacity [45], which is in agreement with the observed increased acceleration under Kobe earthquake when Input 2 (which results in higher isolator stiffness than Input 1) is adopted, hence showing the importance of controlling the isolator effective and post-yield stiffness.

3.6. Superstructure Story Drifts, Shears and Accelerations

Typical story drifts, peak story acceleration and shears are shown in Table 7 for Input 2. It can be seen that the maximum story drifts occur at the first story as previously reported by Hassan and Pal [48]. Furthermore, peak story accelerations are observed to be similar for all investigated equations, and found to be reduced by approximately 34, 50, and 39 % (in comparison with fixed base structure) under Kobe, Duzce and Elcentro, respectively. Similar reductions are also observed in terms of peak story shear forces as can be seen in Table 7. From this observation, conventional sliding bearings can have their best performance under earthquakes with NF such as Duzce (with small PGV) and LP moderate like Elcentro, outlining that behavior of these bearings is significantly influenced by the type of earthquakes.

Table 7. Peak story acceleration and shear, and story drifts.

Slider	Kobe Earthquake			Duzce Earthquake			Elcentro Earthquake			
	Eq.(12)	Eq.(13)	Eq.(14)	Eq.(12)	Eq.(13)	Eq.(14)	Eq.(12)	Eq.(13)	Eq.(14)	
PSA (%)		33.699			50.303			38.964		
PSF (%)		33.676			50.303			38.965		
Input2	SD1	0.12	0.14	0.18	0.13	0.09	0.10	0.08	0.05	0.07
	SD2	0.06	0.06	0.06	0.03	0.03	0.03	0.02	0.02	0.02
	SD3	0.07	0.07	0.07	0.03	0.03	0.03	0.02	0.02	0.02
	SD4	0.06	0.06	0.06	0.04	0.04	0.04	0.02	0.02	0.02
	SD5	0.06	0.06	0.06	0.04	0.04	0.04	0.02	0.02	0.02
	SD6	0.08	0.08	0.08	0.02	0.02	0.02	0.02	0.02	0.02
	SD7	0.07	0.07	0.07	0.01	0.01	0.01	0.02	0.02	0.02
	SD8	0.07	0.07	0.07	0.05	0.05	0.05	0.02	0.02	0.02
	SD9	0.05	0.05	0.05	0.04	0.04	0.04	0.02	0.02	0.02
	SD10	0.04	0.04	0.04	0.02	0.02	0.02	0.01	0.01	0.01

Abbreviations: PSA, PSF are peak story acceleration and shear forces respectively, SD: story drift

4. Conclusion

In this study, effectiveness of conventional sliding bearings (flat and curved surface sliders) as seismic-isolators was examined. The study also attempted to improve the existing equation for curved sliding bearing by directly relating the isolator stiffness to the first story stiffness of the investigated structure. Four different input parameters reflecting the superstructure stiffness variation were adopted for a 10 story RC structure model isolated by flat and curved bearings and its structural responses were examined under LP moderate and strong NF earthquake ground motions. To achieve this, Full Structural Response Investigation (FSRI) was applied as a new and desirable strategy to fully investigate the behavior of isolated structures when exposed to seismic-loads, as this can provide a whole picture of the isolated structure behavior. Key findings after applying the FSRI are as follows:

1. All investigated bearings perform similarly and equally in reducing U_{top} for each used Input.

U_{top} is smaller when moderate earthquake is used than when strong one is adopted, though the nature of Duzce (with smaller PGV than Kobe's) makes it behave as Elcentro, indicating that earthquake's PGV (along with PGA) needs consideration when investigating seismic isolation systems. Increase in stiffness leads to decrease in U_{top} , and all the earthquakes tend to result in approximately similar displacement profiles for stiffened superstructure, indicating that for such superstructure the U_{top} may not significantly be affected by the earthquake type. Flat surface slider can be the best in U_{top} control for less stiffened superstructure. On the other hand, both flat and curved bearings are observed to possess equal ability in reducing peak story accelerations and shear forces, and in keeping similar story drifts, except for the first story where moderate Duzce earthquakes tend to render curved slider performance better.

2. Stiffening of superstructure can lead to reduction of base shear forces and accelerations, but affect the bearing flexible, hence causing small isolator displacements, which lead to less EDC. This provides insights about how setting priorities during design is vital as seismic isolation may not be able to provide all desirable FSRI responses. For example, in situations where \ddot{U}_{bmax} reduction and increased EDC are of first priority (rather than reduced U_{top}), equal stiffness for all floors can be adopted for the investigated bearings, as varied story stiffness leads to amplification of \ddot{U}_{bmax} despite of its best performance in reducing U_{top} . Furthermore, curved surface slider results in the smallest \ddot{U}_{bmax} for all earthquakes, thus making it the most effective in reducing \ddot{U}_{bmax} .

3. Strong NF earthquakes are found to result in higher MID than LP moderate earthquake as expected. As story stiffness increases, differences in MID from both earthquakes become less pronounced. This demonstrates that MID of conventional sliding bearings may not significantly be affected by the earthquake magnitude when the superstructure is stiffened. Focusing on the observed

18. Gandelli, E., Quaglini, V. Effect of the Static Coefficient of Friction of Curved Surface Sliders on the Response of an Isolated Building. *Journal of Earthquake Engineering*. 2018. 00 (00). Pp. 1–29. DOI: 10.1080/13632469.2018.1467353.
19. Xu, Y., Guo, T., Yan, P. Design optimization of triple friction pendulums for base-isolated high-rise buildings. 2019. DOI: 10.1177/1369433219849840
20. Mokha, A., Constantinou, M.C., Reinhorn, A.M., Zayas, V.A. Experimental Study of Friction-Pendulum Isolation System. *Journal of Structural Engineering*. 1991. 9445 (November 1991). Pp. 3315–3336. DOI: 10.1061/(ASCE)0733-9445(1991)117
21. Fenz, D.M., Constantinou, M.C. Behaviour of the double concave Friction Pendulum bearing. 2006. (June). Pp. 1403–1424. DOI: 10.1002/eqe
22. Fenz, D.M., Eeri, S.M., Constantinou, M.C., Eeri, M. Modeling Triple Friction Pendulum Bearings for Response-History Analysis. *Earthquake engineering practice*. 2008. 24 (4). Pp. 1011–1028. DOI: 10.1193/1.2982531
23. Xu, Y., Guo, T., Yan, P. Design optimization of triple friction pendulums for base-isolated high-rise buildings. *Advances in Structural Engineering*. 2019. Pp. 1–14. DOI: 10.1177/1369433219849840
24. Moeindarbari, H., Taghikhany, T. Seismic optimum design of triple friction pendulum bearing subjected to near-fault pulse-like ground motions. *Struct. Multidisc Optim*. 2014. DOI: 10.1007/s00158-014-1079-x
25. Fadi, F., Constantinou, M.C. Evaluation of simplified methods of analysis for structures with triple friction pendulum isolators. *Earthquake Engineering & Structural Dynamics*. 2010. 39. Pp. 5–22. DOI: 10.1002/eqe
26. Namirani, P., Amiri, G.G., Veismoradi, S. Near-fault seismic performance of triple variable friction pendulum bearing. *Journal of Vibroengineering*. 2016. 19 (4). Pp. 2293–2303. DOI: 10.21595/jve.2015.16280. URL: <http://dx.doi.org/10.21595/jve.2015.16280>
27. Xu, Y., Guo, T., Asce, M., Yan, P., Li, A. Effect of Semiactive Control on Wind and Seismic Responses of High-Rise Building Supported on Triple Friction Pendulums. *American Society of Civil Engineers*. 2020. 34 (3). DOI: 10.1061/(ASCE)CF.1943-5509.0001427
28. Design, L., Wen, J., Han, Q., Du, X. Shaking table tests of bridge model with friction sliding bearings under bi-directional earthquake excitations. *Structure and Infrastructure Engineering*. 2019. 15 (9). Pp. 1264–1278. DOI: 10.1080/15732479.2019.1618350. URL: <https://doi.org/10.1080/15732479.2019.1618350>
29. Lee, D., Constantinou, M.C. *Quintuple Friction Pendulum Isolator Behavior, Modeling and Validation* New York, 2015.
30. Poornima, B.S., Babu, B.S.J. Comparative Study on Seismic Response of Regular and Irregular RC Framed Buildings with HDRB, LRB and FPS Base Isolation Systems. *International Journal for Research in Applied Science & Engineering Technology*. 2019. 7 (Vi). Pp. 805–813.
31. Pokhrel, A., Jianchun, L., Yancheng, L., Maksis, N., Yu, Y. Comparative Studies of Base Isolation Systems featured with Lead Rubber Bearings and Friction Pendulum Bearings. *Applied Mechanics and Materials*. 2016. 846. Pp. 114–119. DOI: 10.4028/www.scientific.net/AMM.846.114
32. Tsopelas, P., Nagarajaiah, S., Constantinou, M.C., Reinhorn, A.M. 3D-BASIS-M: Nonlinear Dynamic Analysis of Multiple Building Base Isolated Structures. 1991.
33. Hur, D., Hong, S.-C. Analysis of an Isolation System with Vertical Spring-viscous Dampers in Horizontal and Vertical Ground Motion. *Applied Sciences*. 2020. 10 (1411). DOI: 10.3390/app10041411
34. Dushimimana, A., Niyonsenga, A.A., Decadjevi, G.J., Kathumbi, L.K. Effects of model-based design and loading on responses of base-isolated structures. *Magazine of Civil Engineering*. 2019. 92 (8). Pp. 141–153. DOI: 10.18720/MCE.92.12
35. University of California. *Pacific Earthquake Engineering Research Center (PEER) NGA: Ground Motion Database*. 2013.
36. Gunday, F., Dushimimana, A., Tuhta, S. Analytical and Experimental Modal Analysis of a Model Steel Structure Using Blast Excitation. *International Conference on Innovative Engineering Application (CIEA2018)*. 2018. Pp. 686–694.
37. Dushimimana, A., Gunday, F., Tuhta, S. Operational Modal Analysis of Aluminum Model Structures using Earthquake Simulator. *International Conference on Innovative Engineering Application (CIEA2018)*. 2018. Pp. 677–685.
38. Dushimimana, A., Ziada, M., Tuhta, S. Effect of Carbon Fiber Reinforced Polymer (CFRP) Composites Applied to Walls and Slabs of Masonry Building. *International Journal of Advance Engineering and Research Development*. 2018. 5 (04). Pp. 2348–4470. DOI: 10.21090/IJAERD.76958
39. Sena-cruz, J., Correia, L., Ribeiro, F., Figueira, D., Benzo, P.G., Barros, J., Pereira, E., Valente, I. The effect of surface treatment and environmental actions on the adhesive connection between GFRP laminate surface and fresh FRC. *Construction and Building Materials*. 2020. 258. DOI: 10.1016/j.conbuildmat.2020.119594
40. Correia, L., Sena-Cruz, J., Michels, J., França, P., Pereira, E., Escusa, G. Durability of RC slabs strengthened with prestressed CFRP laminate strips under different environmental and loading conditions. *Composites Part B*. 2017. DOI: 10.1016/j.compositesb.2017.05.047. URL: <http://dx.doi.org/10.1016/j.compositesb.2017.05.047>
41. Ebadi, P., Farajloomanesh, S. Seismic design philosophy of special steel plate shear walls. *Magazine of Civil Engineering*. 2020. 95 (3). Pp. 3–18. DOI: 10.18720/MCE.95.1
42. Jain, S.K., Thakkar, S.K. Application of base isolation for flexible buildings. *13th World Conference on Earthquake Engineering*. 2004. Pp. 1924.
43. Belash, T.A., Ivanova, Z.V. Timber frame buildings with efficient junction designs for earthquake-prone areas. *Magazine of Civil Engineering*. 2019. 92 (8). Pp. 84–95. DOI: 10.18720/MCE.92.7
44. Dushimimana, A., Nzamurambaho, F., Shyaka, E., Niyonsenga, A.A. Optimum Performance of Isolation System for Medium Rise Buildings Subject to Long Period Ground Motions. *International Journal of Applied Engineering Research*. 2018. 13 (23). Pp. 16342–16350.
45. Dicleli, M. Supplemental elastic stiffness to reduce isolator displacements for seismic-isolated bridges in near-fault zones. *Engineering Structures*. 2007. 29. Pp. 763–775. DOI: 10.1016/j.engstruct.2006.06.013
46. Matsagar, V.A., Jangid, R.S. Influence of isolator characteristics on the response of base-isolated structures. *Engineering Structures*. 2004. 26 (12). Pp. 1735–1749. DOI: 10.1016/j.engstruct.2004.06.011
47. Dicleli, M., Karalar, M. Optimum characteristic properties of isolators with bilinear force – displacement hysteresis for seismic protection of bridges built on various site soils. *Soil Dynamics and Earthquake Engineering*. 2011. 31 (7). Pp. 982–995. DOI: 10.1016/j.soildyn.2011.03.005. URL: <http://dx.doi.org/10.1016/j.soildyn.2011.03.005>

48. Hassan, A., Pal, S. Effect of soil condition on seismic response of isolated base buildings. *International Journal of Advanced Structural Engineering*. 2018. 10 (3). Pp. 249–261. DOI: 10.1007/s40091-018-0195-z. URL: <https://doi.org/10.1007/s40091-018-0195-z>

Contacts:

Aloys Dushimimana, chenkodu432@gmail.com

Lilies Kathami Kathumbi, 06lilies@gmail.com

Edouard Singirankabo, nkabo12edus@gmail.com



DOI: 10.34910/MCE.108.10

Waste iron powder as aggregate and binder in mortar production

M.J. Miah^{*a} , M.S. Miah^b , S.C. Paul^b , S.Y. Kong^c , A.J. Babafemi^d , M.K. Ali^a ,
M.M.H. Patoary^a 

^a University of Asia Pacific, Dhaka, Bangladesh

^b International University of Business Agriculture and Technology, Dhaka, Bangladesh

^c Monash University Malaysia, Selangor, Malaysia

^d Stellenbosch University, Stellenbosch, South Africa

*E-mail: jihad.miah@uap-bd.edu

Keywords: waste iron powder, fine aggregate, mortar, compressive strength, tensile strength, flexural strength

Abstract. This paper study the feasibility of reusing waste iron powder (WIP) in mortar as both natural fine aggregate (NFA) and cement replacement material. Within this context, the physical and mechanical properties of mortar made with five percentage replacements of 0 %, 25 %, 50 %, 75 %, and 100 % for NFA by WIP and 0 %, 2.5 %, 5 %, 7.5 %, and 10 % for cement by fine waste iron powder (FWIP) are studied at 7, 14 and 28 days. Cube, briquette, and prism specimens for compression, tension, and flexural strength, respectively, tests were used. It is found that the workability decreases, and the density of mortar increase with the increased replacement percentage of NFA by WIP. The compressive, tensile, and flexural strength of mortar made with WIP are significantly higher than NFA. The maximum increase in strength of mortar is observed for 75 % WIP, which is 30 % for compressive, 35 % for tensile, and 37 % for flexural strength, respectively, relative to the control at 28 days. Conversely, when FWIP is used as a cement replacement material, all strength decreases with an increase in FWIP. The maximum decrease in strength is observed for 10 % FWIP, which is 40 % for compressive and tensile, and 16 % for flexural strength, accordingly, relative to the control at 28 days. The results presented in this study demonstrate that, to some extent, WIP and FWIP can be used in concrete/mortar production. Successful application of these waste materials may add economical benefit in the production of sustainable building material as well as conserve the natural aggregates.

1. Introduction

The demand for natural fine aggregate (NFA) is increasing as the activities of the construction industry in building infrastructures keep booming. Nevertheless, the demand for other construction materials such as steel, iron, and cement are also increasing, thereby leading to significant waste generation. The use of waste materials generated from the steel industry in concrete can serve to resolve the disposal problem being encountered [1], reduce the demand for NFA, and produce a sustainable building material. In Bangladesh, natural river sand is mainly used as fine aggregate, which is limited and mostly extracted from the riverbed by dredging, resulting in a threat to the environment. In a developing country like Bangladesh, numerous megaprojects are ongoing, which are made with concrete. Therefore, it is expected that there will be a significant amount of depletion of NFA. Hence, it is necessary to find

Miah, M.J., Miah, M.S., Paul, S.C., Kong, S.Y., Babafemi, A.J., Ali, M.K., Patoary, M.M.H. Waste iron powder as aggregate and binder in mortar production. Magazine of Civil Engineering. 2021. 108(8). Article No. 10810. DOI: 10.34910/MCE.108.10

© Miah M.J., Miah M.S., Paul S.C., Kong S.Y., Babafemi A.J., Ali M.K., Patoary M.M.H., 2021. Published by Peter the Great St. Petersburg Polytechnic University.



This work is licensed under a CC BY-NC 4.0

possible alternative raw construction materials that could be used as fine aggregates in the concrete industry. Moreover, it is recorded that the amounts of aggregates used in concrete production the world yearly (estimated at more than 10-11 billion tons 20 years ago), there is great potential for reuse of wastes as aggregate replacement [2–4]. Besides, cement as a binder is an essential material for concrete, and the production of this material produces a lot of carbon dioxide gas in the air, resulting in negative environmental impacts and risks to human life. Therefore, this study investigates the utilization of waste iron powder (WIP) in mortar as both fine aggregate and cement replacement material.

The WIP is the industrial byproduct generated from the workshops, steel mills, and factories in powder form [5], which is not commonly used and is hazardous material to human health since it can be easily inhaled [6]. WIP can be used as a partial or full replacement of NFA in concrete/mortar. The literature shows that using WIP has better mechanical properties, cost-effective, and environment-friendly. Ghannam *et al.* [6] investigated the mechanical properties of concrete made with five percentage replacements (0 %, 5 %, 10 %, 15 %, and 20 %) of sand by iron powder. An increase in compressive and flexural strength was observed for the concrete replacing up to 20 % of sand with iron powder. It was found that iron powder had increased the compressive as well as the split tensile strength of concrete, which is about 25 % higher when fine aggregate was replaced entirely by iron powder [7]. Tayeh and Saffar [8] found that the incorporation of iron powder decreased the compressive strength of mortar, which is inconsistent with the results found in Satyaprakash *et al.* [7]. The authors explained that the reduction in strength could be due to the small voids appearing on the internal texture of the mortar specimen, which may affect the strength of the mortar.

Furthermore, the replacement of NFA with iron fillings resulted in significantly higher abrasion resistance of concrete. Enhancement of mechanical properties compared to normal concrete was also observed for concrete made with recycled scale and steel chips [9–10]. Similarly, Ismail and Al-Hashmi [11] observed an increase in compressive and flexural strength when 20 % of sand was replaced with waste iron, which is 17 % and 28 % for compressive and flexural strength, respectively, higher than the reference concrete. Other researchers found that the compressive strength of concrete containing iron filings was higher than plain concrete. Besides, the presence of iron filings enhances the ductility of the concrete [12]. Kumar *et al.* [13] investigated the effect of partial/full replacement of sand by iron ore tailing as fine aggregate on the compressive and flexural strength of reinforced concrete. The compressive strength was increased up to 40 % replacement of sand by iron ore tailing, while there was an enhancement of flexural strength for all percentages of sand replacement (10, 20, 30, 40, 60, 80, and 100 %). Similarly, the compressive strength of concrete was increased up to 20 % replacement of sand by iron powder, which is 7.4 % higher than the reference concrete [14]. The increase in compressive strength was also observed up to 45% replacement of sand by iron slag as fine aggregate, which is about 23.3 % higher than the reference concrete [15]. Olutoge *et al.* [16] investigated compressive, splitting tensile, and flexural strength of concrete made with iron as a replacement for sand. The authors found that the mechanical strength was increased up to 20 % replacement of sand by iron fillings, which is 13.5 % for compression, 1 % for splitting tensile, and 4.8 % for flexural strength, respectively, higher than the reference concrete. While above that replacement, the mechanical strength was decreased. Conversely, a decreasing trend of compressive strength was observed with the increasing addition of steel scale waste by Furlani and Maschio [17].

Yunhong *et al.* [18] investigated the effect of iron tailings on the compressive strength of concrete as supplementary cementing material as four different replacements of cement (10 %, 20 %, 30 %, and 40 %). It was found that as the replacement of cement was increased, the compressive strength was decreased. Similarly, it was found that the increasing content of iron tailing powder has a negative effect on the mechanical strength of autoclaved aerated concrete, and the finer iron tailings can effectively enhance the strength of concrete blocks [19]. The enhancement of mechanical strength could be increased by incorporating mineral admixtures such as fly ash, blast furnace slag, and silica fume in cement with WIP [20–22].

Though several studies have been carried out to investigate the mechanical performance of concrete/mortar made with WIP, some researchers found that WIP enhances the mechanical properties, while other researchers found opposite behavior. To the authors' knowledge, more research is needed to clarify the real effect of WIP as a replacement of NFA and fine waste iron powder (FWIP) as a replacement of cement on the mechanical properties of concrete/mortar. In Bangladesh, this WIP is not commonly used due to the lack of research data. Therefore, the lack of research data, limited information, and knowledge on the mechanical performance of concrete/mortar made with WIP as a replacement for NFA and FWIP as a replacement for cement motivate this research work. Within this context, comprehensive experimental studies are conducted on the possibility of using WIP as fine aggregate and cement replacement. The physical and mechanical (i.e., compressive, tensile, and flexural strength) performances of mortar made with five percentage replacements of 0 %, 25 %, 50 %, 75 % and 100 % for NFA by WIP and 0 %, 2.5 %, 5 %, 7.5 % and 10 % for cement by FWIP are studied here. Additionally, the experimental results are compared with the existing results available in the literature.

2. Materials and Methods

2.1. Materials

Natural river sand passing through a sieve size of 4.75 mm (ASTM standard No. 4 sieve) was used as fine aggregate. The waste iron powder (WIP) is an industrial byproduct generated from the workshops, steel mills, and factories in powder form was used as a replacement for natural fine aggregate (NFA). This byproduct is left largely unused and is hazardous to human health. The WIP image as a fine aggregate and fine waste iron powder (FWIP) as supplementary cementitious material (SCM) is shown in Fig. 1 a & b, respectively. The microscopic morphology of the WIP through the Scanning Electron Microscopy (SEM) was performed. The SEM test was carried out on the surface of WIP, which was dried at 100 °C for 24 h, and the test was performed using JEOL JSM-7600F Schottky Field Emission Scanning Electron Microscope. The SEM image of WIP is presented in Fig. 1c. Both fine aggregates (NFA and WIP) were sieved in the laboratory using the ASTM standard sieves [23]. The grading curves of both NFA and WIP are compared with the upper and lower limits recommended in the ASTM C33 standard [24] are shown in Fig. 2.

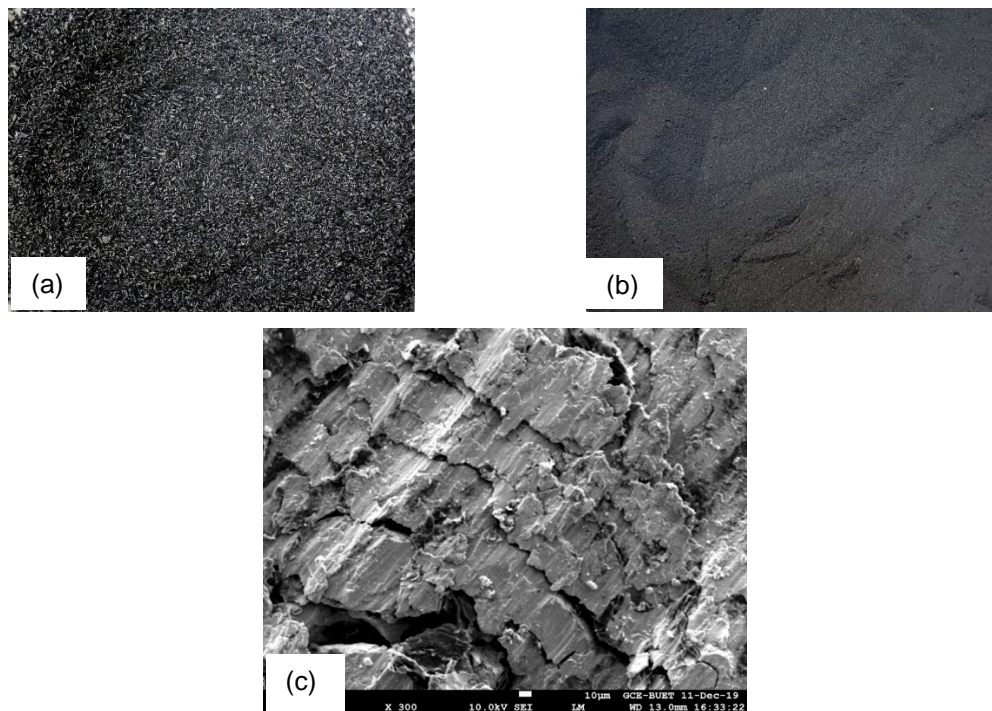


Figure 1. The WIP as fine aggregate (a) and FWIP as supplementary cementitious material (b), and SEM image of WIP (c).

It is observed that both fine aggregates are within the limits of the ASTM C33 [24] standard that ensures a lower void in the mortar mix. It is also interesting to see that the particle distribution of both WIP and NFA are almost the same. Moreover, the specific gravity and absorption capacity of both fine aggregates (NFA and WIP) were tested as per ASTM C128-15 [25]. The specific gravity, fineness modulus, and absorption capacity of the NFA and WIP are 2.56, 3.10 and 5.9, respectively, for NFA and 4.31, 3.15 and 2.6 for WIP, accordingly.

The chemical composition of WIP and cement was determined by X-ray fluorescence (XRF) analysis. The results of the XRF analyses are presented in Table 1. The chemical composition of the WIP has an agreement, as reported by Ghannam et al. [6]. As expected, the Fe_2O_3 content of WIP is significantly higher, resulting in higher specific gravity than natural sand (4.31 for WIP and 2.56 for NFA).

Table 1. Chemical compositions of cement and waste iron powder.

Chemical composition	Cement [%]	WIP [%]
SiO ₂	24.90	8.46
Fe ₂ O ₃	3.96	87.46
Al ₂ O ₃	7.52	0.87
K ₂ O	1.00	0.28
CaO	53.43	1.08
TiO ₂	1.18	0.08
MgO	2.52	0.32
Na ₂ O	0.27	0.27
SO ₃	4.77	0.88
P ₂ O ₅	0.21	0.17
Cr ₂ O ₃	0.08	0.13

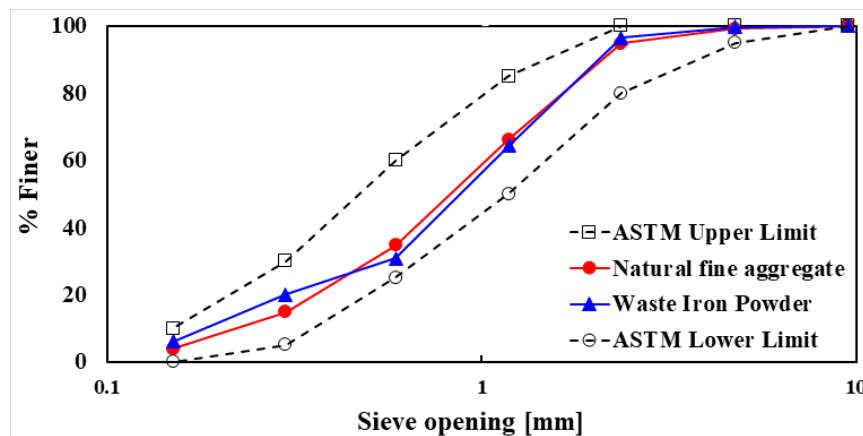


Figure 2. Grading curve of natural fine aggregate and waste iron powder, and comparison with the upper and lower limits recommended in the ASTM C33 standard [24].

2.2. Experimental programs and test procedures

The weight basis mix design with water to cement ratio of 0.45 is used for all mortar mixes, and superplasticizer (SikaPlast®-204 TH) as chemical admixture was used (0.5 % by mass of total cement) to ensure the workability of fresh mortar. In order to investigate the effect of NFA replacement by WIP, five different percentage replacements (0, 25 %, 50 %, 75 %, and 100 %) of NFA are replaced by WIP. Concerning the cement replacement, the FWIP was passed through a sieve size of 75 μm (#200 sieve) and used to replace cement at five different replacement levels (0 %, 2.5 %, 5 %, 7.5 %, and 10 %). The mixture proportions of the mortar mixes for the replacement of NFA and cement are summarized in Tables 2 and 3. The workability of the fresh mortar mixes was studied by measuring the slump values of fresh mortar, and the temperature of the fresh mortar mixes was monitored by using a digital thermometer before pouring the steel molds.

Cube specimens (50 mm) for compression, briquette specimens for tension, and prism specimens (40 mm \times 40 mm \times 160 mm) for flexural strength tests were made and tested as per ASTM C109 [26], ASTM 307 [27], and ASTM 348 [28], accordingly. The evolution of compressive, tensile, and flexural strength as a function of the mortar age is investigated at 7, 14 and 28 days. A total of 270 specimens (135 for NFA and 135 for cement replacement) were made and tested to attain the goal of the study. 24 h after casting, all the mortar specimens were demoulded and cured underwater (20 ± 2 °C) until the day of the tests. Moreover, the dry density of mortar specimens was measured on the same specimens used for mechanical tests.

Table 2. Mixture proportion of mortar mixes for replacement of NFA by WIP.

Mix ID	Cement [kg/m ³]	Fine Aggregate [Kg/m ³]		Water [kg/m ³]
		NFA [kg/m ³]	WIP [Kg/m ³]	
WIP 0 %	504	1512	0	227
WIP 25 %	504	1134	642	227
WIP 50 %	504	756	1283	227
WIP 75 %	504	378	1925	227
WIP 100 %	504	0	2567	227

Table 3. Mixture proportion of mortar mixes for replacement of cement by FWIP.

Mix ID	Binder [Kg/m ³]		NFA [kg/m ³]	Water [kg/m ³]
	Cement [kg/m ³]	FWIP [Kg/m ³]		
FWIP 0 %	504	0	1512	227
FWIP 2.5 %	491	13	1512	227
FWIP 5 %	479	25	1512	227
FWIP 7.5 %	466	38	1512	227
FWIP 10 %	454	50	1512	227

3. Results and Discussion

3.1. Performance of mortar made with WIP as replacement for NFA

3.1.1. Fresh properties of mortar

The workability of different mortar mixes is evaluated by measuring the slump value of fresh mortar at the time of placing and presented in Table 4. It is observed that the workability of mortar decreased with the increasing replacement percentage of natural fine aggregate (NFA) by waste iron powder (WIP). This behavior could be linked to the highly angular and rough surface texture of WIP (see Fig. 1c). In contrast, the NFA is round in shape (rolling effect), resulting in the reduction of the flowability of the mortar made with WIP due to better interlocking in the mix. The reduction in the flowability could also be linked to the temperature of the mortar at the time of placing. As shown in Table 4, as the temperature of the fresh mortar increases, the workability of the mortar decreases due to the higher heat of hydration of cement paste.

Table 4. Slump and temperature of fresh mortar made with five mortar mixes.

WIP	0 %	25 %	50 %	75 %	100 %
Slump [cm]	24	22	19	17	16
Temperature [°C]	23	26	28	29	31

3.1.2. Mechanical properties

The compressive strength of mortar made with five different percentage replacements (0 %, 25 %, 50 %, 75 %, and 100 %) of NFA by WIP was recorded at 7, 14, and 28 days and presented in Fig. 3a. Three cubic mortar blocks were tested for every data set, and then the average value was calculated. It is clearly seen that mortar made with WIP as fine aggregate has significantly improved the compressive strength at all curing ages compared to the control mortar (100 % NFA). None of the specimens show lower compressive strength as compared to the control specimen. For example, the average compressive strength of mortar measured at 28 days of 0 %, 25 %, 50 %, 75 %, and 100 % are, respectively, 38.5 MPa, 41.9 MPa, 47.9 MPa, 49.9 MPa, and 48.2 MPa. This behavior could be linked to the higher rough surface (see Fig. 1c), higher density, and higher strength of WIP than NFA. By the visual inspection, it has been observed that the WIP is highly sharp in shape and has a rough surface texture than NFA. Probably, this sharp and rough surface provides a better bond between cement and WIP that provides higher strength. While NFA is round in shape, thus provides a weak bond, i.e., a weak interfacial transition zone between sand particle and cement paste, resulting in lower compressive strength.

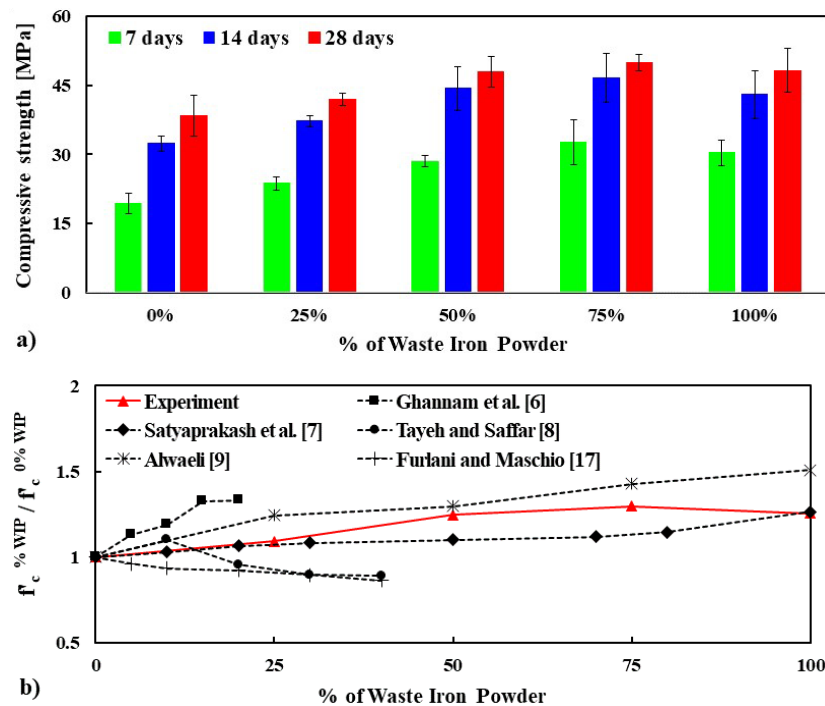


Figure 3. Compressive strength (f'_c) of mortar tested at 7, 14, and 28 days (a), and normalized f'_c of mortar measured at 28 days is compared with results found in the literature (b), respectively.

To gain a deeper understanding the role of different percentage replacement of NFA by WIP on the compressive strength of mortar, normalized compressive strength at 28 days is calculated by dividing the strength of mortar made with 100 % NFA (i.e., f'_c ^{WIP %} / f'_c ^{WIP = 0%}) and compared with the results found in the literature [6–9, 17], see Fig. 3b. The maximum increase in compressive strength is observed for 75 % WIP mortar, which is about 70 %, 40 %, and 30 % at 7, 14, and 28 days, respectively, higher than 100 % NFA mortar. It is observed that the experimental results are in good agreement with the results found in the literature [7–9].

The tensile and flexural strength of mortar mixes made with different percentage replacement of NFA by WIP is presented in Fig. 4a and 5a, respectively. The normalized tensile and flexural strength at 28 days are compared with the results found in the literature and presented in Fig. 4b and 5b, respectively. It is seen that the tensile and flexural strength increases with the increasing percentage of WIP for all curing ages, which is in good agreement with the results of the compressive strength. The maximum increase in tensile and flexural strength is observed for the mortar made with 100 % WIP and 75 % WIP, respectively. The increase in tensile and flexural strength of mortar for all curing ages are on average 20 % and 38 %, respectively, higher than the mortar made with 100 % NFA. These results are consistent with the results available in the existing studies [6–8]. As described previously, these higher tensile and flexural strengths of mortar made with WIP could be linked to higher strength, higher angularity, and excellent surface roughness (see Fig. 1c), which ensured better bonding between cement paste and WIP than NFA. It is also noted that the WIP provides additional tensile strength to the mortar that prevents the formation of cracking, resulting in higher tensile and flexural strength. These experimental results demonstrate that the NFA could be replaced by up to 75 % with WIP since above that replacement, the flexural and compressive strength decreases, but not below the strength of the control mortar (mortar made with 100 % NFA). The reduction in strength of mortar made with 100 % WIP could be attributed to the small voids appearing on the internal texture of the WIP (see Fig. 1c) and lower workability (see Table 4) that could increase the porosity of mortar and consequently reduce the strength.

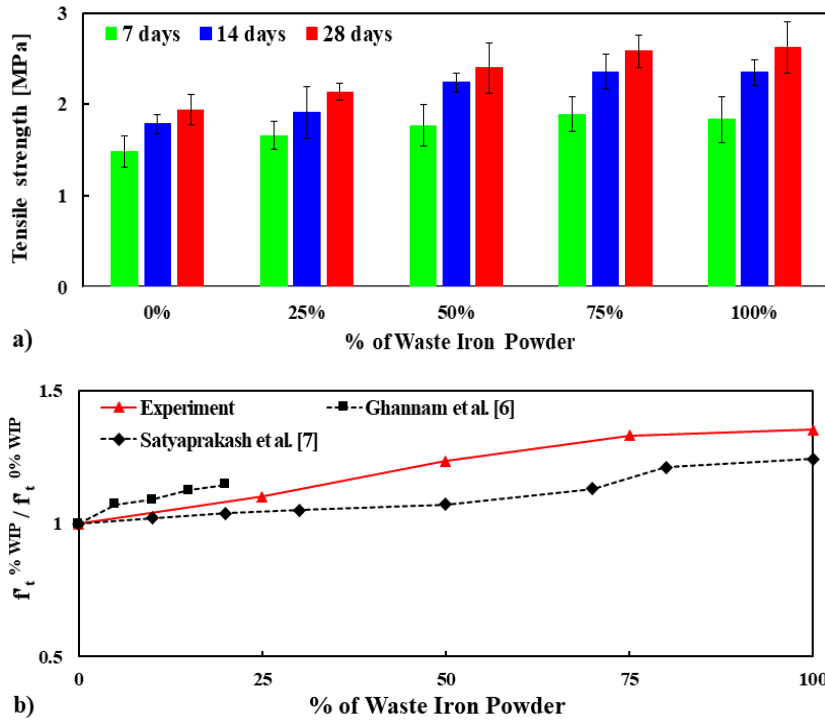


Figure 4. Tensile strength (f'_t) of mortar tested at 7, 14, and 28 days, and normalized f'_t of mortar mixes measured at 28 days is compared with other results found in the literature (b), respectively.

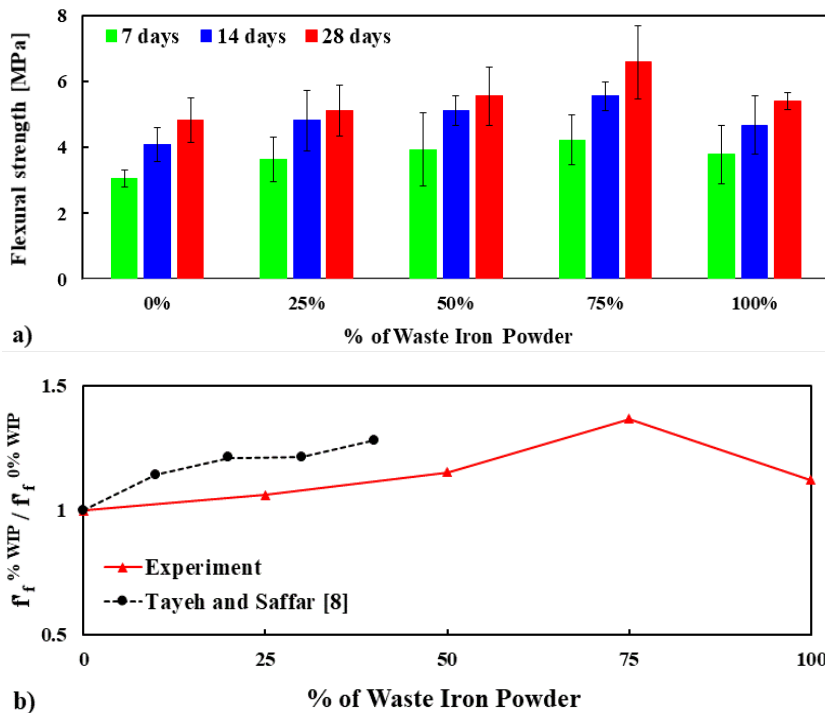


Figure 5. Flexural strength (f'_f) of mortar performed at 7, 14, and 28 days, and normalized f'_f of mortar mixes performed at 28 days is compared with other results found in the literature (b), respectively.

This high strength (compressive, tensile, and flexural) of mortar made with WIP provides a better future direction for sustainable construction building materials. For example, in Bangladesh, the ferrocement technique is commonly used to retrofit the structure due to the availability of materials and cost-effectiveness [29–30], where the strength of mortar and bond between mortar and parent concrete play an important role. Based on the results presented in this paper, this high strength mortar (≈ 50 MPa or

7250 psi) could be used in the ferrocement technique/repair work, which will not only provide higher strength as well as a better bond among mortar, ferrocement steel wire mesh, and parent concrete. It also demonstrates that this mortar will provide higher ductility due to its higher tensile and flexural strength of iron that will prevent the brittle collapse of the structures and save the people inside the structure during extreme external loads, such as earthquake, wind, blast, and fire. Furthermore, the durability performance of ferrocement is also depended on mortar properties due to its lower net cover of mortar, higher surface area of the steel wire mesh (i.e., higher risk of corrosion), the higher porosity and permeability of mortar due to lower strength (i.e., higher penetration of water, higher corrosion) [29].

3.1.3. Dry density

The evolution of the dry density of mortar made with WIP as a function of time is presented in Fig. 6a, and the normalized dry density measured at 28 days are compared with the results found in the literature and presented in Fig. 6b, respectively. As expected, with an increase in the percentage replacement of NFA by WIP, the dry density of mortar increases. The average density of mortar made with 0 %, 25 %, 50 %, 75 % and 100 % WIP are 2240 kg/m³, 2434 kg/m³, 2759 kg/m³, 2791 kg/m³ and 3298 kg/m³, respectively, at 28 days. The highest density is observed for the mortar made with 100 % WIP, which is about 10–40 % higher for all curing ages than the mortar made with 100 % NFA. This higher density of mortar made with WIP is directly linked with the higher specific gravity (4.31 for WIP and 2.56 for NFA) and better interlocking between WIP and cement paste than NFA. The higher density of mortar made with WIP is in agreement with other researchers [8, 9]. It is noted that the compressive, tensile, and flexural strength of mortar made with WIP is significantly higher as compared to the mortar made with NFA, which could be another reason for the higher density of mortar made with WIP than NFA.

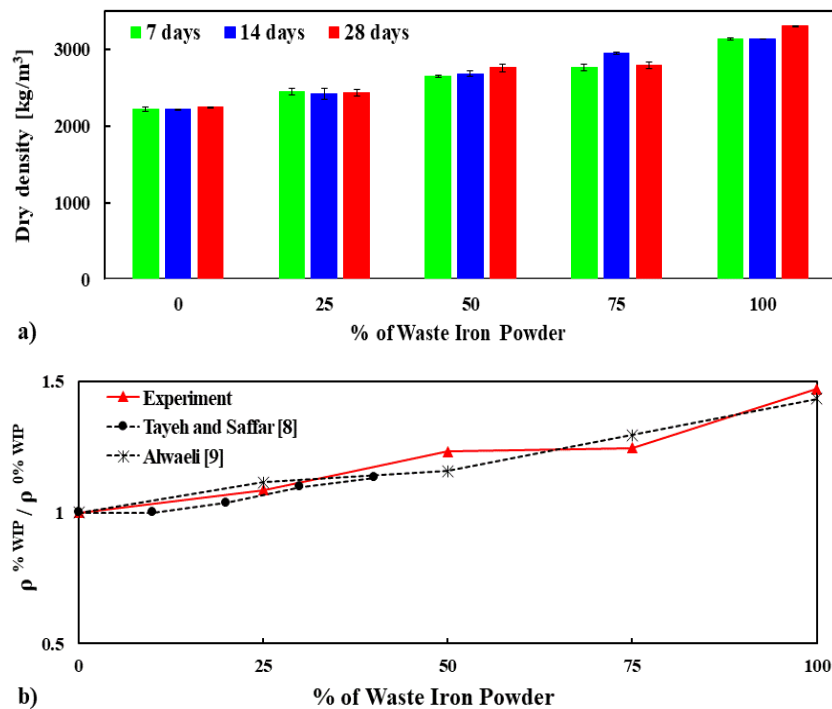


Figure 6. Dry density (ρ) of mortar tested at 7, 14, and 28 days, and normalized ρ of mortar mixes performed at 28 days is compared with other results found in the literature (b), accordingly.

3.2. Performance of mortar made with FWIP as replacement for cement

The compressive, tensile, and flexural strengths of mortar were investigated using different percentage replacements (0 %, 2.5 %, 5 %, 7.5 %, and 10 %) of cement by fine waste iron powder (FWIP). To fall into the size range of the cement, the FWIP was passed through a sieve opening of 75 μ m (#200 sieve). The compressive, tensile, and flexural strength of mortar made with partial replacements of cement by FWIP were performed at 7, 14 and 28 days and are presented in Fig. 7. For every data set, three specimens were tested, and then the average value was calculated.

It is found that the replacement of cement by FWIP decreases the strength of mortar for all curing ages. For example, the average compressive strength of mortar measured at 28 days of 0 %, 2.5 %, 5 %, 7.5 % and 10 % of FWIP are, respectively, 38.5 MPa, 34.2 MPa, 29.4 MPa, 27.4 MPa and 22.4 MPa. Almost similar behavior is observed for tensile and flexural strength of mortar made with FWIP. The

decrease in strength of mortar at 28 days as partial replacement of cement by FWIP is 10–40 % lower for compressive and tensile strength, and 4–16 % lower for flexural strength than the mortar made with 100 % cement. This reduction of mechanical strength is in agreement with the literature [19–22]. It is noted that a lower reduction in flexural strength is observed as compared to tensile and compressive strength when cement is replaced by FWIP. Probably, FWIP does not have cementitious as well as pozzolanic behavior (i.e., lower amount of calcium silicate hydrate, CSH), which could explain the lower strength of this mortar. However, incorporating mineral admixtures such as fly ash, blast furnace slag, and silica fume in cement with FWIP could enhance the mechanical strength of mortar. In the literature, it was found that the concrete made with iron tailing powder, cement, and mineral admixture such as slag and fly ash enhances the mechanical properties as well as microstructure of concrete [20–22, 31–33].

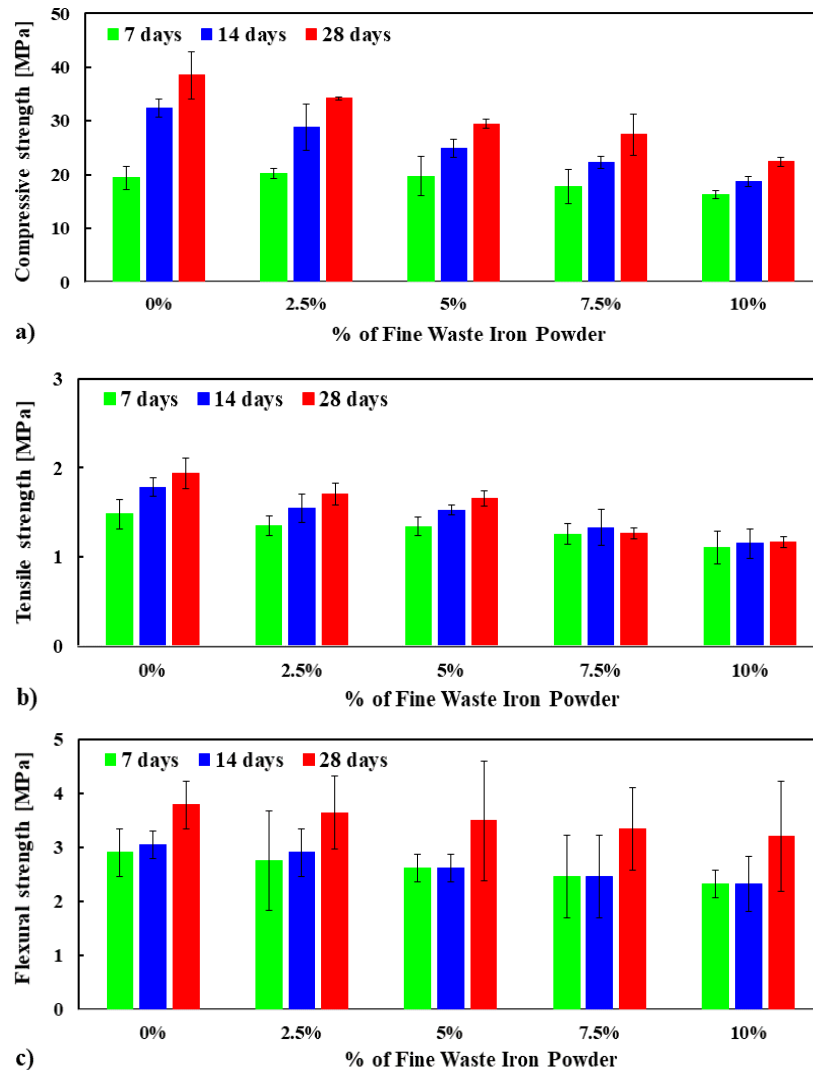


Figure 7. Compressive (a), tensile (b), and flexural (c) strength of mortar made with FWIP as replacement of cement tested at 7, 14, and 28 days, respectively.

4. Conclusions

This paper dealt with the compressive, tensile, and flexural strength as well as dry density of mortar made with five different percentage replacements of 0 %, 25 %, 50 %, 75 %, and 100 % for natural fine aggregate (NFA), and 0 %, 2.5 %, 5 %, 7.5 % and 10 % for cement by fine waste iron powder (FWIP). The cube, briquette, and prism specimens were made to perform compression, tension, and flexural strength of mortar at 7, 14, and 28 days. Based on the results presented herein, the following conclusions can be drawn:

I. The use of WIP as a replacement for NFA in mortar shows significantly higher compressive, tensile, and flexural strength, which is 30 % for compression, 35 % for tensile, and 37 % for flexural strength, respectively, higher when NFA is replaced by 75 % WIP. By contrast, adding FWIP (passed through sieve opening of 75 μm) as partial replacement of cement decreases the compressive, tensile, and flexural strength of mortar.

II. Lower workability is noticed for the mortar made with WIP than NFA, which could be attributed to the highly angular and rough surface texture of WIP than NFA as well as better interlocking, which reduces the mobility of fresh mortar.

III. An increased dry density is observed with the increasing replacement percentage of NFA by WIP. This higher density of mortar made with WIP is directly linked with the higher specific gravity (4.31 for WIP and 2.56 for NFA) and better interlocking between WIP and cement paste than NFA.

IV. From the experimental results of the five mixes, this study implies that WIP can be used up to 75 % replacement of NFA as fine aggregate since WIP is stronger, higher angular, and has an excellent sharp surface texture, which provides better mechanical performances. In contrast, to produce low strength and ultra-low strength mortar, FWIP could be used as partial replacement of cement since the reduction of strength is about 40 % for compression and tension, and 16 % for flexural strength lower compared to 100 % cement mortar at 28 days.

V. The outcome of this research will encourage iron waste producers to continue collecting and storing these hazardous materials, which are cost-effective, enviro-friendly, and sustainable construction building materials.

5. Acknowledgments

The authors acknowledge funding and facilities provided by the Department of Civil Engineering, University of Asia Pacific (UAP) to undertake this research.

6. Conflicts of Interest

The authors declare no conflict of interest.

References

- Miah, M.J., Miah, M.S., Sultana, A., Shamim, T.A., Alom, M.A. The Effect of Steel Slag Coarse Aggregate on the Mechanical and Durability Performances of Concrete. *Key Engineering Materials*. 2020. 833. Pp. 228–232.
- Mehta, K.P. Reducing the environmental impact of concrete. *Concrete international*. 2001. 23. Pp. 61–66.
- Pacheco-Torgal, F., Ding, Y., Koutamanis, A., Colangelo, F., Tuladhar, R. *Advances in construction and demolition waste recycling: Management, processing and environmental assessment*, eds. 2. 2019. Abington Hall, Cambridge: Elsevier Science and Technology.
- Mahpour, A. Prioritizing barriers to adopt circular economy in construction and demolition waste management. *Resources, Conservation and Recycling*. 2018. 134. Pp. 216–227.
- Ramakrishnan, P. Iron powder from iron scrap. *Conservation & Recycling*. 1983. 6 (1/2). Pp. 49–54.
- Ghannam, S., Najm, H., Vasconez, R. Experimental study of concrete made with granite and iron powders as partial replacement of sand. *Sustainable Materials and Technologies*. 2016. 9. Pp. 1–9.
- Satyaprakash, Helmand, P., Saini, S. Mechanical properties of concrete in presence of Iron filings as complete replacement of fine aggregates. *Materials Today: Proceedings*. 2019. 15. Pp. 536–545.
- Tayeh, B.A., Al Saffar, D.M. Utilization of waste iron powder as fine aggregate in cement mortar. *Journal of engineering Research and Technology*. 2018. 5. Pp. 22–27.
- Alwaeli, M. The implementation of scale and steel chips waste as a replacement for raw sand in concrete manufacturing. *Journal of Cleaner Production*. 2016. 137. Pp. 1038–1044.
- Alwaeli, M., Nadziakiewicz, J. Recycling of scale and steel chips waste as a partial replacement of sand in concrete. *Construction and Building Materials*. 2012. 28. Pp. 157–163.
- Ismail, Z.Z., Al-Hashmi, E.A. Reuse of waste iron as a partial replacement of sand in concrete. *Waste Management*. 2008. 28. Pp. 2048–2053.
- Adeyanju, A.A., Manohar, K. Effects of steel fibers and iron filings on thermal and mechanical properties of concrete for energy storage application. *Journal of Minerals & Materials Characterization & Engineering*. 2011. 10. 1429–1448.
- Kumar, P.W.P., Ananthayya, M.B., Vijay, K. Effect of replacing sand by iron ore tailings on the compressive strength of concrete and flexural strength of reinforced concrete beams. *International Journal of Engineering Research & Technology*. 2014. 3. Pp. 1374–1376.
- Abraham, A.C., Sindhu, P.K. Optimization of granite and iron powder as partial replacement of fine aggregate in concrete. *International Journal of Innovative Research in Science, Engineering and Technology*. 2017. 6 (5). Pp. 7973–7981.
- Saxena, R., Kushwaha, A.S., Pal, S. Effect on compressive strength of concrete with partial replacement of sand using iron slag. *Journal of Civil Engineering and Environmental Technology*. 2015. 2 (6). Pp. 510–513.
- Olutoge, F.A., Onugba, M.A., Ocholi, A. Strength properties of concrete produced with iron filings as sand replacement. *Current Journal of Applied Science & Technology*. 2016. Pp. 1–6.
- Furlani, E., Maschio, S. Steel scale waste as component in mortars production: An experimental study. *Case Studies in Construction Materials*. 2016. 4. Pp. 93–101.
- Yunhong, C., Fei, H., Wenchuan, L., Rui, L., Guanglu, L., Jingming, W. Test research on the effects of mechanochemically activated iron tailings on the compressive strength of concrete. *Construction and Building Materials*. 2016. 118. Pp. 164–170.
- Cai, L., Ma, B., Li, X., Lv, Y., Liu, Z., Jian, S. Mechanical and hydration characteristics of autoclaved aerated concrete (AAC) containing iron-tailings: Effect of content and fineness. *Construction and Building Materials*. 2016. 128. Pp. 361–372.

20. Han, F., Luo, A., Liu, J., Zhang, Z. Properties of high-volume iron tailing powder concrete under different curing conditions. *Construction and Building Materials*. 2020. 241. Pp. 118108.
21. Han, F., Song, S., Liu, J., Huang, S. Properties of steam-cured precast concrete containing iron tailing powder. *Powder Technology*. 2019. 345. Pp. 292–299.
22. Han, F., Li, L., Song, S., Liu, J. Early-age hydration characteristics of composite binder containing iron tailing powder. *Powder Technology*. 2017. 315. Pp. 322–331.
23. ASTM. C136/C136M-14. Standard test method for sieve analysis of fine and coarse aggregates. ASTM International, West Conshohocken, PA. 2014.
24. ASTM C33/C33M-18. Standard specification for concrete aggregates. ASTM International, West Conshohocken, PA. 2018.
25. ASTM. C128-15. Standard test method for relative density (specific gravity) and absorption of fine aggregate. ASTM International, West Conshohocken, PA. 2015.
26. ASTM. C109/C109M-16a. Standard test method for compressive strength of hydraulic cement mortars (using 2-in. or [50-mm] cube specimens). ASTM International, West Conshohocken, PA. 2016.
27. ASTM. C307-18. Standard test method for tensile strength of chemical-resistant mortar, grouts, and monolithic surfacings. ASTM International, West Conshohocken, PA. 2018.
28. ASTM. C348-19. Standard test method for flexural strength of hydraulic-cement mortars. ASTM International, West Conshohocken, PA. 2019.
29. Miah, M.J., Miah, M.S., Alam, W.B., Lo Monte, F., Li, Y. Strengthening of RC beams by ferrocement made with unconventional concrete. *Magazine of Civil Engineering*. 2019. 89 (5). Pp. 94–105.
30. Miah, M.S., Miah, M.J. An Effective Retrofitting Scheme for Flat-Slab Systems Made with Unconventional Type Concrete. *International Journal of Structural and Civil Engineering Research*. 2020. 9 (1). Pp. 19–24.
31. Papayianni, I., Anastasiou, E. Production of high-strength concrete using high volume of industrial by-products. *Construction and Building Materials*. 2010. 24. Pp. 1412–1417.
32. Yusuf, M.O. Microstructure and strength of iron-filing Portland cement paste and mortar. *Magazine of Civil Engineering*. 2019. 90 (6). Pp. 28–36.
33. Yusuf, M.O. Synergistic-effect of iron-filing and silica-fume on the absorption and shrinkage of cement paste. *Magazine of Civil Engineering*. 2019. 91 (7). Pp. 16–26.

Contacts:

Md Jihad Miah, jihad.miah@uap-bd.edu

Mohammad Shamim Miah, mmshamim@iubat.edu

Suvash Chandra Paul, suvashpl@iubat.edu

Sih Ying Kong, kong.sih.ying@monash.edu

Adewumi John Babafemi, ajbabafemi@sun.ac.za

Md Kawsar Ali, kawsar.uap@gmail.com

Md Munir Hossain Patoary, 3dcometdesign@gmail.com



DOI: 10.34910/MCE.108.11

Properties of tropically sourced timber subjected to elevated temperature

N.N. Kencanawati* , A. Rofaida, I.W. Sugiarta, A. Beriman, A.I.T. Putri

Mataram University, Mataram, Indonesia

*E-mail: nkencanawati@unram.ac.id

Keywords: Elevated temperature, tropical hardwood, charring rate, timber, glulam

Abstract. Char layer is an important parameter for the fire-resistance design of timber. The char-layer insulates the inner layer (core) from high temperature to prevent further damage due to fire. This paper assesses the post-fire properties of tropical solid and laminated timber originating from Indonesia. The species are white teak, bayur, rajumas, and sengon. The timber was exposed to fire at time interval of 30, 45, and 60 min. The temperature growth was set according to ISO 834 standard heating curve. The result shows that the average of charring rate of species with greater density and longer time of exposure is smaller than that of species with smaller density and shorter time of exposure. The charring rate of tropical solid and glulam timber has a linear inverse relationship to the density at each time of exposure. The average experimental data linear regression suggests that tropically sourced timber with a density of more than 400 kg/m³ meets the charring rate of European standard. However, all experimental results agree with the Australian standard. Furthermore, according to post-fire mechanical properties examination, the solid timber core shows increased strength after fire; meanwhile, a strength decrease exists in glulam core.

1. Introduction

Wood is one of the preferred construction materials because of the advantages offered such as high stiffness and strength-to-weight ratio, eye-pleasing, and renewable resources, relatively compared to other construction materials. Therefore, the tendency of using wood has been continuing to increase, both for structural and industrial purposes [1–4]. However, due to the natural substance, several challenges must be considered in wood application especially the behavior of being exposed to elevated temperature. Wood is a combustible material consisting of cellulose, lignin, and hemicellulose. The basic form of those compositions is carbon, hydrogen, and oxygen which are combustible when there is room temperature increase excessively [5–9].

When the temperature rises and starts from 150 °C, the surface of the wood structures will experience a degradation thermal process (pyrolysis). As the temperature increases, the outside part of wood decomposes into a char layer. The char layer does not have any strength or stiffness, but it acts as an insulating material to inhibit further degradation to the inner layer (core). The char-layer insulates the core from high temperature to prevent further damage due to fire. Char-line is a boundary between pyrolysis, the thermal degradation of wood, and the actual char. This interface is generally characterized by a temperature of 300 °C [10]. The depth of charring is measured from the outer surface of the undamaged cross-section to the char-line position. The growth of charring depth during a fire is called the charring rate. Within fire safety design, the charring rate is the significant factor for calculating the remaining strength of the core, that is an intact cross-section of the timber [11, 12]. Some methods have been established to calculate the residual strength of timber to sustain load continuously after a fire. The concept of calculation is based on a reduction in the cross-sectional area in which the char layer has no strength

Kencanawati, N.N., Rofaida, A., Sugiarta, I.W., Beriman, A., Putri, A.I.T. Properties of tropically sourced timber subjected to elevated temperature. Magazine of Civil Engineering. 2021. 108(8). Article No. 10811. DOI: 10.34910/MCE.108.11

© Kencanawati, N.N., Rofaida, A., Sugiarta, I.W., Beriman, A., Putri, A.I.T., 2021. Published by Peter the Great St. Petersburg Polytechnic University.



This work is licensed under a CC BY-NC 4.0

[10, 13–15]. The thickness of the char depends on wood species, density, moisture, permeability, composition, or direction of fire [11]. Char layer of wood species from the tropical country is discussed in this paper. Studies on solid and lamination timber with species which widely used in many western countries have been conducted by many researchers [6, 11, 16–21]. Char-layer thickness of pine wood, which is commonly used for construction in Portugal has been determined. It is found that after 30 minutes exposed to high temperature, char thickness of 1 cm existed on the top surface of specimens. For this position, the temperature was investigated around 250-300 °C [11]. In addition, a study on the mechanical properties of Parica wood from the cultivated forest in Brazil was conducted. At the highest temperature level (230 °C) caused a decrease of 35 % of the compression strength at ambient temperature and a decrease in the strain as well. The exposure of the specimens to high temperatures resulted in changes in the wood color, internal and externally, which were more pronounced at temperatures above 150 °C [18]. Furthermore, the charring rate of seven species of tropical wood has been examined under fire by [17]. The species are azobe (*Irophira alata*), afzelia (*afzelia bipindensis*), balau (*shorea spp.*), bilinga (*nauclea diderrichi*), meranti (*shorea rubro*), merbau (*intsia*), and wenge (*milletia laurentii*). The woods are the type of hardwood which frequently being used in construction. The density of wood determines the behavior during the fire and the new model of charring is proposed. The charring rate model of tropical woods are compared to various standards such as EC5, however, the standards are not entirely satisfactory the tropical wood charring rates. Due to the limited study provided on the charring rate of tropical hardwood species, therefore, more research on the tropical wood charring rate is on demand.

There are various species of tropical wood. Indonesia has a forest potential of around 4,000 types of wood. Among them have been widely studied. The physical and mechanical properties of 15 tropical wood species that were commonly used in Indonesia have been reported [22]. The wood ranging from softwood to hardwood. The hardwood is widely used in construction meanwhile softwood to be used in structural should be associated with hardwood in form of glued-laminated timber (glulam). One of the research on the properties of tropical glulam wood at ambient temperature has been conducted by [23]. However, there is limited research is available on the tropical wood species of solid and glulam timber at high temperature and the charring rate is not covered yet in the Indonesian national code for timber structures design [24]. Therefore, the properties of solid and glulam produced from some local woods after a fire are discussed in this paper.

2. Methods

2.1. Charring Rate Determination

A national code for wood structures must consider the fire resistance required for a structure when a fire occurs, both in the form of a protective material (insulation) and in the analysis of dimensions. Fire resistance in wood is based on standard fire test procedures and allows identifying the amount of time for the structure to carry enough load [13]. Eurocode 5 provides notional charring rates for multi-face exposure of solid and glulam hardwood which are 0.7 and 0.55 for the density of 290 kg/m³ and 450 kg/m³ respectively. In addition, the code sets a linear interpolation that may be used to obtain the charring rates of solid hardwoods for densities between 290 and 450 kg/m³ [14].

Similar to Eurocode 5, the Australian standard gives a charring rate of woods which depends on the density. The relationship between the density and charring rate as given by Eq. 1.

$$\beta = 0.4 + \left(\frac{280}{\rho} \right)^2, \quad (1)$$

where β is the charring rate of wood (mm/min) and ρ the density of the wood (kg/m³) [25].

Another standard provides a charring rate based on the timber type and species. British standard (BS 5268) states that the value of the notional charring rate for hardwood is 0.5. Meanwhile according to Forest Research Institute Malaysia, Malaysian tropical wood of balau and merbau possess a charring rate of 0.3 and 0.33 respectively [17]. In this paper, the charring rate of some tropical solid and glulam timber is calculated based on the depth of charring and the time of exposure experimentally.

2.2. Materials

The main materials used in this research were tropical woods obtained from the area of West Nusa Tenggara Region-Indonesia that has just been cut down and free from defects. The species are commonly found as well in South-East Asia Region and India. Solid and glulam timber were used in this study. Species of hardwood, which were white teak wood, bayur, and rajumas are the types of wood that are often used by the community in the form of a solid structure [22] and these solid woods were used in the previous study of pyrolysis and charring depth [26, 27]. Meanwhile, sengon is a softwood that is often used as the

inner lamina in glulam timber [23]. Therefore, white teak wood, bayur, rajumas, and sengon were considered as the specimens in the form of solid and glued laminated timber. The average physical properties and mechanical properties of these materials are shown in Table 2. The properties of the wood presented in Table 1 are obtained experimentally according to Indonesian National Code for timber structures [24] and were measured at 12–15 % moisture content.

The mechanical properties of the woods indicate that the quality of the woods between *E15-E26*, according to National Standard [24]; therefore, these local woods are considered to be strong and stiff to be utilized as building structure materials. The average density of white teak wood: 0.462, bayur: 0.407, rajumas: 0.381. This indicates that these woods are included in the category of wood with moderate weight because of the specific gravity of the wood in the ranges from 0.36 to 0.56. Meanwhile, sengon is recognized as softwood with an average density of 0.282.

Table 1. The average of physical and mechanical properties of wood.

Species	Specific gravity	Compressive strength (MPa)	Tensile strength (MPa)	Shear strength (MPa)	Bending strength (MPa)
White Teak (<i>Gmelina arborea</i>)	0.462	28.3	65.51	5.53	53.19
Bayur (<i>Pterospermum</i>)	0.407	39.25	41.54	5.47	56.76
Rajumas (<i>Duabanga mollucana</i>)	0.381	32.53	53.95	4.46	48.92
Sengon (<i>Paraserianthes falcataria</i>)	0.282	23.86	26.2	5.27	37.34

The size of the specimens for high temperatures was 80 mm by 120 mm by 500 mm in thickness, width, and length, respectively [11]. Solid timber was produced from hardwood (S-1: white teak wood, S-2: bayur, and S-3: rajumas). Meanwhile, the glulam timber consisted of sengon as the core lamina and the face laminas were the hardwoods. All laminas were constructed with parallel fiber orientation. Laminas with a thickness of 40 mm were used for three-layer construction (G-1: white teak-sengon-white teak; and G-2: rajumas-sengon-rajumas). The number of specimens was three pieces for each variation of solid and glulam timber. The cross-section of the specimen can be seen in Fig. 1. The adhesive was applied to bond the laminas according to the technical standards specified by the manufacturer. The cold press was applied for 24 hours at 1 N/mm² pressure, followed by conditioning for 1 week and finishing. The average specific gravity of G-1 and G-2 was 0.401 and 0.357 respectively. The average of shear strength and modulus of rupture (*MoR*) of glulam is presented in Table 2.

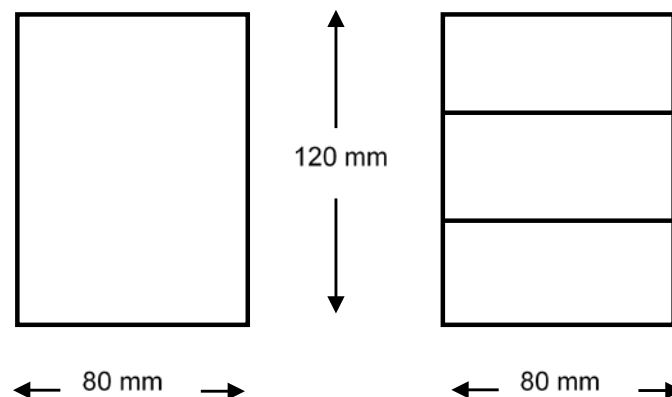


Figure 1. Solid and glulam cross section.

Table 2. The average of mechanical properties of glulam timber.

Glulam specimen	Shear strength (MPa)	<i>MoR</i> (MPa)
G-1	5.38	26.39
G-2	5.37	25.98

2.3. Fire Experiments

The heating periods were in the interval of 30, 45, and 60 min. The temperature growth is according to standard furnace test which is regulated on an international basis by ISO 834 [14]. The temperature-time relationship given in Eq. 2 and Fig. 2. The standard curve gives temperatures of 842 °C at 30 min, 902 °C at 45 min, and 945 °C at 60 min and 1049 °C at 120 min.

$$T = 345 \log(8t + 1) + 20, \quad (2)$$

where T is temperature (°C) and t is time period of fire (minute).

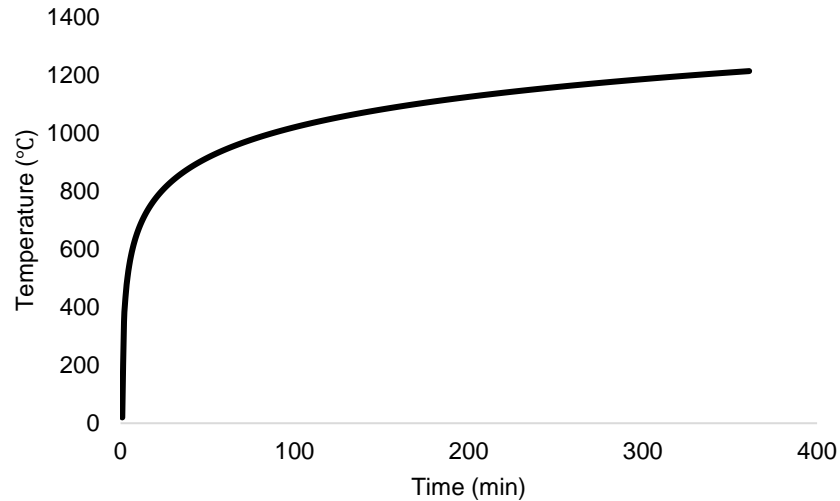


Figure 2. Temperature growth curve according to ISO 834 [14].

Fig. 3 shows the experimental fire test set up in the laboratory. The furnace is equipped by four burners, however, to meet the temperature growth required by the code, only two burners have been set up. The positioning of the wood in the furnace allowed the wood surface exposed to fire in the lateral direction. During the fire, the furnace was locked and two thermocouples were attached to control the temperature inside the furnace. After being exposed to elevated temperature, the depth of char layer and pyrolysis zone was investigated in five different points of the specimens by cutting the cross-section of the timber at 1 cm, 2 cm, 3 cm, 5 cm, and 25 cm apart from the top surface of the specimen as shown in Fig. 4 [11]. To determine the residual strength, the char layer was removed. The intact cross-section was then set for mechanical properties examination.



Figure 3. Fire test set up.

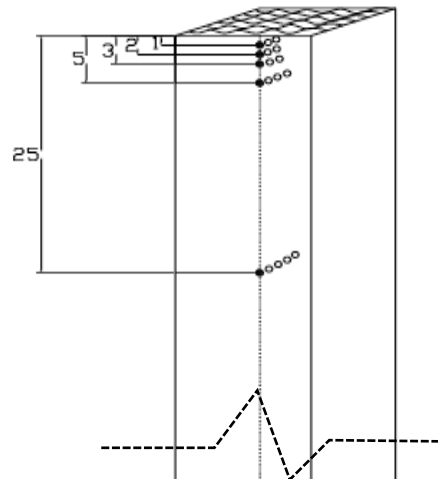


Figure 4. Char position observation [11].

3. Result and Discussion

3.1. Depth of charring

During the fire test, the solid and glulam timbers were exposed from lateral sides. The heating temperature inside the furnace reached 900 °C, 970 °C, and 1000 °C after 30 min, 45 min, and 60 min respectively. The maximum temperature on each heating was higher than those of the standard. The maximum temperature ratio between the experimental and the standard was 1.07, 1.07, and 1.06 respectively for 30 min, 45 min, and 60 min period of exposure.

To examine the depth of char, the timber was cooled to room temperatures naturally. Calculation of the charcoal depth was done by measuring the average thickness of the char laterally from each side. The cross-section that is closer to the top surface of the specimen and with a longer time interval of exposure experiences a thicker char layer as shown in Table 3 and Fig. 5.

Table 3. Average depth of charring.

Species	Time (min)	Distance from top surface (mm)				
		10	20	30	50	250
S-1	30	6.33	0.00	0.00	0.00	0.00
	45	12.24	5.90	0.00	0.00	0.00
	60	21.30	10.08	7.50	6.96	6.36
S-2	30	9.51	0.00	0.00	0.00	0.00
	45	19.13	13.23	5.74	0.00	0.00
	60	35.88	22.41	16.08	16.62	10.01
S-3	30	11.25	6.51	0.00	0.00	0.00
	45	23.72	14.80	11.52	10.67	0.00
	60	40.56	24.88	16.49	14.84	11.86
G-1	30	8.01	7.77	7.23	5.76	4.69
	45	16.79	14.19	9.45	9.05	8.24
	60	28.50	26.46	35.45	28.49	22.11
G-2	30	14.19	12.69	8.16	7.68	6.64
	45	29.16	24.84	19.76	15.28	13.43
	60	47.52	42.69	38.28	31.92	28.86



Figure 5. Charring depth at some positions.

In general, the char thickness increases due to increased fire exposure time. Less char thickness is observed in solid wood than glulam wood. White teak wood (S-1) does not show a significant char layer after 30 min exposure, even after exposure of 45 min, the char-layer is at the position of 10 and 20 mm from the top surface. Similar to S-1, bayur (S-2) shows a char layer only at a position nearby top surface after 30 min exposure, and no char-layer is found anymore beyond the position. And from 45 to 60 minutes of exposure, the char-layer is found until the position of 20 mm and 250 mm respectively from the top surface. For species S-3, char begins to exist at 30 min of fire and continued until the distance of 20 mm from the top, and it becomes thicker until exposure time of 45 and 60 min, where char is found up to position of 50 and 250 mm from the top surface.

Charcoal formation behavior in glulam is more severe compared to solid wood. G-1 glulam wood shows a thinner char-layer than G-2 because the resistance behavior to fire of white teak is better than rajumas wood. Even the G-2 glulam char has covered all wood surfaces after the time of 45 minutes. The surface area of the total cross-section turns into char was found up to a position of 20 mm from the top surface.

3.2. Charring rate

Calculation of the charring rate is evaluated at the position of 10 mm from the top because this condition generates the worst effect of fire. Table 4 shows the charring depth and charring rate of the species along with the density. In general, both for solid and glulam timber, the greater density shows lower charring depth and charring rate as suggested by many studies [10, 17, 25]. For solid timber, white teak has the greatest density presents the lowest charring rate. Meanwhile, glulam timber with density bigger than 400 kg/m³ show smaller charring rate than the glulam with a density of less than 400 kg/m³.

Table 4. Charring rate.

Species	Density (kg/m ³)	Fire exposure Time (min)	Average char depth (mm)	Char rate (mm/min)
S-1	462	30	6.33	0.211
		45	12.24	0.272
		60	21.30	0.355
S-2	407	30	9.51	0.317
		45	19.13	0.425
		60	35.88	0.598
S-3	381	30	11.25	0.375
		45	23.72	0.527
		60	40.56	0.676
G-1	401	30	8.01	0.267
		45	16.79	0.373
		60	28.50	0.475
G-2	357	30	14.19	0.473
		45	29.16	0.648
		60	47.52	0.792

Fig. 6 reveals that the development of char is almost constant from the initial (30 min) to final (60 min) heating time found in the species with greater density (solid wood: S-1 and S-2). Conversely, for the species with lower density (solid wood: S-1 and glulam wood: G-1 and G-2), the charring rate at the heating time of 45 min to 60 min develops faster than those charring rate at the heating time of 30 min to 45 min. The wood density not only determines the value of the charring rate but also influences the development of the charring rate itself over the fire exposure time. This finding agrees with [25], where the charring rate after a fire exposure of 60 min is greater than that after a fire exposure of 45 min due to increasing temperature inside the wood.

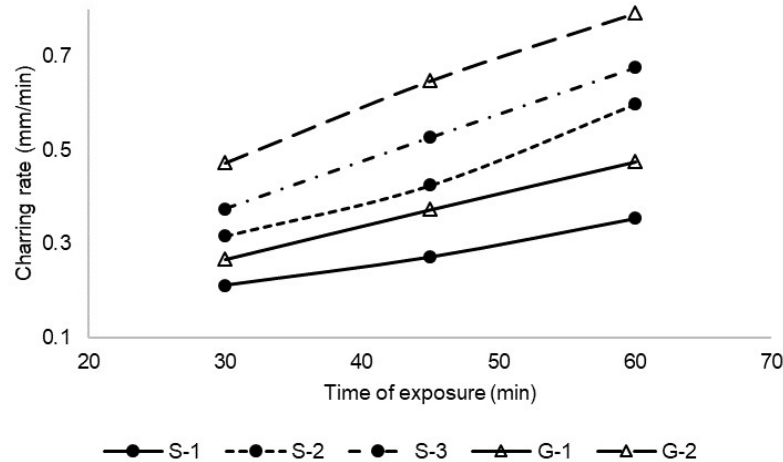


Figure 6. Development of charring rate.

In addition, the result shows that the average of charring rate of species with greater density and longer time of exposure, is smaller than that of species with smaller density and shorter time of exposure, for example species S-1 with a density of 462 kg/m^3 and exposure time of 60 min has a charring rate of 0.355 compared to species S-3 with a density of 381 kg/m^3 and exposure time of 30 min shows a charring rate of 0.375. Wood with a density greater than 400 kg/m^3 has more fire resistance over the fire exposure time. After a fire exposure of 60 min, the charring rate of solid and glulam timber has the inverse order to the density. The charring rate order of solid wood: $S-1 < S-2 < S-3$ and the density order: $S-1 > S-2 > S-3$. Similarly, for glulam timber, the order of charring rate: $G-2 < G-1$ and the order of density $G-1 > G-2$.

The value of charring rates are approaching with the finding of [17], where the tropical hardwood species, balau and merbau with the density range of $500\text{--}1000 \text{ kg/m}^3$ show the charring rate of 0.3 and 0.33 respectively. In this research, the hardwood species which has the largest density (S-1) show about the same value of the charring rate (0.355).

3.3. Influence of density on charring rate

Many researchers have been published the relationship between wood density and the charring rate, however, there are a few related to tropical wood. Fig. 7 presents the relationship between the density of timber and the charring rate of solid and glulam timber.

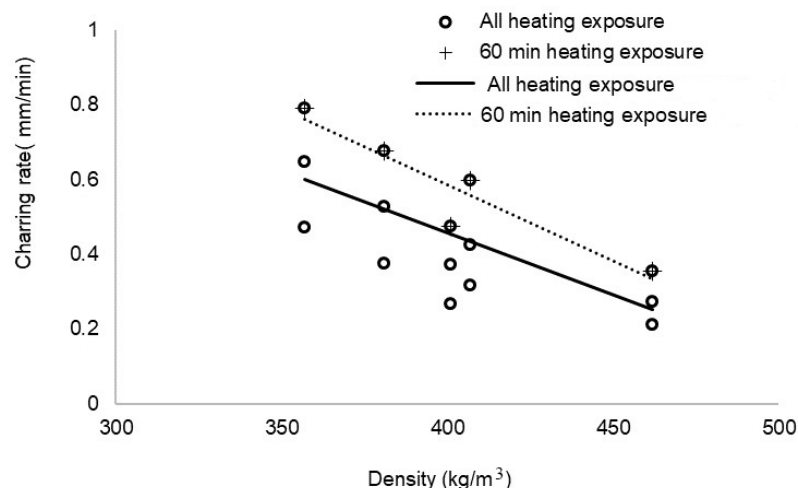


Figure 7. Relationship between density and charring rate.

A linear shape is obtained from the experimental result for the relationship between density and charring rate in all heating period of exposure (solid line), which is inline as stated in EN 1992-1-2 that a linear interpolation may be used to obtain the charring rates of solid hardwoods for densities between 240 and 450 kg/m³ [14]. Due to the nearly linear character of the curves of the average charring rates for the exposure time of 30, 45 and 60 minutes, the charring rate presented in that figure is the charring rate at 60 minutes (dashed line) [10]. The following linear regression (Eq. 3–6) is obtained for 30, 45, and 60 min and the average of 30, 45, and 60 min exposure time.

$$\text{Charring rate}_{(30)} = (-2.385 \times \text{density}) + 1.286, \quad (3)$$

$$\text{Charring rate}_{(45)} = (-3.490 \times \text{density}) + 1.851, \quad (4)$$

$$\text{Charring rate}_{(60)} = (-4.082 \times \text{density}) + 2.218, \quad (5)$$

$$\text{Charring rate}_{(\text{average})} = (-0.003 \times \text{density}) + 1.785. \quad (6)$$

Eurocode 5 recommends charring rates according to timber type for fire safety in building design. It is recommended a charring rate of 0.70 mm/min for solid and glulam hardwood for the density of 290 kg/m³ and a charring rate of 0.55 for the density of more than 450 kg/m³ [14]. Australian standard gives the relationship between the density and charring rate in a quadratic relationship and similar to Eurocode 5, it also reveals the negative relationship between density and charring rate. Fig. 8 illustrates the comparison of the experimental data of charring rates with Eurocode and Australian standard. The experimental regression which is discussed earlier is also attached in this figure.

Compared to European standard recommendation, in general, the solid and glulam timber are safe except timber with the lowest density (solid: S-3 and glulam: G-2) result in unsafe conditions due to higher charring rate. The average experimental data linear regression suggests that tropically sourced timber with a density of more than 350 kg/m³ meets the charring rate of European standard. However, according to the Australian standard, all experimental result agrees to the standard.

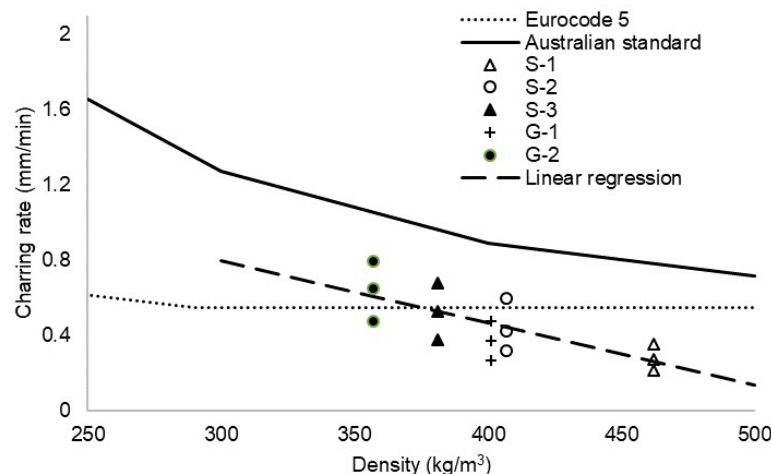


Figure 8. Comparison charring rate with other standard.

3.4. Post-fire mechanical properties

To investigate the properties of wood after elevated temperature can be approached by several methods. Principally, the concept is the same which is the char has no strength [14]. To examine the residual strength, the char layer was removed completely. The core was the inner part which was not affected by the fire due to the char insulation. The mechanical properties testing was conducted for the specimens which were affected by 60 min fire exposure because it was considered as the most severe condition of the timber. This core was prepared to determine the representative of the mechanical properties. Shear test was conducted on solid timber which required a small specimen size which enables to be obtained from the post-fire timber to observed post-fire shear strength. Meanwhile, the flexure test was conducted to glulam specimens. The same cross-section of intact specimens as the char removed cross-section was provided in advance as a comparison. Fig. 9 shows post-fire shear strength compared to the actual one.

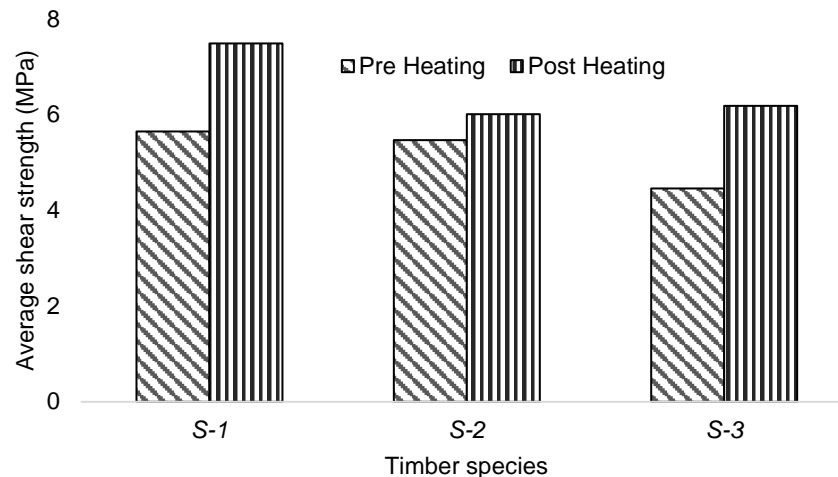


Figure 9. Shear strength comparison.

It is clearly can be seen that solid timber shows an increase in the shear strength after combustion. The timber gained strength around 1.3 times on average compared to the previous strength. The biggest increase occurred in S-3 which has the smallest density. The increase in properties in wood is assumed to be similar to wood given a heating treatment to improve its properties. The heat treatment usually does not exceed a temperature of 200 °C [1], [28], so it is assumed that the cores experience such temperatures because the inside core is protected by the char layer; thus, the properties of the core increase. Conversely, in the case of the glulam residual cross-section, there is a decrease of flexural load about 22.11 % and 18.45 % for G-1 and G-2 respectively after high temperature exposure. The decrease is assumed due to the bonding between the lamina being worsened after the fire [20].

4. Conclusion

The experimental procedures conducted in this paper are for assessing the post-fire properties of solid and glulam timber from tropical wood species. The following points can be drawn.

- The wood density not only determines the value of the charring rate but also influences the development of the charring rate itself over the fire exposure time.
- The average of charring rate of species with greater density and longer time of exposure is smaller than that of species with smaller density and shorter time of exposure
- After a fire exposure of 60 min, the charring rate of tropical solid and glulam timber have the inverse order as the density. The charring rate of solid wood in increasing order: white teak < bayur < rajumas and the density in decreasing order: white teak > bayur > rajumas. Similarly, for glulam timber, the charring rate in increasing order: white teak-sengon-white teak < rajumas-sengon-rajumas and the density in decreasing order: white teak-sengon-white teak > rajumas-sengon-rajumas.
- A linear relationship is obtained between wood specific gravity and charring rate at each exposure temperature
- The average experimental data linear regression suggests that tropically sourced timber with a density of more than 400 kg/m³ meets the charring rate of European standard. However, according to the Australian standard, all experimental result agrees to the standard.
- According to post-fire mechanical properties examination, the solid timber shows increased strength after fire; meanwhile, glulam timber does not.

References

- Ramage, M.H., Burrige, H., Busse-Wicher, M., Fereday, G., Reynolds, T., Shah, D.U., Wu, G., Yu, L., Fleming, P., Densley-Tingley, D., Allwood, J., Dupree, P., Linden, P.F., Scherman, O. The wood from the trees: The use of timber in construction. *Renewable and Sustainable Energy Reviews*. 2017. 68. Pp. 333–359. DOI: <https://doi.org/10.1016/j.rser.2016.09.107>.
- Claisse, P.A. Chapter 33 – Timber. *Civil Engineering Materials*. Butterworth-Heinemann. Boston, 2016. Pp. 369–386.
- Ajuong, E., Pinion, L.C., Bhuiyan, M.S.H. Degradation of Wood☆. *Reference Module in Materials Science and Materials Engineering*. Elsevier, 2018.
- Cheung, K.C.K. *Wooden Structures*☆. *Reference Module in Materials Science and Materials Engineering*. Elsevier, 2019.
- Woodard, A.C., Milner, H.R. 7 – Sustainability of timber and wood in construction. *Sustainability of Construction Materials (Second Edition)*. Second Edi. Woodhead Publishing, 2016. Pp. 129–157.

6. Wiesner, F., Bisby, L. The structural capacity of laminated timber compression elements in fire: A meta-analysis. *Fire Safety Journal*. 2019. 107. Pp. 114–125. DOI: <https://doi.org/10.1016/j.firesaf.2018.04.009>.
7. Östman, B., Brandon, D., Frantzich, H. Fire safety engineering in timber buildings. *Fire Safety Journal*. 2017. 91. Pp. 11–20. DOI: <https://doi.org/10.1016/j.firesaf.2017.05.002>.
8. Cabrero, J.M., Iraola, B., Yurrita, M. Chapter 7 – Failure of timber constructions. *Handbook of Materials Failure Analysis*. Butterworth-Heinemann, 2018. Pp. 123–152.
9. White, R.H., Woeste, F.E. Post-fire analysis of solid-sawn heavy timber beams. *Structure Magazine*. November 2013. Pp. 38–40.
10. Cachim, P.B., Franssen, J.-M. Assessment of Eurocode 5 charring rate calculation methods. *Fire technology*. 2010. 46 (1). Pp. 169. DOI: <https://doi.org/10.1007/s10694-009-0092-x>
11. Fonseca, E.M.M., Barreira, L.M.S. Charring rate determination of wood pine profiles submitted to high temperatures. *WIT Transactions on The Built Environment*. 2009. 108. Pp. 449–457. DOI: 10.2495/SAFE090421
12. White, R.H., Dietsberger, M.A. Fire safety of wood construction. *Wood handbook: wood as an engineering material: chapter 18*. Centennial ed. General technical report FPL; GTR-190. Madison, WI: US Dept. of Agriculture, Forest Service, Forest Products Laboratory, 2010: p. 18.1–18.22. 2010. 190. Pp. 11–18.
13. Gravit, M.V., Serdjuk, D., Bardin, A.V., Prusakov, V., Buka-Vaivade, K. Fire Design Methods for Structures with Timber Framework. *Magazine of Civil Engineering*. 2019. 85 (1). DOI: 10.18720/MCE.85.8
14. Purkiss, J.A. *Fire Safety Engineering Design of Structures*. Second. Elsevier, 2007.
15. Schmid, J., Klippel, M., Just, A., Frangi, A. Review and analysis of fire resistance tests of timber members in bending, tension and compression with respect to the Reduced Cross-Section Method. *Fire Safety Journal*. 2014. 68. Pp. 81–99. DOI: <https://doi.org/10.1016/j.firesaf.2014.05.006>.
16. Thi, V.D., Khelifa, M., Oudjene, M., Ganaoui, M., El, Rogaume, Y. Finite element analysis of heat transfer through timber elements exposed to fire. *Engineering Structures*. 2017. 143. Pp. 11–21. DOI: <https://doi.org/10.1016/j.engstruct.2017.04.014>.
17. Njankouo, J.M., Dotreppe, J.-C., Franssen, J.-M. Fire resistance of timbers from tropical countries and comparison of experimental charring rates with various models. *Construction and Building Materials*. 2005. 19(5). Pp. 376–386. DOI: <https://doi.org/10.1016/j.conbuildmat.2004.07.009>.
18. Manríquez, M.J., Moraes, P.D. Influence of the temperature on the compression strength parallel to grain of paricá. *Construction and Building Materials*. 2010. 24(1). Pp. 99–104. DOI: <https://doi.org/10.1016/j.conbuildmat.2009.08.003>.
19. Fahrni, R., Klippel, M., Just, A., Ollino, A., Frangi, A. Fire tests on glued-laminated timber beams with specific local material properties. *Fire Safety Journal*. 2019. 107. Pp. 161–169. DOI: <https://doi.org/10.1016/j.firesaf.2017.11.003>.
20. Zelinka, S.L., Sullivan, K., Pei, S., Ottum, N., Bechle, N.J., Rammer, D.R., Hasburgh, L.E. Small scale tests on the performance of adhesives used in cross laminated timber (CLT) at elevated temperatures. *International Journal of Adhesion and Adhesives*. 2019. 95. Pp. 102436. DOI: <https://doi.org/10.1016/j.ijadhadh.2019.102436>.
21. Klippel, M., Frangi, A. Fire safety of glued-laminated timber beams in bending. *Journal of Structural Engineering*. 2017. 143 (7). Pp. 4017052. DOI: [https://doi.org/10.1061/\(ASCE\)ST.1943-541X.0001781](https://doi.org/10.1061/(ASCE)ST.1943-541X.0001781)
22. Anshari, B., Rofaida, A., Sugiarta, I.W., Pathurahman, P. Study on Quality of Local Wood of Lombok Island Based on National Standard (in Indonesian). *Indonesian Wood Research Community*. 2015. Pp. 62–67. URL: www.mapeki.org
23. Komariah, R.N., Hadi, Y.S., Massijaya, M.Y., Suryana, J. Physical-mechanical properties of glued laminated timber made from tropical small-diameter logs grown in Indonesia. *Journal of the Korean Wood Science and Technology*. 2015. 43(2). Pp. 156–167.
24. SNI-7973-2013. *Indonesian National Standard: Design Specifications for Timber Structures* Jakarta, Indonesia, 2013.
25. Yang, T.-H., Wang, S.-Y., Tsai, M.-J., Lin, C.-Y. The charring depth and charring rate of glued laminated timber after a standard fire exposure test. *Building and Environment*. 2009. 44 (2). Pp. 231–236. DOI: <https://doi.org/10.1016/j.buildenv.2008.02.010>. URL: <http://www.sciencedirect.com/science/article/pii/S036013230800036X>
26. Kencanawati, N.N., Anshari Buan, Rofaida, A., Sugiarta, I.W., Handayani, T. Fire Resistance of Jati Putih Wood (in Indonesian). *National Conference on Science and Technology*. 2018. URL: <https://ppm.unram.ac.id/seminar-nasional-2018/>
27. Kencanawati, N.N., Anshari, B., Fajrin, J., Hariyadi, H. Post Behaviour of Laminated Timber After Fire. *UKARST*. 2020. 4 (2). Pp. 207–221. DOI: <http://dx.doi.org/10.30737/ukarst.v4i2.909>
28. Percin, O., Peker, H., Atilgan, A. The effect of heat treatment on the some physical and mechanical properties of beech (*Fagus orientalis lipsky*) wood. *Wood Research*. 2016. 61 (3). Pp. 443–456.

Contacts:

Ni Nyoman Kencanawati, nkencanawati@unram.ac.id

Aryani Rofaida, aryanirofaida@unram.ac.id

I Wayan Sugiarta, sugiartha88@gmail.com

Anfal Beriman, anfalberiman27@gmail.com

Aisya Intan Tajina Putri, aisyaaintan@gmail.com



DOI: 10.34910/MCE.108.12

Differential characteristics of concrete in centrifugally spun and vibrospun building structures

L.R. Mailyan , S.A. Stel'makh , E.M. Shcherban' 

Don State Technical University, Rostov-on-Don, Russia

*E-mail: au-geen@mail.ru

Keywords: concretes, mechanical properties, compressive strength, tensile strength, bending strength, elastic moduli, strain-stress curves

Abstract. This paper presents research into the variatropic structural characteristics of experimental circular-section concrete specimens as well as the related differential (varying depthwise) structural characteristics of concrete subjected to centrifugal spinning and vibrospinning. The researchers sought to assess how the production technology (centrifugal spinning or vibrospinning) could affect the differential (varying depthwise) characteristics of concrete: density; cube and prism axial compressive strength; ultimate axial compressive strain; axial tensile strength and tensile bending strength; ultimate axial tensile strain; the elastic modulus; the strain-stress curve for compression and tensioning. The researchers made and tested six basic centrifugally spun and vibrospun circular-section specimens that had an outer diameter D of 450 mm, an inner diameter d of 150 mm, and a total height $H = 1200$ mm. The manufacturing technology differed in the experiments, as the team used both centrifugal spinning and vibrospinning. Experimental research into the differential characteristics of centrifugally spun and vibrospun concrete aged 7, 28, and 180 days as exposed by compression and tension revealed that the outer concrete layer had the best characteristics, while the inner layer was the worst. The experiments thus back the three-layer model of the variatropic structure in centrifugally spun and vibrospun concrete. The following differentiation was observed in variatropic concrete: the outer layer had the best strength and elastic modulus, while being less deformable; the inner layer had the least strength and elastic modulus, while being more deformable; the mid-layer concrete was average in terms of everything. Stress-strain curves of centrifugally spun and vibrospun concrete did differ by layer, too, further proving that such concrete had a variatropic structure. The curves showed the greatest strength for the outer layer and the lowest for the inner layer, while the mid layer had average values.

1. Introduction

The physical fundamentals of variatropic structure in centrifugally spun concrete are detailed in [1–9]. The way it emerges essentially boils down to the fact that as the mold starts rotating at low rpm, the material is distributed evenly across the circular section; then, as the rotation accelerates, centrifuging squeezes some of the curing water out of the cement dough together with highly-dispersed particles; this brings larger filler particles closer together to condense the concrete mix.

Yu.Ya. Steyermann was the first to study the mechanism of filler drift in centrifugal condensing in detail. Assuming that the filler grains were suspended in the cement dough, he found that the dough exerted hydrodynamic pressure on the filler particles and quantified the distribution of fillers and cement dough across the section [8].

Mailyan, L.R., Stel'makh, S.A., Shcherban', E.M. Differential characteristics of concrete in centrifugally spun and vibrospun building structures. Magazine of Civil Engineering. 2021. 108(8). Article No. 10812. DOI: 10.34910/MCE.108.12

© Mailyan, L.R., Stel'makh, S.A., Shcherban', E.M., 2021. Published by Peter the Great St. Petersburg Polytechnic University.



This work is licensed under a CC BY-NC 4.0

Later, I.N. Akhverdov showed that this pressure depended on the geometric size of the spun product as well as on the mold rotation speed. The pressure alters depthwise in the wall: it is the lowest on the inner surface and peaks on the outer surface, which affects the specifics of how the liquid is being squeezed out of the concrete mix. The characteristic uneven depthwise distribution of cement dough in the product is associated with the emergence of multiple directed radial filtration channels increasing cross-section and number towards the inner surface. This is why the inner slurry layer of a concrete circle has a very high porosity [1].

Some other authors have shown that when using a mix of filler grains different in average density, properly attuned centrifuging speeds can produce more even, and thus more desirable depthwise distribution of those grains, as it is the unevenness of distribution that destabilizes the physical and mechanical properties [3, 4, 6, 7].

Research into the strength of centrifugally spun concrete has found that physical and mechanical properties differ significantly in inner and outer layers of concrete circles. These results not only prove that a single centrifugally spun specimen may differ physically and mechanically layer from layer; they also show that such concrete does differ from its vibrospun counterparts in terms of such properties [4, 6, 7].

V.M. Batashev and S.T. Androsov studied the strain-related properties of centrifugally spun concrete: the elastic moduli, the parametric points of microfracturing, creep, and shrinkage. The strengths of centrifugally spun concrete are scale-dependent, which is why it is important that experimental specimens be made under such conditions that mimic the real-world setting as much as possible. The strain-related properties of centrifugally spun concrete differ significantly depthwise in a circular section, as the inner layers have greater shrinkage and compressibility. Difference in properties may also depend on the specimen age; thus, layers may differ in strain by 50...100 % in freshly made concrete, 20...40 % after 50...60 days [2].

When in use, centrifugally spun concrete products are exposed to volatile stress and strain due to the uneven temperature and humidity fields emergent in the concrete body.

V.I. Podolsky [5] has found that the closed circle of a centrifugally spun reinforced-concrete pole carries two types of forced strain that determine the emergence of stresses:

- inner strain that occurs regardless of the element's static diagram due to the curvilinear distribution of moisture across over the cross-section;
- forced strain that occurs in a closed circle due to strain being limited along the entire outline or in a section of it.

Cyclical moistening and drying causes significant shrinkage-related strain that contributes to fracturing.

The way centrifugally spun concrete resists periodic freezing and thawing also has some specifics pertaining to the structural heterogeneity or variatropy of the material [10, 11].

It can be assumed that sequential molding layer-by-layer or use of associated vibration in centrifuging can direct the structuring of variatropic centrifugally spun concrete [12].

Today's research focuses more and more on circular-section reinforced-concrete products of variatropic structure; when exposed to a variety of impacts, such products cannot be modeled by conventional calculations as their stress-strain state is far more complex [13–15]. Papers [1–9] present the fundamentals behind the existing methods for calculating the parameters of centrifugally spun reinforced-concrete circular-section structures.

For instance, these methods can be used to calculate the parameters of circular-section reinforced-concrete products in a variety of stress-strain states [16–18].

G.A. Aksomitas researched short centrifugally spun circular-section columns that contained direct-axis reinforcements; the columns were exposed to short-term compression [9].

Centrifugal spinning and vibrospinning induce significantly different centrifugal and centripetal forces acting on outer, mid, and inner layers of the cross-section; this in turn induces a significant difference in the structure and characteristics of concrete in these layers, which must be taken into consideration when calculating [10–23].

This paper presents research into the variatropic structural characteristics of experimental circular-section concrete specimens as well as the related differential (varying depthwise) structural characteristics of concrete subjected to centrifugal spinning and vibrospinning.

The purpose of the work is to study concretes of a variatropic structure, vibrocentrifuged structures made of them with concrete characteristics differing in cross-section, and to develop recommendations for the design assessment of concrete characteristics and the operation of structures.

Research objectives:

- to investigate the differential (differing in cross-section) design characteristics of centrifuged and vibro-centrifuged concretes of variatropic cross-sections;
- to propose theoretical recommendations for the design determination of the structural characteristics of centrifuged and vibrocentrifuged concretes, taking into account variatropy.

The object of research is centrifuged and vibrocentrifuged concretes of variatropic structure and compressed elements from them.

The subject of research is the structural characteristics of variatropic concretes and taking into account the variatropicity in the calculation and design of compressed reinforced concrete elements from them.

2. Methods

The researchers made and tested six basic centrifugally spun and vibrospun circular-section specimens that had an outer diameter D of 150 mm, an inner diameter d of 1200 mm, and a total height $H = 1200$ mm.

For equipment and methods, see [24–28]. The manufacturing technology differed in the experiments, as the team used both centrifugal spinning (designated as C hereinafter) and vibrospinning (V).

After the analysis of scientific data, the following were accepted for research:

- crushed stone granite JSC "Pavlovsk Nerud" fraction 5-20 mm;
- quartz sand of the Grushevskoye deposit ($M_k = 2.0$).

As a binder, we used no additives Portland cement Evrocement of the group "Oskolcement" grade 500 normally hardening, the physical and mechanical properties of which are presented in Table 1.

Table 1. Physical and mechanical properties of cement.

Name	Specific surface, m ² /kg	Normal density, %	Setting time, hours-min.		Activity, MPa	
			start	end	R_b	R_{bt}
Portland cement	365	25.5	1-05	3-15	5.9	51.5

The researchers sought to assess how the production technology (centrifugal spinning or vibrospinning) could affect the differential (varying depthwise) characteristics of concrete: density; cube and prism axial compressive strength; ultimate axial compressive strain; axial tensile strength and tensile bending strength; ultimate axial tensile strain; the elastic moduli; the stress-strain curve for compression ($\sigma_b - \varepsilon_b$) and tension ($\sigma_{bt} - \varepsilon_{bt}$).

The test methodology differed in a sense that each basic experimental specimen was subjected to multiple different tests. Each basic specimen was tested aged 7, 28, and 180 days.

A quadrant was outlined in the specimen section that was further split into three layers (outer, mid, and inner), each 5 cm thick; then the layer-specific characteristics were found, see Fig. 1 and 2.

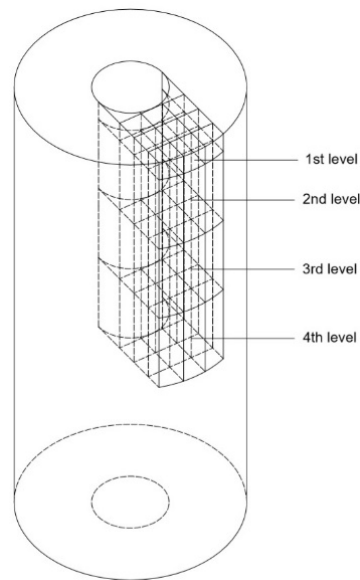


Figure 1. Diagram of taking small-size concrete samples for testing the depthwise differential characteristics of the basic full-size circular-section specimens.

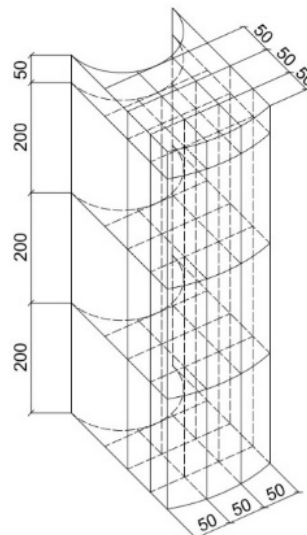


Figure 2. Experimental small-size concrete samples taken from experimental basic full-size circular-section specimens to test their differential characteristics.

For axial compression and tension tests, 9 cubes sized 5×5×5 cm were saw-cut out of the quadrant along the entire specimen (Level 1, axial compression tests), and so were 9 prisms sized 5×5×20 cm (Level 2, bending tension tests), 9 prisms sized 5×5×20 cm (Level 3, axial compression tests), and an additional 9 prisms sized 5×5×20 cm (Level 4) for axial tension tests.

Cube-based axial compression tests returned the values $R_{b,cub,i}$, prism-based axial compression tests returned the values $R_{b,i}$, $\varepsilon_{bR,i}$, $R_{bt,i}$, $\varepsilon_{btR,i}$, $E_{b,I} = E_{bt,i}$ as well as the stress-strain curves $\sigma_{b,i} - \varepsilon_{b,i}$, while prism-based axial tension tests returned $R_{bt,i}$ and $\sigma_{bt,i} - \varepsilon_{bt,I}$, and the prism-based bending tension tests returned $R_{btb,i}$.

All the specimens were tested aged 7, 28, and 180 days as required by Russian State Standard GOST 10180. Scaling factor was applied to correctly compare samples of different size.

Tests were carried out in accordance with Russian State Standard GOST 10180: an IPS-10 press was used for axial compressive tests of prisms, while a special unit based on a P-10 test press was used for axial tensile tests of prisms.

Strain in concrete was measured by a chain of tensor sensors with a base of 50 mm and clock-type indicators graduated at 0.001 mm.

Tests were carried out at a constant straining rate to derive not only the strength and strain-related characteristics of concrete, but also its complete stress-strain curves $\sigma - \varepsilon$ with descending branches. To that end, the experiments involved not only tensometers but also oscillographs.

The load would first increase until hitting the peak value, then decrease while the strain continued to increment. Thus, the tests recorded the descending branch of the stress-strain curve, which in this study had fairly stable outline up to $\sigma = 0.8 R$ in both stress and strain, then turned volatile.

Below are the test variables:

- manufacturing technology: centrifugal spinning and vibrospinning;
- stress-strain type: axial compression and axial tension;
- sample type: 5×5×5 cm and 15×15×15 cm cubes, 5×5×20 cm and 15×15×60 cm prisms;
- test mode: constant loading rate or constant straining rate;
- concrete age: 7, 28, or 180 days.

Centrifugally spun and vibrospun specimens were variatropic depthwise, i.e. they could be conditionally split into multiple layers that differed in material properties due to the manufacturing technology.

To detect how layers differed in terms of properties, a Pulsar 2.2 unit was used for preliminary ultrasonic scanning. To that end, 3 prisms sized 1200×150×50 mm were conventionally outlined in the wall of each specimen. The unit's sensors were attached as shown in Fig. 3 in all the three conventional layers (inner, mid, and outer) of the variatropic structure across the wall.

Declared concrete class – B40.

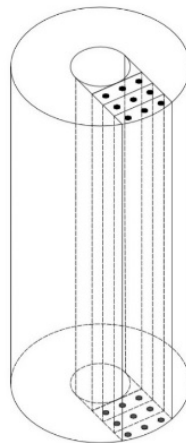


Figure 3. Ultrasonic sensor locations.

3. Results and Discussion

Table 2 shows the qualitative and quantitative distribution of density and strength in centrifugally spun and vibrospun concrete.

Table 2. The results of ultrasonic scanning of experimental specimens.

Indicator	Technology					
	Centrifugal spinning Layer			Vibrospinning Layer		
	outer	mid	inner	outer	mid	inner
Density	2495	2403	2316	2544	2492	2396
Compressive strength, MPa	43.4	35.5	32.2	68.2	65.1	41.6
Elastic moduli, MPa	34.3	27.8	24.8	38.8	35.2	28.5

As shown in Table 2, the outer layer had the greatest strength regardless of the manufacturing technology, as it was exposed to maximum centrifugal force; the inner layer was the weakest.

For centrifugally spun concrete, the curve of strength as a function of layer (from the outer to the inner layer) is a curve that slopes down and has downward concavity as shown in Fig. 4, while for vibrospun concrete, the concavity faces up, see Fig. 5.

That being said, the mid layer is between its inner and outer counterparts in terms of strength, which is below the arithmetic mean of inner+outer layer in centrifugally spun concrete but above that in vibrospun concrete, hence the difference in concavity.

The experiments thus back the three-layer model of the variatropic structure in centrifugally spun and vibrospun concrete.

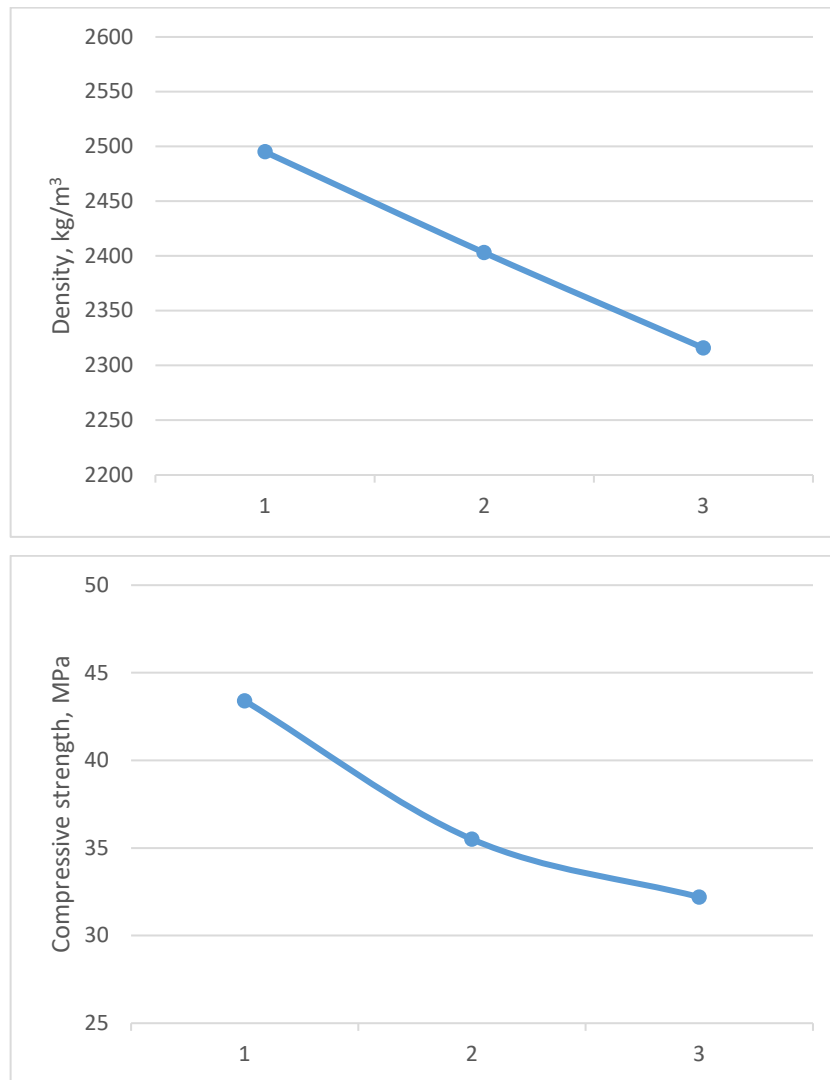
Similar changes are observed in layer strain and elastic moduli. It is the outer layer that should have the greatest elastic moduli, while the inner layer should have the lowest elastic moduli, with that of the mid layer being in between, slightly below average in centrifugally spun concrete and slightly above in vibrospun concrete, as evidenced in [4, 7] for centrifuged concrete.

Accordingly, all this causes the difference in the $\sigma - \varepsilon$ curves for different concrete layers.

Mechanical tests prove that, see below.

The 5 cm inner, mid, and outer layers were compared against each other in terms of compressive and tensile strength.

Conclusions were drawn from the analysis of experimentally found strength (Table 3) and its deviations (Table 4) shown in Fig. 6 for compression and in Fig. 7 for tension.



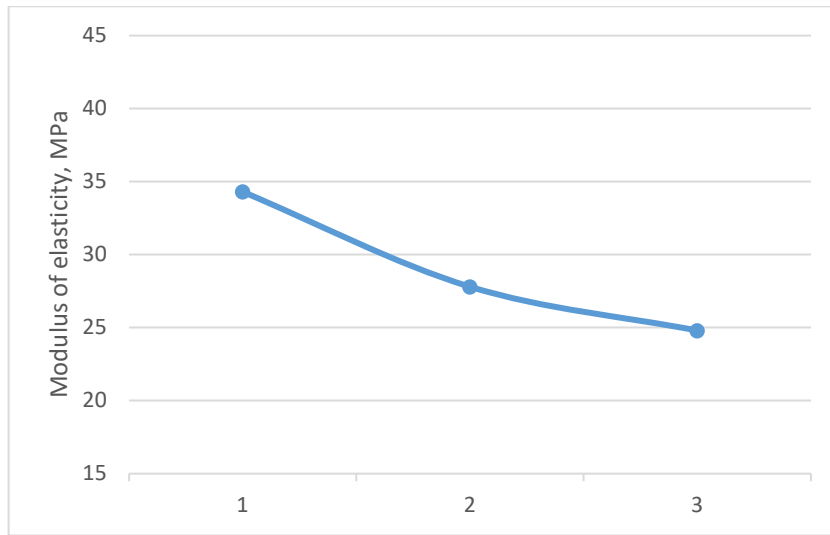
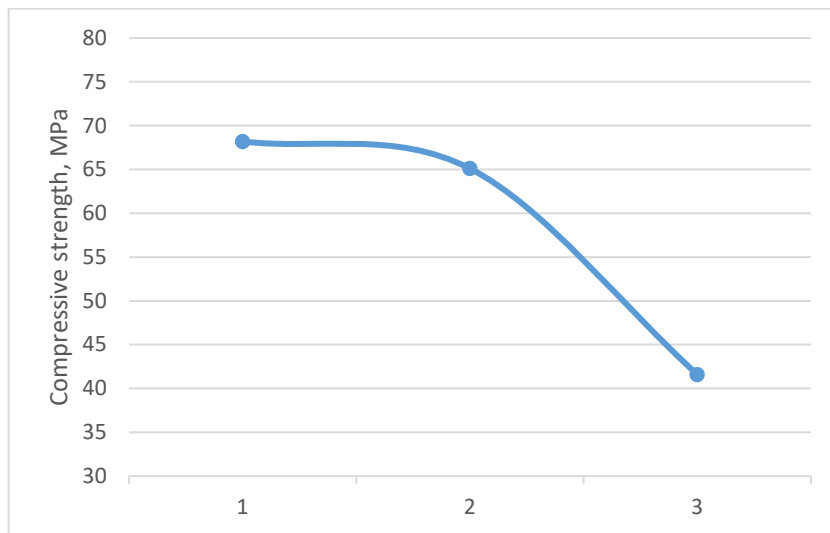
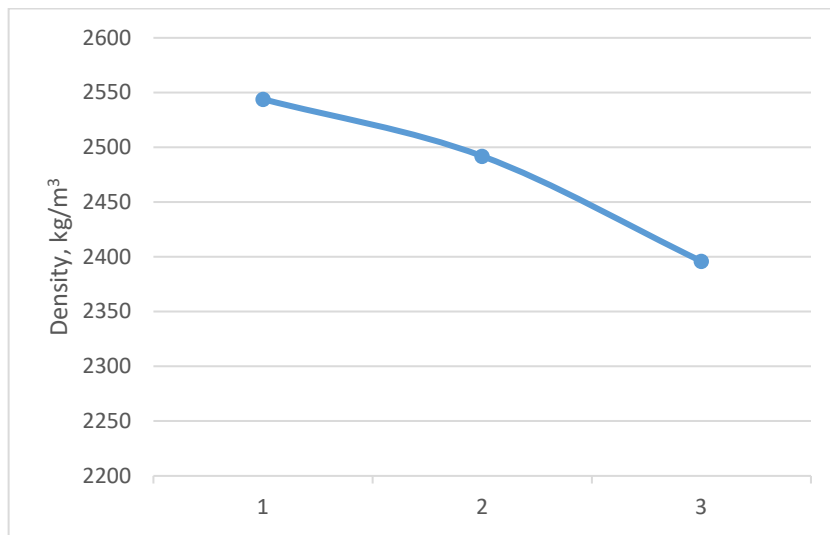


Figure 4. Layer-by-layer distribution of density, strength, and elastic moduli in centrifugally spun concrete: 1 is for the outer layer; 2 is for the mid layer; 3 is for the inner layer.



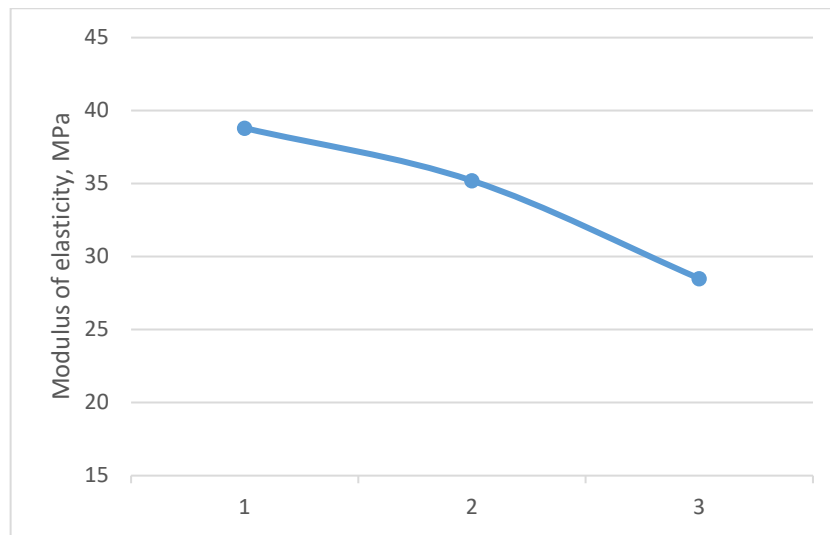


Figure 5. Layer-by-layer distribution of density, strength, and elastic moduli in vibrospun concrete: 1 is for the outer layer; 2 is for the mid layer; 3 is for the inner layer.

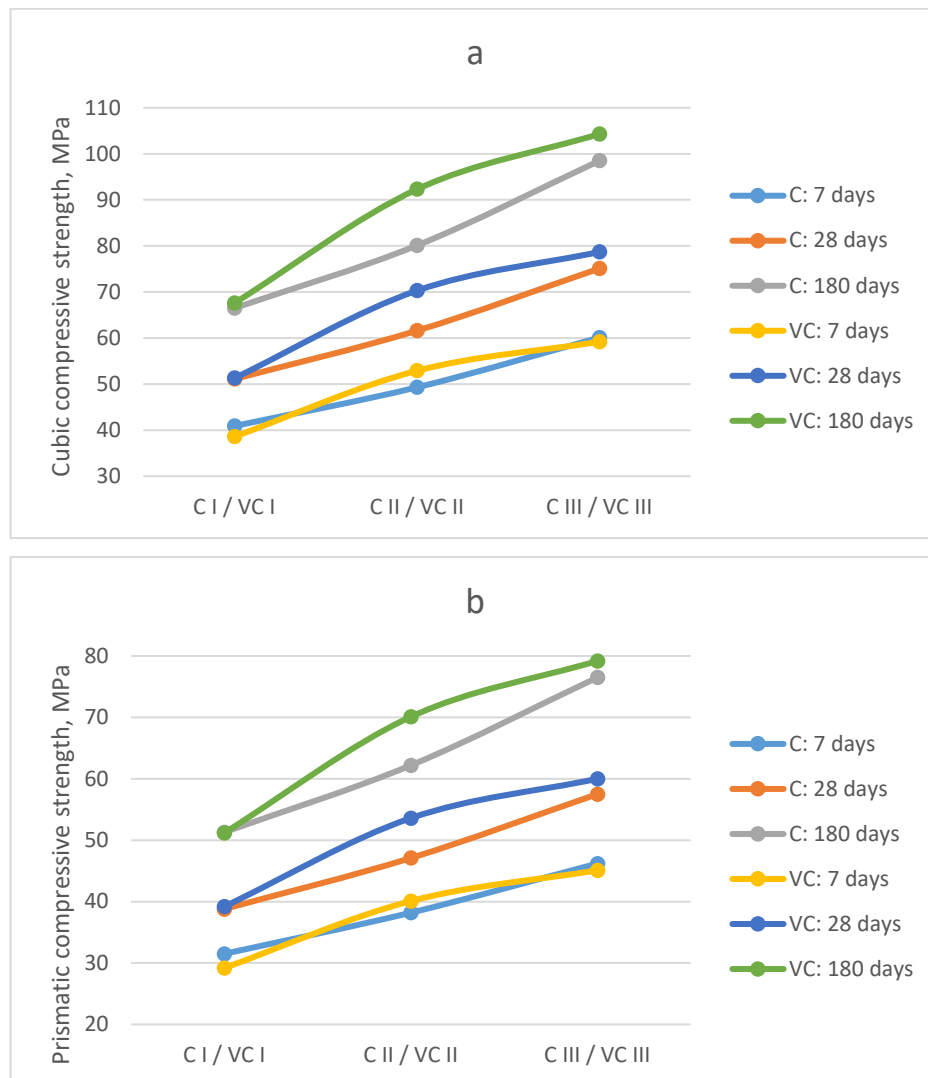


Figure 6. Compressive strength of centrifugally spun (C) and vibrospun (V) concrete: (a) cubes; (b) prisms.

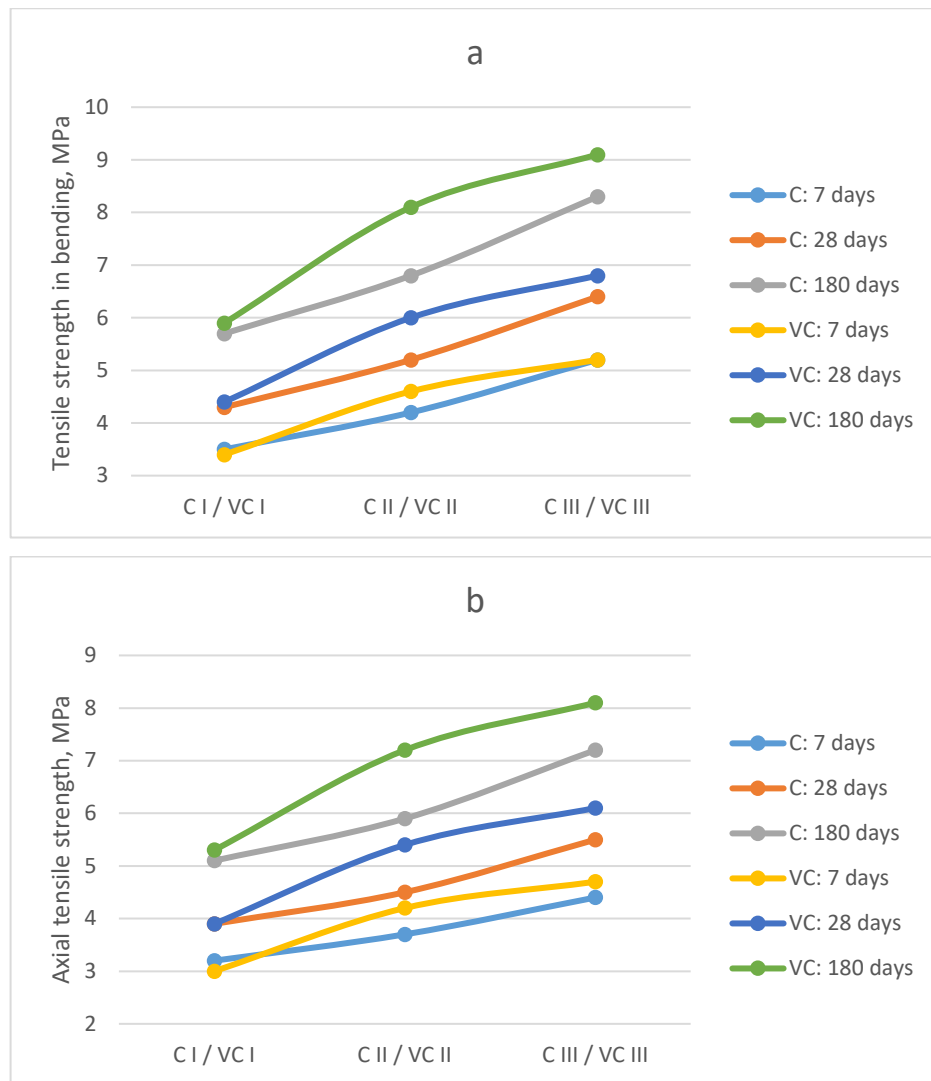


Figure 7. Tensile strength of centrifugally spun (C) and vibrospun (V) concrete: (a) bending; (b) axial.

Table 3. Experimental differential characteristics of variotropic structural layers in centrifugally spun and vibrospun concrete.

Characteristics of concrete	Manufacturing technology					
	Centrifugal spinning (C)			Vibrospinning (V)		
	Layers			Layers		
	inner CI	mid CII	outer CIII	inner VI	mid VII	outer VIII
Density, kg/m ³	2342/2335/2319	2443/2432/2411	2502/2495/2470	2350/2344/2329	2466/2455/236	2515/2502/277
Compressive strength, MPa:						
(a) cubes	40.9/51.1/66.5	49.3/61.6/80.1	60.1/75.1/98.5	38.6/51.3/67.6	52.9/70.3/92.3	59.2/78.7/104.3
(b) prisms	31.5/38.8/51.3	38.2/47.1/62.2	46.2/57.5/76.5	29.2/39.2/51.2	40.1/53.6/70.1	45.1/60.0/79.2
Tensile strength, MPa:						
(a) bending	3.5/4.3/5.7	4.2/5.2/6.8	5.2/6.4/8.3	3.4/4.4/5.9	4.6/6.0/8.1	5.2/6.8/9.1
(b) axial	3.2/3.9/5.1	3.7/4.5/5.9	4.4/5.5/7.2	3.0/3.9/5.3	4.2/5.4/7.2	4.7/6.1/8.1
Ultimate axial compressive strain, mm/m*10 ⁻³	3.40/2.64/2.10	2.80/2.15/1.72	2.35/1.82/1.45	3.10/2.40/1.80	2.80/2.12/1.61	2.00/1.54/1.17

Characteristics of concrete	Manufacturing technology					
	Centrifugal spinning (C)			Vibrospinning (V)		
	Layers			Layers		
	inner CI	mid CII	outer CIII	inner VI	mid VII	outer VIII
Ultimate axial tensile strain, mm/m*10 ⁻⁴	1.97/1.48/1.35	1.60/1.20/1.05	1.38/1.04/0.90	1.64/1.30/1.00	1.49/1.14/0.90	1.10/0.83/0.65
Elastic moduli, MPa	19.6/23.9/31.3	22.5/27.8/36.4	27.2/33.9/44.8	16.8/21.6/28.0	22.8/29.2/38.2	25.7/33.0/43.1

Note. Slash separates the values at 7, 28, and 180 days of age.

Table 4. Deviations in differential characteristics of variatropic structural layers in centrifugally spun and vibrospun concrete.

Characteristics of concrete	Deviations, %								
	C			V			V — C		
	Layers			Layers			Layers		
	Δ1	Δ2	Δ3	Δ4	Δ5	Δ6	Δ7	Δ8	Δ9
Density, kg/m ³	4.3/4.2/4.0	2.4/2.6/2.4	6.8/6.9/6.5	4.9/4.7/4.6	2.0/1.9/1.7	7.0/6.7/6.4	0.3/0.4/0.4	0.9/0.9/1.0	0.5/0.3/0.3
Compressive strength, MPa:									
(a) cubes	20.5/20.5/20.5	21.9/21.9/23.0	46.9/47.0/48.1	37.0/37.0/36.5	11.9/11.9/13.0	53.4/53.4/54.3	5.6/0.4/1.7	7.3/14.1/15.2	1.5/4.8/5.9
(b) prisms	21.3/21.4/21.2	20.9/22.1/23.0	46.7/48.2/49.1	37.3/36.7/36.9	12.5/11.9/13.0	54.5/53.1/54.7	7.3/1.0/0.2	5.0/13.8/12.7	2.4/4.3/3.5
Tensile strength, MPa:									
(a) bending	20.0/20.9/19.3	23.8/23.1/22.1	48.6/48.8/45.6	35.3/36.4/37.3	13.0/13.3/12.3	52.9/54.5/54.2	2.9/2.3/3.5	9.5/15.4/19.1	0.0/6.2/9.6
(b) axial	15.6/15.4/15.7	18.9/22.2/22.0	37.5/41.0/41.2	40.0/38.5/35.8	11.9/13.0/12.5	56.7/56.4/52.8	6.3/0.0/3.9	13.5/20.0/22.0	6.8/10.9/12.5
Ultimate axial compressive strain, mm/m*10 ⁻³	17.65/18.56/18.10	16.07/15.35/15.70	30.88/31.06/30.95	9.68/11.67/10.56	28.57/27.36/27.33	35.48/35.83/35.00	8.82/9.09/14.29	0.00/1.40/6.40	14.89/15.38/19.31
Ultimate axial tensile strain, mm/m*10 ⁻⁴	18.78/18.92/22.22	13.75/13.33/14.29	29.95/29.73/33.33	9.15/12.31/10.00	26.17/27.19/27.78	32.93/36.15/35.00	16.75/12.16/25.93	6.88/5.00/14.29	20.29/20.19/27.78
Elastic moduli, MPa	14.8/16.3/16.3	20.9/21.9/23.1	38.8/41.8/43.1	35.7/35.2/36.4	12.7/13.0/12.8	53.0/52.8/53.9	14.3/9.6/10.5	1.3/5.0/4.9	5.5/2.7/3.8

Notes: slash separates the values at 7, 28, and 180 days of age.

$$\Delta_1 = \frac{C_{II} - C_I}{C_I} \cdot 100\%; \quad \Delta_2 = \frac{C_{III} - C_{II}}{C_{II}} \cdot 100\%; \quad \Delta_3 = \frac{C_{III} - C_I}{C_I} \cdot 100\%;$$

$$\Delta_4 = \frac{VC_{II} - VC_I}{VC_I} \cdot 100\%; \quad \Delta_5 = \frac{VC_{III} - VC_{II}}{VC_{II}} \cdot 100\%; \quad \Delta_6 = \frac{VC_{III} - VC_I}{VC_I};$$

$$\Delta_7 = \frac{VC_I - C_I}{C_I} \cdot 100\%; \quad \Delta_8 = \frac{VC_{II} - C_{II}}{C_{II}} \cdot 100\%; \quad \Delta_9 = \frac{VC_{III} - C_{III}}{C_{III}} \cdot 100\%.$$

Vibrospun concrete has virtually the same patterns of layer-by-layer compressive strength distribution, although slightly less pronounced qualitatively: while in variatropic centrifugally spun concrete, the curve of strength as a function of layer was slightly concave downwards, it was concave upwards for the vibrospun counterpart.

The same pattern was observed with respect to tensile strength.

The outer layer had 18.9%/23.8% greater axial and bending strength than the mid layer in centrifugally spun concrete. The mid layer was 15.7%/20.9% stronger than the inner one.

As of vibrospun concrete, its mid layer had slightly greater values of both types of tensile strength; the outer layer, too, was stronger than that of centrifugally spun concrete, while the inner layer was low compared to either of the others.

This analysis makes clear that when designing a structure, the variatropic nature of sections and the associated changes in concrete strength have to be taken into account.

The next step was to find how it could affect the layer-specific compressive and tensile strain. The outer layer had the lowest ultimate tensile and compressive strain, the inner layer had the highest values, and the mid layer was in between, slightly above average in centrifugally spun concrete and below average in vibrospun concrete, see Fig. 8 and 9.

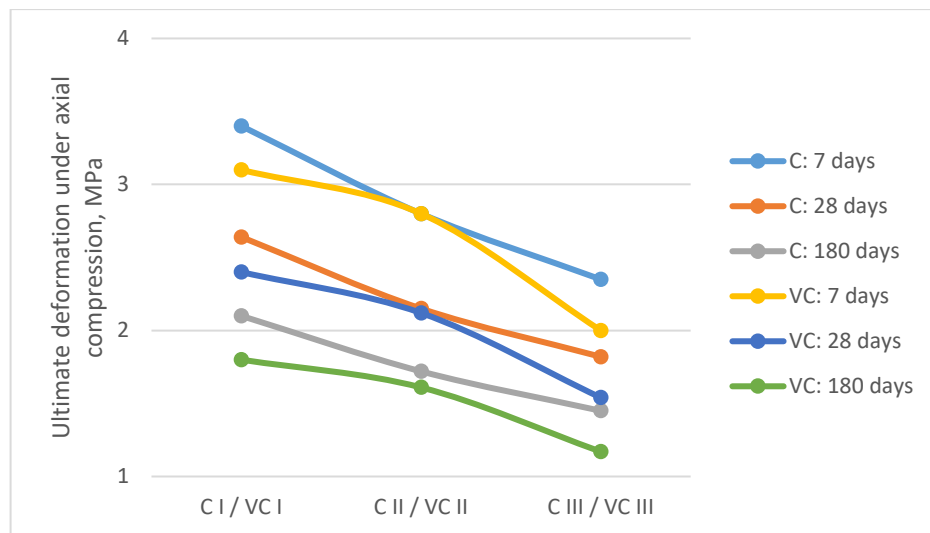


Figure 8. Ultimate compressive strain as a function of variatropic layer in centrifugally spun (C) and vibrospun (V) concrete.

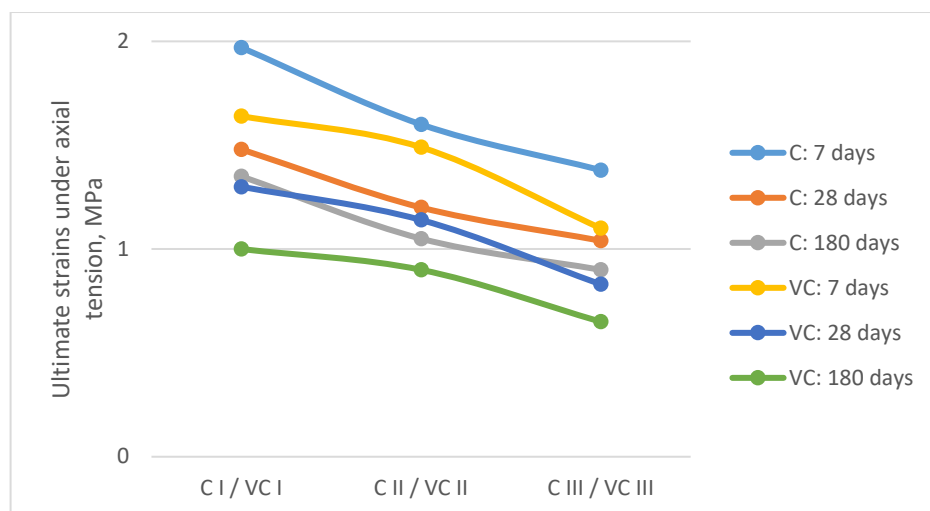


Figure 9. Ultimate tensile strain as a function of variatropic layer in centrifugally spun (C) and vibrospun (V) concrete.

It was the outer layer that had the greatest elastic moduli, while the inner layer had the lowest elastic moduli, with that of the mid layer being in between, slightly below average in centrifugally spun concrete and slightly above in vibrospun concrete, see Fig. 10.

The same applies to compressive and tensile elastic moduli, which did not differ significantly.

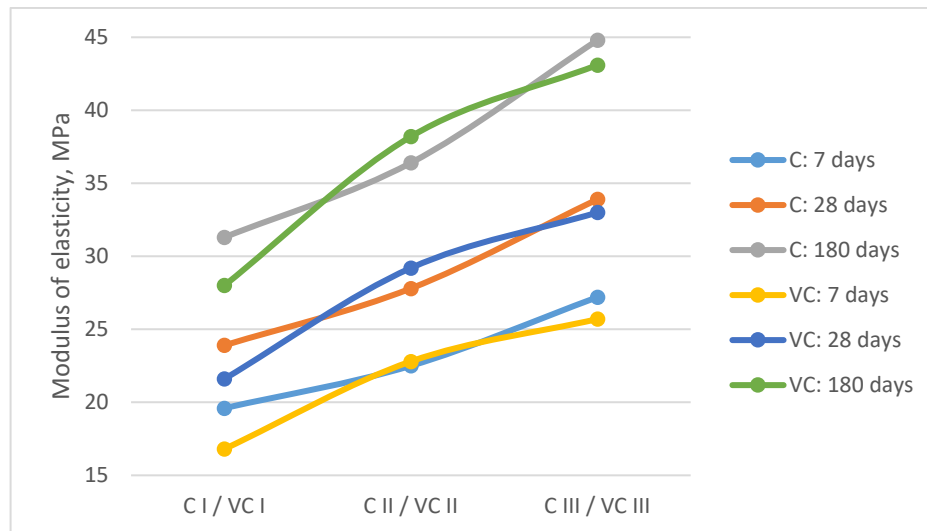


Figure 10. Elastic moduli as a function of variatropic layer in centrifugally spun (C) and vibrospun (V) concrete.

Accordingly, all this caused the difference in the $\sigma - \varepsilon$ curves for different concrete layers. Fig. 11 shows three experimental curves for inner, mid, and outer layers, where the difference matches the patterns observed for strength and strain-related characteristics.

For centrifugally spun concrete, it was the inner layer that had the lowest and shallowest $\sigma - \varepsilon$ curve associated with the lowest strength, the greatest associated ultimate strain, and the lowest elastic moduli that in such curves manifests itself as a bulge in the curve.

On the contrary, the outer layer that featured the greatest strength, the smallest ultimate strain, and a greater elastic moduli, the $\sigma - \varepsilon$ curve peaked at a more northwestern point with a more dramatic uprise in the ascending segment and a more drastic decline in the descending segment.

The mid-layer curve is in between, closer to that of the inner layer.

Similar patterns are observable in case of vibrospun concrete. The only thing to note here is that the inner/outer layer curves differ even more drastically, while the mid-layer curve is closer to its outer-layer counterpart.

Fig. 1 shows the experimental $\sigma - \varepsilon$ curves.

To sum it up, the results are as follows.

First, the curves do differ layer-by-layer, whether the concrete is centrifugally spun or vibrospun, proving both structurally variatropic.

Secondly, the greatest strength (the Y-axis) was observed for the outer layer, and the lowest was shown by the inner layer regardless of the concrete technology.

Thirdly, the greatest strain (the X-axis) was observed for the inner layer, while the outer layer showed the least strain, also regardless of the concrete technology.

Fourthly, the greatest uprise (the elastic moduli) was seen in the outer-layer strain curves, and the lowest was found in the inner-layer curves.

Fifthly, whether for centrifugally spun or vibrospun concrete, the mid layer had average values, being closer to the arithmetic means for the former and closer to the outer-layer strain curves for the latter.

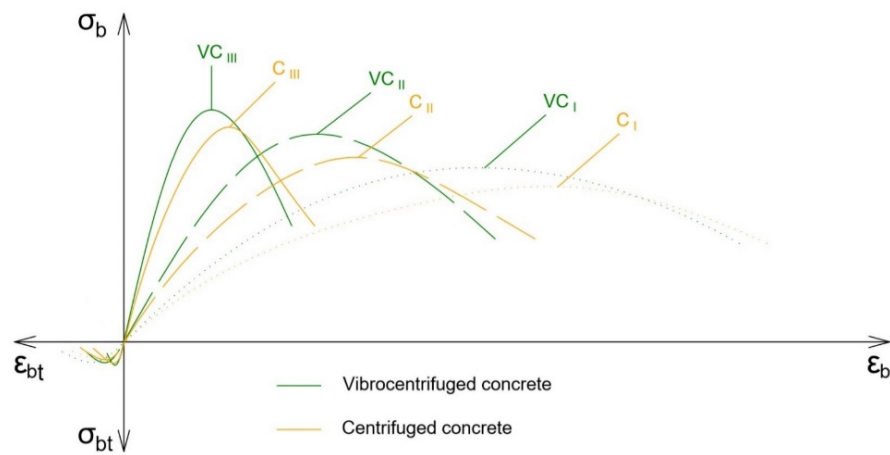


Figure 11. Transformation of variatropic layer-specific $\sigma - \varepsilon$ curves of centrifugally spun and vibrospun concrete.

Above is the analysis of how strength and strain-related characteristics changed from layer to layer in centrifugally spun and vibrospun concrete aged 28 days. However, concrete specimens were also tested aged 7 and 180 days.

The analysis generally shows that both types of concrete are immediately variatropic regardless of their age. In other words, the qualitative patterns of strength and strain-related differential characteristics did not change with age.

However, the quantitative indicators did, as concrete grew stronger with age.

The 7-day compressive and tensile strength was 73...81 % of the 28-day value. The corresponding ultimate strain was 21...29 % higher. The elastic moduli was 13...17 % lower.

At the age of 180 days, concrete had 11...13 % greater compressive and tensile strength, 9...12 % lower ultimate strain, and up to 15 % greater elastic moduli, although these changes are generally not as significant.

Accordingly, the age affected the stress-strain curves: compared to the 28-day curves, the 7- and 180-day counterparts differed in uprise, shallowness, and peak shift, see Fig. 12.

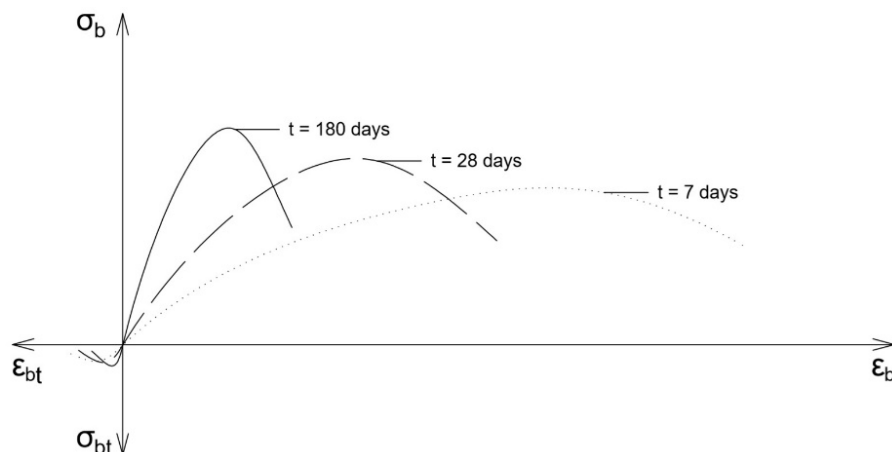


Figure 12. Fundamental changes in compressive and tensile strain curves at different ages of concrete.

4. Conclusion

The following conclusions were drawn.

Experimental research into the differential characteristics of centrifugally spun and vibrospun concrete aged 7, 28, and 180 days as exposed by compression and tension revealed that the outer concrete layer had the best characteristics, while the inner layer was the worst.

The experiments thus back the three-layer model of the variatropic structure in centrifugally spun and vibrospun concrete. The following differentiation was observed in variatropic concrete: the outer layer

had the best strength and the elastic moduli, while being less deformable; the inner layer had the least strength and elastic moduli, while being more deformable; the mid-layer concrete was average in terms of everything.

Stress-strain curves of centrifugally spun and vibrospun concrete did differ by layer, too, further proving that such concrete had a variatropic structure. The curves showed the greatest strength for the outer layer and the lowest for the inner layer, while the mid layer had average figures.

Thus, the analysis of variatropy and differential characteristics of centrifugally spun and vibrospun concrete structures leads to a conclusion that such characteristics mostly have to be taken into account in calculations.

References

1. Akhverdov, I.N. *Osnovy fiziki betona* [Fundamentals of concrete physics]. Moscow: Stroyizdat, 1981. 464 p. (rus)
2. Batashev, V.M. *Issledovanie prochnosti i deformatsii zhelezobetonnykh elementov kol'tsevoogo secheniya pri izgibe, szhatii i rastyazhenii* [The study of the strength and deformation of reinforced concrete elements of the annular cross section during bending, compression and tension]. *Trudy instituta Energoset'proekt.* 1975. 6. Pp. 70–86. (rus)
3. Dmitriev, S.A., Batashev, V.M. *Deformatsii (progiby) zhelezobetonnykh elementov kol'tsevoogo secheniya i raskrytie treshchin v nikh* [Deformations (deflections) of reinforced concrete elements of annular cross-section and crack opening in them] // *V sb.: Osobennosti deformatsii betona i zhelezobetona i ispol'zovanie EVM dlya otsenki ikh vliyaniya na povedenie konstruktssii* [Features of the deformation of concrete and reinforced concrete and the use of computers to assess their impact on structural behavior]. Moscow: Stroyizdat, 1969. Pp. 157–189. (rus)
4. Petrov, V.P. *Tekhnologiya i svoistva tsentrifugirovannogo betona s kombinirovannym zapolnitelem dlya stoek opor kontaktnoi seti: dis. ... kand. tekhn. nauk* [Technology and properties of centrifuged concrete with combined aggregate for racks of supports of the contact network: dis. ... cand. tech. of sciences]. Rostov-on-Don: RCEI, 1983. 175 p. (rus)
5. Podolsky, V.I. *Zhelezobetonnye opory kontaktnoi seti. Konstruktsiya, ekspluatatsiya, diagnostika* [Reinforced concrete supports of the contact network. Design, operation, diagnostics]. Moscow: Intekst, 2007. 152 p. (rus)
6. Romanenko, E.Yu., Trubitsin, M.A. *Sposoby povysheniya nadezhnosti tsentrifugirovannykh opor kontaktnoi seti* [Ways to improve the reliability of centrifuged supports of the contact network]. *Inzhenernyj vestnik Dona (Rus).* 2018. 1 [Online]. URL: <http://www.ivdon.ru/magazine/archive/n1y2018/4680> RU (reference date: 15.05.2020). (rus)
7. Radzhan, S. *Svoistva tsentrifugirovannogo betona i sovershenstvovanie proektirovaniya tsentrifugirovannykh zhelezobetonnykh stoek opor LEP: dis. ... kand. tekhn. nauk* [The properties of centrifuged concrete and the improvement of the design of centrifuged reinforced concrete pillars of power transmission towers: dis. ... cand. tech. of sciences]. Rostov-on-Don: RSUCE, 1997. 267 p. (rus)
8. Steyermann, Yu.Ya. *Tsentrifugirovannyi beton* [Centrifuged concrete]. Tiflis: Tekhnika da Shroma, 1933. 107 p. (rus)
9. Aksomitas, G.A. *Prochnost' korotkikh tsentrifugirovannykh kolonn kol'tsevoogo secheniya s prodol'noi armaturoi klassa At-V pri kratkovremennom szhatii: dis. ... kand. tekhn. nauk* [The strength of short centrifuged columns of annular cross-section with longitudinal reinforcement of class At-V during short-term compression: dis. ... cand. tech. of sciences]. Vilnius: VCEI, 1984. 261 p. (rus)
10. Aktham, H.A., Bunnori, N.M., Ahmed, T.N., Majid, T.A. *Durability performance of a novel ultra-high-performance PET green concrete (UHPPGC).* *Construction and Building Materials.* 2019. No. 209. Pp. 395–405.
11. Tasevski, D., Ruiz, M.F., Muttoni, A. *Compressive strength and deformation capacity of concrete under sustained loading and low stress rates.* *Journal of Advanced Concrete Technology.* 2018. No. 16. Pp. 396–415.
12. Ferrotto, M.F., Fischer, O., Cavaleri, L. *Analysis-oriented stress-strain model of CRFP-confined circular concrete columns with applied preload.* *Mater Struct.* 2018. 51 (44) [Online]. URL: <https://doi.org/10.1617/s11527-018-1169-0> (date of application: 18.05.2020).
13. Maruyama, I., Lura, P. *Properties of early-age concrete relevant to cracking in massive concrete.* *Cement and Concrete Research.* 2019. 123(105770) [Online]. URL: <https://doi.org/10.1016/j.cemconres.2019.05.015> (date of application: 18.05.2020).
14. Kim, J.-J., Yoo, D.-Y. *Effects of fiber shape and distance on the pullout behavior of steel fibers embedded in ultra-high-performance concrete.* *Cement and Concrete Composites.* 2019. No. 103. Pp. 213–223.
15. Li, K., Li, L. *Crack-altered durability properties and performance of structural concretes.* *Cement and Concrete Research.* 2019. 124(105811) [Online]. URL: <https://doi.org/10.1016/j.cemconres.2019.105811> (date of application: 18.05.2020).
16. Kirthika, S.K., Singh, S.K. *Durability studies on recycled fine aggregate concrete.* *Construction and Building Materials.* 2020. 250(118850) [Online]. URL: <https://doi.org/10.1016/j.conbuildmat.2020.118850> (date of application: 18.05.2020).
17. Hameed, M.A.S., Maula, B.H., Bahnam, Q.M. *An empirical relationship between compressive strength and ultrasonic pulse velocity for concrete.* *International Review of Civil Engineering.* 2019. No. 10 (6) [Online]. URL: <https://doi.org/10.15866/irece.v10i6.17061> (date of application: 18.05.2020).
18. Alexander, M., Beushausen, H. *Durability, service life prediction, and modelling for reinforced concrete structures – review and critique.* *Cement and Concrete Research.* 2019. No. 122. Pp. 17–29.
19. Geiker, M.R., Michel, A., Stang, H., Lepech, M.D. *Limit states for sustainable reinforced concrete structures.* *Cement and Concrete Research.* 2019. No. 122. Pp. 189–195.
20. Khalaf, M.A., Ban, C.C., Ramli, M. *The constituents, properties and application of heavyweight concrete: A review.* *Construction and Building Materials.* 2019. No. 215. Pp. 73–89.
21. Sediek, O.A., Wu, T.-Y., McCormick, J., El-Tawil, S. *Collapse behavior of hollow structural section columns under combined axial and lateral loading.* *Journal of Structural Engineering.* 2020. No. 6 [Online]. URL: [https://doi.org/10.1061/\(ASCE\)ST.1943-541X.0002637](https://doi.org/10.1061/(ASCE)ST.1943-541X.0002637) (date of application: 18.05.2020).
22. Trapko, T. *Effect of eccentric compression loading on the strains of FRCC confined concrete columns.* *Construction and Building Materials.* 2014. No. 61. Pp. 97–105.

23. Lu, W.-Y., Chu, C.-H. Tests of high-strength concrete deep beams. Magazine of Concrete Research. 2019. No. 71 (4). Pp. 184–194.
24. Shuyskiy, A.I., Stel'makh, S.A., Shcherban', E.M., Kholodnyak, M.G. Investigation of the influence of the initial composition of heavy concrete designed for the manufacture of ring-section products on its properties. Materials Science Forum. 2018. No. 931, Pp. 508–514. DOI: 10.4028/www.scientific.net/msf.931.508
25. Stel'makh, S.A., Shcherban', E.M., Kholodnyak, M.G. Analysis of concrete deformation diagram, received by different ways of formation, and their separate layers. IOP Conf. Ser.: Mater. Sci. Eng. 2019. 687 (022008) [Online]. URL: <https://iopscience.iop.org/article/10.1088/1757-899X/687/2/022008> (date of application: 18.05.2020).
26. Mailyan, L.R., Stel'makh, S.A., Shcherban', E.M., Kholodnyak, M.G. Determination and use of hidden strength reserves of centrifuged reinforced constructions by means of calculation and experimental methods. Russian Journal of Building Construction and Architecture. 2020. No. 1 (45). Pp. 6–14. DOI: 10.25987/VSTU.2020.45.1.001
27. Stel'makh, S.A., Shcherban', E.M., Zholobova, O.A. Prescription and Technological Aspects of Manufacturing High-Quality Centrifuged Products and Structures from Heavy Concrete. IOP Conf. Ser.: Mater. Sci. Eng. 463 (022056) [Online]. URL: <http://iopscience.iop.org/article/10.1088/1757-899X/463/2/022056> (date of application: 18.05.2020).
28. Stel'makh, S.A., Shcherban', E.M., Shuyskiy, A.I., Nazhnev, M.P. Theoretical and Practical Aspects of the Formation of the Variational Structure of Centrifuged Products from Heavy Concrete. Materials Science Forum. No. 931. Pp. 502–507. DOI: 10.4028/www.scientific.net/msf.931.502

Contacts:

*Levon Mailyan, Irm@aaanet.ru
Sergei Stel'makh, sergej.stelmax@mail.ru
Evgenii Shcherban', au-geen@mail.ru*

© Mailyan L.R., Stel'makh S.A., Shcherban' E.M., 2021



DOI: 10.34910/MCE.108.13

Strength of earth dams considering elastic-plastic properties of soil

M.M. Mirsaidov* , T.Z. Sultanov, J.Y. Yarashov 

Tashkent Institute of Irrigation and Agricultural Mechanization Engineers, Tashkent, Uzbekistan

*E-mail: theormir@mail.ru

Keywords: optimal design, earthquake engineering, soil mechanic, soil-structure interaction, seismic response

Abstract. The paper provides a detailed analysis of known publications devoted to various models and methods, as well as the results of the study of the stress state of structures, taking into account the elastoplastic properties of soil. A mathematical model, methods, and an algorithm to assess the stress-strain state of earth dams were built considering elastoplastic properties of soil, inhomogeneous structural features and the filling level of the reservoir under various influences. A variational equation of the principle of virtual displacements, and the finite element method and the method of elastic solutions were used to solve the problem. The reliability assessment of the results obtained was verified by studying the practical convergence of various model problems. The stress-strain state of three earth dams (of different heights) was investigated taking into account the elastic, elastoplastic properties of soil at different filling levels of the reservoir. At that, various mechanical effects were revealed, i.e., the appearance of additional strains in the most stressed places inside the dam body, and the occurrence of significant plastic shear strain in the slope zones and the smoothing of the arch effect in the core zone. It was found that an account of elastoplastic properties of soil at a completely filled reservoir significantly changes the pattern of shear stresses distribution in the body of the dam, i.e. they increase both in the upper retaining prism and in the lower prism.

1. Introduction

An assessment of strength parameters of earth dams is often made with account for elastic properties of soil only, which does not lead to adequate results.

Today, many different theories are applied to describe physical state of soil, most of them are difficult to implement when solving specific problems. One of the important problems in determining the strength parameters of earth dams is to take into account the elastic-plastic properties of soil that arise in the structure under various effects [1–11].

Recently, researchers have paid great attention to inelastic properties of soil when assessing the stress-strain state of earth dams.

Consider several publications:

- in [6, 10, 11] an assessment of strength and stability of dam slopes was given with account of plastic strains, the stage-by-stage erection of the structure and water seepage through the dam body;
- in [7], a numerical-analytical procedure was proposed to analyze the elastic-plastic “nonlinear” state of earth dam during earthquakes;

Mirsaidov, M.M., Sultanov, T.Z., Yarashov, J.Y. Strength of earth dams considering elastic-plastic properties of soil. Magazine of Civil Engineering. 2021. 108(8). Article No. 10813. DOI: 10.34910/MCE.108.13

© Mirsaidov, M.M., Sultanov, T.Z., Yarashov, J.Y., 2021. Published by Peter the Great St. Petersburg Polytechnic University.



This work is licensed under a CC BY-NC 4.0

- in [12] nonlinear models were given that satisfactorily describe the elastic-plastic properties of earth materials;
- in [13], a finite element method was used for numerical calculation of earth dams; it takes into account water-saturated (unsaturated) and plastic properties of soil. With the proposed model, three dams were calculated;
- in [14], the behavior of high dams with strengthened soil was modeled using an elastic-plastic model;
- in [15], the stability of earth dams' slopes was investigated using an elastic-plastic model;
- in [16], the results of the stress-strain state prediction of a high earth dam in an elastic-plastic statement were considered, taking into account the stage-by-stage erection of the dam and reservoir filling. It was shown that the operation of earth dam with a vertically located diaphragm at water-filled reservoir is characterized by horizontal displacement of the downstream retaining prism;
- in [17, 18], the methods were proposed for numerical study of elastic-plastic strain of bodies considering finite strains. It is assumed that the soil under strain obeys the law of dry friction. Total strain is represented as the sum of plastic and elastic strains. The defining relations of elastic strain are written in the form of Hooke's law;
- in [19], a geomechanical model of an enclosing fill hydro-technical structure – a dam – was proposed. A pattern of strain and displacement of a structure body was investigated in elastic-plastic statement by computer simulation methods;
- in [20], a two-dimensional problem of estimating the slope stress-strain state in elastic-plastic statement using a numerical method was solved;
- in [21], the possibility of using a structurally heterogeneous elastic-plastic calculation model to describe the strain behavior of water-saturated clay soils was considered.

Along with this, the studies in [22–35] deal with the stress-strain state and dynamic behavior of various structures considering their strain features.

These are just several publications in which along with elastic properties, the elastic-plastic properties of soil are taken into account when assessing the stress-strain state and stability of slopes of earth dams. Above review of publications shows that the assessment of strength parameters of earth structures in different studies is treated differently, and each theory or method used has its advantages and disadvantages.

As is known, at present a universal theory to determine strength parameters of earth structures, considering various soils characteristics under different loads, as well as the methods to determine strength properties of soils and structures is still under development.

An adequate assessment of strength parameters of earth dams with account for elastic-plastic properties of soil remains insufficiently studied and requires extensive research.

So, this problem is relevant and requires further research.

2. Methods

2.1. Models, methods and algorithms for assessing the stress-strain state of earth dams taking into account elastic-plastic properties of soil

To assess the stress-strain state of earth dams, considering elastic-plastic properties of soil under various effects, a plane-strained model of a dam is considered (Fig. 1); it takes into account inhomogeneous features of a structure. The base surface Σ_0 is rigidly fixed, the downstream slope surface Σ_3 is stress-free and on the surface Σ_1 (on the part of the upstream slope, i.e., on S_p), the hydrostatic water pressure \vec{p} acts.

The dam material (earth) in various parts of a structure is considered as elastic or elastic-plastic one. In calculations, the mass forces \vec{f} , acting on the structure and water pressure \vec{p} [34] acting on the surface S_p are taken into account.

The task is to determine the fields of displacements and stresses arising in the dam body (Fig. 1) under mass forces \vec{f} and hydrostatic water pressure \vec{p} , taking into account elastic-plastic properties of soil in the case of a plane-strained state of a structure.

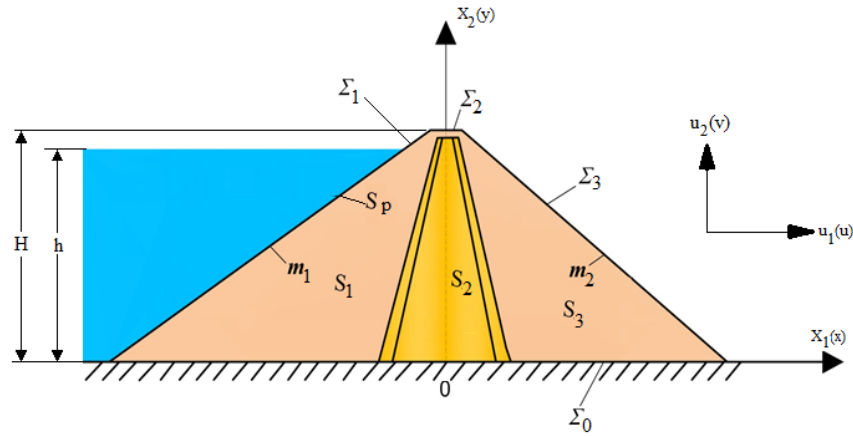


Figure 1. Plane model of an inhomogeneous earth dam.

To simulate the process of earth dam strain (Fig. 1), a variational equation based on the principle of virtual displacements is used:

$$-\int_{S_1} \sigma_{ij} \delta \varepsilon_{ij} dS - \int_{S_2} \sigma_{ij} \delta \varepsilon_{ij} dS - \int_{S_3} \sigma_{ij} \delta \varepsilon_{ij} dS + \int_{S_1+S_2+S_3} \bar{f} \delta \bar{u} dS + \int_{S_p} \bar{p} \delta \bar{u} dS = 0. \quad (1)$$

Here, physical properties of the structure material are described by the relations between stresses σ_{ij} and strains ε_{ij} [22]:

$$\sigma_{ij} = \lambda_n \varepsilon_{kk} \delta_{ij} + 2\mu_n \varepsilon_{ij}, \quad (2)$$

the relationship between the components of the strain tensor and the displacement vector is described by Cauchy linear relations [22].

$$\varepsilon_{ij} = \frac{1}{2} \left(\frac{\partial u_i}{\partial x_j} + \frac{\partial u_j}{\partial x_i} \right). \quad (3)$$

To create mathematical models, homogeneous kinematic boundary conditions are also taken into account:

$$\bar{x} \in \Sigma_0: \bar{u} = 0. \quad (4)$$

Here \bar{u} , ε_{ij} , σ_{ij} are the components of the displacement vector, tensors of strains and stresses, respectively; $\delta \bar{u}$, $\delta \varepsilon_{ij}$ are isochronous variations of the components of displacements and strains; \bar{f} is the vector of mass forces; \bar{p} is the hydrostatic water pressure; index $n = 1, 2, 3$, means separate inhomogeneous parts of the dam to which this characteristic belongs.

λ_n and μ_n are the Lamé constants, determined through the Young's modulus E_n and Poisson's ratio ν_n as follows:

$$\lambda_n = E_n \nu_n / ((1 + \nu_n)(1 - 2\nu_n)); \mu_n = E_n / (2(1 + \nu_n)). \quad (5)$$

The structure under consideration is inhomogeneous in the sense that the physical properties of its parts vary greatly.

The problem to be solved is considered in the framework of the plane-strained state of structures, i.e. the displacement vector in the coordinate system $\bar{x} = \{x_1, x_2\} = \{x, y\}$ has two components $\bar{u} = \{u_1, u_2\} = \{u, v\}$, in all ratios $i, j, k = 1, 2$.

In the case when the dam material of the n -th part (Fig. 1) is elastic, the relationship between the stresses σ_{ij} and strains ε_{ij} tensor components is expressed through the generalized Hooke's law (2).

In the case when the material is elastic-plastic, the hypothesis of the energy forming is used to describe the equation of state of soil medium; here the transition from elastic state to the plastic one occurs at the point of soil medium $\sigma_i = \sigma_y$. The state of the medium in different parts of the dam under consideration is described differently (according to elastic or elastic-plastic law), depending on whether the yield strength of the material σ_y is overcome or not.

Here σ_y are the normal stresses in the yield strength of the material.

The intensities of normal stresses σ_i and strains ε_i are determined by the formulas

$$\sigma_i = \frac{1}{2} \sqrt{(\sigma_{11} - \sigma_{22})^2 + (\sigma_{11} - \nu(\sigma_{11} + \sigma_{22}))^2 + (\sigma_{22} - \nu(\sigma_{11} + \sigma_{22}))^2 + 6\sigma_{12}^2},$$

$$\varepsilon_i = \frac{\sqrt{2}}{2(1+\nu)} \sqrt{(\varepsilon_{11} - \varepsilon_{22})^2 + \varepsilon_{11}^2 + \varepsilon_{22}^2 + \frac{3}{2}\varepsilon_{12}^2}.$$
(6)

In the elastic-plastic case, relationships of the form (2) are used to describe the stresses-strains relations. Moreover, in quantities λ_n and μ_n instead of elastic parameters E_n, ν_n, μ_n , variable parameters E_n^*, ν_n^*, μ_n^* are used, determined as follows [23, 26, 27]:

$$E_n^* = \frac{\frac{\sigma_i}{\varepsilon_i}}{1 + \frac{1-2\nu_n}{3E_n} \frac{\sigma_i}{\varepsilon_i}}; \mu_n^* = \frac{\sigma_i}{3 \cdot \varepsilon_i}; \nu_n^* = \frac{\frac{1}{2} \frac{1-\nu_n}{3E_n} \frac{\sigma_i}{\varepsilon_i}}{1 + \frac{1-2\nu_n}{3E_n} \frac{\sigma_i}{\varepsilon_i}}.$$
(7)

The relationship between the "variable elasticity parameters" has the same form as for elastic constants E_n, ν_n, μ_n , that is:

$$\mu_n^* = \frac{E_n^*}{2(1+\nu_n^*)}.$$
(8)

The changed physical-mechanical parameters (7)-(8), at every point of the dam (Fig. 1), are determined based on the reached strain state ε_i (strain intensity) and corresponding stress σ_i^* (stress intensity) according to strain diagram $\sigma_i^* = \sigma_i^*(\varepsilon_i)$ (Fig. 2), selected from experimental data for specific types of soil [2, 23, 24, 26].

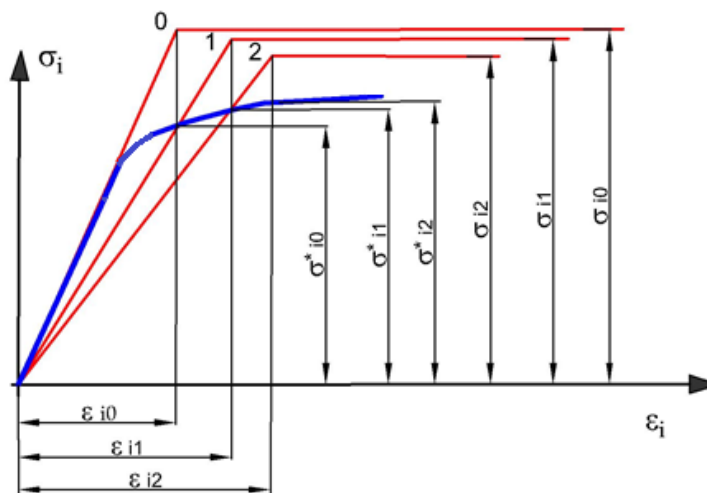


Figure 2. Elastic-plastic diagram of the material strain and the scheme for implementing the method of variable parameters of elasticity.

The variational problem for assessing the stress-strain state of earth dams (Fig. 1), taking into account elastic-plastic properties of the material and inhomogeneous features of the structure, can be formulated as follows: it is necessary to determine the fields of displacements $\vec{u}(\vec{x}, t)$, strains $\varepsilon_{ij}(\vec{x}, t)$ and stresses in an inhomogeneous elastoplastic system (Fig. 1) arising under mass forces (\vec{f}) and hydrostatic pressure (\vec{p}) , satisfying equation (1) considering (2), (3), (5), (7), (8) and the corresponding kinematic boundary conditions (4) for any virtual displacement $\delta\vec{u}$.

The above stated variational problem is solved by the method of finite elements (FEM) [4, 36].

Using the procedure of the finite element method, the considered variational problem for a structure (Fig. 1) is reduced to a system of nonlinear algebraic equations of the form

$$[K(\sigma_i, \varepsilon_i)]\{u\} = \{F\}. \quad (9)$$

Here: $\{u\}$ is the sought for vector of nodal displacements; $\{F\}$ is the vector of amplitudes of total external loads (mass forces, and hydrostatic pressure, etc.).

The difference of equation (9) from ordinary systems of linear algebraic equations is that here the coefficients of equation (9), being the elements of stiffness matrix $[K(\sigma_i, \varepsilon_i)]$, depend not only on the geometric and elastic parameters of the materials, but also on the reached stress-strain state of a structure.

The calculation is carried out in several stages. The solution of equations (9) at each stage of the process is obtained by the Gauss method or the square root method.

At the first stage, an elastic calculation of earth structure (Fig. 1), which is in equilibrium under applied load, is performed. Then the transition to the second stage of the calculation is done; it consists of the stress-strain state (SSS) analysis in all the finite elements into which the structure is divided. If the stress intensity σ_i in finite elements exceeds the yield strength σ_y (σ_y is determined from experiments for specific materials), it is believed that plastic strains begin to develop in them due to the changes in the body shape.

Then, using (7)-(8), (5), (2), elastic parameters are determined for these finite elements; the stiffness matrices and then the general matrix $[K(\sigma_i, \varepsilon_i)]$ of equation (9) for the entire structure are compiled. The solution of the obtained new system of equations (9) taking into account elastic-plastic properties of the material for certain finite elements is analyzed; if necessary, new parameters of elasticity are introduced; then the process continues until the convergence of the sequence σ_i over the entire structure within the specified accuracy is reached. The described method is a method of variable parameters of elasticity [23, 26]. The implementation scheme of the method of variable parameters of elasticity is shown in Fig. 2.

In a plane-strained state, the following formulas are used to transform the relationship between stresses and strains [22, 23, 26]:

$$\begin{aligned} \sigma_{11} &= \frac{E_n^*(1-\nu_n^*)}{(1+\nu_n^*)(1-2\nu_n^*)} \varepsilon_{11} + \frac{\nu^* E_n^*}{(1+\nu_n^*)(1-2\nu_n^*)} \varepsilon_{22}, \\ \sigma_{22} &= \frac{E_n^*(1-\nu_n^*)}{(1+\nu_n^*)(1-2\nu_n^*)} \varepsilon_{22} + \frac{\nu^* E_n^*}{(1+\nu_n^*)(1-2\nu_n^*)} \varepsilon_{11}, \\ \sigma_{12} &= 2\mu_n^* \varepsilon_{12}. \end{aligned} \quad (10)$$

where E_n^* , ν_n^* , μ_n^* are the variable parameters of elasticity determined by formulas (7) and (8).

Using the above methods, the stress-strain state of earth dams is studied taking into account the elastic-plastic properties of soil under various effects, with/without account of hydrostatic pressure of water and different levels of reservoir filling with water.

2.2. Study of practical convergence of the developed method of calculation on a test example

In this part of the paper, the practical convergence of the method of elastic-plastic calculation at individual points (Fig. 3) of the model problem is investigated. For this, the plane-strained state of a homogeneous dam as a model of earth structure is considered (Fig. 3) under its own weight, and with account for elastic and elastic-plastic properties of the material. The geometrical characteristics of the structure and the averaged physical and mechanical parameters of soil are taken as: the height of the structure $H = 86.5$ m; the crest width $b = 10$ m; the slope coefficients $m_1 = 2.5$, $m_2 = 2.2$; elastic modulus $E = 3.07 \cdot 10^3$ MPa; specific gravity $\gamma = 1980$ kgf/m³; Poisson's ratio $\nu = 0.36$. The elastic-plastic properties of soil [24] are described by a bilinear diagram (Fig. 2) with a degree of hardening $\bar{\lambda} = (1 - E_p / E) = 0.67$ and yield strength for soil $\sigma_y = 4 \cdot 10^{-1}$ MPa. Here E_p is the inclination angle of the plastic part of the diagram.

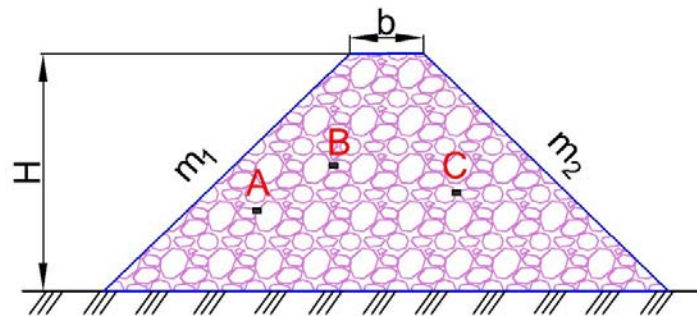


Figure 3. Check of solution convergence at individual points (A, B, C) of a structure.

The aim of solving this problem is to study the convergence of results $(u_2, \sigma_i, \sigma_{11})$ depending on the number of divisions of the model structure (Fig. 3) into a different number N of finite elements for elastic and elastoplastic problems. To do this, several points were selected in the structure (for example, A, B, C), and the results obtained in these points $(u_2, \sigma_i, \sigma_{11})$ at different number of divisions into finite elements were compared with the results of previous calculations. The research results are presented in Table 1.

Here u_2 is the vertical displacement of the considered point, σ_{11} is the horizontal normal stress; σ_i is the intensity of normal stresses. Stress values (σ_{11} and $\sigma_i \cdot 10^{-1}$) are given in MPa.

The data in Table 1 show that elastoplastic strain leads to an increase in vertical displacements of structure points. Satisfactory accuracy is ensured when the structure is divided into no less than at $N = 350$ finite elements (Fig. 3), (Table 1).

Table 1. Numerical convergence of results.

Considered points of a structure	Types of quantities	Elastic solutions obtained for various finite element numbers		
		$N = 280$	$N = 336$	$N = 576$
1	2	3	4	5
Elastic solution				
A	u_2	-0.009660	-0.007812	-0.007517
	σ_i	69.5095	66.4327	66.4696
	σ_{11}	-31.6746	-33.7946	-33.8024
B	u_2	-0.01630	-0.01633	-0.01634
	σ_i	627767	57.9882	58.3452
	σ_{11}	-22.0782	-20.1421	-19.8845
C	u_2	-0.003849	-0.005693	-0.005505
	σ_i	30.1014	27/9418	6/3410
	σ_{11}	-229702	-20.7274	-21.2614

Considered points of a structure	Types of quantities	Elastic solutions obtained for various finite element numbers		
		$N = 280$	$N = 336$	$N = 576$
1	2	3	4	5
Elastic-plastic solution				
A	u_2	-0.01686	-0.01559	-0.01595
	σ_i	64.3873	61.8528	61.7691
	σ_{11}	-36.2867	-38.6386	-39.2341
B	u_2	-0.02767	-0.03178	-0.03236
	σ_i	57.8172	53.9147	52.8176
	σ_{11}	-22.6110	-21.5393	-21.0727
C	u_2	-0.00444	-0.007457	-0.007936
	σ_i	27.3915	30.9518	29.9756
	σ_{11}	-32.9834	-29.2085	-30.6014

To validate the accuracy of the results obtained, a dam model with symmetrical slopes (i.e., $m_1 = m_2$) was considered. The fact that the shear stress is $\sigma_{12} = 0$ on the axis of symmetry confirms the reliability of results.

The solutions obtained for model problems show that, with the required number of finite elements, the developed technique works quite reliably when determining the dam SSS in a plane statement, with account for elastic and elastic-plastic properties of the structure material.

These results give reason to use the developed technique in solving specific problems for earth dams.

3. Results and Discussion

As a specific example, an assessment of the stress-strain state of the Sokh earth dam is considered taking into account elastic and elastic-plastic properties of soil under mass forces and the hydrostatic pressure of water at different levels of reservoir filling.

The Sokh dam is located in the northern foothill of the Alai Range in the lower reaches of the Sokh River. The main design parameters of the dam are as follows: the height of the dam – 87.3 m, the crest width – 10.0 m, the length along the crest – 487.3 m, the rate of slopes: the upper prism $m_1 = 2.5$, and the lower prism $m_2 = 2.2$.

The Sokh dam is built from local materials and is a stone-earth dam with a loamy core and side retaining prisms built of pebbles. The central core of the dam is vertical, symmetrical in shape with a width of 4.0 m at the upper part, 47.15 m at the base. The dam is built of sandy loamy soils and refers to the 1st class structure.

The recommended design physical-mechanical characteristics of the material are: γ is volumetric weight; G is shear modulus of elasticity; μ is Poisson's ratio. For the core: $\gamma = 1700 \text{ kgf/m}^3$; $G = 282 \text{ MPa}$; $\mu = 0.40$. For the retaining prism: $\gamma = 2100 \text{ kgf/m}^3$; $G = 316 \text{ MPa}$; $\mu = 0.35$. For the slope paving: $\gamma = 1850 \text{ kgf/m}^3$; $G = 310 \text{ MPa}$; $\mu = 0.35$.

3.1. Elastic calculation

Using the developed methods, the stress-strain state of the Sokh dam was assessed taking into account the homogeneous and inhomogeneous features of the structure in an elastic statement.

Fig. 4 shows the isolines of strain intensity distribution ε_i and the components of shear strains ε_{12} , and Fig. 5 shows the intensities of normal σ_i and shear stresses σ_{12} of the Sokh dam, obtained considering elastic properties of soil with a central loamy core. An analysis of the results shows that due to the greater strain properties of loamy soil in the core, the values of vertical strains in the central part of the

dam increase when comparing with homogeneous dams. Large strain intensities ε_i appear in the lower part of the dam (Fig. 4).

The distribution of shear stresses σ_{12} (Fig. 5) repeats the character of shear strains ε_{12} distribution throughout the dam cross section (Fig. 4). A zero level of shear strains (Fig. 4) is observed near the dam symmetry axis (since the dam has almost symmetrical slopes); with the distance from the axis, shear strains increase, reaching a maximum in the lower part of the slopes.

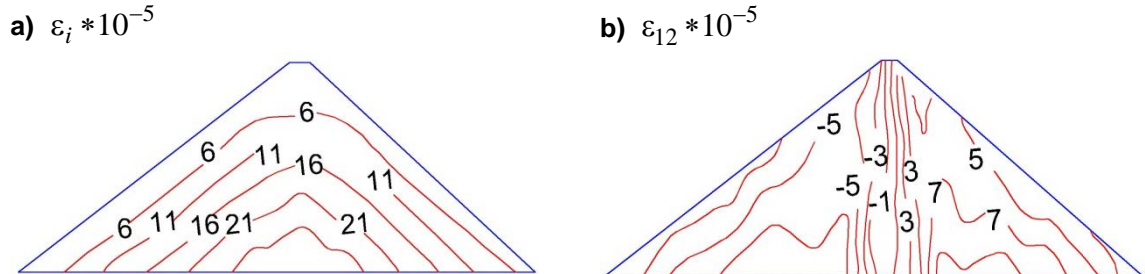


Figure 4. Isolines of strain intensity distribution ε_i and the component of shear strain ε_{12} in the inhomogeneous Sokh dam.

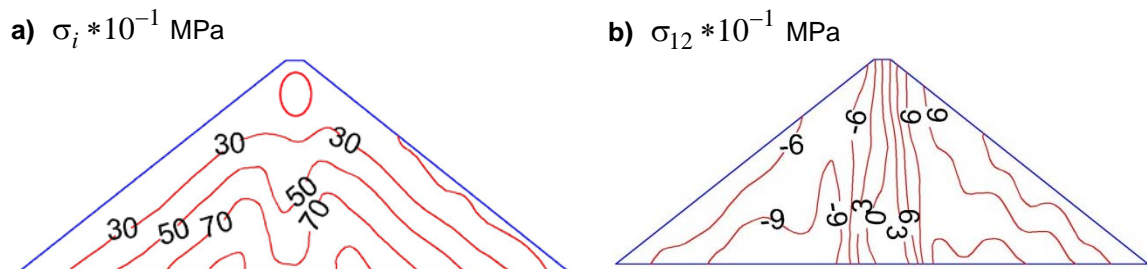


Figure 5. Isolines of the intensity distribution of normal σ_i and shear σ_{12} stresses in the inhomogeneous Sokh dam.

An analysis of the results showed that when considering inhomogeneous features of the structure, the stress state of the dam undergoes significant changes compared to a homogeneous structure; these changes are expressed in a decrease in intensity of normal σ_i and vertical σ_{22} stresses in the dam core by $\approx 25\%$, in an increase in shear stresses σ_{12} by $\approx 40\%$, and horizontal stresses σ_{11} by $\approx 10\%$.

3.2. Elastic-plastic calculation

Using the developed methods, the stress-strain state of the Sokh dam was assessed taking into account homogeneous and inhomogeneous structural features in an elastic-plastic statement.

When assessing the stress-strain state of the Sokh earth dam, the elastic-plastic properties of soil are taken into account according to bilinear diagram $\sigma_i = f(\varepsilon_i)$ (Fig. 2) with a degree of hardening $\bar{\lambda} = (1 - E_p / E) = 0.75$, i.e. the inclination angle of plastic part E_p is supposed to be four times less than the inclination of elastic part E : $E_p = E/4$ [22]. The yield strength according to [24], is taken for the core material (loam) $-\sigma_i = 3 \cdot 10^{-1}$ MPa, and for the material of retaining prisms within $\sigma_y = (45 - 50) \cdot 10^{-1}$ MPa.

Fig. 6 shows the isolines of the intensity distribution of normal σ_i (a) and tangential – σ_{12} (b) stresses of the Sokh dam, obtained considering structural features and the elastic-plastic properties of soil under its own weight. Comparison of these results with the results obtained for the same dams in elastic statement (Fig. 5) shows that an account for elastic-plastic properties of soil of the prism and core leads to a change in values and nature of the dam stress state. An account for elastic-plastic properties of soil leads to a decrease in the stress intensity σ_i and vertical stresses σ_{22} in the core down to $\approx 20\%$; the arch effect observed in the dam core zone increases.

The reason for this is the difference in strain properties and yield strengths of soil in the core and retaining prisms. Horizontal stresses σ_{11} increase to $5 \cdot 10^{-1}$ MPa, mainly in the upper part of the dam, as a result of which a change in the dam profile is possible. The values of vertical stresses σ_{22} decrease to $\approx 20\%$ in the middle and lower parts of the dam core. In sloping zones, the tangential stresses σ_{12} increase by $(5-6) \cdot 10^{-1}$ MPa, which can also lead to a change in the profile and to a decrease in the safety factor of the dam slopes.

Fig. 7 shows isolevel lines of strain intensity ε_i and shear strain ε_{12} in an inhomogeneous Sokh dam taking into account the elastic-plastic properties of soil.

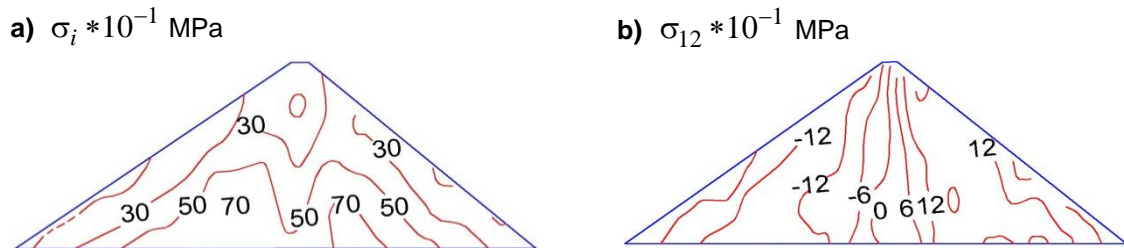


Figure 6. Isolines of intensity distribution of normal σ_i and shear σ_{12} stresses in the inhomogeneous Sokh dam, obtained taking into account the elastic-plastic properties of the material.

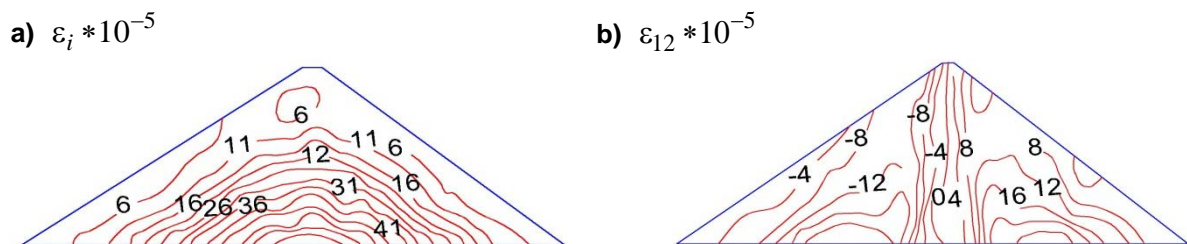


Figure 7. Isolines of strain intensity distribution ε_i and shear strain ε_{12} in the inhomogeneous Sokh dam taking into account the elastic-plastic properties of soil.

An analysis of the results obtained (Figs. 4 and 7) shows that an account for elastic-plastic properties of soil leads to the appearance of additional strain in the most stressed areas inside the dam body. Plastic strains do not appear near the slopes and crest surfaces. Despite this, significant shear strains ε_{12} occur in the slope zones.

The principal normal σ_1, σ_2 and maximum tangential stresses τ_{\max} in the Sokh dam were studied with account for elastic and elastic-plastic properties of soil; the study showed that an account of elastic-plastic properties of soil leads to a decrease in stresses in the dam body and the arch effect smoothing in the core zone. The values of principal stress σ_1 in the zones of upstream and downstream slopes slightly decrease. The principal stress σ_2 decreases to a greater extent in the slope zones (to $\approx 10-17\%$) and in the core (to $\approx 15-25\%$). The value of the maximum tangential stress τ_{\max} in the slope zones slightly increases near the core, and decreases by $\approx 20-50\%$ in the core.

The results obtained showed that with a decrease of plastic section slope in soil strain diagram $\sigma_i = f(\varepsilon_i)$, the difference in the results of solving elastic-plastic and elastic problems is more significant.

Therefore, a justified approach to the selection of the law of soil strain is necessary.

Similar studies were performed for high-rise earth dams, such as the Gissarak dam ($H = 138.5$ m) and the Tupolang dam ($H = 185$ m).

An analysis of the results obtained for high-rise dams of various geometries and heights showed that an account for elastic-plastic strain of the material of retaining prisms and cores significantly affects the change in the dam SSS. In the core of the Tupolang dam the values of stress intensity σ_i decrease to

$\approx 18\%$, and vertical stresses σ_{22} to $\approx 20\%$, which increases the arch effect. In the upstream and downstream retaining prisms, tangential stresses σ_{12} increase significantly – up to $\approx 40\text{--}55\%$. The greatest difference is observed near the slopes, which can lead to shear strains and the occurrence of landslides. In the core zone, the values of tangential stresses σ_{12} remain insignificant.

The above theoretical studies have shown that when designing high and medium-high dams, it is necessary to conduct calculations with account for structural features of the dam and real elastic-plastic properties of soil.

3.3. Elastic-plastic calculation taking into account the level of reservoir filling

Using the developed methods, the stress-strain state of the Sokh dam was assessed taking into account inhomogeneous features of the structure, elastic-plastic properties of soil and the level of reservoir filling with water. The stress-strain state of the dam obtained at each level of reservoir filling was compared with the results from section 4.2 when the reservoir filling was not taken into account.

Fig. 8 shows the isolines of intensity distribution of normal σ_i (a) and tangential σ_{12} (b) stresses of the Sokh dam, obtained considering elastic-plastic properties of soil with a fully filled reservoir.

When the reservoir is filled to the half height of the dam, the components of the stress tensor change only in the upper prism zone, the symmetric pattern of the stress distribution in the dam profile is violated. Here: σ_i increases by $\approx 30\text{--}40\%$: σ_{11} up to $40\text{--}45\%$ and σ_{22} up to $\approx 40\%$. The effect of water mainly manifests itself in the pattern of horizontal stresses σ_{11} distribution in the dam.

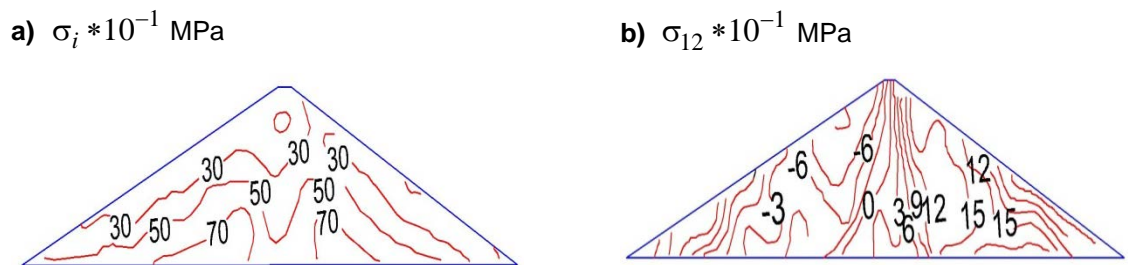


Figure 8. Isolines of intensity distribution of normal σ_i (a) and tangential stresses σ_{12} (b) in the Sokh dam, taking into account the elastic-plastic properties of soil at fully filled reservoir.

When the reservoir is fully filled (Fig. 8.), the stress-strain state of the dam is redistributed, symmetrical distribution of stress isolines is violated, and the values of stress components change significantly. The stress intensity σ_i (Fig. 8) in the Sokh dam increases to $\approx 70\text{--}100\%$ relative to the results obtained without water effect.

The changes are observed mainly in the upstream retaining prism. Horizontal stresses σ_{11} vary throughout the dam profile, they increase to $\approx 10\text{--}120\%$, and the greatest difference in the results relates to the slopes of the upstream prism.

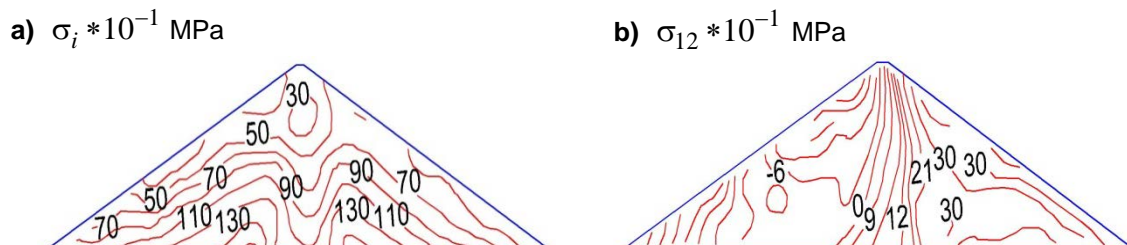


Figure 9. Isolines of the intensity distribution of normal σ_i (a) and tangential stresses σ_{12} (b) in the Tupolang dam, taking into account the structural features and the elastic-plastic properties of soil with fully filled reservoir.

Vertical stresses σ_{22} increase to $\approx 70\text{--}80\%$ and the greatest difference relates to the lower part of the upstream slope. The distribution pattern of shear stresses σ_{12} changes significantly throughout the

dam profile. Values of tangential stresses in the downstream prism increase to $\approx 1\text{--}20\%$. These phenomena are undesirable, since they may cause the landslides (instability) in the downstream prism slope. Therefore, in the most cases, along with stability assessment of the upstream slope, the stability of the dam downstream slope is also evaluated. The need to assess the stability of the downstream slope is confirmed by the results of observation of strong earthquakes aftermath [2].

Fig. 9 shows the isolines of the intensity distribution of normal σ_i (a) and tangential σ_{12} (b) stresses in the Tupolang dam, taking into account the elastic-plastic properties of soil with fully filled reservoir.

An analysis of these results (Fig. 9) confirms the above reasoning on the stress distribution in the dam body, with the only difference in numerical values of stresses.

Based on the results obtained, it can be concluded that when assessing the strength of earth dams of any height, it is necessary to evaluate the strength taking into account the level of reservoir filling with water, since it significantly changes the stress distribution in the dam body, and the slope stability of the dam as a whole.

4. Conclusions

1. A mathematical model, methods and algorithms have been developed for assessing the stress-strain state of earth dams taking into account the elastic-plastic properties of soil under static impacts, based on the method of variable parameters of elasticity.
2. The stress-strain state of earth dams was investigated taking into account the elastic-plastic properties of soil and structural features of a dam at different levels of reservoir filling.
3. Studies have revealed that an account of elastic-plastic properties of soil leads to:
 - a significant change in the stress-strain state of earth dams compared with the elastic case;
 - the appearance of additional strains in the most stressed points inside the dam body, the strains ε_{11} , ε_{22} are insignificant near the surfaces of slopes and crests, significant plastic shear strains ε_{12} arise in the slope zones;
 - the reduced stresses in the body of the dam and the smoothing of the arch effect in the core zone.
4. An account of both elastic-plastic properties of soil and the level of reservoir filling showed that:
 - when the reservoir is half full, the changes in the values of stress tensor components occur only in the zone of the upstream retaining prism of the dam;
 - when the reservoir is fully filled, the distribution pattern of tangential stresses in the dam body changes significantly, both in the upstream retaining prism and in the downstream prism;
 - the greatest values of stress intensity σ_i are reached in the lower part of the upstream slope near the dam core.

References

1. Zaretsky, Yu.K., Lombardo, V.N. Statika i dinamika gruntovykh plotin. [Statics and Dynamics of Earth Dams]. Moscow: Energoizdat, 1983. 256 p. (rus)
2. Krasnikov, N.D. Seysmostoykost gidrotekhnicheskikh sooruzheniy iz gruntovykh materialov. [Seismic Stability of Hydro-technical Structures from Soil Materials]. Moscow: Energoizdat, 1981. 240 p. (rus)
3. Lyakhter, V.M., Ivashchenko, I.N. Seysmostoykost gruntovykh plotin. [Seismic Stability of Earth Dams]. Moscow: Nauka, 1986. 233p. (rus)
4. Mirsaidov, M.M., Sultanov, T.Z. Theory and methods of strength assessment of earth dams. Germany: Lambert Academic Publishing, 2015. 341p.
5. Mirsaidov, M.M., Sultanov, T.Z., Sadullaev, Sh.A. An assessment of stress-strain state of earth dams with account of elastic-plastic, moist properties of soil and large strains. Magazine of Civil Engineering. 2013. 40 (5). Pp. 59–68. DOI: 10.5862/MCE.40.7
6. Afiri, R., Gabi, S. Finite element slope stability analysis of Souk Tleta dam by shear strength reduction technique. Innov. Infrastruct. Solut. 2018. 3 (6). DOI: 10.1007/s41062-017-0108-1
7. Bakhodirov, A.A., Ismailova, S.I., Sultanov, K.S. Dynamic deformation of the contact layer when there is shear interaction between a body and the soil. Journal of Applied Mathematics and Mechanics. 2015. 79 (6). Pp. 587–595. DOI: 10.1016/j.jappmathmech.2016.04.005
8. Bakhodirov, A.A., Sultanov, K.S. Waves in a Viscoelastic Bar Surrounded by Soils under Smooth Loading. Mechanics of Solids. 2014. 49(3). Pp. 349–359. DOI: 10.3103/S002565441403011X
9. Sultanov, K.S., Bakhodirov, A.A. Laws of Shear Interaction at Contact Surfaces Between Solid Bodies and Soil. Soil Mechanics and Foundation Engineering. 2016. 53 (2). Pp. 71–74. DOI: 10.1007/s11204-01693677

10. Amnyattalab, J., Rezaie, H. Study of the effect of seepage through the body of earth dam on its stability by predicting the affecting hydraulic factors using models of Brooks–Corey and van Genuchten (Case study of Nazluchay and Shahrchay earth dams). *Int. J. Environ. Sci. Technol.* 2017. 15. Pp. 2625–2636. DOI: 10.1007/s13762-017-1549-y
11. Qi, L., Chen, Q., Cai, J. Effect of seismic permanent deformation on safety and stability of earth-rock dam slope. *Transactions of Tianjin University.* 2015. 21 (2). Pp. 167–171. DOI: 10.1007/s12209-015-2379-y
12. Eskin, Yu.M., Krasnikov, N.D., Eisler, L.A. Raschet seysmonapryajennogo sostoyaniya i deformatsiy zemlyanix plotin s uchedom uprugoplasticheskix svoystv gruntov [Calculation of the seismic stress–strain state of earth dams, taking into account the elastic-plastic properties of soils]. *Bulleten of All-Russian Research Institute of Hydraulic Engineering. B.E. Vedenevaya.* 1977. No. 118. Pp. 24–34. (rus)
13. Khoei, A.R., Azami, A.R., Haeri, S.M. Implementation of Plasticity Based Models in Dynamic Analysis of Earth and Rockfill Dams: A Comparison of Pastor–Zienkiewicz and Cap Models. *Computers and Geotechnics.* 2004. 31 (5). Pp. 384–409. DOI: 10.1016/j.compgeo.2004.04.003
14. Sukkarak, R., Pramthawee, P., Jongpradist, P. A modified elasto-plastic model with double yield surfaces and considering particle breakage for the settlement analysis of high rockfill dams. *KSCE Journal of Civil Engineering.* 2017. 21 (3). Pp. 734–745. DOI: 10.1007/s12205-016-0867-9
15. Orekhov, V.V. Ustoychivost gruntovoy plotiny s vertikalnoy diafragmoy [The stability of earth dam with a vertical diaphragm]. *Vestnik MGSU. Hydraulics. Hydrological Engineering. Hydraulic engineering.* 2016. No. 1. Pp. 143–149. (rus)
16. Shahba, S., Soltani, F. Analysis of Stress and Displacement of Taham Earth Dam. *Indian Journal of Science and Technology.* 2016. 9 (45). DOI: 10.17485/ijst/2016/v9i45/104182
17. Sultanov, L.U., Davydov, R.L. Numerical analysis of large deformation by finite element method. *Magazine of Civil Engineering.* 2013. 44(9). Pp. 64–68. (rus). DOI: 10.5862/MCE.44.8
18. Sultanov, L.U., Berezhnoi, D.V., Karamov, A.V. FEM-based calculation of soil mass with the impact of dilatancy. *Magazine of Civil Engineering.* 2014. 48 (4). Pp. 3–9. (rus). DOI: 10.5862/MCE.48.1
19. Kalashnik, N.A. Kompyuternoye modelirovaniye nasyynoy zemlyanoy plotiny kak prototipa ogradhdayushchey damby khvostokhranilishcha. [Computer simulation of a fill earth dam as a prototype of the fencing tailing dam]. *International Research Journal.* 2012. 4 (4). Pp. 54–55. (rus)
20. Kusbekova, M.B., Zhambakina, Z.M., Permyak, M.B. Napryazhenno-deformirovannoye sostoyaniye otkosa [Stress-strain state of a slope]. *Scientific research.* 2017. 5 (16). Pp. 15–17. (rus)
21. Panov, S.I., Goldin, A.L. Deformatsii glinistykh gruntov pri tsiklicheskom nagruzhenii [Strain in clay soils under cyclic loading]. *Bulleten of All-Russian Research Institute of Hydraulic Engineering. B.E. Vedenevaya.* 2016. Vol. 280. Pp. 79–86. (rus)
22. Aleksandrov, A.V., Potapov, V.D. Osnovy teorii uprugosti i plastichnosti [Fundamentals of the theory of elasticity and plasticity]. Moscow: Higher school, 1990. 400 p. (rus)
23. Malinin, N.N. Prikladnaya teoriya plastichnosti i polzuchesti [Applied theory of plasticity and creep]. Moscow: Mechanical Engineering, 1975. 400 p. (rus)
24. Barkan, D.D. Dinamika osnovaniy i fundamentov [Dynamics of foundations and bases]. Moscow: Stroyvoenizdat, 1948. 411 p. (rus)
25. Ilyushin, A.A. Plastichnost [Plasticity]. Moscow: Gostekhizdat, 1948. 376 p. (rus)
26. Birger, I.A. Nekotoryye obshchiye metody resheniya zadach teorii plastichnosti [Some general methods for solving problems of the theory of plasticity]. *Applied Mechanics.* 1951. 15 (6). Pp. 765–770. (rus)
27. Birger, I.A. Raschet konstruksiy s uchedom plastichnosti i polzuchesti [Structural analysis taking into account ductility and creep]. *Izvestiya AN. Mechanics-Mechanical Engineering.* 1965. No. 2. Pp. 113–119. (rus)
28. Mirsaidov, M.M., Toshmatov, E.S. Spatial stress state and dynamic characteristics of earth dams. *Magazine of Civil Engineering.* 2019. 89 (5). Pp. 3–15. DOI: 10.18720/MCE.89.1
29. Usarov, M., Ayubov, G., Mamatisaev, G., Normuminov, B. Building oscillations based on a plate model. *IOP Conf. Series: Materials Science and Engineering.* 2020. 883 (012211). DOI: 10.1088/1757-899X/883/1/012211
30. Khodzhaev, D., Abdikarimov, R., Normuminov, B. Dynamic stability of viscoelastic rectangular plates with concentrated masses. *IOP Conference Series: Materials Science and Engineering.* 2020. 896 (012030). DOI: 10.1088/1757-899X/896/1/012030
31. Elgamel, A.M., Abdelghaffar, A.M. Earthquake induced plastic deformation of earth dams. *Proc. 2nd International Conference on Soil Dynamics and Earthquake Engineering, on board of the liner, the Queen Elizabeth 2.* 1985. No. 5. Pp. 45–54.
32. Abdikarimov, R., Khodzhaev, D., Mirzaev, B. Dynamic Stability of Orthotropic Rectangular Plates with Concentrated Masses. *Lecture Notes in Civil Engineering.* 2020. 70. Pp. 167–176. DOI: 10.1007/978-3-030-42351-3_15
33. Toshmatov, E., Usarov, M., Ayubov, G., Usarov, D. Dynamic methods of spatial calculation of structures based on a plate model. *E3S Web of Conferences.* 2019. 97 (04072). DOI: 10.1051/e3sconf/20199704072
34. Mirsaidov, M., Matkarimov, P. Dinamicheskaya zadacha dlya gruntovykh sooruzheniy, vzaimodeystvuyushchikh s zhidkostyu [Dynamic problem for soil structures interacting with a liquid]. *Doklady AN RUz.* 2007. No. 1. Pp. 25–28.
35. Mirsaidov, M.M., Sultanov, T.Z., Rumi, D.F. An assessment of dynamic behavior of the system "structure –foundation" with account of wave removal of energy. *Magazine of Civil Engineering.* 2013. 39 (4). Pp. 94–105. (rus). DOI: 10.5862/MCE.39.10
36. Bate, K., Wilson, E. Chislennyye metody analiza i MKE [Numerical methods of analysis and FEM]. Moscow: Stroyizdat, 1982. 448 p. (rus)

Contacts:

Mirziyod Mirsaidov, theormir@mail.ru

Tahirjon Sultanov, tohir-zs@mail.ru

Javlon Yarashov, zhavlon.yarashov@bk.ru



DOI: 10.34910/MCE.108.14

Thermal conductivity of granular insulation in conditions of soil freezing

K.S. Ivanov 

*Earth Cryosphere Institute SB RAS, Tuymen, Russia,
E-mail: sillicium@bk.ru*

Keywords: insulating materials, frost protection, glass ceramics, aggregates, frozen soils

Abstract. Thermal insulation materials are widely used in engineering practice to reduce the depth of seasonal freezing. The effective thermal conductivity of the material is the main criterion for predicting the freezing depth of the structure base and determining the required thickness of the thermal insulation layer. However, the effective thermal conductivity of granular thermal insulation materials can significantly depend on the seasonal temperature, hydrological conditions of the soil and the degree of water content of the material. In this regard, calculating the effective thermal conductivity of granular thermal insulation materials in natural conditions is an urgent scientific and practical task. Granular foam-glass ceramic with a bulk density of 250 kg/m³ was used in the study. To solve the problem, we employed an experimental set to simulate the natural conditions of heat transfer in a horizontal layer, which makes it possible to change the magnitude and direction of the temperature gradient. It was established that the magnitude and direction of the temperature gradient have no significant influence on the layer of granules with a size of 5–10 mm. A predictive calculation of the temperature fields of the roadbed using experimental values depending on the water content degree was carried out. It was found that the depth of freezing of the roadbed covered with a 20 cm layer of foam-glass ceramic with effective thermal conductivity of 0.075, 0.111 and 0.138 W/(m·°C), respectively, is 12, 3.8 and 3 times lower than without the thermal insulation layer. A graphical interpretation of the temperature field in the form of -2°C isotherms shows that there is a dangerous zone of intense frost heaving with a depth of 58 cm forming at the roadbed without thermal insulation. Complete absence of zones of intense frost heaving in the roadbed covered with granular foam-glass ceramic was confirmed.

1. Introduction

Ensuring the reliable and stable functioning of engineering structures in conditions of seasonal freezing and thawing of their bases is an urgent engineering task. Linear objects such as highways and railways, pipelines, etc., as well as buildings with shallow foundations are at risk of deformation. For example, a quarter of the entire budget of the Swedish Road Administration is spent on the annual elimination of the consequences of frost heaving of the roadbed [1]. Frost heave deformations are due to the presence of three factors at the base of the structure: frost susceptible soil, high soil water content and negative temperature. Depending on the listed factors, there are three ways to limit frost heaving process:

1. Replacement of frost susceptible soil with the one less sensitive to heaving.
2. Reducing soil water content due to drainage measures.
3. Covering the base with a layer of thermal insulation material.

Ivanov, K.S. Thermal conductivity of granular insulation in conditions of soil freezing. Magazine of Civil Engineering. 2021. 108(8). Article No. 10814. DOI: 10.34910/MCE.108.14

© Ivanov, K.S., 2021. Published by Peter the Great St. Petersburg Polytechnic University.



This work is licensed under a CC BY-NC 4.0

Special methods of engineering practice to protect structures from frost heaving deformations are constantly being improved [2–6]. According to a number of experts, one of the most effective and cheap ways to reduce the depth of seasonal freezing of bases is the use of thermal insulation materials [6–8]. These materials must have low thermal conductivity, sufficient compressive strength and low water absorption capacity.

Such lightweight aggregates as expanded clay and crushed foam glass as well extruded polystyrene boards are used in modern engineering practice [7–11]. The main advantage of extruded polystyrene boards is the lowest thermal conductivity during the entire period of operation, since the material does not absorb moisture. At the same time, the volumetric water absorption of lightweight aggregates can reach 30 % [10, 11]. Convection, grain size, layer compaction degree, etc. can have a significant effect on heat transfer in the layer of lightweight aggregates. In this regard, the thickness of the layers of lightweight aggregates can be several times greater than that of extruded polystyrene foam.

As an example, we can consider the temperature monitoring data of an experimental road section in Norway, where extruded polystyrene boards and lightweight aggregates were used [8]. It was found that the extruded polystyrene boards and crushed foam glass layers 3 and 15 cm thick, respectively, have equal thermal resistance. Thus, the required thickness of crushed foam glass insulation layer is 5 times that of polystyrene boards. In the case of using expanded clay, a layer 7 times the thickness of polystyrene boards layer is required.

Despite this, a number of studies indicate the successful use of lightweight aggregates in road construction in Norway, Sweden and Finland. [1, 7, 10, 11]. The standards governing the use of lightweight aggregates on heaving road sections have been developed in these countries. The granular structure of lightweight aggregates is considered an important advantage in the art. Unlike extruded polystyrene boards, mechanized laying is possible in this case. In addition to performing thermal insulation functions, the layer of lightweight aggregates is drainage. Due to climatic and geological conditions, structural layers above extruded polystyrene boards can accumulate water. Under the same conditions, water drainage through the insulation lightweight aggregates can have a positive effect on the stability of the engineering structure.

The foregoing testifies to the relevance and practical significance of the use of lightweight aggregates during construction under conditions of seasonal soil freezing. Foam-glass ceramics is an alternative thermal insulation lightweight aggregate, which has recently found application in industrial and civil construction [12–14]. Granular foam-glass ceramic have a closed porous structure, due to which the volumetric water absorption of the material is about 6% [15–18].

A significant advantage of granular foam-glass ceramic is a widespread raw material base: opal-cristobalite (diatomite, tripoli, flask) and zeolite-bearing rocks. Their deposits are widespread throughout Russia, which makes it possible to organize the production of material near the construction site [14, 15]. Due to the high length of the country, a reduction in the distance of transportation of thermal insulation material can reach several thousand kilometers, which will give a significant economic effect. Such lightweight aggregates as crushed foam glass and expanded clay are produced, respectively, from waste glass and special types of clays that significantly limits their raw material base.

At present, experience has been accumulated in the experimental use of granular foam-glass ceramic. Temperature monitoring of the experimental section of the existing highway in the south of the Tyumen region (Russia) has been carried out since 2016. In the same year, on the section of the Trans-Baikal Railway (Russia), the material was used to insulate drainage reinforced concrete structures in order to exclude freezing of drainage waters in winter [20]. Based on the positive experience of the experimental use of the material, since 2017 its practical application in construction is regulated by the Russian State rules and regulations: SP 313.1325800.2017 “Automobile roads in permafrost regions. Design and construction rules”.

One of the tasks for the further development of the use of granular foam-glass ceramic in engineering practice is an accurate assessment of the effective thermal conductivity as a fundamental characteristic of thermal insulation material. A significant contribution to the value of the effective thermal conductivity of a granular material is made by the convective component of heat transfer. Its value depends on the magnitude and direction of the temperature gradient, the intergranular void volume, the shape of the grains, their size, etc. In nature, the process of heat transfer through granular material is accompanied by changes in soil and geological conditions, moisture gradient and temperature, which will eventually cause fluctuations in the effective thermal conductivity of the layer [21, 22]. For example, an increase in the volumetric water content in expanded clay to 20 % leads to an increase in its effective thermal conductivity from 0.11 to 0.21 W/(m·°C) [9, 10]. The above research data [8] refer to only one season of freezing-thawing of the roadbed (from November to March). Therefore, it is impossible to reliably assess the influence of water saturation and other factors on the change in the effective thermal conductivity of granular heat insulation layers over a longer period.

Unfortunately, the above-mentioned features of heat and mass transfer and possible seasonal fluctuations in the values of the effective thermal conductivity are not taken into account in modern numerical methods for calculating the temperature fields of the bases [23, 24]. As a rule, one averaged value is taken in the calculations, which is incorrect and leads to a discrepancy between the actual and calculated values of the base temperature. In this regard, the aim of the work was to study the influence of environmental factors corresponding to seasonal freezing on the effective thermal conductivity of granular foam-glass ceramic layer. The solution to this problem is of great practical importance in the design and assessment of the bearing capacity of the bases of engineering structures in areas of seasonal soil freezing. Correction of the effective thermal conductivity values when calculating the temperature fields will make it possible to more accurately predict the occurrence of dangerous zones of frost heaving in the base and determine the required thickness of the thermal insulation layer.

A review of literary sources has shown that the problem posed is highlighted in most detail in the works [21, 25]. A significant effect of the grain size, direction and magnitude of the temperature gradient on the effective thermal conductivity and free convection in the layer of granular materials had been established by the authors. Tested materials intended for road construction were placed in experimental setups, which were an insulated box with internal dimensions of 1 m x 1 m x 1 m. Nevertheless, the experimental technique had the following disadvantages:

1. Heat flow sensors were installed only at the top of the test layer, as a result the heat balance and heat flow dissipation by the side walls of the setups cannot be evaluated.
2. The dimensions of the setups were not related to the average grain size of the materials under study, which varied from about 10 to 100 mm. For example, according to the requirements of Russian State Standard GOST 7076-99, the thickness of the layer of granular material during the study of its effective thermal conductivity must be at least 10 times the average grain size, while the length of the inner horizontal edge of the box must be at least 5 times the thickness of this layer. Therefore, the minimum internal length and width of the box must be 5 m.
3. The average experimental error of the measuring system was 0.11 W/(m·K), while the effective thermal conductivity of the studied materials themselves: expanded clay and crushed foam glass was 0.1 and 0.115 W/(m·K), respectively.

In this regard, one of the tasks for solving the problem posed was the development of an experimental technique for determining the effective thermal conductivity of granular foam-glass ceramic, taking into account the mentioned above features of its application.

2. Methods

The study was carried out using foam-glass ceramic with a fraction of 5–10 mm. The properties of the material were determined in accordance with the method of Russian State Standard GOST 9758-2012 and had the following values: bulk density 250 kg/m³, compressive strength in the cylinder 1.8 MPa, moisture 0.2 %, water absorption by volume 7 %. The choice of the fraction was justified by the fact that foam-glass ceramic with a grain size of less than 5 mm has a higher thermal conductivity and water absorption. In this regard, the use of fine fractions in the bases is unjustified.

The solution to the problem of determining the effective thermal conductivity was carried out using an experimental setup for simulating the natural conditions of heat transfer in a horizontal layer of granules. The design of the experimental setup and the calculation of the effective thermal conductivity were carried out in accordance with the requirements of Russian State Standard GOST 7076-99. A cross-sectional view of setup is shown in Figure 1. The body of the setup is made in the form of a horizontally located disk. The bottom, cover and side walls 5 are made of extruded polystyrene boards having a thermal conductivity of 0.033 W/(m·°C). The width of the walls is 12.5 cm, the thickness and diameter of the bottom and cover are 10 and 125 cm, respectively.

A layer of granulated foam-glass ceramic 2 with a thickness of 10 cm is placed in the setup body. The thickness of the layer was taken taking into account the tenfold excess of the largest grain foam-glass ceramic, equal to 10 mm. The diameter of layer 2 (100 cm) was taken taking into account the tenfold excess of its thickness. The layer 2 was leveled and tamped by hand to a compaction factor of 1.2. As a result, the density of the material in the compacted layer was 300 kg/m³.

There are identical thermostating systems made of copper tubes 4 with a diameter of 12 mm on the upper and lower sides of the foam-glass ceramic layer 2. The upper and lower thermostating systems 4 are connected to separate thermostat, each of which set the temperature up and down respectively. Two counter-flow loops on each side of layer 2 are formed by the movement of the coolant in tubes 4. The direction of the coolant flow is shown by arrows at the top in Figure 1.

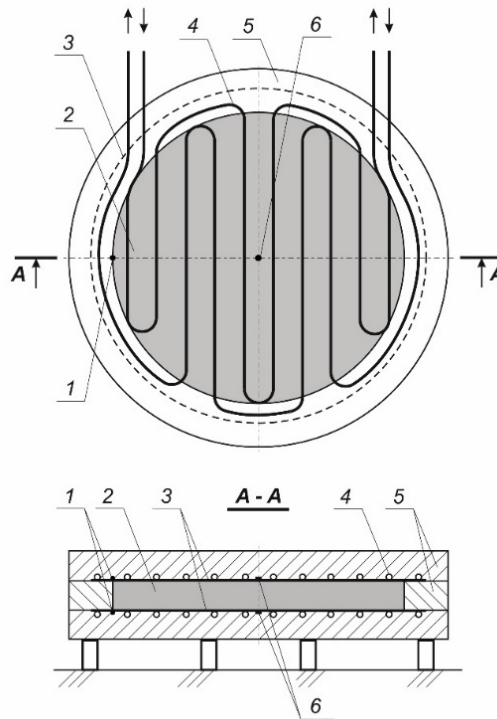


Figure 1. Experimental setup (cross section): 1 – Side temperature sensors; 2 – Foam-glass ceramic layer; 3 – Steel sheets; 4 – Tubes of the thermostating system; 5 – Expanded polystyrene; 6 – Heat flow sensors combined with temperature sensors.

The tubes of system 4 are attached to steel sheets 3 with a thickness of 3 mm. Due to the counter-flow loops of thermostating systems the temperature is uniformly distributed over the surface of the sheets 3 that are in contact with the upper and lower surfaces of layer 2. The sheets 3 serve to equalize the heat flow and more uniform temperature transfer from the coolant to the granular material. The diameter of the sheets 3 is 10 cm larger than the diameter of layer 2 in order to minimize the lateral temperature gradient in layer 2. The counter-flow loops of the upper and lower thermostating systems 4 have an increased diameter for the same purpose.

Due to the above-described setup design (Figure 1) the required temperature can be set and maintained on the upper and lower steel sheets 3. As a result, a vertical temperature gradient and its direction in the investigated layer 2 are set. For example, there is an upward temperature gradient at freezing conditions because the base temperature is higher than the air temperature. During defrosting, when the air temperature rises above the base temperature, the gradient is reversed.

From the above ratios of the thickness and diameter of layer 2, it follows that the dimensions of the setup directly depend on the size of the largest grain. For example, an increase in the maximum grain size from 10 to 20 mm will cause an increase in the area of steel sheets 3 by 4 times. As a result, it will be necessary to increase the sheets thickness, use a more complex thermostating system 4, increase the power or the number of thermostats, etc. The listed design features served as a rationale for the choice of the 5–10 mm fraction in these studies. This fraction can be used in bases along with a larger one (for example, 10–20 mm), however, the determination of the effective thermal conductivity of larger fractions will require separate studies using more complicated setup.

The value of the temperature gradient is measured using temperature sensors 6 with an absolute error of ± 0.1 °C. Temperature sensors 6 are combined with heat flow sensors in order to place them on the central setup axis. Due to the fact that the material of layer 2 is represented by individual grains, the sensors 1 and 6 are fixed on steel sheets 3 using a heat-conducting paste. Temperature sensors 1 are designed to assess the horizontal (lateral) temperature gradient caused by the influence of the ambient temperature. The air temperature in the room where the setup was located was maintained at 20 ± 0.2 °C.

The heat flow density in layer 2 is determined using heat flow sensors 6 with an error of ± 0.1 W/m². Sensors 1 and 6 are connected to an analog-to-digital converter that records temperature and heat flow data at 20 minute intervals. The measuring cycle begins from the moment the upper and lower thermostating systems are switched on until a steady state heat flow in layer 2 is formed. The heat flow in layer 2 was considered as steady state under the following conditions:

1. Deviations of the values of five consecutive measurements of temperature and heat flow density should not exceed the absolute error of sensors 1 and 6 (Figure 1).
2. The difference between the readings of the side and central temperature sensors (1 and 6, respectively) should not exceed the absolute error of this sensor.
3. The values of the heat flow density measured by the upper and lower sensors should not differ by a value exceeding their absolute error.

If at least one of the above conditions was not met, then the number of measurement intervals increased until it was fulfilled, or measurements were repeated from the beginning of the measuring cycle. If the above conditions are met, the effective thermal conductivity of layer 2 was calculated by the formula:

$$\lambda = q \frac{h}{t}$$

where λ is effective thermal conductivity, W/(m·°C); q is heat flow density, W/m²; h is test material layer thickness, m; t is absolute value of the temperature difference between steel sheets 3, determined by sensors 6, °C.

The q value was obtained by averaging the readings of the upper and lower sensors 6 (Figure 1). The arithmetic mean λ of three measurement cycles was taken as the final result. The absolute error of the λ value was calculated by the formula [26]:

$$\Delta\lambda = \lambda \sqrt{\left[\frac{\Delta q}{q}\right]^2 + \left[\frac{\Delta h}{h}\right]^2 + \left[\frac{\Delta t}{t}\right]^2}$$

where $\Delta\lambda$, Δq , Δh and Δt are the absolute errors of the values of λ , q , h ($\pm 0.5 \cdot 10^{-3}$ m) and t , respectively.

3. Results and Discussion

3.1. Laboratory thermal conductivity test

The obtained values of t , q and the results of calculating λ of tested layer are presented in Table 1. For measurements 1–3 and 4–6 heat flow was directed upward and downward respectively. Under natural conditions, these temperature gradients correspond to freezing and thawing of bases, i.e. negative (and close to 0 °C) temperature can be both above and below the thermal insulation layer. Numbers 1–6 corresponded to measurements of tested layer in a dry state.

Table 1. Measurement results.

No	Compacted layer properties		Temperature, °C			q , W/m ²	λ , W/(m·°C)	$\Delta\lambda \cdot 10^{-3}$, W/(m·°C)
	Density, kg/m ³	Volumetric water adsorption, %	top	bottom	t			
1	300	0	0.8	10.5	9.7	7.3	0.076	1.4
2	300	0	2.9	19.4	16.5	12.5	0.076	0.9
3	300	0	-3.2	22.3	25.5	19.6	0.077	0.6
4	300	0	11.0	0.9	10.1	7.4	0.073	1.3
5	300	0	20.1	3.1	17.0	12.7	0.075	0.8
6	300	0	19.9	-3.2	23.1	17.2	0.074	0.7
7*	340	0	1.6	19.1	17.5	15.5	0.089	0.9
8	324	3.7	1.7	16.6	14.9	16.5	0.111	1.1
9	346	7.0	1.4	15.6	14.2	19.7	0.138	1.4

*Grains size of 2.5–5 mm

It follows from Table 1 that a change in the value of t for measurement numbers 1–3 and 4–6 does not significantly affect the values of λ . Average values of λ with upward heat flow (numbers 1–3) and reverse (numbers 4–6) differ by $1 \cdot 10^{-3}$ W/(m·°C). In view of the fact that the average value of $\Delta\lambda$ for measurements 1–6 is $\pm 1 \cdot 10^{-3}$ W/(m·°C), it can be concluded that the influence of the heat flow direction and the values of t on λ is insignificant. Thus, according to the averaging of measurements 1–6, the value of λ for the 5–10 mm fraction in the dry state is 0.075 W/(m·°C).

Measurement number 7 in the Table 1 shows the results of determining λ of a finer fraction of foam-glass ceramic with a size of 2.5–5 mm and a bulk density of 340 kg/m³. As follows from the Table 1, the λ value of this fraction is almost 20 % higher in comparison with the 5–10 mm fraction. In this regard, the use of fractions with a grain size of less than 5 mm is less effective.

Due to the inevitable moistening and water absorption of granular foam-glass ceramic layer at the base, λ measurements in the water-saturated state were carried out. The results for the fraction 5–10 mm numbered 8 and 9 in Table 1. The water absorption of the granules by volume was 3.7 and 7 % in the first and second cases, respectively, which corresponded to the intermediate and maximum water absorption of the material.

The Table 1 shows that the λ values of measurements 8 and 9 exceed the obtained average λ of measurements 1–6 by approximately 1.5 and 1.8 times, respectively. Consequently, the effect of water saturation of granular foam-glass ceramic on the λ value is much more significant in comparison with the direction of the heat flow, t value and the size of the granules. In this regard, the use of the material in practice will require special methods to maintain the calculated thermal resistance of the layer, for example, the use of protective membranes, films, etc. In the case of direct contact of the layer granules with the soil, the λ value will fluctuate in the range from 0.075 to 0.138 W/(m·°C), depending on the degree of soil moisture at the base of the structure. As a result, in order to maintain the calculated thermal resistance of the layer, it will be necessary to increase its thickness up to 1.8 times.

For predictive calculations of the temperature fields of the bases and the freezing depth, two experimental values of λ can be distinguished for a layer of 5–10 mm fraction. In the event that the base is located in a high area with a low level of groundwater, an intermediate value of λ should be taken in the calculations, equal to 0.111 W/(m·°C). If the base is located in an area characterized by the accumulation and stagnation of surface water, which will contribute to the maximum water saturation of the thermal insulation material, then the maximum λ value of 0.138 W/(m·°C) should be taken.

The result obtained can be compared with the data of other authors. For example, in studies [21], the value of λ in the dry state was experimentally established for crushed foam glass aggregate with a close bulk density equal to 223 kg/m³. However, the average grain size of the fraction 10–60 mm was 4.7 times greater than that of the foam-glass ceramic. Taking into account the downward heat flow condition the experimental value of λ was 0.34 W/(m·K), which is 4.5 times more than for foam-glass ceramics in a dry state. Apparently, such a significant difference is caused by the influence of free convection due to the larger grains of crushed foam glass.

3.2. Mathematical modeling

For the purpose of a comparative assessment of the influence of three experimental λ values on the base freezing depth, a calculation was carried out using finite-difference methods of mathematical modeling [23, 24]. The calculations were carried out on the example of a highway located in the south of the Tyumen region, Russia (Golysmanovsky district). The area is distinguished by a large seasonal freezing depth. The average January temperature between 2006 and 2019 is -17.9 °C.

The right side of the typical road cross section is shown at the top in Figure 2 (the left part is symmetrical to the road axis and is not shown). The thickness of insulation layer 1 was set taking into account the provision of a deviation of ± 1 cm during mechanized compaction of material with specialized road equipment. The main calculated characteristics of the layers are presented in Table. 2. For the pavement layer, the average value of thermal conductivity of asphalt concrete and crushed stone is taken. The heat of the phase transition of pavement materials was not taken into account in the calculations.

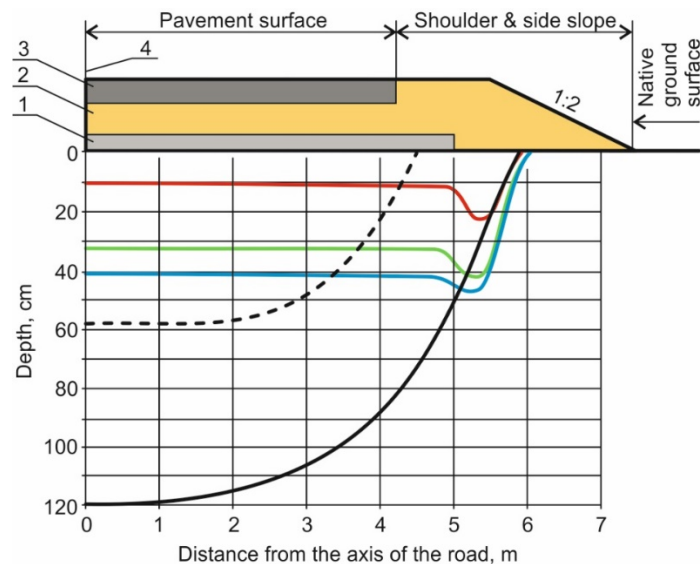


Figure 2. Road cross section and calculation results: 1 – Foam-glass ceramic layer (20 cm); 2 – Coarse sand layer (38 cm); 3 – Pavement: asphalt concrete and crushed stone (42 cm); 4 – Road axis. Red, green and blue lines correspond to $-0.5\text{ }^{\circ}\text{C}$ isotherms with λ 0.075, 0.111 and 0.137 W/(m \cdot $^{\circ}\text{C}$), respectively. Black solid and dotted lines correspond to -0.5 and $-2\text{ }^{\circ}\text{C}$ isotherms without insulating layer. The scale of the vertical axis is increased by 4 times for clarity.

Because the thickness of the insulation layer is significantly less than the base freezing depth, its λ values in the thawed and frozen state were equated to the corresponding experimental λ values obtained above. The phase transition heat of the foam-glass ceramic in the water-saturated state was not taken into account in the calculations for the same reason. The specific heat capacity of the material was taken equal to the reference value for silicate glass, which is 840 J/(kg \cdot $^{\circ}\text{C}$) [27], due to the close chemical composition [14, 15]. Therefore, taking into account the density of the heat insulation layer in dry compacted state (300 kg/m 3), its calculation specific heat capacity per 1 m 3 is 252 kJ/(m 3 \cdot $^{\circ}\text{C}$).

Table 2. Characteristics of layers and base.

No	Name of the material	Thermal conductivity, W/(m \cdot $^{\circ}\text{C}$)		Heat capacity, kJ/(m 3 \cdot $^{\circ}\text{C}$)		Phase transition heat, MJ/m 3
		thawed	frozen	thawed	frozen	
1	Pavement	2.05		1870		-
2	Coarse sand	1.97	2.15	2250	1790	82
3	Silt sandy loam	2.02	2.30	2740	2120	96

The roadbed (subsoil) was represented by silty sandy loam with high frost heave rate of 9 % and a low degree of salinity. This type of soil is widespread in the region under consideration. In accordance with the Russian State rules and regulations SP 25.13330.2012 "Bases and foundations on permafrost soils", the calculated temperature of the subsoil phase transition was $-0.5\text{ }^{\circ}\text{C}$.

When solving an axisymmetric problem, the computational domain was represented by a square with sides of 15 m. The axis of the road (Figure 2) coincided with the left side of the computational domain. The horizontal dimension of the computational domain was set taking into account the two-fold excess of the foot of the road structure (7.5 m, Figure 2), and vertically, taking into account the attenuation of annual air temperature fluctuations at a depth of 15 m [28]. Boundary conditions of the first kind with a constant temperature of $0.9\text{ }^{\circ}\text{C}$ were set on the lower side. According to Russian State rules and regulations SNIP 23-01-99 this temperature corresponds to the average annual air temperature in the area under consideration. Boundary conditions of the second kind (without heat flow) were set on the lateral sides of the computational domain.

In the three types of surfaces of the computational domain (Figure 2) boundary conditions of the third kind were set. Average monthly values of air temperature, wind speed, and thickness of snow cover on the surface were calculated for the period from 2006 to 2019 according to the data of meteorological station No. 28478 (Tyumen region, Golyshmanovsky district). Due to snow removal in winter the snow cover on the pavement surface was not taken into account in the calculations. For this reason, a doubled layer of snow was taken on the road shoulder and the side slope. In order to reduce the freezing depth of these areas under the influence of the exposed layer 3, the thermal insulation layer 1 had an increased width

(Figure 2). A sod cover with a thickness of 10 cm and a thermal conductivity of $0.75 \text{ W}/(\text{m}\cdot^\circ\text{C})$ was taken into account in the road shoulder, the side slope and the native ground surface.

The initial calculation conditions corresponded to the date of October 1, 2020 and a surface temperature of 6°C . The final calculated date March 15, 2023 corresponded to the maximum seasonal freezing depth of the base. The calculation results in the form of lines denoting the isotherms are shown in Figure 2. Isotherms of -0.5°C , corresponding to the phase transition temperature of sandy loam, characterize the base freezing depth.

As follows from the calculation results in Figure 2, the freezing depth of the base without taking into account the insulation layer is characterized by black solid -0.5°C isotherm. The maximum value of the freezing depth of 120 cm near the axis of the road was reached. Calculations taking into account the thermal insulation layer with λ equal to: 0.075, 0.111 and $0.137 \text{ W}/(\text{m}\cdot^\circ\text{C})$ are characterized by red, green and blue -0.5°C isotherms, respectively. Neglecting the bends of the isotherms at a distance of 5–6 m from the axis of the road, it was found that the computational freezing depth in this case is 10, 32 and 40 cm at λ equal to: 0.075, 0.111 and $0.137 \text{ W}/(\text{m}\cdot^\circ\text{C})$, respectively.

It is known that the degree of frost heaving significantly depends on the type of soil and its moisture content. The frost heave process begins to develop most intensively at a certain temperature, for example, for loams from -1.5 to -2.5°C [28]. Assuming this temperature for sandy loam equal to -2°C , then the zone of frost heaving at the base will be limited by the -2°C isotherm. A graphical interpretation of the calculated temperature fields without an insulating layer shows the -2°C isotherm in Figure 2, marked with a black dotted line. This isotherm limits the dangerous zone of intense frost heaving to a depth of 58 cm near the axis of the road. Taking into account the accepted high frost heave rate of the base soil, the absolute deformation of frost heaving near the axis of the road can reach 5 cm. As a result, the annual freezing-thawing processes will cause seasonal deformations of the pavement surface and its gradual destruction.

The formation of the -2°C isotherm taking into account the variations in experimental λ values of the thermal insulation layer was not confirmed in Figure 2. At the same time, there are no deformations of frost heaving of the roadbed, causing the pavement surface destruction, which significantly increases the overhaul interval of the road.

The results of mathematical modeling can be compared with the experimental data of field test of crushed foam glass with a bulk density of $220 \text{ kg}/\text{m}^3$ in climatic conditions of Norway [8]. A layer of the material 15 cm thick ensured that a positive temperature at the roadbed had been maintained. On a road section without thermal insulation, the 0°C isotherm at a depth of 35 cm had been reached.

The advantage of using granular foam-glass ceramic is not only in reducing the freezing depth of the base. It is known that during the construction of highways in areas with unfavorable soil and hydrological conditions, there is a need for a frost-protective layer. The thickness of this layer, ensuring the exclusion of freezing of the base, can be more than two meters (depending on the climatic zone) [29]. For the construction of frost-protective layers of highways, as a rule, coarse sands are used. Taking into account the high length of the road under construction, the transportation distance of coarse sands can exceed 500 km. Thus, the use of granular glass-ceramic foam can give a significant economic effect as a result of reducing the volume of materials transportation and earthworks.

4. Conclusion

1. The experimental values of the effective thermal conductivity of granular foam-glass ceramic with a fraction of 5–10 mm in a dry and water volumetric saturated states of 3.7 and 7 % were established: 0.075, 0.111 and $0.138 \text{ W}/(\text{m}\cdot^\circ\text{C})$, respectively. The effect of changing the direction and magnitude of the temperature gradient was insignificant, since it is within the absolute error of the measuring setup.

2. A predictive calculation of the temperature fields of the roadbed using experimental values depending on the water content degree was carried out. It was found that the freezing depth of the roadbed covered with a 20 cm layer of foam-glass ceramic with effective thermal conductivity of 0.075, 0.111 and $0.138 \text{ W}/(\text{m}\cdot^\circ\text{C})$, respectively, is 12, 3.8 and 3 times lower than without the thermal insulation layer. Due to graphical interpretation of the temperature field in the form of -2°C isotherms at the roadbed without thermal insulation the formation of a dangerous zone of intense frost heaving with a depth of 58 cm was shown. The complete absence of zones of intense frost heaving in the roadbed covered with granular foam-glass ceramic was confirmed.

3. The obtained experimental data can be applied in methods for calculating temperature fields in order to assess the risk of occurrence of cryogenic zones in bases using granular foam-glass ceramic.

4. Due to the wide mineral resource base, the production of granulated foam-glass ceramic can be deployed in territories remote from industrialized regions, for example, in the Far North and the Arctic. The

development of these territories will require both the modernization of the existing and the creation of a new transport infrastructure, which requires the use of special technologies and innovative road materials of local production.

5. Acknowledgments

The work was carried out within the framework of the state assignment: registration No. AAAA-A17-117051850061-9. The research was partially funded by: Autonomous Nonprofit Organization "Provincial Academy", Tyumen, Russia.

References

1. Furuberg, T., Want, A., Amundsgard, K.O. Effects of Leca insulation in roads and railways. Proceedings of IX International Symposium on Ground Freezing and Frost Action in Soil. Louvain-la-Neuve, 2000. Pp. 203–207.
2. Chao, G., Lu, Z. Frost heaving of foundation pit for seasonal permafrost areas. Magazine of Civil Engineering. 2019. 86(2). Pp. 61–71. DOI:10.18720/MCE.86.6.
3. Wang, Y., Zhang, K. Heavy metal pollution in soil and agricultural products on roadside of highway in seasonally frozen soil area. Revista de la Facultad de Agronomia. 2019. 36(3). Pp. 754–763.
4. Hagh, N.T., Hashemian, L., Bayat, A. Effects of seasonal variation on the load-bearing capacity of pavements composed of insulation layers. Transportation Research Record. 2016. 2579. Pp. 87–95. DOI: 10.3141/2579-10.
5. Xu, J., Niu, F.-J., Li, A.-M., Lin, Z.-J. Analysis of the prevention effect of thermal-insulation method on frost heave of railway subgrade in seasonal frozen regions. Tiedao Xuebao/Journal of the China Railway Society. 2010. 32(6). Pp. 124–131. DOI:10.3969/j.issn.1001-8360.2010.06.021.
6. Yin, Y., Zhang, D., Feng, C., Ji, C., Yang, H. Insulation and anti-freezing test research of channel lining project in Linhe district of Inner Mongolia. Paiguan Jixie Gongcheng Xuebao/Journal of Drainage and Irrigation Machinery Engineering. 2016. 34(10). DOI:10.3969/j.issn.1674-8530.15.0232.
7. Klochkov, Ya.V., Nepomnyashchikh, Ye.V., Lineytsev, V.Yu. Primeniye penostekla dlya regulirovaniya teplovogo rezhima gruntov v slozhnykh klimaticheskikh usloviyakh [The use of foam glass to control the thermal state of soils in difficult climatic conditions]. Vestnik ZabGU. 2015. 6. Pp. 9–15.
8. Øiseth, E., Aabøe, R., Hoff, I. Field test comparing frost insulation materials in road construction. Proceedings of the International Conference on Cold Regions Engineering. Orono, 2007. Pp. 62. DOI:10.1061/40836(210)62.
9. Øiseth, E., Refsdal, G. Lightweight aggregates as frost insulation in roads – Design chart. Proceedings of the International Conference on Cold Regions Engineering. Orono, 2007. Pp. 63. DOI:10.1061/40836(210)63.
10. Hoff, I., Want, A., Øiseth, E., Emdal, A., Amundsgard, K.O. Light weight aggregate (LWA) used in road pavements. Proceedings of VI International Conference on the Bearing Capacity of Road and Airfields. Lisbon, 2002. Pp. 1013–1022.
11. Frydenlund, T.E., Aaboe, R. Foamglass – A new vision in road construction. Proceedings of XXII PIARC World Road Congress. Durban, 2003. P. 96.
12. Portnyagin, D.G. Improving the thermal performance of the building envelopes with the use of foam glass-ceramics. Magazine of Civil Engineering. 2015. 60(8). Pp. 56–67. DOI:10.5862/MCE.60.7.
13. Ivanov, K.S., Korotkov, E.A. Investigation of the Effect of a Layer of Granulated Foam-Glass Ceramic on the Temperature Conditions of Frozen Soil. Soil Mechanics and Foundation Engineering. 2017. 54(5). Pp. 349–355. DOI:10.1007/s11204-017-9480-2.
14. Yatsenko, E.A., Goltsman, B.M., Ryabova, A.V. Complex protection of pipelines using silicate materials based on local raw materials of the Far East. Materials Science Forum. 2019. 945. Pp. 46–52. DOI: 10.4028/www.scientific.net/MSF.945.46.
15. Erofeev, V.T., Rodin, A.I., Kravchuk, A.S., Kaznacheev, S.V., Zaharova, E.A. Biostable silicic rock-based glass ceramic foams. Magazine of Civil Engineering. 2018. 84(8). Pp. 48–56. DOI:10.18720/MCE.84.5.
16. Ivanov, K.S. Optimization of the structure and properties of foam-glass ceramics. Magazine of Civil Engineering. 2019. 89(5). Pp. 52–60. DOI:10.18720/MCE.89.5.
17. da Silva, R.C., Kubaski, E.T., Tenório-Neto, E.T., Lima-Tenório, M.K., Tebcherani, S.M. Foam glass using sodium hydroxide as foaming agent: Study on the reaction mechanism in soda-lime glass matrix. Journal of Non-Crystalline Solids. 2019. 511. Pp. 177–182. DOI:10.1016/j.jnoncrysol.2019.02.003.
18. Ivanov, K.S. Foam-Ceramic-Glass Synthesis Using a Mechanized Extrusive Method of Batch Preparation. Glass and Ceramics. 2020. 76(9–10). Pp. 381–386. DOI:10.1007/s10717-020-00205-8
19. Ivanov, K.S. Granulated foam-glass ceramics for ground protection against freezing. Magazine of Civil Engineering. 2018. 79(3). Pp. 95–102. DOI:10.18720/MCE.79.10.
20. Melnikov, V.P., Korotkov, Ye.A., Ivanov, K.S., Shekhtman, Ye.V., Dashinimayev, Z.B., Sigachev, N.P., Klochkov, Ya.M. Utepleniye zhelezobetonnykh konstruktiv dlya propuska drenazhnykh vod na Zabaykalskoy doroge [Thermal insulation of reinforced concrete structures for the passage of drainage water on the Trans-Baikal Railway]. Put i Putevoye Khozyaystvo. 2017. 7. Pp. 13–15.
21. Rieksts, K., Hoff, I., Scibilia, E., Côté, J. Laboratory investigations into convective heat transfer in road construction materials. Canadian Geotechnical Journal. 2020. 57(7). Pp. 959–973. DOI:10.1139/cgj-2018-0530.
22. Goering, D.J., Kumar, P. Winter-time convection in open-graded embankments. Cold Regions Science and Technology. 1996. 24(1). Pp. 57–74. DOI:10.1016/0165-232X(95)00011-Y.
23. Melnikov, V.P., Melnikova, A.A., Anikin, G.V., Ivanov, K.S., Spasennikova, K.A. Engineering solutions for building on permafrost in perspective energy-efficient enhancement. Earth's Cryosphere. 2014. 18(3). Pp. 82–90.
24. Spasennikova, K.A., Anikin, G.V., Gubarkov, A.A. Stochastic forecasting of the state of the soil under the roadbed. E3S Web of Conferences. 2019. 91. Pp 1–6. DOI:10.1051/e3sconf/20199107008.
25. Côté, J., Fillion, M.-H., Konrad, J.-M. Intrinsic permeability of materials ranging from sand to rock-fill using natural air convection tests. Canadian Geotechnical Journal. 2011. 48(5). Pp. 679–690. DOI:10.1139/t10-097.

26. Kassandrova, O.N., Lebedev, V.V. Obrabotka rezultatov nablyudeniya [Processing of observation results]. Moscow: Nauka, 1970. 111 p.
27. Perry's Chemical Engineers' Handbook. 9 edn. McGraw-Hill Education. New York, 2019. 2561 p.
28. Orlov, V.O., Dubnov, Yu.D., Merenkov, N.D. Pucheniye promerzayushchikh gruntov i yego vliyaniye na fundamenty sooruzheniy [Heaving of freezing soils and its effect on the foundations of structures]. Moscow: Stroyizdat, 1977. 183 p.
29. Ruvinskiy, V.I. Posobiye po ustroystvu teploizoliruyushchikh sloyev iz penoplasta Styrofoam na avtomobilnykh dorogakh Rossii [Manual for the installation of heat-insulating layers of Styrofoam foam on the roads of Russia]. Moscow: Transport, 2000. 71 p.

Contacts:

Konstantin Ivanov, sillicium@bk.ru



DOI: 10.34910/MCE.108.15

Corrosion resistance of steel structures in marine conditions

A.A. Alkhimenko , N.O. Shaposhnikov, A.A. Kharkov, D.A. Strekalovskaya , E.L. Alekseeva ,
M. A. Kovalev, M.L. Shishkova*

Peter the Great St. Petersburg Polytechnic University, St. Petersburg, Russia

*E-mail: shishkova_ml@spbstu.ru

Keywords: steel corrosion, corrosion rate, corrosion resistance, steel structures, coating, corrosion protection, corrosion resistant coatings, zinc coating, marine environment

Abstract. The article is devoted to the study of the corrosion resistance of steel pile supports made of pipe steel 09Mn2Si (09G2S), under conditions of cyclic wetting (conditional waterline), where conditions are created for the occurrence of corrosion processes at maximum speeds, and also a study of the protective ability of zinc coating applied to the railing (balustrade) of a steel bridge made of carbon steel of normal quality (St3). It was the bridge structures that became the subject of research. We considered the effects of cyclic wetting, wear, and climatic factors on the materials of piled supports, fences, and coatings intended for operation in the marine structure. We investigated the corrosion resistance of the 09Mn2Si steel used as pile supports of offshore structures. We have found that the corrosion rate of the 09Mn2Si steel does not exceed 0.32 mm/year in the zone of cyclic wetting. We have confirmed that the corrosion rate of steel practically does not change in the sections with damaged coatings and does not depend on the area of the uncoated zone. Measuring the electrochemical potential of 09Mn2Si steel, we have found that short-term friction against a solid only weakly affects the corrosion rate of steel in seawater. We have proposed a methodological approach to assessing the service life of hot-dip galvanized coatings on components of steel structures made of carbon steel of normal quality (St3) intended for operation in marine conditions. A forecast of the durability of 120 μm -thick zinc coatings, expected to provide anti-corrosion protection of steel products for 60 years, was made based on the proposed technique.

1. Introduction

Aside from ships and other watercraft operating at sea, numerous onshore port facilities, fences and fixed bridges across sea straits are installed on supports. Ensuring reliability and durability of such steel structures is a major challenge; for this purpose, data on the corrosion resistance of materials under operating conditions should be obtained at the design stage [1]–[4]. Reference data are generally used to select a corrosion margin; however, the real data may differ considerably because mechanical factors such as wear can have a critical impact in addition to corrosion. To combat this, protective coatings are applied on many structures [5], [6]. The degradation of these coatings depends on their properties and a combination of other characteristics.

Reliable real data on the degree of material degradation can be obtained by conducting experimental field tests, or laboratory studies simulating the service conditions of the structure, in particular accounting for the most aggressive/critical environmental effects.

A steel pile can be schematically represented as consisting of three sections: the upper section is constantly exposed to the marine environment; the medium section is occasionally splashed with seawater; the lower section is immersed in water [7]. This difference in exposure to the corrosive environment largely

Alkhimenko, A.A., Shaposhnikov, N.O., Kharkov, A.A., Strekalovskaya, D.A., Alekseeva, E.L., Kovalev, M.A., Shishkova, M.L. Corrosion resistance of steel structures in marine conditions. Magazine of Civil Engineering. 2021. 108(8). Article No. 10815. DOI: 10.34910/MCE.108.15

© Alkhimenko, A.A., Shaposhnikov, N.O., Kharkov, A.A., Strekalovskaya, D.A., Alekseeva, E.L., Kovalev, M.A., Shishkova, M.L., 2021. Published by Peter the Great St.Petersburg Polytechnic University.



This work is licensed under a CC BY-NC 4.0

determines the distribution and rate of corrosion in objects that are not fully immersed in water. The experience accumulated for operating such steel structures not completely immersed in seawater indicates that the maximum corrosion rates are observed in the region that is periodically exposed to water (splash zone) [8]–[10].

Fig. 1 shows the variation in the corrosion rate for a pile in the zone of cyclic wetting. Furthermore, it was established in [11], [12] that the height of the region with the maximum corrosion damage above the splash zone depends on the wave height at the site where the pile is installed. Therefore, the corrosive wear of piles in operating conditions can be assessed by determining the corrosion rate of the steel from which the piling is made upon cyclic immersion in seawater.

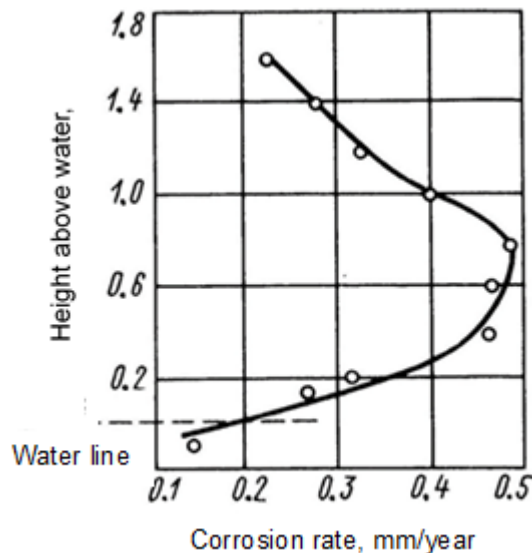


Figure 1. Corrosion rate distribution over a steel pile in the zone of cyclic wetting.

Different polymer coatings can be used to increase the service life of piled supports. If the technology for applying such coatings is exploited correctly, their protective properties are preserved for up to 10 years or more. However, an ice cover forms on most of Russia's inland seas during the winter, so protective polymer coatings of piled supports can be damaged in ice breakup, with bare metal abraded by ice. It is hypothesized that the corrosion rate of bare metal increases significantly in this case [13], which is yet to be fully confirmed experimentally. Experiments on steel wear during friction against ice were carried out in [14]–[19], finding that ice is heavily destroyed even at a 5 MPa pressure against the steel specimen that is not worn out in the process. Assuming that solid objects can be frozen into the ice, leading to mechanical wear of the surface in contact with steel, the corrosion rate of steel in this point can be increased due to the electrode potential difference generated between the mechanically worn segment and the rest of the surface, where an iron oxide film forms in seawater. Ref. [20] determined the magnitude of this potential difference and the time in which the metal surface remains 'activated' (without oxides) after the interaction with the rubbing object has stopped.

Zinc coatings are used for steel onshore structures that need to be in long-term service in the marine environment. Accordingly, the corrosion rates and the durability of the coatings for a specific climatic region should be established rather quickly. The service life of zinc coatings is proportional to their thickness regardless of the application method [10], [21], [22]. Thus, it can be assumed that corrosion of zinc coatings develops over time at an approximately constant rate, which is confirmed experimentally during 8-year tests of zinc in a tropical marine environment, including a sea coast (Fig. 5) [23].

One of the most common methods for assessing the corrosion resistance of coatings in a marine environment is the salt spray test (SST). The temperature in the salt spray chamber is constantly maintained at a level of +35 °C, and the humidity at over 90% by spraying finely atomized droplets of the salt solution, which greatly accelerates the corrosion process. Unfortunately, the results obtained by SST do not answer the question of durability of zinc coatings with a given thickness in real conditions. Full-scale climatic tests make it possible to obtain the most accurate corrosion rates, since they simulate the real operating conditions of the product and allow calculating the durability. However, their main drawback is the considerable time they take. The minimum exposure times of zinc coatings during field tests range from 3 to 8 years. Clearly, a specialized procedure estimating corrosive wear should be worked out for more rapid assessment of durability.

The goal of the study consists in estimating the durability and reliability of structures made of steel materials and steels with coatings in the conditions of the Kerch Strait, exposed to climatic, corrosive and

mechanical impacts. The objectives of the study were an experimental study of the corrosion resistance of steel bridge supports under conditions of variable wetting by sea water, including with local destruction of the paint coating and with short-term mechanical impact on an unprotected metal surface; carrying out accelerated and full-scale climatic tests of zinc-coated steel samples to determine the acceleration coefficient required to calculate the service life of coatings in long-term operation conditions.

2. Methods

The data given in literature indicate that the main critical impacts in the marine environment are cyclic wetting, corrosive abrasion wear, exposure to a salt fog. The correct testing procedure for assessing the durability of steel structures and coated metals can be selected by analyzing the climatic conditions taking into account the level of precipitation (wetting frequency) and temperature, the composition of the environment at the zone of operation, external factors (ice impact, mechanical loads, etc.) to be recreated during the tests.

2.1. Selection of the environment

Before corrosion tests with cyclic wetting can be carried out, the wetting frequency of the specimens should be selected. Fig. 2 shows the effect of the frequency of cyclic wetting in a 0.5 N sodium chloride solution for CT3 steel specimens [24].

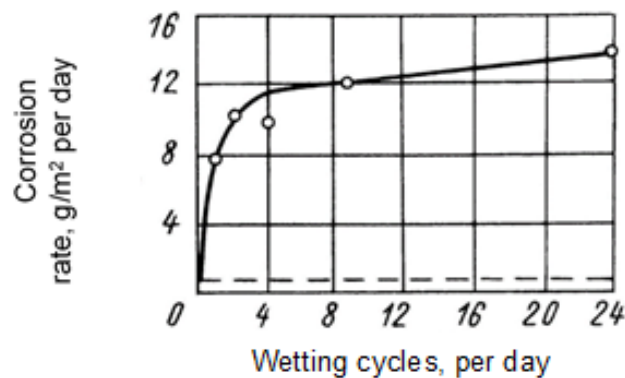


Figure 2. Effect of wetting frequency on corrosion rate for mild steel (ST3 steel).

As follows from Fig. 2, increasing the number of times that the specimens tested are wetted from 4 to 24 a day only slightly affects the corrosion rate. For this reason, the tests were carried out with the specimens periodically immersed in the solution 4 times a day.

The corrosiveness of the environment largely depends on the relatively high concentration of chloride salts, high content of dissolved oxygen and high electrical conductivity. The location of the bridge under construction in the Kerch Strait, connecting the Azov and Black Seas, was the decisive factor in determining the composition and concentration of salts for preparing the test solution. The Azov Sea is small, with a substantial freshwater runoff, making its waters slightly saline (11–13 g/l). The maximum levels of water salinity were observed in the Kerch Strait (13–15 g/l), see Table 1.

Table 1. Ionic composition of water in the Kerch Strait.

Calculated sample composition at depth of 0.7 m		Calculated sample composition at depth of 4.5 m	
Formula	Concentration, mg/dm ³	Formula	Concentration, mg/dm ³
NaCl	3396	NaCl	4457
NaHCO ₃	379	NaHCO ₃	293
CaCl ₂	75	Na ₂ SO ₄	738
CaSO ₄	598	CaSO ₄	2046
MgSO ₄	495	MgSO ₄	1015
Total	4943	Total	8546

The composition corresponding to the most corrosive environment was chosen for the corrosion tests, i.e., the total salinity was 8.55 g/l, Table 2.

Table 2. Calculated salt composition of water samples.

Reagent	Concentration, g/L	Total salinity
NaCl	4.46	
NaHCO ₃	0.29	
CaSO ₄ *2H ₂ O	2.63	8.56
MgSO ₄ *7H ₂ O	2.09	
Na ₂ SO ₄	0.74	

2.2. Estimation of corrosion resistance under cyclic wetting

Tests with cyclic wetting were carried out on flat-plate specimens 50×30×5 mm in size, cut from 09Mn2Si low-alloy pipe steel used in pile-supported bridges. The potential effect of damage to the protective paint coating on the corrosion rate of steel was tested in specimens with various simulated damages and an undamaged paint coating applied to only one side of the specimen (2), specimens with a coating damage area of ~60 mm² (3), specimens with a coating damage area of ~150mm² (4) (Fig. 3).

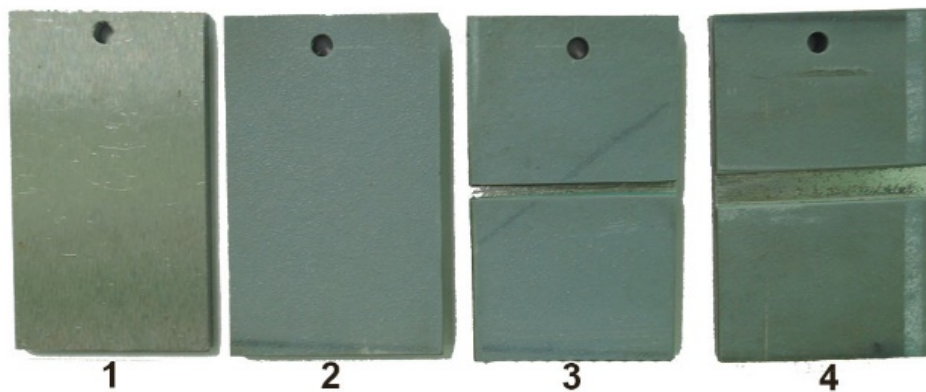


Figure 3. Specimens before testing: 1, uncoated specimen; 2, specimen with coating on one side; 3, no coating over an area of 60 mm²; 4, no coating over an area of 150 mm².

Unpainted and painted specimens with damaged coatings were subjected to cyclic wetting for 30 days. The solution was replaced every 7 days with a freshly prepared one, so the solution of the components was not controlled. Corrosion products consisting of iron hydroxides, which were formed during the interaction of dissolved oxygen and iron ions, did not affect the aggressiveness of the solution. This is due to the fact that the solution was in an open container of a large volume, and this ensured a constant oxygen content in the solution. After the tests were concluded, the specimens were removed from the test solution and cleaned from corrosion products in accordance with Russian State Standard GOST R 9.907-2007 to determine the weight loss and calculate the corrosion rate.

The corrosion rate was found from the weight loss and recalculated in mm/year. The total corrosion rate was calculated by the formula:

$$V = \Delta m / (S \cdot \tau), \quad (1)$$

where Δm is the weight loss, g; S is the surface area of the sample affected by corrosion, m²; τ is the duration of the test, h.

2.3. Estimation of ice-induced wear

We studied the simulated effect of ice on wear using an electrochemical technique, consisting in measuring the electrochemical potential of a steel surface during and after mechanical cleaning. The electrochemical potential of the specimen was measured using a VERSA potentiostat. An EVL-1M3.1 silver chloride electrode was used as a reference electrode. A VED-06 setup was used to rotate the working electrode. A cylindrical specimen serving as the working electrode was fixed in a coupling. The entire surface of the specimen, with the exception of the end face, which was subjected to abrasive friction, was isolated. The appearance of the setup is shown in Fig. 4.

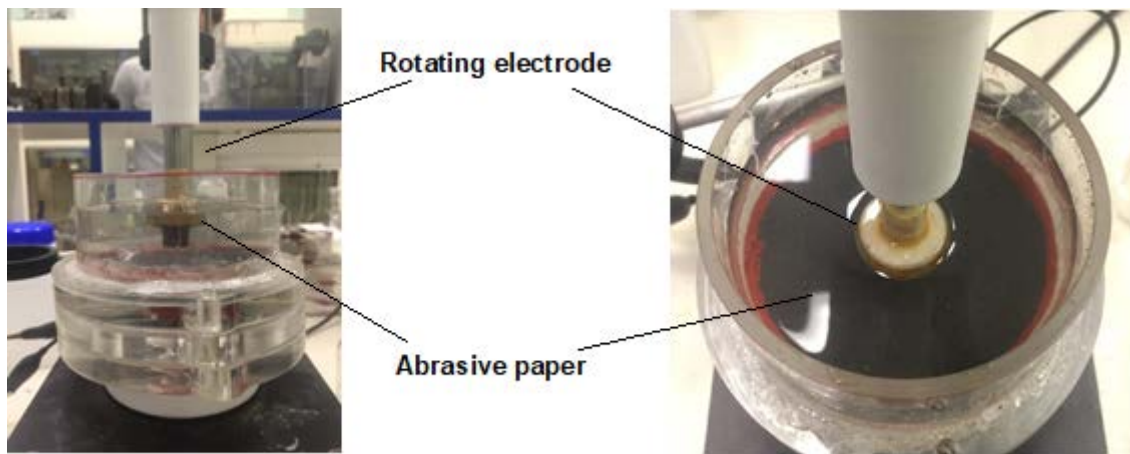


Figure 4.

Appearance of experimental setup.

2.4. Estimation of corrosion resistance in zinc coatings

The specimens for assessing the durability of zinc coatings were plates made of mild steel (St3sp steel) sized 100×50×3 mm with a 120 μm thick hot-dip galvanized (HDG) coating.

Because long-term environmental tests on the coast of the Kerch Strait were not possible, accelerated tests were carried out in a salt spray chamber for 2 months, along with full-scale tests lasting 1 year. In both cases, the corrosion rate of zinc coatings was determined during intermediate examinations of the specimens to estimate the test time required for a constant dissolution rate to be established.

The ratio of the final corrosion rate during tests in a salt spray chamber and in a marine coastal environment can be used to calculate the acceleration factor K . This allows subsequently finding the durability of zinc coatings of any thickness for a given climatic region without long-term environmental tests:

$$T = K \cdot \frac{t}{V_y} \quad (2)$$

$K = V_y/V_a$, where

T is the service life of the zinc coating, years;

K is the acceleration factor;

t is the coating thickness, μm;

V_y is the steady-state corrosion rate of zinc coatings during accelerated tests, μm/year;

V_a is the steady-state corrosion rate of zinc coatings during environmental tests, μm/year;

A more detailed description of the test procedure and metallographic studies of zinc coatings are given in [25]–[28].

3. Results and Discussion

The 09Mn2Si steel specimens were tested under cyclic wetting in a solution with the total salinity of 8.55 g/l (pH 7.4) at room temperature.

Loose reddish brown corrosion products with weak adhesion to the metal were produced during the tests, distributed evenly over the entire surface of unpainted specimens of 09Mn2Si steel. The appearance of the specimens after testing is shown in Fig. 5 (a), the test results are given in Table 3.

As follows from the data obtained, the specimens that were left unpainted had an average corrosion rate of 0.32 mm/year. The specimens which had intact paintwork on one side with the remaining surfaces not isolated from the test solution had an average corrosion rate of 0.30 mm/year. The painted area was not taken into account in the calculations of the corrosion rate.

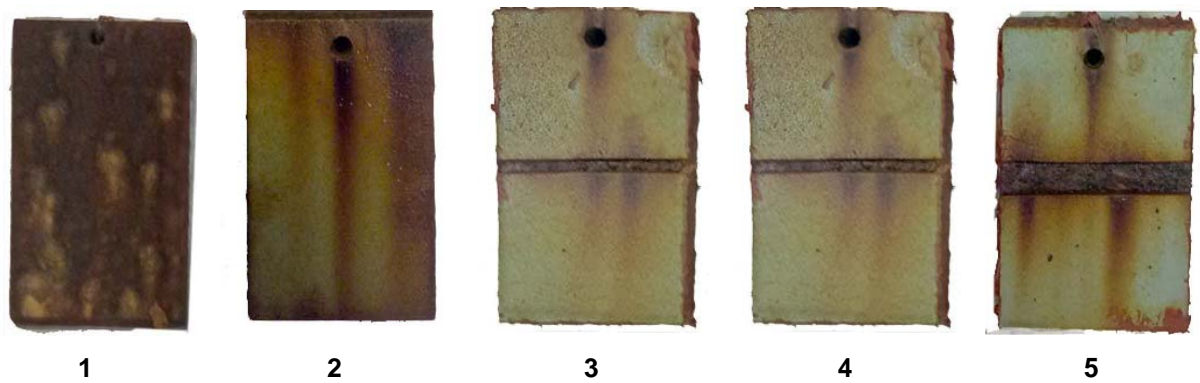


Figure 5. Appearance of specimens after cyclic wetting tests: 1, uncoated specimen; 2, specimen painted on one side; 3, no coating on an area of 60 mm²; 4, no coating on an area of 150 mm².

Table 3. Test results for 09Mn2Si steel specimens at cyclic wetting.

No Specimen	Coating	Corrosion rate, g/m ² *h	Corrosion rate, mm/year	Average corrosion rate, mm/year
1-1		0.3034	0.3198	
1-2	Uncoated specimens	0.3056	0.3236	0.32
1-3		0.3041	0.3211	
2-1		Specimens coated on one side	0.2745	
2-2	0.2606		0.2909	
3-1	No coating over area of 60mm ²	0.2630	0.2935	0.31
3-2		0.2988	0.3335	
3-3		0.2819	0.3147	
4-1	No coating over area of 150 mm ²	0.3072	0.3429	0.32
4-2		0.2786	0.3109	
4-3		0.2735	0.3053	

Specimens with the damaged coating area of 60 mm² and 150 mm² had an average corrosion rate of 0.31 mm/year and 0.32 mm/year. Thus, comparative tests revealed that the presence of mechanical damage to the paintwork does not lead to increased corrosion rates regardless of the area of damage. The corrosion rate of all specimens considered was in the range of 0.30–0.32 mm/year, that is, practically the same. It should be noted that a similar tendency for an increase in the corrosion rate in the zone of variable wetting was shown during the survey of stationary offshore platforms on the shelf of the Black Sea and steel pipes of the pier trestle in the Kola Bay [26, 27].

We experimentally studied the effect of short-term mechanical cleaning of the steel surface during friction against a solid, simulating corrosion-abrasive wear, on the corrosion rate. The experiments consisted in measuring the change in the electrochemical potential during cleaning of the steel surface. We discovered (Fig. 6) that the potential shifts abruptly to negative values from -505 mV to -620 mV from the onset of friction (section 2). This means that the potential difference between cleaned and uncleaned metal surfaces is more than 100 mV. With this potential shift, the corrosion rate of steel increases by more than an order of magnitude. As the friction stops, the potential of the specimen returns to its steady-state value in approximately 17 seconds (section 3). Sections 1 and 4 in Fig. 6 show the electrochemical potential of the specimen in solution before friction started and after it stopped.

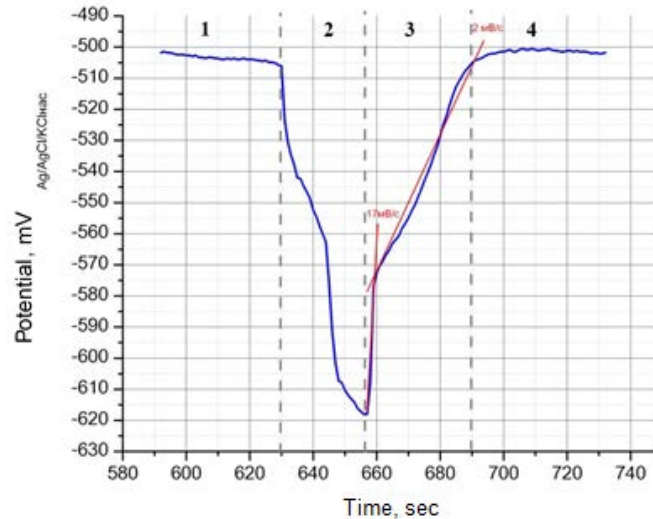


Figure 6. Variation of electrochemical potential of 09Mn2Si steel during friction against a solid.

The total duration of the period when the specimen surface reaches the steady-state electrochemical potential is ~30 s. The data obtained indicate that the metal spends no more than 30 seconds in an active state in a corrosive environment during friction against another solid. A thin oxide film is restored in that time on the surface after friction stops (section 4 in Fig. 6), and the metal potential acquires a steady state when the corrosion rate does not exceed 0.32 mm/year even in the zone with cyclic wetting in the solution whose composition reproduces the seawater in the Kerch Strait. This is a very short period (30 seconds is $\sim 2.5 \cdot 10^{-7}$ of one year), so even assuming that the corrosion rate in the cleaned area increases by 100 times, this metal in this area is expected to thin out by $8.75 \cdot 10^{-6}$ mm ($0.35 \text{ mm/year} \times 100 \times 2.5 \cdot 10^{-7} = 8.75 \cdot 10^{-6} \text{ mm}$) per year. If contact with ice or other solid object at the same point on the surface is repeated 1000 times (which is statistically unlikely), the annual wear of the metal will not increase by more than 10 μm even in this case.

The zinc coatings were measured by a method relying on analysis and processing of the durability data obtained in accelerated tests in the salt spray chamber (Fig. 7) and climatic environmental tests carried out at the coast of the Kerch Strait for 1 year (Fig. 8).

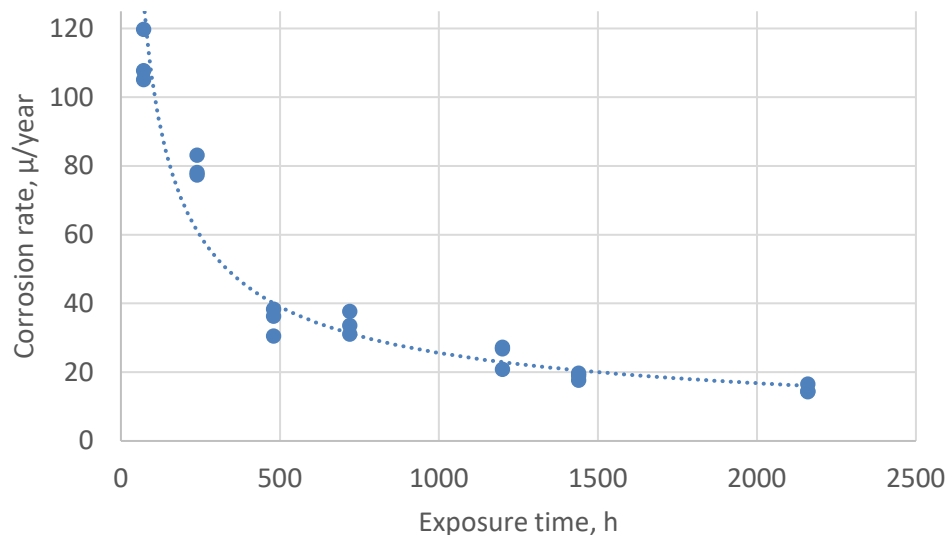


Figure 7. Specimen exposure times in the salt spray chamber versus corrosion rates of zinc coatings.

It is evident from the results obtained in the SST that the corrosion rate decreases from 120 $\mu\text{m}/\text{year}$ to 19 $\mu\text{m}/\text{year}$ upon exposure from 72 to 1440 h, respectively, slightly decreases to 15–17 $\mu\text{m}/\text{year}$ and an increase in exposure to 2280 h, remaining practically unchanged. A possible explanation for this is that

corrosion products form, preventing the corrosive environment from reaching the coating and thus slowing down the dissolution of the zinc coating. Therefore, we can assume that the corrosion rate of zinc coatings takes on a constant value equal to 15–20 $\mu\text{m}/\text{year}$ after accelerated tests lasting about two months.

The corrosion rates established in full-scale tests of the specimens for HDG zinc coatings are shown in Fig. 8. The experiment and results are described in detail in [28].

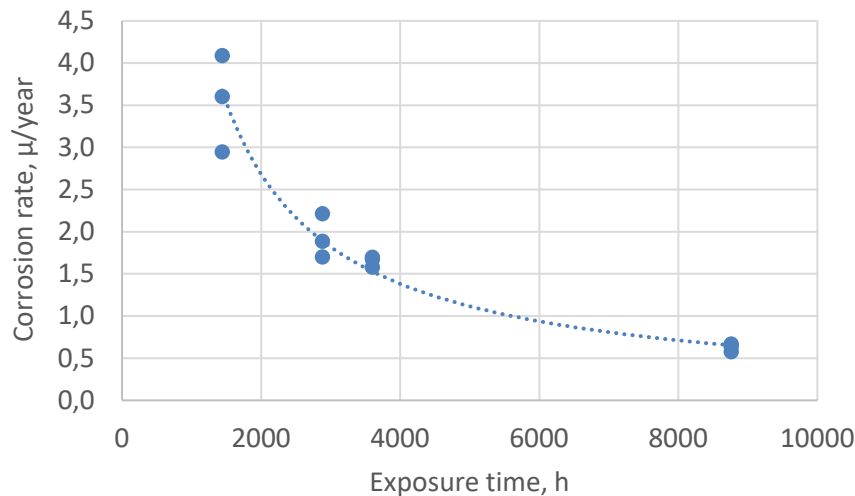


Figure 8. Specimen exposure times in marine environment versus corrosion rates of zinc coatings.

The results of full-scale tests confirm that the corrosion rate of HDG zinc coatings falls from 3.54 $\mu\text{m}/\text{year}$ to 0.63 $\mu\text{m}/\text{year}$ upon exposure from 1440 to 8760 h, respectively. Moreover, a significant drop in the corrosion rate is observed in the first half of the test period, subsequently varying within 1.5 $\mu\text{m}/\text{year}$ (from 1.89 $\mu\text{m}/\text{year}$ to 0.63 $\mu\text{m}/\text{year}$). This means that corrosion processes attenuate during full-scale tests as well as during laboratory tests, which may be due to the protective effect of the resulting zinc corrosion products. The HDG zinc coatings could have been exposed to seasonal changes during 1-year-long climatic tests in the Kerch Strait area.

Assuming that the corrosion rate of zinc coatings has stabilized to 15 $\mu\text{m}/\text{year}$ during tests in the salt spray chamber, the acceleration factor K amounts to ~ 7.9 . Given the steady-state corrosion rate in the accelerated tests, the obtained acceleration factor can be used to find the durability of zinc coatings of any thickness, produced by a different technology, for a given climatic region without long-term environmental tests.

Therefore, it seems reasonable to take the steady-state corrosion rate in climatic tests as equal to 1.9 $\mu\text{m}/\text{year}$ for durability calculations of the zinc coating and the acceleration factor K . In this case, the service life of a 120 μm thick coating will amount to about 63 years.

4. Conclusions

1. We have found that the reliability of steel structures exposed to different impacts in the marine environment can be assessed by designing and conducting various types of tests that simulate individual or combined factors in a specific location: corrosive effect of the environment, effect of climatic factors, mechanical effect in a corrosive environment, effect of emerging defects, etc.

2. The tests performed for the 09Mn2Si pipe steel used for a pile-supported bridge in the Kerch Strait have revealed that the corrosion rate in the cyclic wetting zone, which is the most susceptible to corrosion, does not exceed 0.32 mm/year. Mechanical damage to the paintwork does not lead to an increase in corrosion rates regardless of the damaged area.

3. Considering the effect of short-term mechanical cleaning of the steel surface, simulating friction against a solid body, on the corrosion rate, we have carried out experiments on measuring the variation in the electrochemical potential during cleaning of the steel surface, establishing that the annual wear of the metal should not increase by more than 10 μm even with repeated exposure.

4. Climatic tests of steel specimens with a zinc coating 120 μm thick at the coast of the Kerch Strait showed that the annual wear of the coatings should not exceed 1.9 μm during long-term service. In this

case, the estimated service life of the hot-dip galvanized zinc coating 120 μm thick is expected to last over 60 years.

5. The tests carried out for zinc specimens in a salt spray chamber made it possible to find the acceleration factor in comparison with climatic tests in a marine environment. The obtained acceleration factor can be used to assess the durability of a zinc coating of any thickness, produced by a different technology, for a given climatic region without long-term environmental tests.

5. Acknowledgement

The research is partially funded by the Ministry of Science and Higher Education of the Russian Federation as part of World-class Research Center program: Advanced Digital Technologies (contract No. 075-15-2020-934 dated 07.11.2020)

References

- Ahmad, Z. Selection of Materials for Corrosive Environment. Principles of Corrosion Engineering and Corrosion Control. Elsevier, 2006. Pp. 479–549.
- Makarov, V.N., Ovsyannikov, S. V., Ovchinnikov, I.G. Anti-corrosion protection of bridge structures [Antikorrozionnaya zashchita mostovykh sooruzheniy]. Saratov: Tsentr "Nauka," 2007. 192 p.
- Bashirzade, S.R.O., Ovchinnikov, I.G., Ovchinnikov, I.I. Predicting the behavior of pipeline structures in difficult soil-geological conditions. Part 3. Consideration of the effect of corrosive wear [Prognozirovaniye povedeniya truboprovodnykh konstruksiy v slozhnykh gruntovo-geologicheskikh usloviyakh. Chast' 3. Uchet vliyaniya korrozionnogo iznosa]. Naukovedenie. 2017. 9(5). URL: <https://cyberleninka.ru/article/n/prognozirovanie-povedeniya-truboprovodnykh-konstruksiy-v-slozhnykh-gruntovo-geologicheskikh-usloviyah-chast-3-uchet-vliyaniya> (date of application: 14.10.2021).
- Ovchinnikov, I.I., Ovchinnikov, I.G., Kuznetsov, S.N. The effectiveness and feasibility of applying full pavement paint systems metal structures in the factory [The effectiveness and feasibility of applying full pavement paint systems metal structures in the factory]. Naukovedenie. 2016. 8(4). URL: <http://naukovedenie.ru/index.php?p=vol8-4URLстатья:http://naukovedenie.ru/PDF/87TVN416.pdf> (date of application: 14.10.2021).
- Dawson, J.L., John, G., Oliver, K. Management of corrosion in the oil and gas industry. Shreir's Corrosion. Elsevier, 2010. Pp. 3230–3269.
- Harris, G.M., Lorenz, A. New coatings for the corrosion protection of steel pipelines and pilings in severely aggressive environments. Corrosion Science. 1993. 35(5–8). Pp. 1417–1423. DOI: 10.1016/0010-938X(93)90366-O.
- Galvin, R., Hanley, C., Ruane, K., Murphy, J.J., Jaksic, V. Environmental Impact on Corrosion Rates of Steel Piles Employed in Marine Environment.
- Wang, H.H., Du, M. Corrosion behavior of a low-carbon steel in simulated marine splash zone. Acta Metallurgica Sinica (English Letters). 2017. 30(6). Pp. 585–593. DOI: 10.1007/s40195-017-0535-1.
- Zhao, W.M., Wang, Y., Liu, C., Dong, L.X., Yu, H.H., Ai, H. Erosion-corrosion of thermally sprayed coatings in simulated splash zone. Surface and Coatings Technology. 2010. 205(7). Pp. 2267–2272. DOI: 10.1016/j.surfcoat.2010.09.011.
- Bogorad, I.Y., Iskra, E.V., Klimova, V.A., Kuzmin, Y.L. Korroziya i zashchita morskikh sudov [Corrosion and protection of marine vessels]. Leningrad: Sudostroenie, 1973. 286 p.
- Cole, I.S., Ganther, W.D., Sinclair, J.D., Lau, D., Paterson, D.A. A Study of the Wetting of Metal Surfaces in Order to Understand the Processes Controlling Atmospheric Corrosion. Journal of The Electrochemical Society. 2004. 151(12). Pp. B627. DOI: 10.1149/1.1809596.
- Dillmann, P., Mazaudier, F., science, S.H.-C., 2004, undefined. Advances in understanding atmospheric corrosion of iron. I. Rust characterisation of ancient ferrous artefacts exposed to indoor atmospheric corrosion. Elsevier. URL: <https://www.sciencedirect.com/science/article/pii/S0010938X03002713> (date of application: 18.05.2021).
- Mneniye: o protivokorroziionnoy zashchite trubchatykh opor Kerchenskogo mosta [Opinion: on the anti-corrosion protection of the tubular supports of the Kerch bridge]. URL: <https://territoryengineering.ru/proekty/mnenie-o-protivokorroziionnoj-zashchite-trubchatyh-opor-kerchenskogo-mosta/> (date of application: 17.05.2021).
- Evans, D.C.B., Nye, J.F., Cheeseman, K.J. The kinetic friction of ice. Proceedings of the Royal Society of London. A. Mathematical and Physical Sciences. 1976. 347(1651). Pp. 493–512. DOI: 10.1098/rspa.1976.0013.
- Kennedy, F.E., Schulson, E.M., Jones, D.E. The friction of ice on ice at low sliding velocities. Philosophical Magazine A: Physics of Condensed Matter, Structure, Defects and Mechanical Properties. 2000. 80(5). Pp. 1093–1110. DOI: 10.1080/01418610008212103.
- Maeno, N., Arakawa, M. Adhesion shear theory of ice friction at low sliding velocities, combined with ice sintering. Journal of Applied Physics. 2004. 95(1). Pp. 134–139. DOI: 10.1063/1.1633654.
- Rist, M.A. High-stress ice fracture and friction. Journal of Physical Chemistry B. 1997. 101(32). Pp. 6263–6266. DOI: 10.1021/jp963175x.
- Marmo, B.A., Blackford, J.R., Jeffree, C.E. Ice friction, wear features and their dependence on sliding velocity and temperature. Journal of Glaciology. 2005. 51(174). Pp. 391–398. DOI: 10.3189/172756505781829304.
- Breki, A., Kurakin, M., Liashenko, D., Moskvina, S., Balakin, S. Laws carbonite friction VK8 solid alloy in water environment. Materials Today: Proceedings. 2019. 30. Pp. 718–721. DOI: 10.1016/j.matpr.2020.01.546.
- Alkhimenko, A.A., Kolyushev, I.E., Kharkov, A.A., Shaposhnikov, N.O., Tsvetkov, A.S. Corrosion resistance of steel piling supports

- in sea water. Corrosion: Materials, Protection. 2020. (2). Pp. 16–20. DOI: 10.31044/1813-7016-2020-0-2-16-20.
21. Autengruber, R., Luckeneder, G., Hassel, A.W. Corrosion of press-hardened galvanized steel. Corrosion Science. 2012. 63. Pp. 12–19. DOI: 10.1016/j.corsci.2012.04.048.
 22. Batsunova, T.P. Zashchita Metallicheskih Konstruktsiy ot Korrozii [Protection Of Metal Constructions About Corrosion]. Novosibirsk, 2008, 30 p.
 23. Southwell, C.R., Forgeson, B.W., Alexander, A.L. Corrosion of Metals in Tropical Environments. Corrosion. 1960. 16(10). Pp. 512t-518t. DOI:10.5006/0010-9312-16.10.120.
 24. Rosenfeld, I.L., Zhigalova, K.A. Uskorenyye metody korrozionnykh ispytaniy metallov [Accelerated Methods of Corrosion Testing of Metals]. Moscow: Metallurgy, 1966. 349 p.
 25. Bahadori, A. Engineering Guidelines for Protective Coatings in Buried and Submerged Steel Structures. Essentials of Coating, Painting, and Lining for the Oil, Gas and Petrochemical Industries. Elsevier, 2015. Pp. 411–439.
 26. Popoola, A.P.I., Aigbodion, V.S., Fayomi, O.S.I. Surface characterization, mechanical properties and corrosion behaviour of ternary based ZnZnOeSiO 2 composite coating of mild steel. Journal of Alloys and Compounds. 2016. 654. Pp. 561–566. DOI: 10.1016/j.jallcom.2015.09.090
 27. Org, W.E., Fayomi, O.S.I., Popoola, A.P.I. Electrochemical science An Investigation of the Properties of Zn Coated Mild Steel. 72012. 6555–6570 p.
 28. Kovalev, M., Alekseeva, E., Shaposhnikov, N., Povyshev, A. Predicting the durability of zinc coatings based on laboratory and field tests. E3S Web of Conferences. 2019. 121. Pp. 01008. DOI: 10.1051/e3sconf/201912101008.

Contacts:

Alexey Alkhimenko, 9586435@mail.ru

Nikita Shaposhnikov, shaposhn_no@spbstu.ru

Alexander Kharkov, harkov_aa@spbstu.ru

Darya Strekalovskaya, darya.strek@gmail.com

Ekaterina Alekseeva, alexeeva__ekaterina@mail.ru

Mark Kovalev, kovalev_ma@spbstu.ru

Margarita Shishkova, shishkova_ml@spbstu.ru



ПОЛИТЕХ
Санкт-Петербургский
политехнический университет
Петра Великого

Инженерно-строительный институт
Центр дополнительных профессиональных программ

195251, г. Санкт-Петербург, Политехническая ул., 29,
тел/факс: 552-94-60, www.stroikursi.spbstu.ru,
stroikursi@mail.ru

Приглашает специалистов проектных и строительных организаций,
не имеющих базового профильного высшего образования
на курсы профессиональной переподготовки (от 500 часов)
по направлению «Строительство» по программам:

П-01 «Промышленное и гражданское строительство»

Программа включает учебные разделы:

- Основы строительного дела
- Инженерное оборудование зданий и сооружений
- Технология и контроль качества строительства
- Основы проектирования зданий и сооружений
- Автоматизация проектных работ с использованием AutoCAD
- Автоматизация сметного дела в строительстве
- Управление строительной организацией
- Управление инвестиционно-строительными проектами. Выполнение функций технического заказчика

П-02 «Экономика и управление в строительстве»

Программа включает учебные разделы:

- Основы строительного дела
- Инженерное оборудование зданий и сооружений
- Технология и контроль качества строительства
- Управление инвестиционно-строительными проектами. Выполнение функций технического заказчика и генерального подрядчика
- Управление строительной организацией
- Экономика и ценообразование в строительстве
- Управление строительной организацией
- Организация, управление и планирование в строительстве
- Автоматизация сметного дела в строительстве

П-03 «Инженерные системы зданий и сооружений»

Программа включает учебные разделы:

- Основы механики жидкости и газа
- Инженерное оборудование зданий и сооружений
- Проектирование, монтаж и эксплуатация систем вентиляции и кондиционирования
- Проектирование, монтаж и эксплуатация систем отопления и теплоснабжения
- Проектирование, монтаж и эксплуатация систем водоснабжения и водоотведения
- Автоматизация проектных работ с использованием AutoCAD
- Электроснабжение и электрооборудование объектов

П-04 «Проектирование и конструирование зданий и сооружений»

Программа включает учебные разделы:

- Основы сопротивления материалов и механики стержневых систем
- Проектирование и расчет оснований и фундаментов зданий и сооружений
- Проектирование и расчет железобетонных конструкций
- Проектирование и расчет металлических конструкций
- Проектирование зданий и сооружений с использованием AutoCAD
- Расчет строительных конструкций с использованием SCAD Office

П-05 «Контроль качества строительства»

Программа включает учебные разделы:

- Основы строительного дела
- Инженерное оборудование зданий и сооружений
- Технология и контроль качества строительства
- Проектирование и расчет железобетонных конструкций
- Проектирование и расчет металлических конструкций
- Обследование строительных конструкций зданий и сооружений
- Выполнение функций технического заказчика и генерального подрядчика

По окончании курса слушателю выдается диплом о профессиональной переподготовке
установленного образца, дающий право на ведение профессиональной деятельности

